



# Image reconstruction for Compton camera with application to hadrontherapy

Xavier Lojacono

## ► To cite this version:

Xavier Lojacono. Image reconstruction for Compton camera with application to hadrontherapy. Imaging. INSA de Lyon, 2013. English. NNT : 2013ISAL0126 . tel-01081066

**HAL Id: tel-01081066**

<https://theses.hal.science/tel-01081066>

Submitted on 6 Nov 2014

**HAL** is a multi-disciplinary open access archive for the deposit and dissemination of scientific research documents, whether they are published or not. The documents may come from teaching and research institutions in France or abroad, or from public or private research centers.

L'archive ouverte pluridisciplinaire **HAL**, est destinée au dépôt et à la diffusion de documents scientifiques de niveau recherche, publiés ou non, émanant des établissements d'enseignement et de recherche français ou étrangers, des laboratoires publics ou privés.



Numéro d'ordre:  
2013-ISAL-0126

Année 2013

THÈSE  
présentée devant  
**L’Institut National des Sciences Appliquées de Lyon**  
pour obtenir

**LE GRADE DE DOCTEUR**  
ÉCOLE DOCTORALE : ÉLECTRONIQUE, ÉLECTROTECHNIQUE, AUTOMATIQUE  
Spécialité : STIC Santé

Soutenue publiquement le 26 Novembre 2013 par

Xavier LOJACONO  
Ingénieur ENSEIRB

# **Image reconstruction for Compton camera with application to hadrontherapy**

## Jury

<b>Irène BUVAT</b>	Directeur de Recherche CNRS, Universités Paris 7 et 11	Rapporteur
<b>Magdalena RAFECAS</b>	Professor, University of Valencia	Rapporteur
<b>Denis DAUVERGNE</b>	Directeur de Recherche, CNRS, Université Lyon 1	Examinateur
<b>Laurent DESBAT</b>	Professeur, Université Joseph Fourier, Grenoble	Président du jury
<b>Jean-Michel MOREAU</b>	Professeur, Université Lyon 1	Examinateur
<b>Voichița MAXIM</b>	Maître de Conférences, INSA Lyon	Co-directeur de thèse
<b>Rémy PROST</b>	Professeur, INSA Lyon	Directeur de thèse



# Remerciements

Je ne savais pas trop comment démarrer ces remerciements alors je me suis dit que le plus simple serait d'écrire les choses comme elles viennent, à la volée. Donc il ne s'agit pas d'un classement réfléchi, mais plutôt d'une longue liste de personnes qui m'ont aidé de quelque manière que cela soit au cours de ces 3 années de thèse...

Commençons donc par ces personnes sans qui ces travaux n'auraient pas pu avoir lieu, mes encadrants Voichiță Maxim et Rémy Prost. Un grand merci pour tout, la confiance, ainsi que l'opportunité que vous m'avez proposée à la suite de mon stage au laboratoire CREATIS. Ces travaux ont été conséquents et votre soutien m'a permis d'aller au bout de ces 3 années. Il reste tant à faire, mais si j'ai appris une chose c'est que le plus important dans la recherche n'est pas de voir tout ce qu'il y a encore à accomplir comme un obstacle mais plutôt comme une chance d'aller toujours plus loin. Donc un grand merci à vous.

Il convient alors que mes remerciements vont aussi à toutes les personnes qui ont composé mon jury de thèse et qui ont pu me permettre de franchir cette étape finale de la vie du doctorant. Mes remerciements donc d'abord aux rapporteurs, Magdalena Rafecas et Irène Buvat, mais également aux autres membres, Laurent Desbat, Denis Dauvergne et Jean-Michel Moreau.

Les travaux ont été conduit en lien avec le projet ETOILE et donc conjointement avec le laboratoire IPNL. Ainsi je remercie également Marie-Hélène Richard, Jean-Luc Ley, Etienne Testa, Jochen Krimmer d'une part mais également Marianne Tery d'autre part ainsi que Jean-Michel Létang.

Comme cela est parti, je vais sûrement oublier des personnes, je m'en excuse d'avance. J'ai l'impression de devoir citer l'intégralité du laboratoire CREATIS, et ce n'est pas peu dire, car c'est dans une ambiance des plus sympathiques que j'ai passé ces 3 années et ce aussi bien grâce aux chercheurs/docteurants/ingénieries que grâce au personnel du labo. Commençons par le personnel du labo, avec un grand merci à Marion, Flora, Coupat (Troopa) - JB - Cécilia (le trio fantastique), Christiane, Nadzeu, Fabrice et Pierre (pour le pc et le cluster) et Jérôme.

En ce qui concerne les chercheurs/ingénieries, merci à Olivier et Olivier, Thomas, Denis, Adeline, Elisabeth, Hervé, Maciej, Sébastien, Didier et Claire.

Passons à ces délinquants de docteurs/docteurants. Ils ont eu beau dénigrer mes boules blanches sur fond noir, je tenais à remercier tous ces vilains petits canards ! Merci donc à mes prédécesseurs et mentors...non, en fait juste prédécesseurs, hahaha! Dbbek, Maria (95001), Chris (Oppa salsa style ?), Simon (merci aussi pour la rando neige...), François (ouiii j'ai plein d'amis et alors !), Niaf-Niaf (qui je suis sûr devait stresser pour moi le jour de la soutenance, et juste pour le plaisir, "Merki"), et Rémy...oups, une erreur s'est glissée, Rémy n'est, techniquement, pas un prédécesseur. Allez mon vieux, il va vraiment falloir t'y mettre là... Mouhahaha!

Il y a eu plein de petits jeunots arrivés pour prendre la relève, Hector (Macheteee), ShengFuuuu (qui est complètement fouuu !!), Mae (Help meee), Toulemonde, Estelle (sa

ka maché ? Pani problem), Matthew, Sébastien, Oana, Jérôme (Hey monkey, get funky), merci à vous et un bon courage pour le travail à venir ! CREATIS est un laboratoire riche de différentes cultures, et j'ai pu pleinement profiter de cet aspect pendant 3 ans... je tiens à dire : multumesc à Valentina, Elena (te pup papa!), Andreea, Razvan, Anca și Alina, gracias à Juan (Carlos y Gabriel), Ricardo, Carolina, Diego, William y Alfredo (Yo no soy el tio...), xiè xiè à Pei Dong, Fang Lue, Li Hui, Yang Feng, HongYing, Yue Zhao, XinXin.

Une communauté (malheureusement moins) connue du public devrait aussi être à l'honneur, car elle aussi possède cette richesse culturelle : l'Association des Doctorants de l'Insa de Lyon (ADIL). Merci à vous les amis ADILiens, Romain (En avant pour le CCE...ou la thèse... faudra faire un choix à mon avis), Johan, Dimitri, Julien, Clément, Aurélien, Guillaume (ENSEIRB...,ENSEIRB... tu connais la suite).

À présent, je pense qu'un merci à mon entourage s'impose car ce dernier a pas mal joué sur la conduite de ces travaux. Comment ne pas remercier mes parents pour avoir mis au monde ce petit chef d'œuvre que j'incarne...heu...hum...bref, merci à eux pour leur soutien, et merci à mes frangins...la compétition a parfois du bon (heu, j'ai gagné, non?). Merci à ma Lisa (Choubidou) qui a du supporter l'homme des cavernes que je suis devenu lors de la rituelle hibernation de 3ème année. Ces travaux c'est aussi grâce à toi, donc quelque part, tu es aussi docteur. Au passage, merci aux Patchawaks et compagnie. Merci aussi aux amis, Aurélien, Mélo, Adeline, Mémo, Paula, Jean...et caetera desunt.

Je ne sais pas si j'ai oublié des gens (merci et désolé pour l'oubli), mais il y a une instance à remercier également...car sans elle, cette thèse n'aurait pas pu aller à son terme...et surtout les susnommés vilains petits canards me l'ont expressément demandé...alors : merci Youtube...premier fournisseur de vidéos stupides, mais également, la source de toutes mes playlists musicales.

# Résumé

La caméra Compton est un dispositif permettant d'imager les sources de rayonnement gamma. Les avantages de ce système résident dans sa sensibilité, en raison de l'absence de collimateur mécanique, mais également dans la possibilité de reconstruire des images 3D avec un dispositif immobile. Ce système est également adapté pour des sources à large spectre énergétique. Ses avantages en font un candidat prometteur en médecine nucléaire (Single Photon Emission Computed Tomography) et en hadronthérapie. Cependant, les méthodes de reconstruction sont plus complexes que celles des modalités d'imagerie traditionnelles.

Ces travaux, financés par le projet européen ENVISION (European NoVel Imaging Systems for ION therapy) Coopération-FP7, portent sur le développement de méthodes de reconstruction d'images pour la caméra Compton. La surveillance de la thérapie par ions nécessite idéalement une reconstruction des images en temps réel avec une précision millimétrique, même si le nombre de données acquises est relativement faible.

A partir de la caméra Compton, on obtient des projections coniques de la source de photons. Nous avons développé des méthodes analytiques et itératives afin de reconstruire la source à partir de ces projections. Leurs performances sont analysées dans le contexte d'acquisitions réalistes: géométrie de la caméra, nombre d'événements, . . . . Nous avons développé une méthode analytique de rétroposition filtrée. Cette méthode est rapide mais nécessite beaucoup de projections. Nous avons également développé des méthodes itératives utilisant un algorithme de maximisation de la fonction de vraisemblance. En comparaison avec les méthodes analytiques, les méthodes itératives permettent de prendre en compte les propriétés statistiques des données et la configuration du détecteur via la matrice de formation de l'image(matrice système). Nous avons proposé un nouveau modèle probabiliste pour l'estimation des éléments de cette matrice et différentes approches pour le calcul de ses éléments: l'une néglige les incertitudes de mesure, l'autre prend en compte ces incertitudes en utilisant une distribution gaussienne. Nous avons également proposé une méthode simplifiée (donc plus rapide) utilisant notre modèle probabiliste. La nouveauté des méthodes proposées repose aussi sur le calcul des éléments de la matrice par une discréttisation spécifique des projections coniques. Plusieurs reconstructions sont menées à partir de données simulées, que nous avons obtenues avec Geant4, et aussi de données provenant de plusieurs prototypes simulés de caméra Compton proposés par l'Institut de Physique Nucléaire de Lyon (IPNL) et par le Centre de recherche de Dresde-Rossendorf en Allemagne. Les résultats sont prometteurs et des études plus poussées, à partir de données encore plus réalistes, viseront à les confirmer.

# Abstract

The Compton camera is a device for imaging gamma radiation sources. The advantages of the system lie in its sensitivity, due to the absence of mechanical collimator, and the possibility to reconstruct 3D images with a stationary device. This system is also well suited for imaging wide energy spectrum sources. These advantages make it a promising candidate for application in nuclear medicine (Single Photon Emission Computed Tomography) and hadrontherapy. However, the reconstruction methods are complex compared to conventional modalities.

Funded by the european project ENVISION (European NoVel Imaging Systems for ION therapy) FP7-Cooperation Work Program, this work deals with the development of image reconstruction methods for the Compton camera. Ideally, ion therapy monitoring requires real time reconstruction of images with a millimeter accuracy even when the number of acquired events is relatively low.

From the device, we obtain cone-surface projections of the gamma source distribution. In this work, we developed both analytical and iterative methods in order to reconstruct the source from these cone-surface projections. Their performances are analyzed with regards to the context (geometry of the camera, number of events). We developed an analytical method using a Filtered BackProjection (FBP) formulation. This method is fast but really sensitive to the noise. We have also developed iterative methods using a List Mode-Maximum Likelihood Expectation Maximization (LM-MLEM) algorithm. In contrast with analytical methods, the iterative ones enable to take into account the statistical properties of the data and the configuration of the detector through the system matrix. We have proposed a new probabilistic model for the computation of the elements of the system matrix and different approaches for the calculation of these elements: an approach neglecting the measurement uncertainties; another taking into account these uncertainties using a Gaussian distribution. We also implemented a simplified method using the probabilistic model we proposed. Apart from the model, the novelty of the method lies on the specific discretization of the cone-surface projections. The methods are tested on cameras simulated with MEGAlib (based on Geant4) and the influences of the size of the camera, of the model, and of the number of events are evaluated. Then, several studies are carried out on data simulated from prototypes of Compton cameras under study at the Institut de Physique Nucléaire de Lyon (IPNL) and at the Research Center of Dresden-Rossendorf, respectively. Results are promising, and further investigations on more realistic data are to be done.

# INSA Direction de la Recherche - Ecoles Doctorales - Quinquennat 2011-2015

SIGLE	ECOLE DOCTORALE	NOM ET COORDONNEES DU RESPONSABLE
CHIMIE	<b>CHIMIE DE LYON</b> <a href="http://www.edchimie-lyon.fr">http://www.edchimie-lyon.fr</a>  Insa : R. GOURDON	<b>M. Jean Marc LANCELIN</b> Université de Lyon – Collège Doctoral Bât ESCPE 43 bd du 11 novembre 1918 69622 VILLEURBANNE Cedex Tél : 04.72.43 13 95 <a href="mailto:directeur@edchimie-lyon.fr">directeur@edchimie-lyon.fr</a>
E.E.A.	<b>ELECTRONIQUE, ELECTROTECHNIQUE, AUTOMATIQUE</b> <a href="http://edeeaa.ec-lyon.fr">http://edeeaa.ec-lyon.fr</a>  Secrétariat : M.C. HAVGOUDOUIKIAN <a href="mailto:eea@ec-lyon.fr">eea@ec-lyon.fr</a>	<b>M. Gérard SCORLETTI</b> Ecole Centrale de Lyon 36 avenue Guy de Collongue 69134 ECULLY Tél : 04.72.18 60 97 Fax : 04 78 43 37 17 <a href="mailto:Gerard.scorletti@ec-lyon.fr">Gerard.scorletti@ec-lyon.fr</a>
E2M2	<b>EVOLUTION, ECOSYSTEME, MICROBIOLOGIE, MODELISATION</b> <a href="http://e2m2.universite-lyon.fr">http://e2m2.universite-lyon.fr</a>  Insa : H. CHARLES	<b>Mme Gudrun BORNETTE</b> CNRS UMR 5023 LEHNA Université Claude Bernard Lyon 1 Bât Forel 43 bd du 11 novembre 1918 69622 VILLEURBANNE Cédex Tél : 04.72.43.12.94 <a href="mailto:e2m2@biomserv.univ-lyon1.fr">e2m2@biomserv.univ-lyon1.fr</a>
EDISS	<b>INTERDISCIPLINAIRE SCIENCES-SANTE</b> <a href="http://ww2.ibcp.fr/ediss">http://ww2.ibcp.fr/ediss</a>  Sec : Safia AIT CHALAL Insa : M. LAGARDE	<b>M. Didier REVEL</b> Hôpital Louis Pradel Bâtiment Central 28 Avenue Doyen Lépine 69677 BRON Tél : 04.72.68 49 09 Fax : 04 72 35 49 16 <a href="mailto:Didier.revel@creatis.uni-lyon1.fr">Didier.revel@creatis.uni-lyon1.fr</a>
INFOMATHS	<b>INFORMATIQUE ET MATHÉMATIQUES</b> <a href="http://infomaths.univ-lyon1.fr">http://infomaths.univ-lyon1.fr</a>	<b>M. Johannes KELLENDONK</b> Université Claude Bernard Lyon 1 INFOMATHS Bâtiment Braconnier 43 bd du 11 novembre 1918 69622 VILLEURBANNE Cedex Tél : 04.72. 44.82.94 Fax 04 72 43 16 87 <a href="mailto:infomaths@univ-lyon1.fr">infomaths@univ-lyon1.fr</a>
Matériaux	<b>MATERIAUX DE LYON</b>  Secrétariat : M. LABOUNE PM : 71.70 –Fax : 87.12 Bat. Saint Exupéry <a href="mailto:Ed.materiaux@insa-lyon.fr">Ed.materiaux@insa-lyon.fr</a>	<b>M. Jean-Yves BUFFIERE</b> INSA de Lyon MATEIS Bâtiment Saint Exupéry 7 avenue Jean Capelle 69621 VILLEURBANNE Cédex Tél : 04.72.43 83 18 Fax 04 72 43 85 28 <a href="mailto:Jean-yves.buffiere@insa-lyon.fr">Jean-yves.buffiere@insa-lyon.fr</a>
MEGA	<b>MECANIQUE, ENERGETIQUE, GENIE CIVIL, ACOUSTIQUE</b>  Secrétariat : M. LABOUNE PM : 71.70 –Fax : 87.12 Bat. Saint Exupéry <a href="mailto:mega@insa-lyon.fr">mega@insa-lyon.fr</a>	<b>M. Philippe BOISSE</b> INSA de Lyon Laboratoire LAMCOS Bâtiment Jacquard 25 bis avenue Jean Capelle 69621 VILLEURBANNE Cedex Tél : 04.72.43.71.70 Fax : 04 72 43 72 37 <a href="mailto:Philippe.boisse@insa-lyon.fr">Philippe.boisse@insa-lyon.fr</a>
ScSo	<b>ScSo*</b>  M. OBADIA Lionel  Sec : Viviane POLSINELLI Insa : J.Y. TOUSSAINT	<b>M. OBADIA Lionel</b> Université Lyon 2 86 rue Pasteur 69365 LYON Cedex 07 Tél : 04.78.69.72.76 Fax : 04.37.28.04.48 <a href="mailto:Lionel.Obadia@univ-lyon2.fr">Lionel.Obadia@univ-lyon2.fr</a>

\*ScSo : Histoire, Geographie, Aménagement, Urbanisme, Archéologie, Science politique, Sociologie, Anthropologie



# Contents

Résumé	v
Abstract	vi
Contents	xii
List of symbols	xiii
<b>I General Introduction</b>	<b>1</b>
<b>Introduction (français)</b>	<b>3</b>
Objectifs . . . . .	3
Organisation du manuscrit . . . . .	3
<b>1 Introduction</b>	<b>7</b>
1.1 Objectives . . . . .	7
1.2 Thesis organization . . . . .	8
<b>II Compton imaging</b>	<b>11</b>
<b>Résumé en français (Abstract in French)</b>	<b>13</b>
Imagerie Compton . . . . .	13
État de l'art . . . . .	13
<b>2 Hadrontherapy</b>	<b>19</b>
2.1 Treatment . . . . .	20
2.2 Monitoring: state of the art . . . . .	20
<b>3 Fundamentals of particle physics and <math>\gamma</math>-ray detection devices</b>	<b>23</b>
3.1 Interaction of gamma rays . . . . .	23
3.1.1 Photoelectric absorption . . . . .	24
3.1.2 Compton scattering . . . . .	24
3.1.3 Electron-positron pair creation . . . . .	26
3.2 Detection of gamma photons . . . . .	27
3.3 Gamma cameras . . . . .	28
3.3.1 Anger camera . . . . .	28
3.3.2 Compton camera . . . . .	28
3.4 Compton detection model . . . . .	29

<b>4 Image reconstruction: state of the art</b>	<b>31</b>
4.1 Analytical methods . . . . .	32
4.1.1 Direct reconstruction with a restricted set of cone surface projections	32
4.1.2 Direct reconstruction using a full set of available projections . . . . .	34
4.1.3 Expansion in spherical harmonics . . . . .	34
4.2 Iterative methods . . . . .	36
4.2.1 The LM-MLEM algorithm . . . . .	36
4.2.2 Algebraic Reconstruction Technique (ART) . . . . .	40
4.2.3 Bayesian image reconstruction . . . . .	40
4.2.4 Stochastic Origin Ensemble (SOE) . . . . .	41
 <b>III Analytical method</b>	 <b>43</b>
 <b>Résumé en français (Abstract in French)</b>	 <b>45</b>
Inversion de la transformée Compton . . . . .	45
Rétroprojection filtrée pour imagerie Compton . . . . .	45
Résultats . . . . .	45
 <b>5 Filtered Backprojection algorithm</b>	 <b>53</b>
5.1 Compton transform . . . . .	53
5.1.1 Model for the Compton camera . . . . .	53
5.1.2 Model of the projections . . . . .	54
5.2 Parameterization of the forward projection problem . . . . .	56
5.2.1 Parametrization of the Compton cone . . . . .	56
5.2.2 Expression of the projections . . . . .	58
5.2.3 Dual expression of the projections . . . . .	58
5.3 Inversion of the Compton transform . . . . .	59
5.3.1 Hankel Fourier Transform . . . . .	59
5.3.2 Projection slice theorem . . . . .	60
5.3.3 Inversion formula . . . . .	60
5.4 Filtered Back Projection algorithm . . . . .	61
5.4.1 Mathematical formulation . . . . .	61
5.4.2 Application of the FBP . . . . .	63
 <b>6 Results</b>	 <b>65</b>
6.1 Data simulation . . . . .	65
6.1.1 Compton camera . . . . .	66
6.1.2 Simulated source . . . . .	66
6.1.3 Influence of the number of bins . . . . .	67
6.2 Finite detector size consequences . . . . .	68
6.2.1 Quality of the image as function of the angle $\theta_g$ for a small camera .	68
6.2.2 Quality of the image as function of the angle $\beta$ for a small camera .	71
6.3 Conclusion . . . . .	76

<b>IV Iterative methods</b>	<b>77</b>
<b>Résumé en français (Abstract in French)</b>	<b>79</b>
LM-MLEM: nouvelle formulation mathématique pour l'estimation de la matrice système . . . . .	79
Méthode de sélection des génératrices du cône Compton . . . . .	79
Résultats . . . . .	79
<b>7 LM-MLEM: Novel mathematical formulation for the estimation of the system matrix</b>	<b>89</b>
7.1 Probabilistic model for the system matrix elements . . . . .	90
7.2 Numerical evaluation of the system matrix . . . . .	95
7.2.1 A model that neglects uncertainties on the energy measurements . .	96
7.2.2 A model that accounts for uncertainties on the energy measurements	100
7.3 Simplified method: $t_{ij}$ estimation using voxel centers . . . . .	104
<b>8 Selection of the generatrices</b>	<b>107</b>
8.1 The guiding surface . . . . .	107
8.2 Conic section tracking: initialization . . . . .	109
8.3 Conic section tracking . . . . .	111
8.4 Conic section tracking: discussion . . . . .	112
<b>9 Results</b>	<b>115</b>
9.1 Reconstruction of a spherical source . . . . .	115
9.1.1 Single event back-projections . . . . .	116
9.1.2 Reconstructions with 5000 events . . . . .	116
9.2 Influence of the incomplete absorptions . . . . .	126
9.3 Reconstruction of a line source . . . . .	131
9.3.1 Context of the simulation . . . . .	132
9.3.2 Results . . . . .	132
9.4 Influence of the probabilistic model . . . . .	138
9.5 Conclusion . . . . .	142
<b>V Application to ENVISION project</b>	<b>143</b>
<b>10 Application to data from the Institut de Physique Nucléaire de Lyon, France</b>	<b>145</b>
10.1 Compton camera design . . . . .	145
10.2 Simulations . . . . .	147
10.3 Low statistics reconstruction of the Compton camera Point Spread Function in 3D prompt- $\gamma$ imaging of ion beam therapy . . . . .	147
10.3.1 Source . . . . .	147
10.3.2 Data . . . . .	148
10.3.3 Results . . . . .	148
10.3.4 Point Spread Function . . . . .	150
10.3.5 Influence of the position of the source . . . . .	153
10.3.6 Discussion . . . . .	154

<b>11 Application to data from the Research Center of Dresden-Rossendorf, Germany</b>	<b>157</b>
11.1 Simulation context . . . . .	157
11.2 Three Point Sources . . . . .	158
11.3 Line source . . . . .	159
11.4 Hot-Cold phantom . . . . .	161
11.5 Conclusion . . . . .	164
<b>VI Conclusion</b>	<b>165</b>
<b>Contributions (français)</b>	<b>167</b>
Perspectives . . . . .	167
<b>12 Conclusions and perspectives</b>	<b>171</b>
12.1 Main contributions . . . . .	171
12.2 Perspectives . . . . .	172
<b>Bibliography</b>	<b>183</b>

# List of symbols and abbreviation

## List of symbols

$h$	<i>Plank's constant</i>
$m_e$	<i>mass of an electron at rest</i>
$r_e$	<i>classical radius electron</i>
$c$	<i>speed of light</i>
$E_0$	<i>initial energy of a detected photon</i>
$E_1$	<i>energy delivered to the electron during the Compton scattering process</i>
$E_2$	<i>energy of the Compton scattered photon</i>
$\theta_M$	<i>incident angle of the photon emitted at <math>M</math></i>
$\mathcal{C}(V_1, V_2, \beta)$	<i>Compton cone of apex <math>V_1</math>, axis direction <math>\overrightarrow{V_2V_1}</math>, half-opening angle <math>\beta</math></i>
$\theta_g$	<i>polar angle of the Compton cone axis</i>
$K(\beta, E_0)$	<i>Klein-Nishina coefficient accounting for Compton scattering cross section</i>
$Pf$	<i>Compton projections: cone surface projections</i>
$\mathcal{F}$	<i>1D Fourier transform</i>
$\mathcal{F}_2$	<i>2D Fourier transform</i>
$\mathcal{HF}$	<i>Hankel-Fourier transform</i>
$J_0$	<i>zero-order Bessel function of the first kind</i>
$i$	<i>index of events</i>
$j$	<i>index of voxels</i>
$l$	<i>index of iterations</i>
$v_j$	<i>voxel <math>j</math></i>
$e_i$	<i>event <math>i</math> with the set of parameters <math>(V_1, E_1, V_2, E_2)</math></i>
$N_v$	<i>number of voxels</i>
$N_e$	<i>number of events</i>
$N_l$	<i>number of iterations</i>
$\lambda$	<i>mean number of emitted photons by the voxel <math>v_j</math></i>
$\mathcal{P}$	<i>Poisson law</i>
$\mathbf{T} = (t_{ij})$	<i>System matrix</i>
$s_j$	<i>sensitivity</i>

## List of symbols

$\mu_C$	<i>Compton scattering cross section</i>
$\mu_{1,a}$	<i>cross section of total absorption in the scatterer</i>
$\mu_{2,a}$	<i>cross section of total absorption in the absorber</i>
$\sigma(E_1)$	<i>energetic resolution of the scatterer</i>
$\sigma(E_2)$	<i>energetic resolution of the absorber</i>
$d_1$	<i>distance travelled by the incident photon until it is scattered</i>
$d_{12}$	<i>distance travelled by the scattered photon in the scattering detector</i>
$d_2$	<i>distance travelled by the scattered photon in the second detector until it is absorbed</i>
$h$	<i>spatial kernel, event specific</i>

## Abbreviations

CV	<i>Center of Voxel method</i>
SI	<i>Surface of Intersection method</i>
VI	<i>Volume of Intersection method</i>
NMSE	<i>Normalized Mean Squared Error</i>
FWHM	<i>Full Width at Half Maximum</i>
LM-MLEM	<i>List-Mode Maximum Likelihood Expectation Maximization</i>
ESM	<i>Ellipse Stack Method</i>
RTM	<i>Ray Tracing Method</i>
IQR	<i>Inter Quartile Range</i>
PSF	<i>Point Spread Function</i>
ENVISION	<i>European NoVel Imaging Systems for ION therapy</i>
WP3	<i>WorkPackage 3</i>

# I General Introduction

---



# Introduction (in French)

## Objectifs

Le cancer est une des causes majeures de mortalité dans le monde. En 2008, on comptait 7.6 millions de décès (environ 13% de la mortalité mondiale) dus à cette maladie et environ 12.7 millions de nouveaux cas ont été diagnostiqués. Les plus grands nombres de décès sont provoqués par les cancers du poumon, de l'estomac, du foie, du colon, du sein. D'après les projections, la mortalité due au cancer continuera à augmenter pour atteindre 13.1 millions de décès en 2030, selon les estimations<sup>1</sup>.

Le traitement de cette maladie nécessite souvent plusieurs interventions soigneusement sélectionnées parmi les différentes techniques telles que la chirurgie, la radiothérapie ou la chimiothérapie. Parfois, ces traitements sont combinés. Dans certains cas difficiles, la chirurgie et la chimiothérapie sont impraticables, la radiothérapie étant alors le traitement le plus approprié. Néanmoins, certaines tumeurs sont radiorésistantes. L'hadrithérapie, qui utilise des particules chargées telles que les ions carbone ou des protons, est une alternative possible. Cette modalité de traitement présente certains avantages par rapport à la radiothérapie, offrant une meilleure balistique et une efficacité accrue vis à vis du dépôt de dose. Cependant, ces avantages requièrent un suivi précis du traitement afin de garantir la sécurité du patient.

L'imagerie médicale fournit plusieurs outils pour effectuer un contrôle du traitement. L'utilisation des techniques d'imagerie est aujourd'hui devenue une méthode essentielle permettant de visualiser l'anatomie ou le métabolisme du corps humain et de suivre le traitement d'une maladie ainsi que sa progression. Utilisant des phénomènes physiques tels que l'absorption des rayons X, la résonance magnétique nucléaire, les ultrasons ou la radioactivité, l'imagerie médicale représente tous les moyens qui permettent d'obtenir des informations sur les organes, les cellules ou les lésions (taille, volume, localisation, forme) ou leur fonctionnement (métabolisme). Ces informations servent ensuite à créer une image exploitable en clinique par le corps médical, pour le diagnostic ou le contrôle.

Pour le suivi de traitements du cancer par hadronthérapie, plusieurs méthodes sont utilisées ou à l'étude. Nous avons par exemple la tomographie par émission de positons (TEP), et la Tomographie d'Emission MonoPhotonique (TEMP). C'est dans ce contexte que le projet European NoVel Imaging Systems for ION therapy (ENVISION) a été lancé

---

<sup>1</sup>Source : Organisation mondiale de la Santé , <http://www.who.int/mediacentre/factsheets/fs297/en/index.html>

---

en février 2010. Ce projet est financé par la commission européenne sous la convention de subvention FP7-N.241851. Son objectif est d'améliorer la qualité des outils pour le contrôle en hadronthérapie. Le projet vise à fournir des solutions pour : la surveillance non invasive en temps réel, l'imagerie quantitative, la détermination précise de la dose administrée, la rétroaction rapide pour une planification de traitement optimale, une réponse en temps réel au mouvement des organes, une série d'études en simulation. Le projet ENVISION est une collaboration de seize centres européens de recherche et des partenaires industriels, coordonnés par le Conseil Européen pour la Recherche Nucléaire (CERN) et sous l'égide de ENLIGHT, the European Network for Light Ion Hadron Therapy.

Dans le cadre de ce projet, le groupe de travail 3 se consacre à l'élaboration d'un dispositif d'imagerie pour effectuer le suivi du traitement. Plusieurs systèmes sont à l'étude. Parmi eux, la caméra Compton s'avère être un candidat intéressant. Ce système, également appelé caméra à collimation électronique, permet de détecter, par effet Compton, les photons  $\gamma$  émis par la zone traitée. À partir des mesures réalisées, on peut fournir une image de la source des particules en utilisant des méthodes de reconstruction d'image.

Cette thèse de doctorat s'inscrit dans le cadre des travaux de ce groupe de travail, et plus précisément sur la tâche de reconstruction. L'objectif était de développer des méthodes de reconstruction d'image 3D pour l'imagerie Compton avec application en hadronthérapie. Plusieurs contraintes sont intrinsèques à cette application, en particulier le faible nombre des données recueillies lors du traitement et la surveillance en temps réel. Nos travaux visent à la fois le développement de méthodes analytique et itératives. La contribution principale est double: (i) une méthode de RétroProjection Filtrée pour l'aspect analytique, (ii) un algorithme de maximisation de la fonction de vraisemblance en mode liste pour l'aspect itératif. Pour ce dernier, nous avons proposé un nouveau modèle pour l'estimation des éléments de la matrice système utilisée lors de la reconstruction.

## Organisation du manuscrit

Le manuscrit est composé de quatre parties. Dans la première, nous donnons un aperçu de l'hadronthérapie, son histoire et ses avantages. Nous faisons également un état de l'art des méthodes utilisées actuellement pour la surveillance du traitement. Comme nous nous concentrons sur l'imagerie Compton, nous présentons ensuite le fonctionnement de la caméra Compton, en commençant par donner quelques notions fondamentales de la physique des particules. Ensuite nous décrivons les  $\gamma$  caméras. Nous passons en revue par la suite les méthodes pour l'imagerie Compton en présentant un état de l'art des algorithmes analytiques et itératifs.

Dans la deuxième partie, nous nous focalisons sur les méthodes analytiques, en particulier les travaux effectués par [Maxim *et al.* (2009)]. Ces travaux sont le point de départ de notre première contribution, une méthode de rétroprojection filtrée. Nous détaillons ensuite notre méthode et présentons l'outil MEGALib [Zoglauer (2005)] qui nous a permis d'effectuer les simulations. Nous complétons l'étude théorique par nos résultats de

---

reconstructions obtenus à partir de ces données simulées et nous effectuons une étude de l'influence de la taille des détecteurs de la caméra Compton, ainsi que de l'influence de plusieurs paramètres spécifiques à la reconstruction analytique sur la qualité des images.

La troisième partie traite des méthodes itératives basées sur la maximisation de la vraisemblance par maximisation de l'espérance (MLEM). Nous proposons un nouveau modèle probabiliste d'estimation des éléments de la matrice système. L'évaluation de ces éléments est effectuée par le calcul numérique d'une formule d'intégration. Nous proposons d'abord une première approche pour effectuer ce calcul, dans lequel nous ne prenons pas en compte les incertitudes sur les mesures d'énergie de la caméra Compton. Nous détaillons une seconde approche du calcul numérique de la formule intégrale dans laquelle nous prenons en compte ces incertitudes. Nous nous proposons ensuite d'utiliser une méthode simplifiée avec le modèle probabiliste que nous avons établi. Finalement, nous menons une étude sur la reconstruction de sources distinctes tant par la forme que par leur niveau énergétique. Nous discutons de l'influence des caractéristiques du dispositif d'imagerie, du modèle probabiliste proposé ainsi que des incertitudes dues aux absorptions incomplètes des photons par la caméra.

Dans la dernière partie, nous présentons les reconstructions réalisées dans le cadre du projet ENVISION. Différents prototypes de caméra Compton sont actuellement en cours de développement dans plusieurs équipes qui appartiennent au groupe de travail 3. Nous expérimentons alors nos méthodes sur des données obtenues à l'aide de leurs prototypes simulés. Dans un premier temps, nous étudions la réponse impulsionale du prototype développé par l'Institut de Physique Nucléaire de Lyon (IPNL), dans le cadre d'une de faible acquisition de données. Nous réalisons dans un deuxième temps, une étude sur les reconstructions 2D des données obtenues à partir du prototype simulé de la caméra Compton développé au centre de recherche de Dresden-Rossendorf, en Allemagne. Cette dernière étude s'inscrit dans le cadre d'une collaboration entre les équipes en charge du développement des algorithmes de reconstruction dans le but de comparer les différentes méthodes proposées au sein du groupe de travail 3 du projet ENVISION. Ce travail est toujours en cours, et nous ne présentons ici que les résultats obtenus à partir de nos méthodes.



# Chapter 1

---

## Introduction

---

### 1.1 Objectives

Cancer is a leading cause of death worldwide. In 2008, 7.6 million deaths (around 13% of all deaths) was due to this disease and 12.7 million new cases were diagnosed. Lung, stomach, liver, colon and breast cancer cause the most cancer deaths each year. It is expected that deaths from cancer worldwide will rise to over 13.1 million in 2030<sup>1</sup>.

Treatment of this disease often requires more than one intervention and has to be carefully selected among the different techniques such as surgery, radiotherapy, chemotherapy. In some difficult cases, surgery and chemotherapy are impractical, the tumor is then treated by radiotherapy. Nevertheless, the tumor can be radioresistant. An alternative to classical radiotherapy is then the hadrontherapy technique that uses charged particles such as carbon ions or protons. This treatment modality overcomes radiotherapy by offering an improved ballistics and effectiveness in the dose deposition. However, hadrontherapy requires a precise monitoring in order to guarantee the safety of the patient with regards to the deposited dose.

In this purpose, medical imaging provides several tools to perform a control of the treatment. The use of imaging techniques has nowadays become an essential method that enables to visualize the anatomy or the metabolism of the human body and to follow the treatment of a disease and its progress. Using physical phenomena such as *X*-ray absorption, nuclear magnetic resonance, ultrasounds or radioactivity, medical imaging represents all the means that enables to recover informations from the organs, cells or lesions (size, volume, localization, shape) or their functioning (metabolism). These informations are

---

<sup>1</sup>Source: World Health Organization, <http://www.who.int/mediacentre/factsheets/fs297/en/index.html>

then used to create an image usable in clinical purpose.

Several methods to perform medical imaging for monitoring cancer treatment by hadrontherapy, are investigated such as Positron Emission Tomography (PET), Single Photon Emission Computed Tomography (SPECT), Proton Interaction Vertex Imaging (PIVI). Within this framework, the european project European NoVel Imaging Systems for ION therapy (ENVISION) has been launched in February 2010. This project is funded by the European Commission under FP7 Grant Agreement N. 241851. Its objective is to improve the quality assurance tools for hadrontherapy. In this purpose, the project aims at providing solutions for: real-time non invasive monitoring, quantitative imaging, precise determination of delivered dose, fast feedback for optimal treatment planning, real-time response to moving organs, simulation studies. The ENVISION project is a collaboration of sixteen leading European research centres and industrial partners, coordinated by the Conseil Européen pour la Recherche Nucléaire (CERN) and is under the umbrella of ENLIGHT, the European Network for Light Ion Hadron Therapy.

As part of this project, the WorkPackage 3 is dedicated to the development of an imaging device to perform hadrontherapy treatment monitoring. Several system are under investigations. Among them, the Compton camera seems to be a relevant candidate. This system also called the electronically collimated camera, enables to capture  $\gamma$  photons emitted by the treated zone through Compton scattering. From the measures, one may provide an image of the source of  $\gamma$  particles using image reconstruction methods.

This Ph.D thesis falls in the scope of the WorkPackage 3, and more precisely on the reconstruction task. The objective was to develop 3D image reconstruction methods for Compton imaging with application in hadrontherapy. Several constraints are implied by this application: low statistics data, real-time monitoring. This work then addresses both analytical and iterative reconstruction algorithms and the main contribution is twofold: (i) a Filtered Backprojection formulation for the analytical method, (ii) List Mode Maximum Likelihood Expectation Maximization algorithms using a new model for the estimation of the elements of the system matrix required during the reconstruction process.

## 1.2 Thesis organization

The manuscript is composed of four parts. In the first, we give an overview on the hadrontherapy treatment, its history and advantages. We also present a state of the art of the current monitoring methods used during the treatment. As we focus on Compton imaging, we then present the basics of the Compton camera functioning, starting with the fundamentals of particles physics and describing more generally the  $\gamma$  cameras. Next, we focus on the existing methods to perform Compton imaging. A state of the art of both analytical and iterative algorithms is presented.

In the second part, we focus on the analytical methods. We present the work conducted by [Maxim *et al.* (2009)] on reconstruction from a full set of data acquired by the Compton camera. This work is the starting point of our first contribution, a Fil-

tered BackProjection algorithm. We detail the method and give some insights on the tool MEGALib [Zoglauer (2005)] that we used to perform the simulations. We then show reconstructions obtained from the simulated data and we carry out a study on the influence of the size of the Compton device and of several parameters specific to the method on the quality of reconstruction.

The third part deals with the iterative method. We first present the context of application of the implemented LM-MLEM method. We propose a new probabilistic model for the estimation of the elements of the system matrix. The evaluation of these elements is performed by the numerical evalutation of an integral formula. We propose a first approach that does not take into account energy measurement uncertainties. In a second approach, we do account for these uncertainties, and we obtain another numerical formulation. A simplified method that uses our proposed probabilistic model, has also been implemented. We then carry out a study on the reconstructions for two different kind of sources in terms of shape and energy. We analyze the influence of the size of the camera, of the probabilistic model, and also the influence of the incomplete absorptions of photons by the device.

In the last part, we present reconstructions performed within the framework of ENVISION. Compton camera prototypes are currently under development in several teams that belong to the WorkPackage 3. We experience our methods on data obtained using two simulated prototypes. We study the Point Spread Function of the Compton camera developed by the Institut de Physique Nucléaire de Lyon (IPNL) in France, in case of low statistics data acquisition. We carry out a study on 2D reconstructions with data obtained from simulations using the prototype of Compton camera developed at the Research Center of Dresden-Rossendorf, in Germany. This work is part of a collaborative study in the purpose of comparing the different reconstruction methods proposed within the ENVISION project. This work is still in progress.



## II Compton imaging

---



# Résumé en français (Abstract in French)

## Contexte médical

### Hadronthérapie

Un des avantages majeurs d'un traitement contre le cancer par hadronthérapie est l'amélioration de la balistique en comparaison à la radiothérapie classique. La dose distribuée par le faisceau dans le patient, présentée figure 2.1, est faible au début de la trajectoire. Un pic d'énergie déposée est par la suite observé : le pic de Bragg. Puis la dose diminue drastiquement. Ce profil de distribution très spécifique permet une maximisation du dépôt d'énergie au niveau de la zone tumorale et une minimisation de l'irradiation des cellules saines. Un balayage du faisceau permet de couvrir l'intégralité de la tumeur (figure 2.2). Le dépôt très localisé de l'énergie présente aussi l'inconvénient de nécessiter une grande précision. En cas d'erreur de positionnement du patient, d'une mauvaise planification, de mouvement d'organes, la dose déposée risque d'endommager des cellules saines ou des organes à risques. Le contrôle en ligne est donc une nécessité pour garantir la sécurité du patient. Pour ce faire, nous nous intéressons au rayonnement  $\gamma$  généré par la zone traitée.

### Surveillance du traitement: rayonnement $\gamma$

Lors du traitement, les réactions nucléaires qui ont lieu au sein de la zone traitée produisent des photons  $\gamma$  de deux types: les  $\gamma$ -prompts et les  $\gamma$  produits par l'annihilation d'une paire électron-positon.

Les  $\gamma$  d'annihilation d'une paire électron-positon qui ont une énergie spécifique de 511 keV, sont émis par paire et se propagent dans des directions opposées. Ces rayons  $\gamma$  sont détectés au moyen d'un système d'imagerie TEP (Tomographie par Emission de Positons). Les images reconstruites à partir du scanner TEP sont corrélées à la dose distribuée [Parodi *et al.* (2007), Moteabbed *et al.* (2011)] permettant donc de localiser la position du pic de Bragg, i.e. la localisation du maximum de dépôt d'énergie. Les délais entre le traitement et le passage en scanner TEP impliquent une réduction importante du signal pouvant être récupéré. L'examen TEP concomitant avec le traitement permet

---

d'éviter ce temps d'attente en effectuant l'acquisition durant le traitement [Parodi *et al.* (2008)]. Cependant, la résolution spatiale est réduite. Une solution intermédiaire est à l'étude proposant d'effectuer l'acquisition après le traitement mais dans la même pièce pour réduire le délai traitement-acquisition [España *et al.* (2010)]. Dans le cadre de l'imagerie TEP, la seconde catégorie de photons, les  $\gamma$ -prompts, sont considérés comme une source de bruit.

Les  $\gamma$ -prompts sont de surcroît plus nombreux et représentent une alternative à la TEP au travers de la Tomographie d'Emission MonoPhotonique (TEMP). Les images reconstruites par TEMP sont également corrélées au dépôt de dose [Min *et al.* (2006), Testa *et al.* (2009)]. Le taux d'émission de ces photons serait suffisant pour permettre la surveillance en ligne du traitement [Polf *et al.* (2009)].

## Imagerie Compton

### Caméra Compton

Nous nous concentrons sur la détection des  $\gamma$ -prompts par le dispositif appelé caméra Compton. Aussi appelé caméra à collimation électronique, ce système d'imagerie permet la détection des photons par effet Compton. Il fut d'abord proposé pour l'astronomie [Schönfelder *et al.* (1973)], ensuite pour une application au domaine médical [Todd *et al.* (1974), Everett *et al.* (1977)]. En comparaison avec les  $\gamma$  caméras classiques, comme la caméra Anger, l'absence de collimateur mécanique lui confère une meilleure sensibilité. De plus, cette caméra permet de réaliser une image 3D à partir d'un dispositif fixe. Le large spectre couvert par le dispositif en fait également un candidat potentiel pour une application en hadronthérapie, en thérapie par ion carbones ou protonthérapie [Kang and Kim (2009), Frandes *et al.* (2010), Peterson *et al.* (2010), Kormoll *et al.* (2011), Richard *et al.* (2011), Robertson *et al.* (2011), Roellinghoff *et al.* (2011), Llosá *et al.* (2011), Richard *et al.* (2012), Kim *et al.* (2012)]. Ce système d'imagerie est déjà utilisé en astronomie pour sonder les rayons cosmiques [Bandstra *et al.* (2011)], ainsi qu'en sécurité territoriale pour détecter les matériaux nucléaires représentant une potentielle menace [Herbach *et al.* (2009)].

La caméra est généralement composée de deux détecteurs: le *diffuseur* qui favorise la diffusion Compton et l'*absorbeur* qui favorise l'absorption par exemple par effet photoélectrique. Le diffuseur est en général un composé semi-conducteur, en silicium (Si) [Singh and Doria (1983), Solomon and Ott (1988), Kuykens and Audet (1988)] ou en germanium (Ge). Le silicium permet notamment de réduire l'effet Doppler (effet indésirable lors de la détection) et d'avoir une activité thermique plus facile à gérer. L'absorbeur peut être un composé semi-conducteur ou un scintillateur comme des cristaux d'iodure de césum (CsI). Une étude sur la composition de l'absorbeur a été menée dans [Richard *et al.* (2011)].

Intéressons nous aux interactions physiques mises en jeu. La diffusion Compton est la déviation inélastique d'un photon par un électron libre. Un rayon  $\gamma$  d'énergie  $E_\gamma$

---

entre en collision avec l'électron et lui transfère une partie de son énergie  $E_e$ . Le photon est diffusé sous un angle appelé l'angle Compton, noté  $\beta$ , et emporte une énergie  $E'_\gamma = E_\gamma - E_e$ . La figure 3.3 présente un schéma détaillant l'interaction. L'absorption par effet photoélectrique est présentée dans la figure 3.2. Au cours de cette interaction, un photon  $\gamma$  entre en collision avec un électron lié, une partie de l'énergie du photon  $E_b$  est utilisée pour éjecter l'électron, et le reste  $E_e$  est transmis à ce dernier sous forme d'énergie cinétique. L'espace vacant laissé par l'électron est comblé par un autre électron ou par réarrangement des orbitales atomiques. L'électron à présent libre sera par la suite capturé par le matériau.

## Modélisation de la détection

Nous présentons ici la modélisation de la détection d'un photon  $\gamma$  par la caméra Compton. Une particule provenant d'une source de radiation est émise au point  $M$  avec une énergie initiale  $E_0$ . Le photon interagit avec le diffuseur au point  $V_1$  transférant une énergie  $E_1$  à l'électron. La particule diffusée sous un angle  $\beta$  interagit ensuite avec l'absorbeur au point  $V_2$ , déposant une fraction ou la totalité de son énergie restante  $E_2$ . En hadron-thérapie, l'énergie initiale des photons est inconnue. De ce fait, on l'estime par la somme des énergies mises en jeu lors de la détection. Cependant, le photon n'est pas toujours totalement absorbé. Ainsi, l'énergie initiale ne sera pas correctement estimée entraînant une erreur sur le calcul de l'angle de diffusion. Ce phénomène aura des répercussions sur la reconstruction et sera discuté au chapitre IV. Dans le cas où le photon subit de multiples diffusions au cours de sa détection, la position d'interaction  $V_2$  sera donnée par la seconde interaction dans les détecteurs, et l'énergie  $E_2$  sera également estimée comme étant la somme des énergies mises en jeu après à la première interaction.

Étant données les deux positions d'interaction  $V_1$  et  $V_2$ , la direction de diffusion est donnée par le vecteur  $\overrightarrow{V_2V_1}$ . On sait alors que pour des mesures idéales, l'origine du photon, le point  $M$ , se trouve sur la surface du cône de sommet  $V_1$ , d'axe  $\overrightarrow{V_1V_2}$ , et de demi-angle d'ouverture  $\beta$ , appelé cône Compton et présenté dans la figure 3.6. Lorsque l'on prend les incertitudes de mesure en compte, l'origine du photon ne repose plus sur la surface du cône, mais se trouve à l'intérieur d'un volume entourant cette surface.

Par la suite, à partir des mesures correspondant donc à des projections coniques, le défi est de reconstruire la source de rayonnement  $\gamma$ . Pour cela, plusieurs méthodes ont été proposées, et nous en présentons un état de l'art.

## État de l'art

Deux concepts majeurs se dégagent des méthodes proposées pour l'imagerie Compton. On différencie les algorithmes analytiques des algorithmes itératifs.

Dans le cas des algorithmes analytiques, la solution du problème de reconstruction est exacte pour des modèles continus. On approche ensuite cette solution par une discréétisation adaptée. Une des difficultés associées à ce type d'algorithme est de déterminer un modèle suffisamment proche du problème tout en conservant la possibilité d'en tirer une

---

solution explicite. Des modèles trop complexes, bien que plus réalistes, sont parfois trop difficiles à formuler.

Dans le cas des algorithmes itératifs, l'idée est de considérer dès le départ un modèle discrétilisé. On utilise ensuite des algorithmes pour approcher la solution. Ces méthodes permettent une plus grande flexibilité vis à vis des paramètres pouvant être pris en compte. Cependant, des problèmes de convergence apparaissent associées à la difficulté de choisir un critère pour l'arrêt des itérations. De plus, la résolution du problème peut parfois demander d'importantes ressources mémoire et des temps de calculs relativement longs.

## Méthodes analytiques

Les méthodes analytiques ont pour but l'inversion des projections coniques mesurées par la caméra Compton. La première méthode, proposée par [[Cree and Bones \(1994\)](#)], permet d'effectuer la reconstruction à partir d'un ensemble de projections restreint aux cônes d'axe orthogonal au diffuseur. Dans [[Basko et al. \(1998\)](#)], les projections Compton sont transformées en projections planes en utilisant une méthode de développement en harmoniques sphériques. À partir de ces projections planes, la transformée inverse de Radon peut être utilisée à l'instar de ce qui est fait plus généralement en tomodensitométrie (TDM), pour reconstruire l'image 3D de la source. Une reformulation de cette méthode menant à des améliorations du point de vue numérique a été proposée par [[Parra \(2000\)](#)] puis retravaillée par [[Tomitani and Hirasawa \(2002\)](#), [Hirasawa and Tomitani \(2003\)](#)]. Ces travaux utilisent une approche qui consiste à transformer les projections coniques en projection sur des lignes en utilisant une déconvolution en coordonnées sphériques. Par la suite, des méthodes développées pour la reconstruction de ces projections sont utilisées pour reconstruire l'image de la source. L'avantage de la déconvolution permet d'éviter le développement en harmoniques sphériques qui peut demander des ressources informatiques importantes. Une méthode de reconstruction directe à partir de l'ensemble complet des projections Compton mesurées par la caméra a été développée par [[Maxim et al. \(2009\)](#)]. Cet algorithme permet d'aller plus loin qu'avec l'algorithme proposé par [[Cree and Bones \(1994\)](#)] puisque la limitation aux cônes d'axe orthogonal aux détecteurs est levée. Cette méthode est le point de départ de la Rétroprojection Filtrée que nous proposons.

## Méthodes itératives

Avec les méthodes itératives, il est possible de prendre en compte le caractère aléatoire de l'émission et du dispositif de détection ainsi que les phénomènes physiologiques d'absorption chez le patient.

L'un des premiers algorithmes développés est la technique de reconstruction algébrique (ART) proposé par [[Gordon et al. \(1970\)](#), [Herman and Lent \(1976\)](#), [Singh and Doria \(1983\)](#)]. Ce dernier utilise une approche algébrique linéaire pour effectuer la reconstruction. Une information *a priori* peut facilement être intégrée, mais si on souhaite être plus proche de conditions réelles, la technique nécessite des modifications supplémentaires.

---

La plupart des autres techniques itératives visent à estimer le maximum de vraisemblance par maximisation de l'espérance (MLEM) [Hebert *et al.* (1990), Wilderman *et al.* (1998), Sauve *et al.* (1999), Tornga *et al.* (2009)]. Sa variante OSEM accélère les calculs en distribuant les données dans des sous-ensembles ordonnés [Hudson and Larkin (1994), Kim *et al.* (2007), Kim *et al.* (2010)]. Ces méthodes sont basées sur l'estimation de l'image à l'état suivant en fonction de l'image à l'état courant suivant une formule mettant en jeu les éléments de formation de l'image ou matrice système. Ces méthodes présentent diverses limitations telles que les fluctuations des solutions.

D'autres algorithmes de type bayésien, utilisent des approches de maximum *a posteriori* (MAP) [Lange *et al.* (1987), Liang *et al.* (1989), Huesman *et al.* (2000)] ou d'entropie maximale (ME) [Strong *et al.* (1990), Strong (2003)]. Dans ces méthodes, une information préalable peut être incorporée dans le processus de reconstruction. Toutefois, elles exigent la tâche difficile de choisir l'information *a priori*. Une autre approche bayésienne est proposée par [Lee *et al.* (2008)] utilisant l'algorithme MAP, mais intégrant également une méthode d'Action-Ligne ou un Bloc-Séquentiel. L'étape Action-Ligne ML (RAML) permet d'effectuer une mise à jour spécifique de l'image en utilisant un ensemble disjoint de projections. Le Bloc-Séquentiel EM (BSEM) est une méthode dérivée de OSEM. Une première étape RAML achevée, une régularisation est effectuée en utilisant le gradient de l'information *a priori*.

Une approche complètement différente, et néanmoins intéressante, est proposée par [Andreyev *et al.* (2011), Mackin *et al.* (2012)] avec une méthode d'ensemble d'origines stochastiques. Pour chaque  $\gamma$  détecté, l'origine du photon est choisie aléatoirement sur la surface du cône Compton. Un processus itératif met à jour l'image en déplaçant cette origine selon une fonction de coût. Les résultats sont similaires à ceux obtenus avec MLEM, cependant il existe plusieurs limitations dues à la variance et l'intensité de l'image reconstruite.



## Chapter 2

---

### Hadrontherapy

---

In addition to the conventional techniques such as surgery, chemotherapy, or when these modalities cannot be used to treat a tumor, radiotherapy is often used in cancer treatment or to prevent relapses. This technique uses ionizing radiations to kill malignant cells. Radiotherapy has proven to be efficient, however not all tumors can be treated with this modality. Some of them are radio-resistant, leaving the treatment not sufficiently effective. Moreover, the dose deposition in the patient, from the entrance area until the tumor, even under strict control, remains a risk. Hadrontherapy is a form of radiotherapy that uses heavy particles called hadrons. Carbon ions and protons are the most commonly used. This treatment modality could be a relevant solution to the mentioned constraints.

With the emergence of particle accelerators in the years 1920, treatment of cancer with protons or heavier ions becomes possible. In 1946, Robert R. Wilson is the first to propose to use such beams in cancer therapy. In 1954, at the instigation of Ernest O. Lawrence, a first patient is treated by protontherapy at Berkeley laboratory, using a cyclotron to accelerate the particles. However, even if the idea to use heavy ions emerged soon, it has only been really investigated in the 90's. Since then, several centers have been built or are under construction. Hadrontherapy centers currently in use or under construction can be found all over the world, e.g.:

- Japan: NIRS-HIMAC (Chiba), HIMBC (Hyogo), GHMC (Gunma), HIMAT (Tosu), i-ROCK (Yokohama), Proton Medical Research Center University of Tsukuba (Tsukuba)
- Germany: HIT (Heidelberg), Marburg Center (Marburg), ISL (Berlin), RPTC (Munich), Westdeutschen Protonentherapiezentrum Essen (Essen)
- Italy: CNAO (Pavia), Catania project (Catania)

- United States of America: MGH Francis H. Burr Proton Therapy Center (Boston), University of Florida Proton Therapy Institute (Jacksonville), ProCure Proton Therapy Center (Oklahoma), The Roberts Proton Therapy Center (Philadelphia), Hampton University Proton Therapy Institute (Hampton)
- China: Shanghai Proton and Heavy Ion Hospital (Shanghai), IMP (Lanzhou), Wan-jie Proton Therapy Center (Zibo)
- Austria: MedAutron (Wiener Neustadt)
- Switzerland: Institut Paul Scherrer (Villigen)
- France: Centre Antoine Lacassagne (Nice), Centre de protonthérapie de l’Institut Curie (Orsay)

There are on going projects in France with the ETOILE project (Espace de Traitement Oncologique par Ions Légers dans le cadre Européen) in Lyon, and Archade (Advanced Resource Centre for HADrontherapy in Europe) in Caen.

## 2.1 Treatment

Hadrontherapy consists in an effective cancer treatment that overcomes classical radiotherapy by an improved ballistics through the specific shape of the distribution of the deposited dose. At the end of the beam range, a maximum of energy is delivered giving rise to the so-called Bragg peak. The figure 2.1 shows the example of Bragg curves for a proton beam at 148 MeV and a carbon ion beam at 270 MeV. The idea is then to select the energy range of the beam in order to maximize the dose deposition in the target and to minimize it for sparing healthy cells, as shown in figure 2.2. This advantage is also the main challenge of this treatment modality. Indeed, the important number of uncertainty sources makes the treatment risky. For instance, a shorter penetration depth of the beam will induce severe damage to healthy tissues and underdosage of the tumor. With a too deep range, healthy cells and organ at risk beyond the target might also be severely harmed. An error in the patient positioning or setup, anatomical motion or variations, tumor evolution, abnormal response of the tissues, all lead to uncertainties on the planned region of maximum dose deposition. For these reasons, treatment monitoring is essential.

Nevertheless, this treatment modality is even efficient upon tumors that are radio-resistant. The specific use of carbon ions in hadrontherapy also enhances the Relative Biological Effectiveness (RBE) [[Ando and Kase \(2009\)](#)].

## 2.2 Monitoring: state of the art

Online monitoring of the irradiation is an important issue in hadrontherapy but also a difficult task. Currently, Positron Emission Tomography (PET) is clinically used for

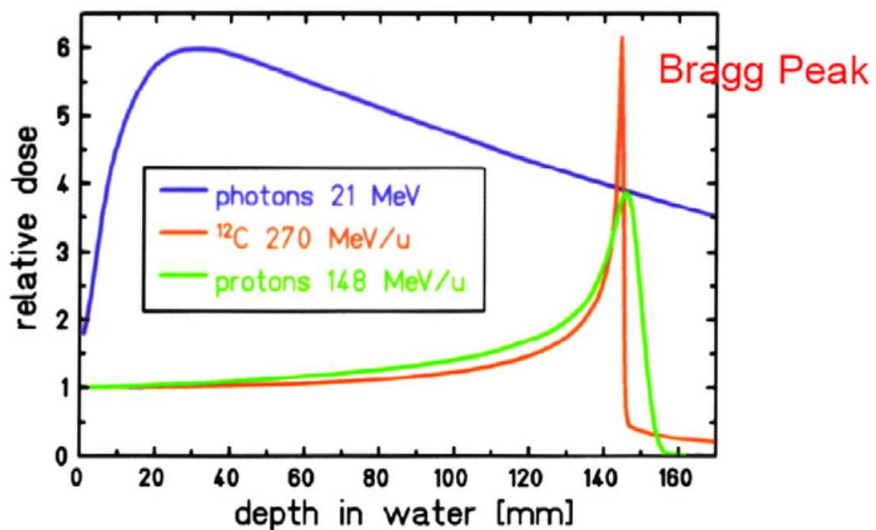


Figure 2.1: Depth dose distribution in water for photons at 21 MeV and monoenergetic Bragg curves for a carbon ion beam at 270 MeV and a proton beam at 148 MeV. Source: [Fokas *et al.* (2009)]

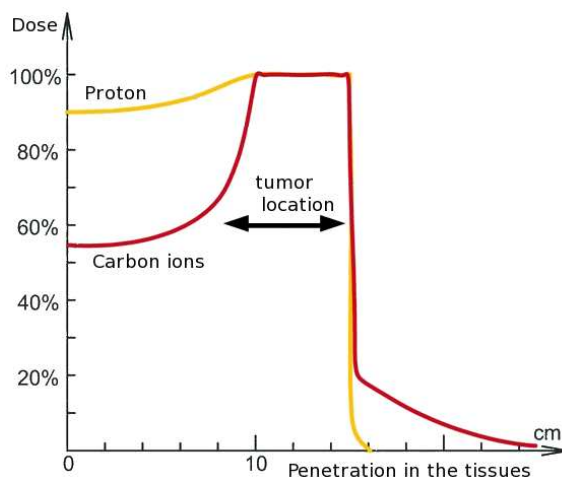


Figure 2.2: Illustration of the Bragg peak, example of a modulated proton beam and carbon ion beam. Source: Centre ETOILE, Lyon

offline monitoring. Typically, a tumor is irradiated using around  $10^7\text{-}10^8$  protons or  $10^5\text{-}10^6$  carbon ions per raster position. During the treatment, interaction of incident ions with the tissue create unstable nuclei. The physical interactions that follow, produce two types of  $\gamma$  particles. Some of them produce prompt- $\gamma$  emitted by excited nuclear fragments in times much lower than a picosecond. Other fragments produce positrons that annihilate and emit pairs of  $\gamma$  photons of specific energy.

The  $\gamma$  photons from annihilations of electron-positron pairs are detected via PET scanners. Images from these detecting devices are correlated to the dose distributions

[Parodi *et al.* (2007), Moteabbed *et al.* (2011)]. However, this modality has several limitations. The data acquisition is a long process. The delays between the treatment and offline PET imaging yield to an important reduction of the signal. Anatomical activity simply due to the metabolism or also the blood perfusion induce an increase of the blood washout effects. In order to avoid these issues, online PET has been investigated. The delays are avoided and blood washout reduced [Parodi *et al.* (2008)]. However, the specific design of online PET induce a reduction of the spatial resolution and angular coverage of the scanner degrade the provided images. An intermediate concept is also investigated. The in-room PET, which enables to reduce the delays, and thus the blood washout [España *et al.* (2010)].

Prompt- $\gamma$  particles contribute to the noise background in imaging via a PET scanner. An appealing alternative to PET is then in-beam Single Photon Emission Computed Tomography (SPECT) imaging that uses these particles. Although the density map of those prompt- $\gamma$  photons is still not identical to the map of the deposited dose, it was shown (*e.g.*, [Min *et al.* (2006), Testa *et al.* (2009)]) that it should allow computing the position of the Bragg peak. As suggested by Monte Carlo simulation studies, the emission rate of prompt- $\gamma$  photons may be sufficient for online monitoring [Polf *et al.* (2009)]. Other online imaging modalities based on prompt secondary radiations were proposed, *e.g.* Proton Interaction Vertex Imaging [Henriquet *et al.* (2012)].

# Chapter 3

---

## Fundamentals of particle physics and $\gamma$ -ray detection devices

---

Since they are more numerous than photons from annihilation of a pair electron-positron, we focus on prompt- $\gamma$  photons. In order to better understand how a  $\gamma$ -radiation imaging system works, we first recall in this section fundamentals of some physical processes taking place during irradiation of matter with charged particles. Then, we describe the functioning of  $\gamma$  cameras.

### 3.1 Interaction of gamma rays

There are several scenarii that might occur when a  $\gamma$  photon travels through matter: (i) the ray may not interact at all; (ii) the photon can be scattered delivering a part of its energy to the medium it interacts with; (iii) the photon can be absorbed, providing all its energy to the medium and resulting in the annihilation of the particle. Among these different processes, we may find photoelectric absorption, Compton scattering, electron-positron pair creation. The nature of the interaction depends on the medium where the interaction takes place but also on the initial energy of the particle. Figure 3.1 shows the predominant interaction depending on the energy in a Silicon (Si) medium. We can already note the range of energy of the Compton scattering from around tens of keV to tens MeV.

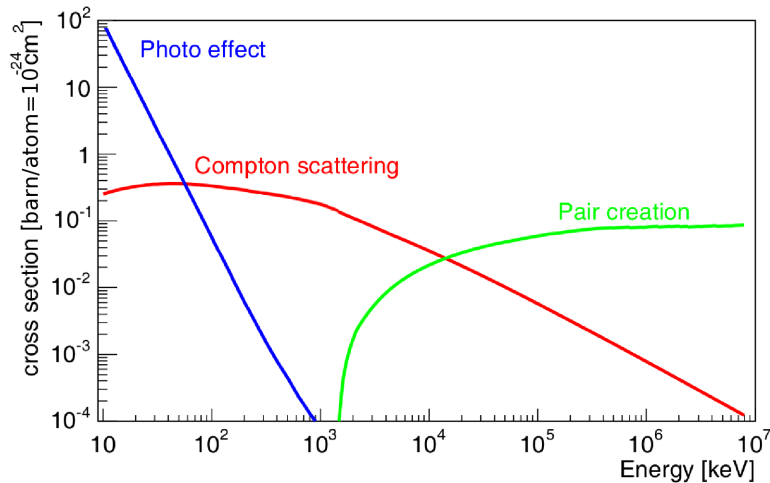


Figure 3.1: Cross-section for photon interactions in Silicon according to the energy of the  $\gamma$  photon. The dominating interaction is photoelectric effect at low energies, Compton scattering at energies from about hundreds of keV to ten MeV, pair creation at high energies. Source: [Zoglauer (2005)]

### 3.1.1 Photoelectric absorption

The photoelectric absorption consists in the interaction of a  $\gamma$  particle of energy from a few eV to over 1 MeV, with an atom of the crossed medium. During the interaction, the photon transfers all its energy to one of the orbital electrons of the atom. Generally, the energy of the  $\gamma$  particle far exceeds the binding energy of the electron involved in the interaction process which leads to its ejection. The  $\gamma$  particle disappears. As for the ejected electron, its kinetic energy  $E_e$  is equal to the incoming energy of the photon  $E_\gamma$  minus the binding energy  $E_b$ :

$$E_e = E_\gamma - E_b. \quad (3.1)$$

The vacancy left is then refilled by a nearby free electron. This process liberates the binding energy in the form of a characteristic photon which will also interact with an electron from less tightly bound shells of the nearby atoms of the medium. The overall process finally consists in the conversion of the photon energy into energies carried by freed electrons. The later are detectable through their Coulomb interactions.

### 3.1.2 Compton scattering

Compton scattering consists in the inelastic deviation of a photon by a free electron. The photon with an initial energy  $E_\gamma$ , collides with the electron which recoils with a kinetic energy  $E_e$  transferred by the  $\gamma$  particle. The photon is scattered through an angle  $\beta$  and conserves an energy  $E'_\gamma = E_\gamma - E_e$ , see figure 3.3.

The relation between the energies  $E_\gamma$ ,  $E'_\gamma$  and the deviation angle is given by the

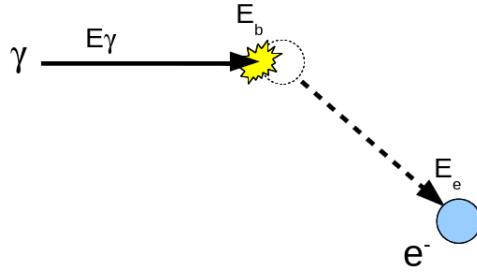


Figure 3.2: Basic scheme of the photoelectric absorption mechanism. A photon with an energy  $E_\gamma$  interacts with a bound electron which causes the electron to recoil.  $E_b$  corresponds to the energy required to produce the ejection and  $E_e$  the energy transferred to the electron.

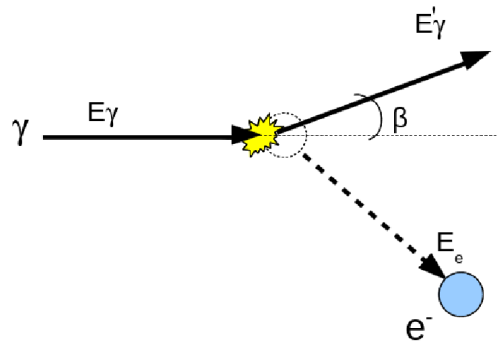


Figure 3.3: Basic scheme of the Compton scattering mechanism. A incident photon with an energy  $E_\gamma$  interacts with an electron which causes the electron to recoil. The photon transfers an energy  $E_e$  to the electron and is scattered through the Compton angle  $\beta$  with a remaining energy of  $E'_\gamma$ .

Compton equation:

$$\cos(\beta) = 1 - \frac{m_e c^2}{E'_\gamma} \left( \frac{1}{E'_\gamma} - \frac{1}{E_\gamma} \right) \quad (3.2)$$

where  $m_e$  is the mass of an electron at rest and  $c$  is the speed of light. For a mathematically valid Compton angle, the following conditions must be verified:

$$\begin{cases} \frac{m_e c^2 E_\gamma}{2E_\gamma + m_e c^2} \leq E'_\gamma \leq E_\gamma \\ 0 \leq E_e \leq \frac{2E_\gamma^2}{2E_\gamma + m_e c^2} \end{cases} \quad (3.3)$$

In this description, it is assumed that the photon interacts with an electron at rest. In reality, this is not the case. This will result in the so-called Doppler broadening that limits the angular precision on the measurement of the Compton scattering angle.

The probability that a photon with an energy  $E_\gamma$  undergoes a Compton scattering through an angle  $\beta$  is given by the Compton scattering cross-section  $K(\beta, E_\gamma)$ . The Klein-Nishina formula [Klein and Nishina (1929)] enables to calculate it for an unpolarized

photon that interacts with an unbound electron.

$$K(\beta, E_\gamma) = \frac{r_e^2}{2} \left( \frac{E'_\gamma}{E_\gamma} \right)^2 \left( \frac{E'_\gamma}{E_\gamma} + \frac{E_\gamma}{E'_\gamma} - \sin^2 \beta \right), \quad (3.4)$$

with  $r_e$  the classical electron radius given by  $r_e = \frac{e^2}{4\pi\varepsilon_0 m_e c^2}$  where  $e$  is the elementary charge and  $\varepsilon_0$  is the permittivity of free space. Since in reality the electrons are bound to nuclei, it is only possible to approximate the cross-section. In figure 3.4, we present Klein-Nishina cross-section as a function of the Compton scattering for different energies. The greater the initial energy of the photon is, the higher is the probability to have a small scattering angle.

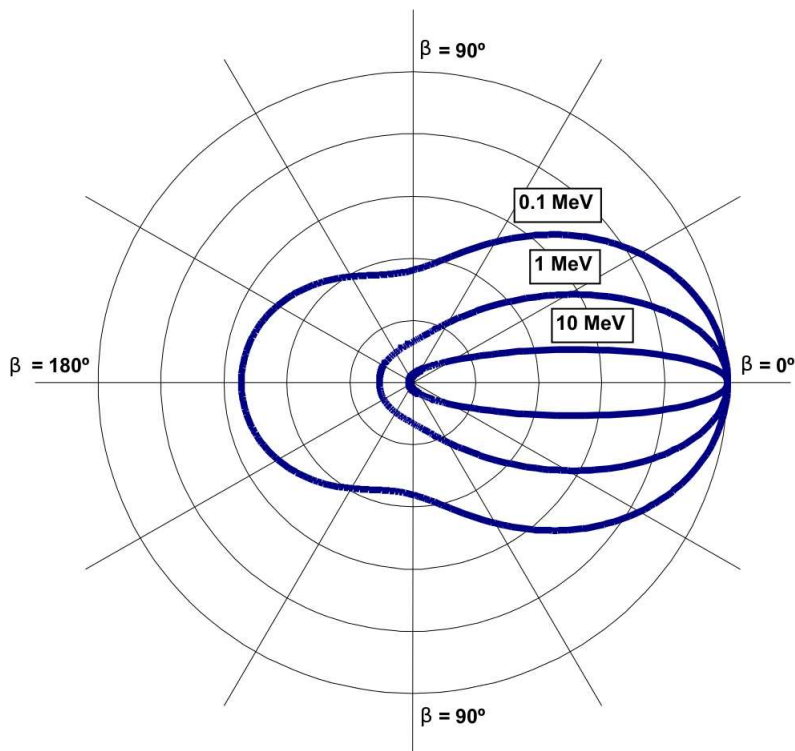


Figure 3.4: Representation of the Klein-Nishina cross section as a function of the Compton angle  $\beta$  at three different energies: 0.1 MeV, 1 MeV and 10 MeV. The higher the energy is, the smaller the average Compton scatter angle is. Source: [Zoglauer (2005)]

### 3.1.3 Electron-positron pair creation

When its energy is superior to  $2m_e c^2$ , i.e. 1.022 MeV, the  $\gamma$  photon can interact in the vicinity of a nucleus and create an electron-positron pair. The figure 3.5 presents the interaction mechanism.

The interaction can take place only if the situation allows both energy and momentum conservation. The photon is fully absorbed, a part of its energy being converted into the mass of an electron-positron pair, the excess of energy transferred in the form of kinetic

energy to the created pair. The nucleus takes over part of the photon momentum. If the photon's energy is superior to four times the rest mass of an electron, the pair creation can occur in the field of an electron. In this case, the momentum is transferred to this electron.

At the end of its range, the positron combines with an electron and both annihilate, producing two  $\gamma$ -rays of 0.511 MeV, propagating in opposite directions.

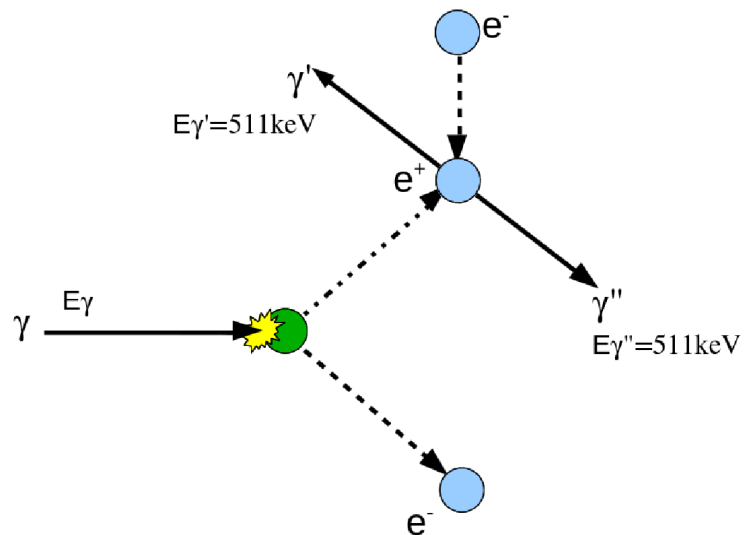


Figure 3.5: Basic scheme of the pair electron-positron creation mechanism and further positron annihilation. A photon with an energy  $E_\gamma$  superior to 1.022 MeV interacts with the electric field of a nucleus (or electron) and creates an electron-positron pair. The positron interacts then with another electron leading to the creation of two  $\gamma$  particles of energy 511 keV that are emitted in opposite directions.

## 3.2 Detection of gamma photons

Detection of  $\gamma$  radiation is an important research tool in nuclear medicine and in hadrontherapy. It is achieved through the interactions, previously described, of  $\gamma$  particles with the imaging device. The detectors are mostly based on scintillation or semiconductor materials. As mentioned previously, depending on the initial energy of the photon, one interaction is predominant over the others. The material has also an impact on the type of interaction that will be predominant. For instance, a low atomic material can facilitate the Compton scattering interaction whereas a high atomic material is well suited for photoelectric absorption.

### 3.3 Gamma cameras

#### 3.3.1 Anger camera

In 1958, Anger proposed a scintillation device in order to image prompt- $\gamma$  [[Anger \(1958\)](#)]. Either referred to as Anger camera or gamma-camera, this device has been a major imaging system in nuclear medicine since its development over 40 years ago. Numerous investigations, often specific to a given domain of application, allowed to continuously improve its spatial and energy resolutions.

In the field of in-beam SPECT, several variants of the Anger camera have been investigated [[Ishikawa et al. \(2001\)](#), [Min et al. \(2006\)](#), [Kim et al. \(2007\)](#), [Testa et al. \(2009\)](#), [Peloso et al. \(2011\)](#)]. Generally, the system is composed of a scintillator, with a shield against neutrons from the background, and a collimator to detect  $\gamma$  particles coming from a specific direction. A 1D-profile corresponding to the projection of the prompt- $\gamma$  production map on the beam direction may be then measured. The concept is appealing, especially when the signal-to-noise ratio is low. However the presence of the collimator limits greatly the particle detection efficiency. In nuclear medicine, typically only one  $\gamma$  ray is observed for every 10000 emissions, because most of particles are absorbed in the collimator [[Bushberg and Boone \(2011\)](#)]. Another drawback of the collimator, it necessitates a rotation of the device to perform a full scan.

#### 3.3.2 Compton camera

A new concept was introduced in [[Todd et al. \(1974\)](#), [Everett et al. \(1977\)](#)], a device based on the Compton effect. This kind of system was already investigated for astronomy applications [[Schönfelder et al. \(1973\)](#)]. The Compton camera also called electronically collimated camera enables to produce a 3D image with a stationary system. It is generally composed of two different detector materials: the *scatterer* facilitating Compton scattering interactions; the *absorber* facilitating photoelectric absorptions. The scatterer generally is a semiconductor such as Silicon (Si) [[Singh and Doria \(1983\)](#), [Solomon and Ott \(1988\)](#), [Kuykens and Audet \(1988\)](#)] or Germanium (Ge). The Silicon seems to be a relevant material since it increases the Compton scattering rate have a good energy resolution but also reduces the Doppler broadening and the thermal activity is easily managed. The absorber is either a semiconductor, or a scintillation detector such as crystals of Caesium Iodide (CsI), Cerium-doped Lutetium Yttrium Orthosilicate (Ce:LYSO or LSO), Bismuth Germanium Oxide (BGO). Since its proposal, different Compton camera devices have been investigated [[Singh and Doria \(1985\)](#), [Singh and Brechner \(1990\)](#), [Gormley et al. \(1996\)](#), [LeBlanc et al. \(1999\)](#), [Sauve et al. \(1999\)](#)].

The Compton camera is already used in astronomy as a telescope to detect atmospheric or cosmic  $\gamma$ -ray sources [[Bandstra et al. \(2011\)](#)], and is also proposed for homeland security applications concerning the detection of nuclear material which could be a threat [[Herbach et al. \(2009\)](#)].

The sensitivity of the device compared to the Anger camera is greatly increased since no mechanical collimator is necessary. This way, a photon coming from an arbitrary direction can be detected. Its superiority over the classic Anger camera in nuclear medicine is investigated by several authors, e.g. [Gormley *et al.* (1997), Han *et al.* (2008)]. With the wide energy range of the prompt- $\gamma$  radiation produced in hadrontherapy application, the device seems to be relevant. Its applicability is currently under investigation either in carbon ion beam or proton beam therapy [Kang and Kim (2009), Frandes *et al.* (2010), Peterson *et al.* (2010), Kormoll *et al.* (2011), Llosá *et al.* (2011), Richard *et al.* (2011), Robertson *et al.* (2011), Roellinghoff *et al.* (2011), Kim *et al.* (2012), Richard *et al.* (2012)].

### 3.4 Compton detection model

In this section, we describe the model for the detection of a prompt- $\gamma$  particle by a Compton camera.

A particle originating from a radiating source is emitted at the point  $M$  with an energy  $E_0$ . The photon is Compton scattered in the first detector at  $V_1$  with high probability, delivering the energy  $E_1$  to an electron. The particle is then deviated and escapes from the scatterer to interact with the absorber at the point  $V_2$ , depositing (a fraction of) its remaining energy  $E_2$ .

As mentioned in chapter 3, the initial energy and the energy transferred to the electron allow to compute the Compton scattering angle  $\beta$ , through the Compton angle equation 3.2.

In hadrontherapy, the initial energy of prompt- $\gamma$  photons is unknown and therefore estimated with the total energy deposited by the particle in the detectors. In case of partial absorption, the resulting lack of energy in the measure will lead to a wrong estimation of the initial energy and thus to a wrong value of scattering angle.

When the initial energy is known, a selection window can be applied in order to only keep photons that have delivered all their energy, thus that have been completely absorbed. The effect of the partial absorption will be discussed in chapter IV. Techniques such as a spectral deconvolution [Xu and He (2007)] allow to correct for partial absorption when several sources of different energies are imaged.

In the case where the photon undergoes multiple scatterings in different layers, the second interaction position  $V_2$  is given by the position of second scattering process. When the multiple scatterings occur in the same layer, the second interaction position  $V_2$  is chosen as the centroid of all the interaction points within the layer. The energy  $E_2$  is then estimated as the summation of all measured energies after the first scattering.

Given the two positions of interaction  $V_1$  and  $V_2$ , the direction of the (first) scattered particle is given by the vector  $\overrightarrow{V_1 V_2}$  (see figure 3.6). For ideal measurements, the particle origin  $M$  lies on the surface of the cone with apex  $V_1$ , axis direction  $\overrightarrow{V_2 V_1}$  and half opening angle  $\beta$ , the so-called Comptone cone denoted  $C(V_1, V_2, \beta)$ . As a matter of fact, uncertainties in both energy and position measurements make that the source does not lie on a

cone surface but within a small volume around it.

Apart of the challenge in elaborating this kind of device, Compton imaging requires complex reconstruction techniques in order to recover an image of the radiating source from the Compton scattered data.

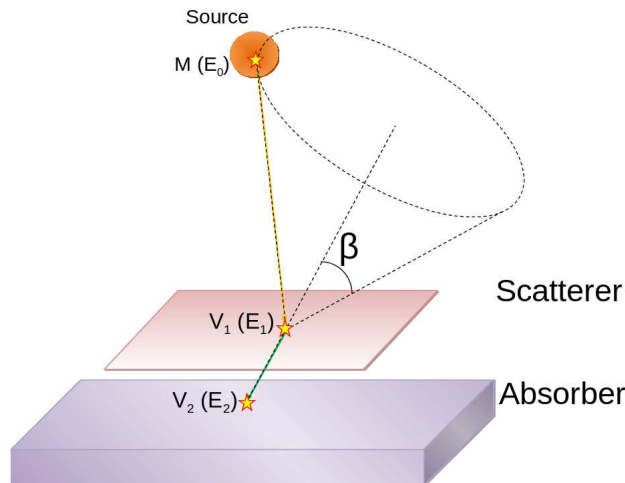


Figure 3.6: Illustration of the detection of a  $\gamma$ -photon. The particle originating from  $M$  with an energy  $E_0$ , collides with the scatterer at  $V_1$ , delivering an energy  $E_1$ . The photon is scattered through the angle  $\beta$  and then interacts with the absorber at  $V_2$  delivering an energy  $E_2$ . The Compton cone is defined from  $V_1$ ,  $V_2$  and  $\beta$ .

# Chapter 4

---

## Image reconstruction: state of the art

---

Several different methods have been investigated since Compton scattering based cameras have been proposed for the imaging of  $\gamma$  sources in medicine. We distinguish two main categories: analytical and iterative algorithms. They both rely on the mathematical formulation of the problem.

Analytical methods aim to find an analytical solution or an analytical operator that will provide the solution. The solution is exact for the continuous model but needs to be discretized in real application. Two significant limitations come out from this approach. Some imaging devices can not be reliably modeled, and the solution might be too difficult to be derived.

The iterative methods start from a discretized model. The solution is then provided using iterated computer evaluations. In this approach, a greater number of imaging devices can be modeled. However, the uniqueness and the exactness of the solution is lost. Moreover, finding a solution can be computationally intensive.

For both approaches, the reconstructed image aims to be close to the real one. The differences that can be observed might come from the imprecision of the model, the inappropriate assumptions and also from the noise which might have several origins: lack of data, noisy measurements, discretization. A reconstruction algorithm must be robust against this kind of errors. We present, in the following, a brief overview of analytical methods in section 4.1 and of iterative ones in section 4.2.

## 4.1 Analytical methods

As mentioned in section 3.4, the origin of a  $\gamma$  particle detected by the camera lies on the surface of a cone. As a consequence, the measured data obtained from the Compton camera are conical surface projections. An analytical reconstruction method intends to recover the source distribution by a direct inversion of the projections. It presents the advantage to be exact for a continuous model. Several different algorithms have been investigated. The first has been proposed by [Cree and Bones (1994)] where the reconstruction is achieved from a specific restricted set of projections. But the restriction limits the number of usable data. In [Basko *et al.* (1998)], the Compton projections are transformed into projections on planes using an expansion in spherical harmonics. This method has been adapted for cone-beam reconstruction methods and extended in [Parra (2000), Tomitani and Hirasawa (2002), Hirasawa and Tomitani (2003)]. A direct reconstruction using a full set of available projections has then been proposed by [Maxim *et al.* (2009)]. This method enables to overcome the limitation encountered in the reconstruction method by [Cree and Bones (1994)]. A major limitation of analytical methods is the difficulty to incorporate noise properties of the measured data caused by the randomness in emission and detection processes [Smith (2005), Qi and Leahy (2006)] in the reconstruction procedure.

In this section, we present some of analytical techniques for Compton imaging.

The backprojection of a photon detection enables to localize the  $\gamma$  source onto the surface of a cone. When a large amount of  $\gamma$  events is measured, the photon counts for some given  $V_1$ ,  $V_2$  and  $\beta$  is proportional to the integral of the source distribution over the surface of the cone  $\mathcal{C}(V_1, V_2, \beta)$ . We consider a source having the intensity function  $f$ , positive and compactly supported. When the measurement uncertainties are neglected, the general formula of the cone surface projections may be written as:

$$Pf(V_1, V_2, \beta) = K(\beta, E_0) \int_{\mathcal{C}(V_1, V_2, \beta)} w(\mathbf{x}) f(\mathbf{x}) d\mathbf{x}, \quad (4.1)$$

with  $w$  a weighting function and  $K(\beta, E_0)$  the Compton scattering cross section,  $E_0$  being the initial energy of the photon. The choice of the weight  $w$  as well as the method proposed for the inversion of 4.1 differs between publications. Hereafter, we give some examples.

### 4.1.1 Direct reconstruction with a restricted set of cone surface projections

A direct reconstruction method of the 3D source distribution from the conical surface projections has been proposed in [Cree and Bones (1994)]. In this work, the authors presented a theorem stating that the cone surface projections are redundant and from a complete set of restricted cone surface projections the distribution of the source can be reconstructed.

Let us consider an orthogonal frame  $Oxyz$  with the origin  $O$  in the plane of the scatterer and the vertical axis  $Oz$  orthogonal to the detectors. We will also consider that the

absorber and the source are in different half-spaces with respect to the horizontal plane  $z = 0$ , namely  $z < 0$  for the first and  $z > 0$  for the second.

In a local frame having the vertical axis aligned with  $\overrightarrow{V_2V_1}$ , a unit vector  $\vec{\alpha} = \vec{\alpha}(\overrightarrow{V_2V_1})$  directing a generatrix makes an angle  $\beta$  with the axis of the cone. It can be described by its spherical coordinates, namely the polar angle  $\beta$  and azimuthal angle  $\phi \in [0, 2\pi)$ . A given generatrix of the cone may be then described by the equation  $r\vec{\alpha}$ , for  $r \geq 0$  and  $\vec{\alpha} = \vec{\alpha}(\beta, \phi)$  for some given value  $\phi$ .

Considering now  $w \equiv 1$  in the equation (4.1), we obtain for the cone surface projections, the equation:

$$Pf(V_1, V_2, \beta) = K(\beta, E_0) \int_0^{2\pi} \int_0^\infty f(\overrightarrow{OV_1} + r\vec{\alpha}) r \sin(\beta) dr d\phi. \quad (4.2)$$

This formula is not invertible with linear analytical methods because of the dependency of  $\vec{\alpha}$  on  $\overrightarrow{V_2V_1}$ . To avoid this problem, the set of the considered cone surface projections is restricted to cones having their axis  $\overrightarrow{V_2V_1}$  orthogonal to the detectors. This method is equivalent to use a parallel hole collimator on the absorber.

In this case, the cone surface integrals do not depend on  $\overrightarrow{V_2V_1}$  anymore. Moreover,  $V_1$  can be characterised by its two coordinates in the plane of the scatterer  $x$  and  $y$ . In order to simplify the notations, in this section we denote  $Pf_{CB}$  the cone surface projections, and let them depend on  $x, y$  and  $t = \cos(\beta)$ , instead of  $V_1, V_2$  and  $\beta$ . Following [Cree and Bones (1994)], the equation (4.1) becomes:

$$Pf_{CB}(x, y, t) = K(t) t \sqrt{1+t^2} \int_0^{2\pi} \int_0^\infty f(x + zt \cos(\phi), y + zt \sin(\phi), z) z dz d\phi. \quad (4.3)$$

From this formula, the inversion is now possible in the frequency domain. Taking the 2D Fourier transform of (4.3) with respect to the variables  $x$  and  $y$  leads to:

$$\mathcal{F}_2[Pf_{CB}](u, v, t) = K(t) t \sqrt{1+t^2} \int_0^{2\pi} \int_0^\infty \mathcal{F}_2[f](u, v, z) e^{i2\pi zt(u \cos(\phi) + v \sin(\phi))} z dz d\phi. \quad (4.4)$$

After permuting the integrals, since  $\mathcal{F}_2[f]$  is independent of the variable  $\phi$ , for the inner integral we recognize the zero-order Bessel function of the first kind  $J_0$ . Thus,

$$\mathcal{F}_2[Pf_{CB}](u, v, t) = 2\pi K(t) t \sqrt{1+t^2} \int_0^\infty \mathcal{F}_2[f](u, v, z) J_0(2\pi zt \sqrt{u^2 + v^2}) z dz. \quad (4.5)$$

The integral from the right-hand side of the equation (4.5) corresponds to a Hankel transform of a  $\mathcal{F}_2(f)$  transform defined by:

$$\mathcal{H}_0(r \rightarrow \sqrt{u^2 + v^2})[ ] = 2\pi \int_0^\infty [ ] r J_0(2\pi zt \sqrt{u^2 + v^2}) dr, \quad (4.6)$$

Thus:

$$\mathcal{F}_2[Pf_{CB}](u, v, t) = \frac{K(t) t \sqrt{1+t^2}}{u^2 + v^2} \mathcal{H}_0[\mathcal{F}_2[f](u, v, z)](z \rightarrow t) \quad (4.7)$$

The Hankel transform being self reciprocal, the 2D Fourier transform  $\mathcal{F}_2[f]$  may be expressed for any  $u, v$  and  $u^2 + v^2 \neq 0$ , from equation (4.7) as:

$$\mathcal{F}_2[f](u, v, z) = \mathcal{H}_0 \left[ \frac{u^2 + v^2}{K(t)t\sqrt{1+t^2}} \mathcal{F}_2[Pf_{CB}](u, v, t) \right] (t \rightarrow z) \quad (4.8)$$

The function  $f$  may finally be recovered by inverting the Fourier transform.

However, the restriction of the useful projections (i.e. the virtual collimator) leads to an important loss of the efficiency of the camera. Using a full set of available projections would be preferable and eventually would improve the Signal to Noise Ratio (SNR).

#### 4.1.2 Direct reconstruction using a full set of available projections

A method that enables to use a larger set of available cone surface projections acquired by the Compton camera has been proposed by [Maxim *et al.* (2009)]. The authors propose a mathematical formulation of the model of the projections that accounts for the detector efficiency at any incident angles but does not take into account the distance between the source and the detector. This work extends the direct reconstruction method proposed by Cree and Bones, no restriction on the axis of the cone is necessary. The reconstructed images from different subsets can be combined in order to increase the SNR. The method is based on a projection slice theorem that enables the inversion of the mathematical formulation. Since this method is the starting point of our work on analytical reconstruction, we will later describe it in chapter 5.

#### 4.1.3 Expansion in spherical harmonics

A different approach consists in converting the conical projections into Radon projections by using an expansion in spherical harmonics. Several methods based on this idea were proposed, e.g. [Basko *et al.* (1998), Parra (2000), Tomitani and Hirasawa (2002), Hirasawa and Tomitani (2003)].

We choose to briefly describe here the method proposed in [Basko *et al.* (1998)]. The model for the projections is identical to the one used in [Cree and Bones (1994)], but a different notation proves to be in this case more suitable. Let us denote by  $\vec{k}$  a unit vector from the three-dimensional space, representing the direction of the axis of some cone having the apex at a given point  $V_1$ . In view of equation (4.1), the cone surface projections  $Pf(V_1, V_2, \beta)$  are identical for all point  $V_2$  belonging to the line directed by  $\vec{k}$ .

Let us now denote

$$q_\beta(\vec{k}) = \int_{\mathcal{C}(V_1, V_2, \beta)} f(\mathbf{x}) d\mathbf{x}, \quad (4.9)$$

where  $V_2$  is a point from the space such that  $\overrightarrow{V_2V_1} = ||\overrightarrow{V_2V_1}|| \vec{k}$ . Note that the equation (4.9) is derived from (4.1) with  $w \equiv 1$  and  $K(\beta, E) = 1$ . The integral from (4.9) may be split into two integrals by considering the generatrices of the cone. Let  $S(\vec{k}, \beta)$  be the set

of unit vectors  $\vec{\alpha}$  directing the generatrices of the cone  $\mathcal{C}(V_1, V_2, \beta)$ . Then, we have:

$$q_\beta(\vec{k}) = \int_{S(\vec{k}, \beta)} p(\vec{\alpha}) d\vec{\alpha}, \quad (4.10)$$

with

$$p(\vec{\alpha}) = \int_0^\infty f(\vec{OV}_1 + r\vec{\alpha}) r dr \quad (4.11)$$

This means that, considering all  $\vec{k}$  and all  $\beta$ ,  $q_\beta$  represents all cone-surface projections for a given point  $V_1$ . If we take  $\beta = \frac{\pi}{2}$ , it comes that  $q_{\frac{\pi}{2}}(\vec{k})$  is equal to the Radon projection along the plane that contains  $V_1$  and is orthogonal to  $\vec{k}$ .

The idea then is to determine  $q_{\frac{\pi}{2}}(\vec{k})$ . By expressing  $p(\vec{\alpha})$  and  $q_\beta(\vec{k})$  in terms of an expansion in spherical harmonics, we have:

$$p(\vec{\alpha}) = \sum_{l=0}^{\infty} \sum_{m=-l}^l p_{lm} Y_{lm}(\vec{\alpha}) \quad (4.12)$$

and

$$q_\beta(\vec{k}) = \sum_{l=0}^{\infty} \sum_{m=-l}^l q_{lm}^{(\beta)} Y_{lm}(\vec{k}) \quad (4.13)$$

where  $Y_{lm}(\vec{\alpha})$  and  $Y_{lm}(\vec{k})$  are associated Legendre polynomials of indices  $l$  and  $m$ .

The relationship

$$q_{lm}^{(\beta)} = \sqrt{2\pi} \sin(\beta) p_{lm} P_l(\cos(\beta)), \quad (4.14)$$

relating the coefficients from equations (4.12) and (4.13), enables to calculate  $p_{lm}$  from  $q_{lm}^{(\beta)}$ . Then, the reconstruction method can be described in three steps. First  $q_{lm}^{(\beta)}$  are evaluated from the data acquired (samples of  $q_\beta(\vec{k})$ ). Then, using the relationship formula (4.14), the  $p_{lm}$  coefficients are calculated. Finally,  $q_{\frac{\pi}{2}}(\vec{k})$  are evaluated from the expansion in spherical harmonics given by (4.13) with  $\beta = \frac{\pi}{2}$ . Once  $q_{\frac{\pi}{2}}(\vec{k})$ , i.e. 3D Radon projections, are known, a Filtered BackProjection (FBP) algorithm can be used to recover  $f$ . However, this method is based on infinite summations. In practice, these summations are truncated at a level corresponding to the angular resolution of the detectors.

A fully analytical inversion algorithm using also a spherical harmonic expansion has been proposed by [Parra (2000)]. This method converts cone-surface projections into cone-beam projections. The inversion method is improved by avoiding the heavy expansion in spherical harmonics during reconstruction and using instead, a deconvolution in spherical coordinates. The event dependent measurement errors may be accounted for.

Since it is almost impossible to acquire full projections covering all scattering angles, several algorithms that can be applied to projection data for limited scattering angles have been proposed by [Tomitani and Hirasawa (2002), Hirasawa and Tomitani (2003)]. These methods are extensions of the method proposed by [Parra (2000)].

## 4.2 Iterative methods

The iterative reconstruction methods were first developed for PET and SPECT imaging modalities. They are also applicable to Compton imaging since in principle, the iterative process is the same. The difference between these modalities arise from the modelling and estimation of the system matrix.

The iterative reconstruction methods do not provide an exact and unique solution. However, they are greatly adaptable and thus allow to take into account the noise properties in the measured data, noise due to the randomness of the emission, to the detecting device and, in medical applications, to physiological phenomena.

One of the first algorithms was the Algebraic Reconstruction Technique (ART) proposed by [Gordon *et al.* (1970), Herman and Lent (1976), Singh and Doria (1983)]. With these methods, a priori information can easily be incorporated, but the technique itself requires adjustments to be closer to the realistic conditions.

Most of the iterative techniques are based on the Maximum Likelihood Expectation Maximization (MLEM) [Hebert *et al.* (1990), Wilderman *et al.* (1998), Sauve *et al.* (1999), Torga *et al.* (2009)], or its variant the Ordered Subset Expectation Maximization (OSEM) [Hudson and Larkin (1994), Kim *et al.* (2007), Kim *et al.* (2010)]. These methods have various limitations e.g., the fluctuations of the solutions, noise propagation during the iterations.

Alternative algorithms use Bayesian approaches leading to the Maximum *A Posteriori* (MAP) method [Lange *et al.* (1987), Liang *et al.* (1989), Huesman *et al.* (2000)] or the Maximum Entropy (ME) [Strong *et al.* (1990), Strong (2003)]. In these methods, a prior can be incorporated in the reconstruction process. This prior includes characteristics of the image to reconstruct. However, the choice of the optimal prior may prove to be a difficult task. Another Bayesian approaches are proposed by [Lee *et al.* (2008)] using a MAP technique but also a Row-Action method or a Block-Sequential method for the iterative process. The Row-Action ML (RAML) step perform a specific update of the image with projections ordered in a sequence of disjoint subsets. The Block-Sequential EM (BSEM) is a relaxed method of OSEM. First a RAML step is achieved, then a regularization step is performed using the gradient direction of the prior.

A completely different approach is proposed by [Andreyev *et al.* (2011)] using a Stochastic Origin Ensemble method based on Markov chains. This method is also used by [Mackin *et al.* (2012)]. The results are similar to the ones obtained with MLEM, but there are several limitations due to an important variance in the image, and an underestimation of the intensity of the reconstructed source.

We present in this section some of these techniques.

### 4.2.1 The LM-MLEM algorithm

As mentioned, the most well-known iterative method is the Maximum Likelihood Expectation Maximization. Our contribution is also based on this algorithm. The principle

relies on the statistical properties of the measured data.

### Maximum Likelihood (ML)

We want to reconstruct the 3D image of the radiating source from the measurements of the Compton camera. The binned image space is denoted  $\mathbf{J}$  and indexed by  $j$ . Each image bin emits a random number of photons. The mean intensity of emission of an image space bin is denoted  $\lambda_j$ .

Let us consider the binned data space of all measured events denoted  $\mathbf{I}$  and indexed by  $i$ . We denote  $\mathbf{Y}$  the vector of measurements and  $y_i$  the number of detected photons in the bin  $i$ . The data space of all not measured events is denoted  $\bar{\mathbf{I}}$ .

We want to obtain an estimate  $\hat{\boldsymbol{\lambda}}$  of the mean emission distribution of the source. The ML criterion states that the best estimate has to give the greatest probability of obtaining the measurements  $\mathbf{I}$ . Assuming for now that we know the system matrix  $\mathbf{T} = (t_{ij})$  of the detector, the mean number of detector counts  $\mathbf{Y}$  that would be obtained for some given  $\boldsymbol{\lambda}$  is:

$$\mu_i = \sum_j t_{ij} \lambda_j. \quad (4.15)$$

The element  $t_{ij}$  corresponds to the probability that a photon emitted in the image bin  $j$  is detected in the data bin  $i$ . We can note that the occurrence of an event does not have any effect on the occurrence of another. Events are independent. Then, assuming an underlying Poisson distribution the probability of observing  $y_i$  given the mean value  $\mu_i$  is written:

$$p(y_i|\mu_i) = e^{-\mu_i} \frac{\mu_i^{y_i}}{y_i!}. \quad (4.16)$$

Furthermore, the likelihood function  $\mathcal{L}$  describes the probability that the measurements  $\mathbf{Y}$  have been generated by the image  $\mathbf{J}$  with the emissions  $\boldsymbol{\lambda}$ . Thus, we have:

$$\mathcal{L}(\mathbf{Y}|\boldsymbol{\lambda}) = \prod_i p(y_i|\mu_i) = \prod_i e^{-\mu_i} \frac{\mu_i^{y_i}}{y_i!}. \quad (4.17)$$

Finding the source distribution that has the highest probability to generate the measured data, amounts to find the maximum of the likelihood function. Since maximizing the likelihood function is tedious, it is common to maximize the log-likelihood function instead, the natural logarithm being monotonically increasing. Consequently, we want to maximize the expression:

$$\ln \mathcal{L}(\mathbf{Y}|\boldsymbol{\lambda}) = \sum_i [-\mu_i + y_i \ln \mu_i - \ln(y_i!)]. \quad (4.18)$$

Replacing (4.15) in (4.18), we also can write:

$$\ln \mathcal{L}(\mathbf{Y}|\boldsymbol{\lambda}) = \sum_i [-\sum_j t_{ij} \lambda_j + y_i \ln(\sum_j t_{ij} \lambda_j) - \ln(y_i!)]. \quad (4.19)$$

Because of the non-linearity of the equation (4.19), in the general case it is impossible to solve the maximization problem. [Lange and Carson (1984)] suggested to use the iterative Expectation Maximization approach in order to achieve the maximization of the likelihood function.

## Expectation Maximization (EM)

As mentioned previously, this approach is an iterative algorithm. For each iteration, the first step (E-step) is to determine the expectation of the likelihood function given the measurement  $\mathbf{Y}$  and the estimation  $\hat{\boldsymbol{\lambda}}^{(\ell)}$  obtained from the previous iteration, where  $\ell$  is the index of the iteration. In order to satisfy the requirement for a complete data set for the EM algorithm, we introduce the random variable  $\mathbf{X} = \{x_{ij}|i = \overline{1, N_I}, j = \overline{1, N_J}\}$  with  $y_i = \sum_j x_{ij}$  and with  $N_I$  and  $N_J$  the number of bins in the data and image space, respectively. The term  $x_{ij}$  represents the number of photons emitted in the bin  $j$  and detected in bin  $i$ . The log-likelihood function is now written:

$$\ln \mathcal{L}(\mathbf{X}|\boldsymbol{\lambda}) = \sum_i \sum_j (x_{ij} \ln(t_{ij} \lambda_j) - t_{ij} \lambda_j - \ln(x_{ij}!)) \quad (4.20)$$

Following [Lange and Carson (1984)], the conditional expectation of the log-likelihood with respect to the measured data is:

$$E \left( \ln \mathcal{L}(\mathbf{X}|\boldsymbol{\lambda}), \mathbf{Y}, \hat{\boldsymbol{\lambda}}^{(\ell)} \right) = \sum_i \sum_j \left( -t_{ij} \lambda_j + E \left( x_{ij}, y_i, \hat{\boldsymbol{\lambda}}^{(\ell)} \right) \ln(t_{ij} \lambda_j) \right) \quad (4.21)$$

with:

$$E \left( x_{ij}, y_i, \hat{\boldsymbol{\lambda}}^{(\ell)} \right) = \frac{t_{ij} \hat{\lambda}_j^{(\ell)}}{\sum_k t_{ik} \hat{\lambda}_k^{(\ell)}} y_i.$$

The second step (M-step) consists in finding the estimation  $\hat{\boldsymbol{\lambda}}^{(\ell+1)}$  which maximizes the equation 4.21 by equaling to zero the derivatives of the expectation function obtained in the E-step. This leads to:

$$\frac{\partial}{\partial \lambda_j} E \left( \ln \mathcal{L}(\mathbf{X}|\boldsymbol{\lambda}), \mathbf{Y}, \hat{\boldsymbol{\lambda}}^{(\ell)} \right) = - \sum_i t_{ij} + \frac{1}{\hat{\lambda}_j} \sum_i \frac{t_{ij} \hat{\lambda}_j^{(\ell)}}{\sum_k t_{ik} \hat{\lambda}_k^{(\ell)}} y_i = 0 \quad (4.22)$$

It finally leads to the MLEM formula [Lange and Carson (1984)]:

$$\hat{\lambda}_j^{(\ell+1)} = \frac{\hat{\lambda}_j^{(\ell)}}{\sum_i t_{ij}} \sum_i \frac{t_{ij} y_i}{\sum_k t_{ik} \hat{\lambda}_k^{(\ell)}} \quad (4.23)$$

The term  $\sum_i t_{ij}$  uses to be called sensitivity and is denoted  $s_j$ . It corresponds to the probability that a photon emitted by the bin  $j$  was detected.

### List Mode

The List Mode (LM) extension of the MLEM algorithm, originally proposed for the Compton camera in [Wilderman *et al.* (1998)] presents a computational advantage in comparison with the binned approach. Each measurement in LM-MLEM is considered unique and detected by an infinitely small bin. As a consequence, the number of counts for the bin  $i$  will be either 0 or 1. Thus, we have  $y_i \rightarrow 1$  for a detected event or  $y_i \rightarrow 0$  if no event is measured.

We then can simplify the iterative formula (4.23) as:

$$\hat{\lambda}_j^{(\ell+1)} = \frac{\hat{\lambda}_j^{(\ell)}}{s_j} \sum_i \frac{t_{ij}}{\sum_k t_{ik} \hat{\lambda}_k^{(\ell)}}, \quad (4.24)$$

However, since the data space is not entirely spanned anymore, we no longer have  $s_j = \sum_i t_{ij}$  with a summation over all measured events. The summation must be achieved on all possible events which includes those not measured:  $s_j = \sum_{I+\bar{I}} t_{ij}$ .

The relationships between the image space and the data space are shown in figure 4.1.

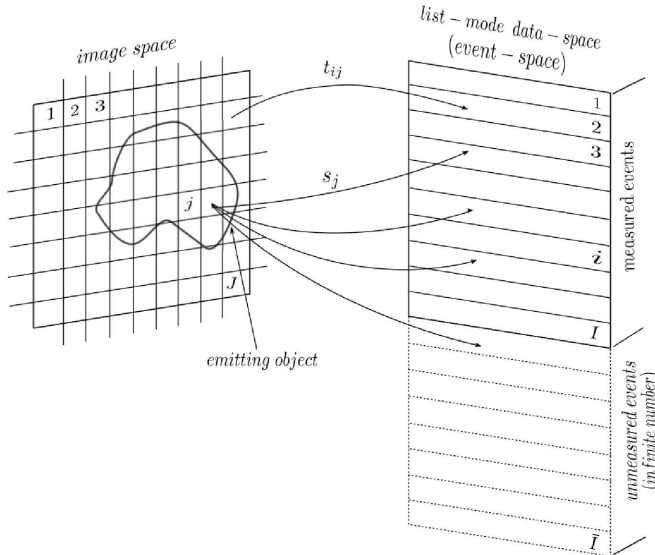


Figure 4.1: Illustration of the relationships between data space and image space. Source: [Zoglauer (2005)]

### Ordered Subset Expectation Maximization (OSEM)

The MLEM algorithm can be really time consuming. In order to accelerate the iterative reconstruction, variations of this algorithm has been investigated producing less iterations.

Originally proposed by [Hudson and Larkin (1994)], the OSEM method has become a popular variation of the MLEM algorithm. In conventional EM, for each iteration, a

comparison between the estimated and the measured projection is performed. With the OSEM algorithm, the comparison is successively based on subsets containing a relatively small number of projections. Thus, it enables to speed up the EM algorithm by replacing the summation over all projections by summations over subsets of data. In [Kim *et al.* (2007), Kim *et al.* (2010)], different versions of the OSEM algorithm for Compton imaging are proposed. All of them outperform the classical EM algorithm in term of speed with the same overall quality on the images.

### 4.2.2 Algebraic Reconstruction Technique (ART)

The Algebraic Reconstruction Technique (ART) is one of the first iterative methods proposed for reconstruction from projections. In numerical linear algebra, this method is known as Kaczmarz method (1937). As for image reconstruction, the method was introduced by [Gordon *et al.* (1970)] and used by [Singh and Doria (1983)].

This method can be considered as an iterative solver of a system of linear equations. The original method proposed by [Gordon *et al.* (1970)] searchs for the solution to  $\mathbf{Y} = \mathbf{T}\boldsymbol{\lambda}$ . Given an initial guess  $\boldsymbol{\lambda}^{(0)}$ , an estimation of the solution  $\boldsymbol{\lambda}^{(l)}$  is provided by the equation:

$$\boldsymbol{\lambda}^{(\ell+1)} = \boldsymbol{\lambda}^{(\ell)} + \frac{y_i - \langle \mathbf{t}_i, \boldsymbol{\lambda}^{(\ell)} \rangle}{\|\mathbf{t}_i\|_2^2} \mathbf{t}_i \quad (4.25)$$

where  $t_i$  is the  $i^{\text{th}}$  row of the matrix  $\mathbf{T}$ , and  $i \equiv \ell[\text{mod}N_J] + 1$  (mod being the mathematical operator modulo).

An advantage of the method is that it makes easy the introduction of prior informations during the reconstruction process. Variations of this method are proposed by [Herman and Lent (1976)].

### 4.2.3 Bayesian image reconstruction

The Bayesian reconstruction approach is also known as the Maximum *a posteriori* (MAP) approach. In comparison with the LM-MLEM approach, it introduces a prior in the estimation process. Considering additional informations from the statistical properties of the object to image, one introduces the probability density function  $p(\boldsymbol{\lambda})$ . The joint probability density function of  $(\boldsymbol{\lambda}, \mathbf{Y})$  is then given by:

$$p(\boldsymbol{\lambda}, \mathbf{Y}) = p(\mathbf{Y}|\boldsymbol{\lambda})p(\boldsymbol{\lambda}) \quad (4.26)$$

Using the Bayes' theorem, we can express the conditional probability of  $\boldsymbol{\lambda}$  given  $\mathbf{Y}$  as:

$$p(\boldsymbol{\lambda}|\mathbf{Y}) = \frac{p(\mathbf{Y}|\boldsymbol{\lambda})p(\boldsymbol{\lambda})}{p(\mathbf{Y})} \quad (4.27)$$

We want to maximize this expression. Considering the logarithmic formulation, the MAP estimator is written:

$$MAP(\boldsymbol{\lambda}) = \ln \mathcal{L}(\mathbf{Y}|\boldsymbol{\lambda}) + \ln(p(\boldsymbol{\lambda})) \quad (4.28)$$

which represents the summation of the log-likelihood function seen in the MLEM method, and the log-prior.

There are different types of prior. They might be independent from the source or following a specific interaction model. The first category of priors includes Gaussian model, e.g. [Huesman *et al.* (2000)] and Gamma prior, e.g. [Lange *et al.* (1987)]. Other kinds of priors can be found in the literature as for instance, prior based on the maximum entropy criterion [Liang *et al.* (1989)].

The *a priori* information may be a real advantage, as the idea is to get a better estimation of  $\hat{\boldsymbol{\lambda}}$  in the reconstruction process. However, depending on the context, the selection of the optimal prior might be challenging.

#### 4.2.4 Stochastic Origin Ensemble (SOE)

This method proposed by [Andreyev *et al.* (2011)] is a fast algorithm that enables to recover the image using an approach based on Markov chains. The reconstruction process is iterative.

First, an arbitrary initial guess of the estimated image is generated by choosing randomly, for each recorded event, a possible origin of the photon. The image of origins selected for all events constitute the Stochastic Origin Ensemble. After the first step of selection, a density value depending on the neighbourhood is calculated for each event. Next, the iterative process starts and can be described as follows.

- An event is randomly selected. A new location of the origin of the photon out of all possible locations on the conical surface of this event is chosen randomly. The new density value is computed.
- An acceptance function is then calculated depending on the densities of the event when it is put at its old and new location.
- Depending on the value of the calculated acceptance, the origin of the event is moved to its new location or remains the same.
- All the steps are repeated  $N$  times with  $N$  the number of recorded events.

During the iteration, the same event can be selected several times. The number of iterations is empirically chosen. The algorithm stops when the origin ensemble reaches a state of quasistationarity.

After post-filtering, this method enables to obtain results similar to the MLEM reconstruction algorithm. Its main advantages are the possibility to be used with any kind of Compton device, and the computational time that is greatly reduced compared to classical

MLEM. However, this method tends to underestimate the intensity values in the reconstructed image and to increase the variance. The method has further been investigated by [Mackin *et al.* (2012)] and evaluated for a ideal Compton camera. The very promising results obtained with an ideal simulated Compton camera would require to be confirmed in more realistic conditions.

### III Analytical method

---



# Résumé en français (Abstract in French)

Dans [Maxim *et al.* (2009)], une méthode de reconstruction analytique pour la caméra Compton utilisant l'ensemble des projections disponibles a été développée. Nous présentons, dans un premier temps, ces travaux qui sont le point de départ de notre méthode. Dans un second temps, nous développons une méthode de rétroprojection filtrée qui mène à une implémentation efficace du théorème coupe projection associé aux projections Compton.

## Inversion de la transformée Compton

### Modèle mathématique

On suppose que la caméra est composée de deux détecteurs plans de taille infinie. La première interaction a lieu dans le diffuseur en  $V_1$  et la seconde dans l'absorbeur en  $V_2$ . On considère l'épaisseur des détecteurs négligeable. Le cône Compton noté  $\mathcal{C}(V_1, V_2, \beta)$  est défini par son sommet  $V_1$ , son axe colinaire à  $\overrightarrow{V_2V_1}$  et son angle de demi-ouverture  $\beta$ . Cet angle est donné par l'équation Compton (3.2). L'axe du cône est paramétré par son angle polaire  $\theta_g \in [0; \frac{\pi}{2}]$  et son angle azimut  $\delta \in [0; 2\pi]$ . Le centre du repère cartésien est placé au niveau du diffuseur afin que le plan  $xOy$  coïncide avec le détecteur. L'axe  $Oz$  est orienté de sorte que les points dans l'absorbeur soient dans le demi-espace de coordonnées  $z < 0$ , comme l'illustre la figure 5.1. La fonction  $f$  qui modélise la source de rayonnement est supposée à support compact. Pour des paramètres  $(\theta_g, \delta, \beta)$  donnés, le nombre moyen de photons émis par la source interagissant en  $V_1(u_1, u_2, 0)$ , diffusés suivant un angle  $\beta$  dans la direction  $\overrightarrow{V_1V_2}$ , est noté  $Pf(u_1, u_2; \theta_g, \delta, \beta)$ . L'application

$$(u_1, u_2) \in \mathbb{R}^2 \mapsto Pf(u_1, u_2; \theta_g, \delta, \beta)$$

est appelée transformée Compton. L'expression mathématique décrivant les projections Compton est donnée par la formule suivante:

$$Pf(u_1, u_2; \theta_g, \delta, \beta) = K(\beta, E_0) \int_{M \in \mathcal{C}(V_1, V_2, \beta)} f(M) \cos \theta_M ds,$$

---

où  $K(\beta, E_0)$  représente le coefficient de Klein-Nishina et  $\theta_M$  l'angle d'incidence du photon. À présent, l'objectif est d'inverser cette formule pour obtenir  $f$  en fonction des projections  $Pf$ .

## Expression duale des projections Compton

On fait l'hypothèse (non restrictive dans le domaine médical) que  $f(x, y, z) = 0$  pour  $z \leq 0$ . Initialement,  $\beta$  est compris dans l'intervalle  $[0; \pi]$ . Dans le cas de  $\beta = 0$ , le cône dégénère en une droite et le modèle mathématique présenté précédemment n'est plus adapté. Pour  $\beta \neq 0$ , nous restreignons le modèle au cas où l'intersection du cône avec un plan parallèle au diffuseur est une ellipse. Pour ce faire,  $\beta$  doit être inférieur à  $\frac{\pi}{2} - \theta_g$ . L'intervalle de valeurs  $\beta$  est donc restreint à  $\beta \in (0, \frac{\pi}{2} - \theta_g)$ .

L'équation du cône Compton  $\mathcal{C}(V_1, V_2, \beta)$  dans le repère orthonormé  $0xyz$  est:

$$(x - u_1)^2 + (y - u_2)^2 = z^2 \tan^2(\beta)$$

Soient les expressions  $a(\theta_g, \beta)$ ,  $b(\theta_g, \beta)$  et  $c(\theta_g, \beta)$  fonction des angles  $\theta_g$  et  $\beta$ :

$$a(\theta_g, \beta) = \frac{\sin \beta \cos \beta}{\cos^2 \theta_g - \sin^2 \beta}$$

$$b(\theta_g, \beta) = \frac{\sin \beta}{\sqrt{\cos^2 \theta_g - \sin^2 \beta}}$$

$$c(\theta_g, \beta) = \frac{\sin \theta_g \cos \theta_g}{\cos^2 \theta_g - \sin^2 \beta}.$$

Un point  $M(x, y, z)$  du cône  $\mathcal{C}(V_1, V_2, \beta)$ , avec  $V_1(u_1, u_2, 0)$ , a la représentation paramétrique suivante:

$$\begin{cases} x = z[(c(\theta_g, \beta) + a(\theta_g, \beta) \cos \varphi) \cos \delta + b(\theta_g, \beta) \sin \varphi \sin \delta] + u_1 \\ y = z[-(c(\theta_g, \beta) + a(\theta_g, \beta) \cos \varphi) \sin \delta + b(\theta_g, \beta) \sin \varphi \cos \delta] + u_2 \\ z = z \end{cases}$$

où  $z \geq 0$  est la distance entre le point  $M$  et le diffuseur. Le paramètre angulaire  $\varphi \in [0, 2\pi)$  caractérise le point  $M$  en tant que point de l'ellipse  $\mathcal{E}(z; \theta_g, \delta, \beta)$  définie par l'intersection du cône Compton avec le plan d'altitude  $z$ , parallèle au détecteur incluant et passant par  $M$ . A partir de cette représentation, on peut exprimer l'élément de surface  $ds$  par :

$$\left\| \frac{\partial OM}{\partial z} \wedge \frac{\partial OM}{\partial \varphi} \right\| = z \frac{\sin \beta}{(\cos^2 \theta_g - \sin^2 \beta)^{\frac{3}{2}}} |\sin \theta_g \sin \beta \cos \varphi + \cos \theta_g \cos \beta|$$

---

On exprime également  $\cos \theta_M$ :

$$\cos \theta_M = \frac{\cos^2 \theta_g - \sin^2 \beta}{|\sin \theta_g \sin \beta \cos \varphi + \cos \theta_g \cos \beta|}$$

En combinant les équations précédentes, on obtient:

$$Pf(u_1, u_2; \theta_g, \delta, \beta) = K(\beta, E_0)b(\theta_g, \beta) \int_0^\infty \int_0^{2\pi} z \\ f(u_1 + (zc(\theta_g, \beta) + za(\theta_g, \beta) \cos \varphi) \cos \delta + zb(\theta_g, \beta) \sin \varphi \sin \delta, \\ u_2 - (zc(\theta_g, \beta) + za(\theta_g, \beta) \cos \varphi) \sin \delta + zb(\theta_g, \beta) \sin \varphi \cos \delta, z) d\varphi dz$$

On considère l'image 3D comme une succession d'images 2D dans la direction  $z$  et on s'intéresse à la transformée de Fourier de ces images. En appliquant le théorème de Fubini-Lebesgue et celui de translation dans le domaine des fréquences pour la transformation de Fourier, on écrit:

$$\mathcal{F}_2[Pf](\eta_1, \eta_2; \theta_g, \delta, \beta) = K(\beta, E_0)b(\theta_g, \beta) \int_0^\infty \int_0^{2\pi} z e^{2i\pi z c(\theta_g, \beta)(\eta_1 \cos \delta + \eta_2 \sin \delta)} \\ \mathcal{F}_2[f](\eta_1, \eta_2, z) e^{2i\pi z(a(\theta_g, \beta)(\eta_1 \cos \delta + \eta_2 \sin \delta) \cos \varphi + b(\theta_g, \beta)(-\eta_1 \sin \delta + \eta_2 \cos \delta) \sin \varphi)} d\varphi dz$$

avec  $\mathcal{F}_2[f]$ , la transformée de Fourier 2D de  $f$  vis à vis des variables  $x$  et  $y$ , la troisième variable étant inchangée, et  $\mathcal{F}_2[Pf]$  la transformée de Fourier 2D des projections Compton. Dans cette expression on reconnaît la fonction de Bessel de première espèce à l'ordre 0, ce qui nous permet d'écrire:

$$\mathcal{F}_2[Pf](\eta_1, \eta_2; \theta_g, \delta, \beta) = K(\beta, E_0)b(\theta_g, \beta) \int_0^\infty z e^{2i\pi z c(\theta_g, \beta)(\eta_1 \cos \delta + \eta_2 \sin \delta)} \mathcal{F}_2[f](\eta_1, \eta_2, z) \\ \times J_0(2\pi z \sqrt{a^2(\theta_g, \beta)(\eta_1 \cos \delta + \eta_2 \sin \delta)^2 + b^2(\theta_g, \beta)(-\eta_1 \sin \delta + \eta_2 \cos \delta)}) dz$$

## Inversion

Dans l'expression précédente, la dépendance à la variable  $\phi$  rend l'inversion trop complexe. Il nous faut donc d'abord éliminer le terme exponentiel. Pour cela, on choisit les vecteurs  $(\eta_1, \eta_2)$  et  $(\cos \delta, \sin \delta)$  de sorte qu'ils soient orthogonaux. Soient  $(\rho, \omega)$  les coordonnées polaires du vecteur  $(\eta_1, \eta_2)$ . Pour chaque point  $(\eta_1, \eta_2)$ , on sélectionne les projections Compton de paramètre

$$\delta = \omega + \epsilon \frac{\pi}{2} [\text{mod } 2\pi], \quad \epsilon = \pm 1.$$

---

Cette condition implique  $\eta_1 \cos \delta + \eta_2 \sin \delta = 0$ , ainsi le facteur exponentiel vaut 1. On a alors:

$$\begin{aligned} \mathcal{F}_2[Pf](\eta_1, \eta_2; \theta_g, \omega + \epsilon \frac{\pi}{2}, \beta) &= 2\pi K(\beta, E_0) b(\theta_g, \beta) \\ &\times \int_0^\infty z \mathcal{F}_2[f](\eta_1, \eta_2, z) J_0(2\pi z b(\theta_g, \beta) \sqrt{\eta_1^2 + \eta_2^2}) dz \end{aligned}$$

On reconnaît pour la partie droite de l'équation, la transformée de Hankel de  $\mathcal{F}_2[f]$  vis à vis de la coordonnée  $z$ . On définit alors la transformée de Hankel-Fourier comme suit:

$$\begin{aligned} \mathcal{HF} : f &\rightarrow \mathcal{HF}[f] \\ \mathcal{HF}[f](\eta_1, \eta_2, \eta_3) &= 2\pi \int_0^\infty z \mathcal{F}_2[f](\eta_1, \eta_2, z) J_0(2\pi z \eta_3) dz \end{aligned}$$

La transformée de Hankel-Fourier représente la transformée de Hankel vis à vis de la variable  $z$ , de la transformée 2D de Fourier vis à vis des variables  $x$  et  $y$  de la fonction 3D  $f$ . On peut alors écrire:

$$\mathcal{HF}[f](\eta_1, \eta_2, b(\theta_g, \beta) \sqrt{\eta_1^2 + \eta_2^2}) = \frac{1}{K(\beta, E_0) b(\theta_g, \beta)} \mathcal{F}_2[Pf] \left( \eta_1, \eta_2; \theta_g, \omega + \epsilon \frac{\pi}{2}, \beta \right)$$

On note  $\mathcal{C}_F(\theta_g, \beta)$  le cône Compton dans le domaine de Fourier:

$$\mathcal{C}_F(\theta_g, \beta) : \quad \eta_1^2 + \eta_2^2 = \frac{\eta_3^2}{b^2(\theta_g, \beta)},$$

et  $\mathcal{P}_F(\delta)$  le plan orthogonal au vecteur  $(\cos \delta, \sin \delta, 0)$ .

Le théorème coupe-projection pour la transformée de Hankel-Fourier donné par [Maxim et al. (2009)] établit que pour des angles  $\theta_g \in [0, \frac{\pi}{2}]$ ,  $\delta \in [0, 2\pi]$  et  $\beta \in (0, \frac{\pi}{2} - \theta_g)$  donnés, la coupe de la transformée de Hankel-Fourier de  $f$  définie par l'intersection de  $\mathcal{C}_F(\theta_g, \beta)$  avec  $\mathcal{P}_F(\delta)$ , pondérée par  $K(\beta, E_0) b(\theta_g, \beta)$ , est égale à la coupe de la projection  $Pf(\cdot, \cdot; \theta_g, \delta, \beta)$  par  $\mathcal{P}_F(\delta)$  dans le domaine de Fourier. On peut alors obtenir les valeurs de  $\mathcal{HF}[f]$  sur la surface du cône en faisant varier ensuite  $\delta$  sur l'intervalle  $[0, 2\pi]$ . La redondance des projections nous permet de limiter l'intervalle de  $\delta$  à  $[0, \pi]$ .

Ainsi, pour réaliser l'inversion de la formule (5.4), nous procédonsons d'abord par l'inversion de la transformée de Hankel, puis par l'inversion de la transformée 2D de Fourier, et nous obtenons la formule:

$$\begin{aligned} f(x, y, z) &= \int_{-\infty}^\infty \int_{-\infty}^\infty \left( \int_0^{\frac{\pi}{2} - \theta_g} \frac{b'_\beta(\theta_g, \beta)}{K(\beta, E_0)} \mathcal{F}_2(Pf) \left( \eta_1, \eta_2; \theta_g, \omega + \epsilon \frac{\pi}{2}, \beta \right) \right. \\ &\quad \times \left. J_0(2\pi z b(\theta_g, \beta) \sqrt{\eta_1^2 + \eta_2^2}) d\beta \right) (\eta_1^2 + \eta_2^2) e^{2i\pi(x\eta_1 + y\eta_2)} d\eta_1 d\eta_2 \end{aligned}$$

Cette formule consiste donc à exprimer  $f$ , la fonction qui modélise la source, en prenant la transformée 2D des projections Compton d'angle polaire  $\theta_g$ , d'angle de demi-ouverture  $\beta$  et d'angle azimut  $\delta = \omega + \epsilon \frac{\pi}{2}$ , pondérée par l'inverse de la section efficace de diffusion

---

Compton, et multipliée par la dérivée de l'expression  $b(\theta_g, \beta)$  vis à vis de la variable  $\beta$  et par un noyau radial de Bessel. On somme cette expression suivant  $\beta$ , et on couvre le demi-espace supérieur dans le domaine de Fourier. En multipliant ensuite par  $\eta_1^2 + \eta_2^2$ , on obtient la transformée 2D de Fourier de  $f$  sur des coupes successives dans la direction  $z$  et parallèles au diffuseur. On obtient finalement  $f$  en prenant l'inverse de la transformée de Fourier. Cette expression montre également que pour un angle d'inclinaison  $\theta_g$  donné, et pour un diffuseur plan, on peut reconstruire une image de la source. Ainsi, on peut reconstruire plusieurs images pour différentes valeurs de  $\theta_g$  et par diffuseur. Ces images devraient théoriquement être identiques, en pratique elles peuvent différer car les hypothèses faites, comme celle de la taille infinie des détecteurs, ne sont pas vérifiées. En moyennant l'ensemble des images, on améliore le rapport signal à bruit de la reconstruction.

## Rétroprojection filtrée pour l'imagerie Compton

Notre contribution reprend les travaux présentés précédemment. Nous proposons une extension de la méthode, sous la forme d'un algorithme de rétroprojection filtrée.

Dans la pratique, l'espace des données est discrétilisé et le nombre de projections acquises est limité. Ainsi, l'espace fréquentiel est peu couvert, surtout dans les hautes fréquences. Les informations sont concentrées sur un nombre fini de cônes, et pour un cône donné, les informations sont réparties sur un nombre fini de demi-droites, les génératrices du cône. De ce fait, certains voxels, dans l'espace fréquentiel, ne seront pas intersectés par ces génératrices et au contraire, certains seront traversés à de nombreuses reprises. Ce phénomène est illustré par le schéma figure 5.3. Avant d'appliquer la transformée inverse de Fourier, une étape d'interpolation doit donc être réalisée afin de combler les espaces dépourvus d'informations. A l'instar des méthodes de reconstruction en tomographie, nous proposons d'utiliser une formulation rétroprojection filtrée.

On introduit les coordonées polaires dans la formule proposée précédemment, avec  $\rho \in \mathbb{R}$  et  $\omega \in [0, \pi]$  comme utilisés usuellement en tomographie. On a alors:

$$\begin{aligned} f(x, y, z) &= \int_{-\infty}^{\infty} \int_0^{\pi} \int_0^{\frac{\pi}{2}-\theta_g} \frac{b'_\beta(\theta_g, \beta)}{K(\beta, E_0)} J_0(2\pi z b(\theta_g, \beta) \rho) |\rho|^3 \\ &\quad \mathcal{F}_2(Pf) \left( \rho \cos \omega, \rho \sin \omega; \theta_g, \omega + \epsilon \frac{\pi}{2}, \beta \right) e^{2i\pi\rho(x \cos \omega + y \sin \omega)} d\beta d\omega d\rho \end{aligned}$$

Notons que pour des angles  $\theta_g, \omega, \beta$  donnés, l'application:

$$\rho \mapsto \mathcal{F}_2[Pf](\rho \cos \omega, \rho \sin \omega; \theta_g, \omega + \epsilon \frac{\pi}{2}, \beta),$$

est une ligne de la transformée de Fourier 2D de  $Pf(\cdot, \cdot; \theta_g, \omega + \epsilon \frac{\pi}{2}, \beta)$ . Le théorème coupe-projection nous permet de remplacer l'expression  $\mathcal{F}_2(Pf)(\rho \cos \omega, \rho \sin \omega; \theta_g, \omega + \epsilon \frac{\pi}{2}, \beta)$  par la transformée de Fourier 1D de la projection de Radon d'angle  $\omega$ , notée  $R_\omega$ , de

---

$Pf(\cdot, \cdot; \theta_g, \omega + \epsilon \frac{\pi}{2}, \beta)$ :

$$\mathcal{F}_2(Pf) \left( \rho \cos \omega, \rho \sin \omega; \theta_g, \omega + \epsilon \frac{\pi}{2}, \beta \right) = \mathcal{F}(R_\omega[Pf]) \left( \rho \cos \omega, \rho \sin \omega; \theta_g, \omega + \epsilon \frac{\pi}{2}, \beta \right).$$

On note  $H_z$  le filtre:

$$H_z(\rho, \beta; \theta_g, E_0) = \frac{b'_\beta(\theta_g, \beta)}{K(\beta, E_0)} J_0(2\pi z b(\theta_g, \beta) \rho) |\rho|^3.$$

En remplaçant dans la formule d'inversion, on obtient la formule de rétroprojection filtrée avec le filtre  $H_z$ :

$$\begin{aligned} f(x, y, z) &= \int_{-\infty}^{\infty} \int_0^{\pi} \int_0^{\frac{\pi}{2} - \theta_g} H_z(\rho, \beta; \theta_g, E_0) \mathcal{F}(R_\omega[Pf]) \left( \rho \cos \omega, \rho \sin \omega; \theta_g, \omega + \epsilon \frac{\pi}{2}, \beta \right) \\ &\quad \times e^{2i\pi\rho(x \cos \omega + y \sin \omega)} d\beta d\omega d\rho, \end{aligned}$$

En d'autres termes, on applique d'abord la projection Radon d'angle  $\omega$  aux projections Compton de paramètres angulaires  $\theta_g$ ,  $\beta$  et  $\delta = \omega + \epsilon \frac{\pi}{2}$ . On prend la transformée de Fourier de l'expression précédente. Puis pour chaque coupe d'altitude  $z$ , on applique le filtre  $H_z$ . On somme ensuite suivant  $\beta \in (0, \frac{\pi}{2} - \theta_g)$  et on applique enfin la transformée de Fourier 2D inverse en coordonnées polaires pour obtenir  $f$ . Cette méthode présente l'avantage d'avoir un échantillonnage adéquat du domaine fréquentiel qui correspond à la distribution des données, et donc évite l'étape d'interpolation.

## Résultats

Nous présentons des reconstructions à partir de données simulées à l'aide de la suite de logiciels MEGAlib [Zoglauer *et al.* (2008)]. Le simulateur est basé sur Géant4 [Agostinelli *et al.* (2003)]. Le pack Livermore permet de modéliser les interactions Compton ainsi que l'effet Doppler grâce à l'extension G4LECS [Kippen (2004)]. Les autres interactions sont modélisées par la liste de modèles QGSP-BIC-HP pour les hadrons. La simulation fournit les mesures effectuées par le dispositif d'imagerie, i.e. un ensemble de positions dans les diffuseurs et énergies d'interaction. Un logiciel d'analyse permet d'identifier les diffusions Compton et de reconstruire les séquences d'interactions subies par les photons détectés. Nous réalisons ensuite un regroupement des données suivant les positions d'interaction et les paramètres angulaires, puis nous appliquons notre méthode de reconstruction.

## Caméra et source

Nous proposons deux configurations de caméra se distinguant par la taille des diffuseurs. La figure 6.1 présente la "petite caméra Compton" composée de trois couches de diffuseurs en silicium (Si) de taille  $12.5 \times 12.5 \times 0.5 \text{ cm}^3$  chacun. La figure 6.10 présente la "grande caméra Compton" dont les 3 couches de diffuseurs ont une taille de  $25 \times 25 \times 0.5 \text{ cm}^3$ .

---

Dans les deux cas, l'absorbeur est un arrangement de cristaux de d'Iodure de Césium (CsI) de taille  $37 \times 37 \times 4$  cm<sup>3</sup> situé à 30 cm du dernier diffuseur.

Nous avons simulé une source mono-énergétique de photons  $\gamma$ . Les photons émis ont une énergie de 1.275 MeV ce qui correspond à une source de rayonnement provenant de l'isotope  $^{22}\text{Na}$ . La source est une sphère de rayon 0.5 cm centrée en (1, 1, 1) cm, située à 11 cm de la caméra, représentée dans la figure 6.2.

## Reconstructions

Nous reconstruisons un volume de  $12.5 \times 12.5 \times 12.5$  cm<sup>3</sup> composé de  $65 \times 65 \times 65$  voxels. Nous avons pu constater que la méthode analytique est très sensible au manque d'événements. Nous avons donc réalisé des reconstructions avec un grande nombre de d'évenements.

Comme mentionné précédemment, la reconstruction nécessite une étape de regroupement de données. Cette dernière consiste dans un premier temps à discréteriser les intervalles des différents paramètres de la reconstruction et dans un deuxième temps à regrouper les événements dans les échantillons.

Nous effectuons une série de tests mettant en lumière l'influence de la discréterisation des paramètres angulaires  $\beta$  et  $\delta$ . Les résultats sont présentés dans les figures 6.3 et 6.4. On observe qu'avec un trop faible nombre d'échantillons, la source est noyée dans le bruit. Une reconstruction de bonne qualité nécessite une discréterisation suffisamment fine de ces paramètres.

La taille des diffuseurs a un fort impact sur la qualité de la reconstruction. L'influence de l'angle solide couvert par les diffuseurs vis à vis d'un point de la source implique une troncature des projections. C'est particulièrement le cas lorsque l'angle de demi-ouverture du cône est grand. On constate alors une elongation de la source dans la direction orthogonale aux détecteurs dans le cas de la petite caméra Compton. Cet effet est illustré dans la figure 6.9. Avec la grande caméra Compton, cet effet indésirable est réduit.

Nous avons également réalisé les reconstructions 3D, figures 6.5 et 6.12, avec les deux caméras en utilisant des isosurfaces dont la valeur seuil est définie empiriquement (environ 85% de la valeur maximum).

La sensibilité de la méthode vis à vis du manque d'événements limite la possibilité de l'utiliser pour la surveillance de traitements par hadronthérapie. Mais elle reste prometteuse car rapide d'exécution.



# Chapter 5

---

## Filtered Backprojection algorithm

---

The analytical method we present here is an extension of a previous work from [Maxim *et al.* (2009)]. We propose a Filtered BackProjection (FBP) formulation for the inversion of the Compton projections. First we recall the reconstruction method proposed in [Maxim *et al.* (2009)], then we present our extension, the FBP method.

### 5.1 Compton transform

We first define the context as in [Maxim *et al.* (2009)]. A description of the mathematical model of the Compton camera and of the cone surface projections are given in this section.

#### 5.1.1 Model for the Compton camera

The Compton camera is assumed to be composed of two infinite parallel planar detectors. The first is the scatter detector, where lies the first interaction point  $V_1$ . The second is the absorber with the second interaction point  $V_2$ . Their thickness is negligible. A Compton cone  $\mathcal{C}(V_1, V_2, \beta)$  is given by its apex  $V_1$ , its axis  $\overrightarrow{V_2V_1}$  and its half opening angle  $\beta$  as represented in chapter 3 figure 3.6. Given by the Compton equation 3.2, the value of  $\beta$  is in the interval  $[0; \pi]$ . The vector  $\overrightarrow{V_2V_1}$  is parameterized by  $\theta_g \in [0; \frac{\pi}{2})$  the polar angle (i.e. inclination angle of the cone axis) and  $\delta \in [0; 2\pi)$  the azimuthal angle. We choose a cartesian coordinate system  $Oxyz$  such that the plane  $xOy$  coincides with the scatter detector. Then the axis  $Oz$  is oriented such that the points from the absorber are in the half space  $z < 0$ , see figure 5.1.

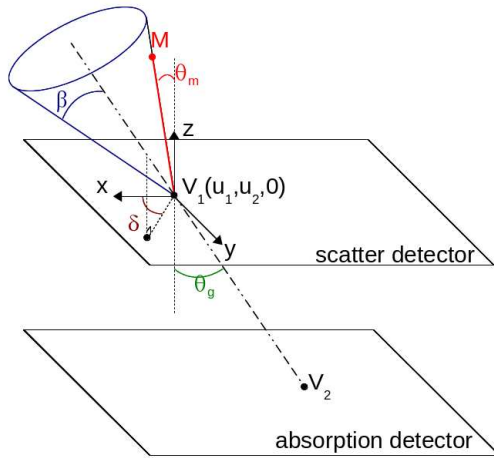


Figure 5.1: Illustration of the mathematical context in the modelling of the Compton transform. The particle originating from  $M$  with an incident angle  $\theta_M$ , collides with the scatterer at  $V_1(u_1, u_2, 0)$ . The photon is scattered through the angle  $\beta$  and then interacts with the absorber at  $V_2$ . The vector  $\overrightarrow{V_2V_1}$  is parameterized by its polar angle  $\theta_g$  and its azimuthal angle  $\delta$ . The Compton cone is defined from  $V_1$ ,  $\overrightarrow{V_2V_1}$  and  $\beta$ .

### 5.1.2 Model of the projections

#### Compton transform

For some given parameters  $(\theta_g, \delta, \beta)$ , and for some intensity distribution of the source denoted  $f$ , the mean number of  $\gamma$ -photons emitted by the source, interacting first at  $V_1(u_1, u_2, 0)$ , scattered with the angle  $\beta$  in direction  $\overrightarrow{V_2V_1}(\theta_g, \delta)$ , is denoted  $Pf(u_1, u_2; \theta_g, \delta, \beta)$ . The mapping

$$(u_1, u_2) \in \mathbb{R}^2 \mapsto Pf(u_1, u_2; \theta_g, \delta, \beta) \quad (5.1)$$

represents one of the Compton projections of  $f$  on the considered detector. The function  $Pf$  is then called the Compton transform of  $f$ .

#### Model of the Compton projections

The intensity of the source at some given point  $M$  in the 3D space will be denoted  $f(M)$ . The polar angle of  $\overrightarrow{V_1M}$  is denoted  $\theta_M$ . Following [Gunter (2006)], the flux of photons  $\phi_{u_1, u_2}(M)ds$  from  $M$ , traveling through an infinitesimal detector surface containing  $V_1$ , is proportional to  $f(M)$  weighted by the solid angle subtended by the element of surface  $ds$  at  $M$ . Thus, the photon flux density will be:

$$\phi_{u_1, u_2}(M) = f(M) \frac{\cos \theta_M}{\|\overrightarrow{V_1M}\|_2^2} \quad (5.2)$$

The value of a Compton projection taken at  $(u_1, u_2)$  is proportional to the integral of the  $\gamma$  flux density on the surface of the Compton cone  $\mathcal{C}(V_1, V_2, \beta)$ . Ignoring the

proportionality constants, we put:

$$Pf(u_1, u_2; \theta_g, \delta, \beta) = K(\beta, E_0) \int_{M \in \mathcal{C}(V_1, V_2, \beta)} f(M) \frac{\cos \theta_M}{\|V_1 M\|_2^2} ds. \quad (5.3)$$

In this expression,  $K(\beta, E_0)$  is the Klein-Nishina coefficient that accounts for Compton scattering cross section. This factor depends on the initial energy of the photon and on the scattering angle.

The term  $\cos \theta_M$  accounts for the dependency of contribution on the incident angle. Indeed, the contribution to the integral (5.3) of the source points from the cone located at the same distance at the detector is not equal. For instance, in the case of the Compton cone  $\mathcal{C}(V_1, V_2, \frac{\pi}{4})$  with an axis inclination angle  $\theta_g = \frac{\pi}{4}$ , the cone surface intersects the scatterer and the  $Oz$  axis, as in figure 5.2. The source points lying on the intersection line between the cone and the scatter detector do not contribute to the Compton projection  $Pf(u_1, u_2; \frac{\pi}{4}, \delta, \frac{\pi}{4})$  whereas the source points lying on the intersection line between the cone and the  $Oz$  axis do.

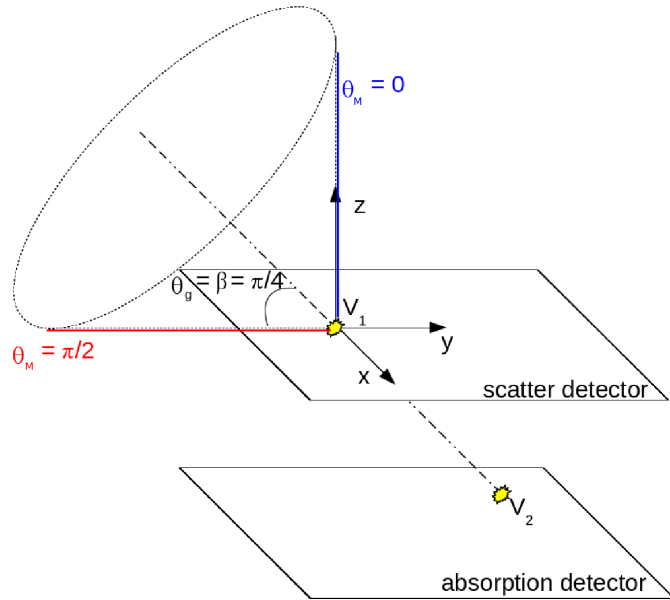


Figure 5.2: Illustration of the dependency of the contribution on the incident angle  $\theta_M$ , with the Compton cone  $\mathcal{C}(V_1, V_2, \frac{\pi}{4})$ . The axis inclination angle is  $\theta_g = \frac{\pi}{4}$ .

As for the factor  $\|V_1 M\|_2^2$ , it is specific to emission imaging modalities such as PET or SPECT. In these modalities, the distance source-detector is not taken into account in the analytical reconstruction. In the same way, in this work, we do not take into account this factor, the model being too complex to invert. Thus, the mathematical model of the

Compton projection that we choose to deal with is:

$$Pf(u_1, u_2; \theta_g, \delta, \beta) = K(\beta, E_0) \int_{M \in \mathcal{C}(V_1, V_2, \beta)} f(M) \cos \theta_M ds \quad (5.4)$$

This model has also been used in [Basko *et al.* (1997)] for a virtual one-dimensional Compton camera. Note that the probabilities that a  $\gamma$  particle interacts with the scatterer and the absorber are considered constant. So does the probability that the Compton scattered particle propagates without interacting in the device before it is absorbed. Note also that in our model the source is considered as monoenergetic. This hypothesis might be questionable since in the hadrontherapy application the radiating  $\gamma$  source has a wide spectrum. In this medical application, this assumption may induce degradation in the reconstructed image.

In [Cree and Bones (1994), Basko *et al.* (1998)] a simplified model is used:

$$Pf(u_1, u_2; \theta_g, \delta, \beta) = K(\beta, E_0) \int_{M \in \mathcal{C}(V_1, V_2, \beta)} f(M) ds \quad (5.5)$$

As presented in section (4.1.1), the model (5.5) has been proven invertible. [Cree and Bones (1994)] carried out its inversion for the specific case of Compton cones with axis direction orthogonal to the detectors, i.e. Compton cones with  $\theta_g = 0$ . In this case,  $\cos(\theta_M) = \cos(\beta)$  is constant with respect to  $M$ .

## 5.2 Parameterization of the forward projection problem

Let us consider that the function  $f$ , representing the source, is compactly supported. As described previously, the horizontal plane  $xOy$  coincides with the scatterer. Towards the absorber, i.e. for  $z \leq 0$ , we suppose that  $f(x, y, z) = 0$ . This hypothesis is not restrictive for medical applications.

### 5.2.1 Parametrization of the Compton cone

#### Restriction of the range of the half-opening angle

For the specific cases of  $\beta = 0$  and  $\beta = \pi$ , the Compton cone degenerates to a line. The integral on the surface of a degenerated cone being equal to zero, the model previously described is not appropriate anymore. So, we exclude this case and we consider  $\beta \in (0, \pi)$ . For the particular case  $\beta = 0$ , parallel beam model is more adapted to describe the projections.

Let us now consider the specific case of the Compton cone  $\mathcal{C}(V_1, V_2, \beta)$  with apex  $V_1(0, 0, 0)$  situated at the origin of the coordinate system and its axis direction included in the plane  $xOz$ . In this case,  $u_1 = u_2 = 0$  and  $\delta = 0$ . The intersection of the cone with

the horizontal plane  $z = z_0 > 0$  is given by the equation:

$$(x(\cos^2 \theta_g - \sin^2 \beta) - z_0 \sin \theta_g \cos \theta_g)^2 + y^2 \cos^2 \beta (\cos^2 \theta_g - \sin^2 \beta) = z_0^2 \sin^2 \beta \cos^2 \beta, \quad (5.6)$$

when  $\cos \theta_g \neq \sin \beta$  and

$$-2xz_0 \sin \theta_g \cos \theta_g + y^2 \cos^2 \beta = z_0^2 (\sin^2 \beta - \cos^2 \beta), \quad (5.7)$$

otherwise. In order to constrain the intersection of the cone with the plane to be an ellipse, we restrict the range of  $\beta$  to:

$$\beta \in \left(0, \frac{\pi}{2} - \theta_g\right). \quad (5.8)$$

The restriction has for consequence that some of projections acquired by the Compton camera will be neglected.

### Parametric representation

In the orthonormal coordinate system  $Oxyz$ , the equation of the Compton cone  $\mathcal{C}(V_1, V_2, \beta)$  is:

$$(x - u_1)^2 + (y - u_2)^2 = z^2 \tan^2(\beta). \quad (5.9)$$

Let us give a parameterization of the equation (5.9). We write out the following angle-dependent expressions  $a(\theta_g, \beta)$ ,  $b(\theta_g, \beta)$  and  $c(\theta_g, \beta)$ :

$$a(\theta_g, \beta) = \frac{\sin \beta \cos \beta}{\cos^2 \theta_g - \sin^2 \beta} \quad (5.10)$$

$$b(\theta_g, \beta) = \frac{\sin \beta}{\sqrt{\cos^2 \theta_g - \sin^2 \beta}} \quad (5.11)$$

$$c(\theta_g, \beta) = \frac{\sin \theta_g \cos \theta_g}{\cos^2 \theta_g - \sin^2 \beta}. \quad (5.12)$$

Then, the parameterization of a cone  $\mathcal{C}(V_1, V_2, \beta)$  with apex  $V_1$  at the origin of  $Oxyz$ , i.e.  $V_1(0, 0, 0)$ , and  $\delta = 0$  is

$$\begin{cases} x = z(c(\theta_g, \beta) + a(\theta_g, \beta) \cos \varphi) \\ y = z b(\theta_g, \beta) \sin \varphi \quad z \geq 0, \varphi \in [0, 2\pi) \\ z = z \end{cases} \quad (5.13)$$

where  $\varphi \in [0, 2\pi)$  is the angular parameter of  $M$  as the point of the ellipse  $\mathcal{E}(z; \theta_g, \delta, \beta)$  defined by the intersection of the Compton cone with the horizontal plane including  $M$ .

For an arbitrary apex and axis direction, we first apply a rotation of an angle  $\delta$  around the  $Oz$  axis. Then, we apply a translation so that the apex  $V_1$  is located at  $(u_1, u_2)$ .

Hence, a point  $M(x, y, z)$  of the cone  $\mathcal{C}(V_1, V_2, \beta)$  with  $V_1(u_1, u_2, 0)$  has the parametric representation:

$$\begin{cases} x = z[(c(\theta_g, \beta) + a(\theta_g, \beta) \cos \varphi) \cos \delta + b(\theta_g, \beta) \sin \varphi \sin \delta] + u_1 \\ y = z[-(c(\theta_g, \beta) + a(\theta_g, \beta) \cos \varphi) \sin \delta + b(\theta_g, \beta) \sin \varphi \cos \delta] + u_2 \\ z = z \end{cases} \quad (5.14)$$

where  $z \geq 0$  is the distance from  $M$  to the scatterer.

### 5.2.2 Expression of the projections

Using the previous parametric representation of the cone, we may express the element of surface  $ds$  from (5.4) as:

$$\left\| \frac{\partial OM}{\partial z} \wedge \frac{\partial OM}{\partial \varphi} \right\| = z \frac{\sin \beta}{(\cos^2 \theta_g - \sin^2 \beta)^{\frac{3}{2}}} |\sin \theta_g \sin \beta \cos \varphi + \cos \theta_g \cos \beta|. \quad (5.15)$$

We express also  $\cos \theta_M$ :

$$\cos \theta_M = \frac{\cos^2 \theta_g - \sin^2 \beta}{|\sin \theta_g \sin \beta \cos \varphi + \cos \theta_g \cos \beta|} \quad (5.16)$$

Combining (5.14), (5.15) and (5.16) we obtain the following expression of the cone surface projections:

$$\begin{aligned} Pf(u_1, u_2; \theta_g, \delta, \beta) &= K(\beta, E_0) b(\theta_g, \beta) \int_0^\infty \int_0^{2\pi} z \\ &\quad f(u_1 + (zc(\theta_g, \beta) + za(\theta_g, \beta) \cos \varphi) \cos \delta + zb(\theta_g, \beta) \sin \varphi \sin \delta, \\ &\quad u_2 - (zc(\theta_g, \beta) + za(\theta_g, \beta) \cos \varphi) \sin \delta + zb(\theta_g, \beta) \sin \varphi \cos \delta, z) d\varphi dz \end{aligned} \quad (5.17)$$

Note that with the general model (5.3), the expression of the Compton projections are more complex. The dependency of  $\cos \theta_M$  on  $\varphi$  makes the inversion more difficult to handle. However, the particular case  $\theta_g = 0$  is feasible as already done in [Truong *et al.* (2007)].

### 5.2.3 Dual expression of the projections

We now consider our 3D images as 2D images stacked up in the  $z$  direction. Recalling that  $f$  is compactly supported, the application of Fubini's theorem and translation theorem to the Fourier transform enables to write:

$$\begin{aligned} \mathcal{F}_2[Pf](\eta_1, \eta_2; \theta_g, \delta, \beta) &= K(\beta, E_0) b(\theta_g, \beta) \int_0^\infty \int_0^{2\pi} e^{2i\pi z c(\theta_g, \beta)(\eta_1 \cos \delta + \eta_2 \sin \delta)} \\ &\quad \mathcal{F}_2[f](\eta_1, \eta_2, z) e^{2i\pi z(a(\theta_g, \beta)(\eta_1 \cos \delta + \eta_2 \sin \delta) \cos \varphi + b(\theta_g, \beta)(-\eta_1 \sin \delta + \eta_2 \cos \delta) \sin \varphi)} zd\varphi dz \end{aligned} \quad (5.18)$$

where  $\mathcal{F}_2[f]$ , the 2D Fourier transform of  $f$  with respect to the first two variables  $x$  and  $y$ , the third being unchanged, and  $\mathcal{F}_2[Pf]$  the 2D Fourier transform of the Compton projections.

The only term depending on  $\varphi$  in (5.18) is the second exponential. Let us denote  $A$  the expression  $a(\theta_g, \beta)(\eta_1 \cos \delta + \eta_2 \sin \delta)$  and  $B$  the expression  $b(\theta_g, \beta)(-\eta_1 \sin \delta + \eta_2 \cos \delta)$ , then we have:

$$A \cos \varphi + B \sin \varphi = \sqrt{A^2 + B^2} \cos(\varphi + \phi), \quad (5.19)$$

where the angle  $\phi$  is given by  $\cos \phi = \frac{A}{\sqrt{A^2 + B^2}}$  and  $\sin \phi = -\frac{B}{\sqrt{A^2 + B^2}}$ . Replacing in the equation (5.18), we can recognize the zero-order Bessel function of the first kind  $J_0$ :

$$J_0(2\pi r) = \frac{1}{2\pi} \int_0^{2\pi} e^{2i\pi r \cos \varphi} d\varphi \quad (5.20)$$

Thus we have:

$$\begin{aligned} \mathcal{F}_2[Pf](\eta_1, \eta_2; \theta_g, \delta, \beta) &= K(\beta, E_0) b(\theta_g, \beta) \int_0^\infty z e^{2i\pi z c(\theta_g, \beta)(\eta_1 \cos \delta + \eta_2 \sin \delta)} \mathcal{F}_2[f](\eta_1, \eta_2, z) \\ &\times J_0(2\pi z \sqrt{a^2(\theta_g, \beta)(\eta_1 \cos \delta + \eta_2 \sin \delta)^2 + b^2(\theta_g, \beta)(-\eta_1 \sin \delta + \eta_2 \cos \delta)}) dz \end{aligned} \quad (5.21)$$

## 5.3 Inversion of the Compton transform

The following section proves that the function  $f$  can be computed from the set of cone-surface projections  $Pf(\cdot, \cdot; \theta_g, \delta, \beta)$ , with  $\delta \in [0, \pi)$  and  $\beta \in (0, \frac{\pi}{2} - \theta_g)$ , for any given  $\theta_g \in [0, \frac{\pi}{2})$ ,

### 5.3.1 Hankel Fourier Transform

To invert the equation (5.21) we first need to eliminate the exponential term. To do so, let us choose vectors  $(\eta_1, \eta_2)$  and  $(\cos \delta, \sin \delta)$  to be orthogonal. For some given angle  $\beta \in (0, \frac{\pi}{2} - \theta_g)$  and an arbitrary but fixed point  $(\eta_1, \eta_2)$  of the plane  $\eta_1 O \eta_2$  from the Fourier domain, having polar coordinate  $(\rho, \omega)$ , we select the set of projections with:

$$\delta = \omega + \epsilon \frac{\pi}{2} [\text{mod } 2\pi], \quad \epsilon = \pm 1. \quad (5.22)$$

This condition implies that  $\eta_1 \cos \delta + \eta_2 \sin \delta = 0$ , thus the exponential factor equals 1. We now have:

$$\begin{aligned} \mathcal{F}_2[Pf](\eta_1, \eta_2; \theta_g, \omega + \epsilon \frac{\pi}{2}, \beta) &= 2\pi K(\beta, E_0) b(\theta_g, \beta) \\ &\times \int_0^\infty z \mathcal{F}_2[f](\eta_1, \eta_2, z) J_0(2\pi z b(\theta_g, \beta) \sqrt{\eta_1^2 + \eta_2^2}) dz \end{aligned} \quad (5.23)$$

The expression on the right part of the equation (5.23) is proportional to the Hankel

transform of  $\mathcal{F}_2[f]$  with respect to  $z$ . The Hankel-Fourier Transform is then defined as:

$$\begin{aligned}\mathcal{HF} : f &\rightarrow \mathcal{HF}[f] \\ \mathcal{HF}[f](\eta_1, \eta_2, \eta_3) &= 2\pi \int_0^\infty z \mathcal{F}_2[f](\eta_1, \eta_2, z) J_0(2\pi z \eta_3) dz\end{aligned}\quad (5.24)$$

The Hankel-Fourier Transform represents the Hankel transform with respect to  $z$  of the 2D Fourier transform with respect to  $x$  and  $y$  of the 3D function  $f$ .

So we write:

$$\mathcal{HF}[f](\eta_1, \eta_2, b(\theta_g, \beta) \sqrt{\eta_1^2 + \eta_2^2}) = \frac{1}{K(\beta, E_0) b(\theta_g, \beta)} \mathcal{F}_2[Pf] \left( \eta_1, \eta_2; \theta_g, \omega + \epsilon \frac{\pi}{2}, \beta \right) \quad (5.25)$$

### 5.3.2 Projection slice theorem

We denote  $\mathcal{C}_F(\theta_g, \beta)$  the cone in Fourier domain:

$$\mathcal{C}_F(\theta_g, \beta) : \quad \eta_1^2 + \eta_2^2 = \frac{\eta_3^2}{b^2(\theta_g, \beta)}, \quad (5.26)$$

and we denote  $\mathcal{P}_F(\delta)$  the plane orthogonal to the vector  $(\cos \delta, \sin \delta, 0)$  namely,

$$\mathcal{P}_F(\delta) : \quad \eta_1 \cos \delta + \eta_2 \sin \delta = 0 \quad (5.27)$$

The projection slice theorem for the Hankel-Fourier transform from [Maxim et al. (2009)] states that given the angles  $\theta_g \in [0, \frac{\pi}{2})$ ,  $\delta \in [0, 2\pi)$  and  $\beta \in (0, \frac{\pi}{2} - \theta_g)$ , the slice from the Hankel-Fourier transform of  $f$  defined by the intersection of  $\mathcal{C}_F(\theta_g, \beta)$  and  $\mathcal{P}_F(\delta)$ , weighted by  $K(\beta, E_0) b(\theta_g, \beta)$  is equal to the slice cut by  $\mathcal{P}_F(\delta)$  in the 2D Fourier transform of the cone surface projection  $Pf(\cdot, \cdot; \theta_g, \delta, \beta)$ . Then, with  $\delta$  spanning the interval  $[0, 2\pi)$ , we can fill in the values of  $\mathcal{HF}[f]$  on the surface of the cone  $\mathcal{C}_F(\theta_g, \beta)$ . The range of  $\delta$  can be restricted to  $[0, \pi)$  because of the redundancy of the two projections  $Pf(\cdot, \cdot; \theta_g, \delta, \beta)$  and  $Pf(\cdot, \cdot; \theta_g, \delta + \pi, \beta)$ . Next, we fill the half-space with cones.

### 5.3.3 Inversion formula

The inversion of the formula (5.25) is realized by first applying the inverse Hankel transform to (5.23) which after a changing of variable leads to:

$$\begin{aligned}\mathcal{F}_2[f](\eta_1, \eta_2, z) &= (\eta_1^2 + \eta_2^2) \int_0^{\frac{\pi}{2}-\beta} \frac{b'_\beta(\theta_g, \beta)}{K(\beta, E_0)} \mathcal{F}_2[Pf](\eta_1, \eta_2; \theta_g, \omega + \epsilon \frac{\pi}{2}, \beta) \\ &\times J_0(2\pi z b(\theta_g, \beta) \sqrt{\eta_1^2 + \eta_2^2}) d\beta,\end{aligned}\quad (5.28)$$

for all  $(\eta_1, \eta_2) \in \mathbb{R}^2 \setminus \{(0, 0)\}$  and  $z > 0$ . In this formula,  $\omega$  is the polar angle of the vector  $(\eta_1, \eta_2)$  and  $b'_\beta(\theta_g, \beta)$  the partial derivative of  $b(\theta_g, \beta)$  with respect to  $\beta$ .

Then, the 2D inverse Fourier transform is applied leading to:

$$\begin{aligned} f(x, y, z) &= \int_{-\infty}^{\infty} \int_{-\infty}^{\infty} \left( \int_0^{\frac{\pi}{2}-\theta_g} \frac{b'_{\beta}(\theta_g, \beta)}{K(\beta, E_0)} \mathcal{F}_2(Pf)(\eta_1, \eta_2; \theta_g, \omega + \epsilon \frac{\pi}{2}, \beta) \right. \\ &\quad \times J_0(2\pi z b(\theta_g, \beta) \sqrt{\eta_1^2 + \eta_2^2}) d\beta \Big) (\eta_1^2 + \eta_2^2) e^{2i\pi(x\eta_1 + y\eta_2)} d\eta_1 d\eta_2 \quad (5.29) \end{aligned}$$

Thus, in order to recover  $f$  the intensity distribution of the source, we first take the 2D Fourier Transform of the Compton projections with as parameters the polar angle  $\theta_g$ , the half opening angle  $\beta$  and the azimuthal angle  $\delta = \omega + \epsilon \frac{\pi}{2}$  weightened by the inverse of the Compton scattering cross-section, the angle-dependent factor  $b'_{\beta}(\theta_g, \beta)$  and a radial Bessel kernel. We sum up this expression following the half opening angle of the projections, i.e. we cover the vertical half space in Fourier domain. Multiplying by  $\eta_1^2 + \eta_2^2$ , we obtain the 2D Fourier transform of  $f$  on successive horizontal slices. We take then the inverse Fourier transform to recover the source distribution.

This expression shows that for each given inclination  $\theta_g$  of the cone axis and for each layer of the scatter detector, one instance of the image of the source can be calculated. Theoretically identical, in practice the images may differ following projection truncation due to finite extent of the detectors and to limited number of projections. An increase of the Signal to Noise Ratio (SNR) may then be achieved by averaging all the reconstructed images.

Note that the radial kernel  $\eta_1^2 + \eta_2^2$  implies a zero-mean reconstructed image. The same issue can be observed in conventional tomography.

## 5.4 Filtered Back Projection algorithm

We propose here an extension of the reconstruction method previously described.

### 5.4.1 Mathematical formulation

In real applications, the data space is discretized and thus the number of projections is limited. The low coverage of the dual space, especially in the high frequencies, is an important issue. The information is concentrated on a finite number of cones, and inside a cone, on a finite number of half-lines, the generatrices of the cone. But some of the voxels will not be crossed by any half-lines and at the contrary, some voxels will be crossed several times, see figure 5.3. Before applying the inverse Fourier transform, the empty voxels must be filled, i.e. an interpolation step must be done. In tomographic reconstruction, the same issue was raised. The solution comes from the Filtered Back Projection (FBP) formulation.

Introducing polar coordinates in the equation (5.29) with as usual in tomography  $\rho \in \mathbb{R}$

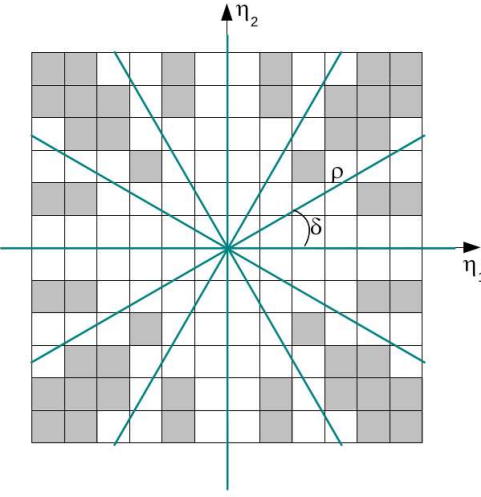


Figure 5.3: Illustration of the information distribution in the dual space. The solid lines represent the information spread over lines. The white pixels contain information, whereas the dark ones don't and will need to be filled by interpolation.

and  $\omega \in [0, \pi)$ , we get:

$$\begin{aligned} f(x, y, z) &= \int_{-\infty}^{\infty} \int_0^{\pi} \int_0^{\frac{\pi}{2}-\theta_g} \frac{b'_{\beta}(\theta_g, \beta)}{K(\beta, E_0)} J_0(2\pi z b(\theta_g, \beta) \rho) |\rho|^3 \\ &\quad \mathcal{F}_2(Pf) \left( \rho \cos \omega, \rho \sin \omega; \theta_g, \omega + \epsilon \frac{\pi}{2}, \beta \right) e^{2i\pi \rho(x \cos \omega + y \sin \omega)} d\beta d\omega d\rho \end{aligned} \quad (5.30)$$

Note that for any given angles  $\theta_g, \omega, \beta$ , the mapping

$$\rho \mapsto \mathcal{F}_2[Pf](\rho \cos \omega, \rho \sin \omega; \theta_g, \omega + \epsilon \frac{\pi}{2}, \beta), \quad (5.31)$$

is nothing but one line of the 2D Fourier transform of  $Pf(\cdot, \cdot; \theta_g, \omega + \epsilon \frac{\pi}{2}, \beta)$ . As stated by the projection slice theorem, we can replace the expression  $\mathcal{F}_2(Pf)(\rho \cos \omega, \rho \sin \omega; \theta_g, \omega + \epsilon \frac{\pi}{2}, \beta)$  from the equation (5.30) by the 1D Fourier transform of the Radon projection of angle  $\omega$ , denoted  $R_{\omega}$ , of  $Pf(\cdot, \cdot; \theta_g, \omega + \epsilon \frac{\pi}{2}, \beta)$ :

$$\mathcal{F}_2(Pf) \left( \rho \cos \omega, \rho \sin \omega; \theta_g, \omega + \epsilon \frac{\pi}{2}, \beta \right) = \mathcal{F}(R_{\omega}[Pf]) \left( \rho \cos \omega, \rho \sin \omega; \theta_g, \omega + \epsilon \frac{\pi}{2}, \beta \right). \quad (5.32)$$

We denote  $H_z$  the filter:

$$H_z(\rho, \beta; \theta_g, E_0) = \frac{b'_{\beta}(\theta_g, \beta)}{K(\beta, E_0)} J_0(2\pi z b(\theta_g, \beta) \rho) |\rho|^3. \quad (5.33)$$

Replacing (5.32) and (5.33) in (5.30) yields to:

$$\begin{aligned} f(x, y, z) &= \int_{-\infty}^{\infty} \int_0^{\pi} \int_0^{\frac{\pi}{2}-\theta_g} H_z(\rho, \beta; \theta_g, E_0) \mathcal{F}(R_\omega[Pf]) \left( \rho \cos \omega, \rho \sin \omega; \theta_g, \omega + \epsilon \frac{\pi}{2}, \beta \right) \\ &\quad \times e^{2i\pi\rho(x \cos \omega + y \sin \omega)} d\beta d\omega d\rho, \end{aligned} \quad (5.34)$$

which is a Filtered BackProjection formulation with kernel  $H_z$  of the equation (5.29). In other words, we first apply the Radon transform of angle  $\omega$  to the Compton projections with as parameter the angle  $\theta_g$ , the half opening angle  $\beta$ , and azimuthal angle  $\delta = \omega + \epsilon \frac{\pi}{2}$ . We take the 1D Fourier transform of the previous expression. Then for each  $z$ , we filter by the kernel  $H_z$  the horizontal slice at altitude  $z$ . Next, we sum up following  $\beta \in (0, \frac{\pi}{2} - \theta_g)$ . We then apply the inverse Fourier transform in 2D and polar coordinates to recover the source distribution  $f$ .

With this method, a more adequate sampling of the Fourier space is obtained since the FBP consists in calculating the integral formula in the spherical coordinate system  $(\rho, \omega, \beta)$  which naturally corresponds to the data distribution. At the contrary of the previous method, we can note that the discrete calculation of the equation (5.34) does not require any interpolation of the data in the Fourier space. Note also that as in (5.29), we can reconstruct one instance of the image of the source for each  $\theta_g$  and each scatter detector and we also can increase the SNR by achieving an average on all the images. The issue concerning to finite extent of the detectors still remains and is later discussed in section 6.2.

#### 5.4.2 Application of the FBP

In practice, during backprojection, we applied the Hanning filter of equation:

$$h(\rho) = \frac{1}{2} \left( 1 + \cos \left( 2\pi \frac{\rho}{N} \right) \right) \quad (5.35)$$

where  $N$  is the number of samples. It reduces the artifacts resulting from the frequency cut-off.

We also have used a zero padding of  $R_\omega[Pf]$  which is necessary in order to prevent spatial domain aliasing. The influence of the zero padding is critical when  $\beta$  gets close to its upper limit  $\frac{\pi}{2} - \theta_g$  and for large values of  $\theta_g$ . Incidentally, this technique also reduces the bias from zero-setting the mean of the image in the discrete version of the inversion formula.



# Chapter 6

---

# Results

---

## 6.1 Data simulation

In this chapter, the data have been obtained by Monte Carlo simulations, using the software suite MEGAlib [[Zoglauer et al. \(2008\)](#)]. In this package, one may find: simulation softwares *geomega* and *cosima*, data analyzers *revan* and *sivan*, and an iterative reconstruction tool *mimrec*. These softwares constitute a chain of simulation, analysis and reconstruction for  $\gamma$ -ray sources.

The simulation tool *cosima* is based on Geant4 and can be used to mimic the detection of  $\gamma$  particles by a Compton camera. We can select the physical interaction models of Geant4 used during the simulation. In our work, we used the Geant4 Livermore package modeling the Compton interactions. This package includes the Doppler-broadening extension G4LECS [[Kippen \(2004\)](#)]. For the other physical interactions, the standard physics list QGSP-BIC-HP for hadronic interactions was used. The simulation (like real measurements) provides a set of positions and energies of interaction.

Once the simulation is performed, the data analyzer *revan* [[Zoglauer \(2005\)](#)] is applied to the output file to reconstruct the sequence of interactions undergone by the detected photons. The software implements different methods of the sequence reconstruction such as a Bayesian approach [[Zoglauer et al. \(2007\)](#)] and a neural network approach [[Zoglauer and Boggs \(2007\)](#)]. The software has been designed to manage simulations but also real data analysis. The properties of the detection of the photons such as interaction type, location, uncertainties, can be reconstructed. Ideal simulated data may be obtained by analyzing the output file by *sivan*. With the aim of getting close to reality, we chose to use the *revan* software.

### 6.1.1 Compton camera

Our detection system is composed of a single Compton camera immobile all along the acquisition process. A sketch of the device is shown in figure 6.1.

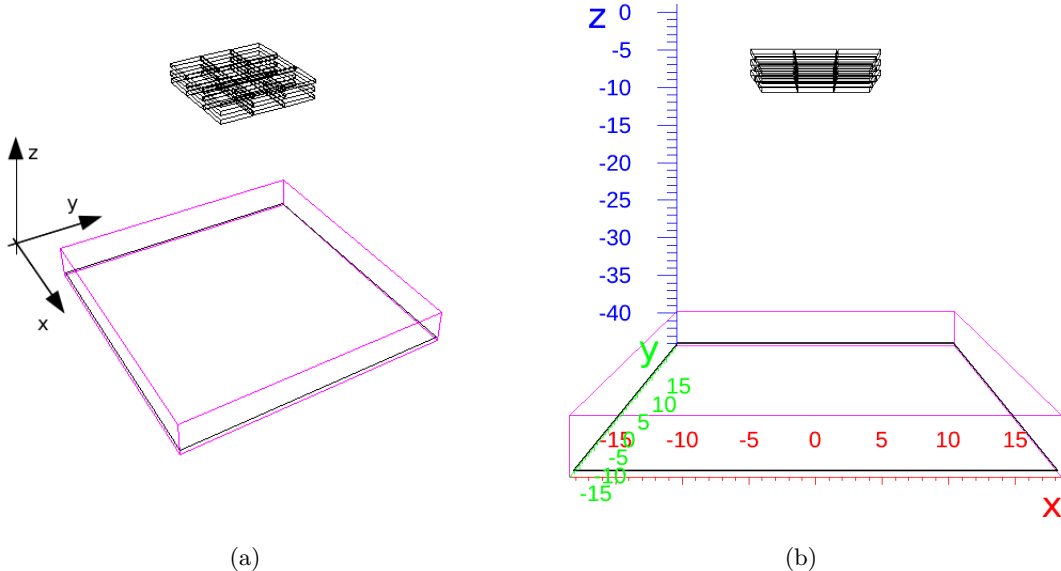


Figure 6.1: - Simulated Compton camera composed of three scatterers of  $12.5 \times 12.5 \times 0.5 \text{ cm}^3$  in Si and one absorber of  $37 \times 37 \times 4 \text{ cm}^3$  in CsI crystals.

The scattering part of the camera is made of three layers of microstrip detectors in Silicon of dimension  $12.5 \times 12.5 \times 0.5 \text{ cm}^3$ . A layer is separated from another by 1 cm of air. The energetic resolution of the detector is modeled by a Gaussian distribution with a uniform  $1-\sigma$  of value 1 keV.

The absorbing part of the device is composed of an  $37 \times 37 \times 4 \text{ cm}^3$  arrangement of CsI crystals of size  $0.5 \times 0.5 \times 4 \text{ cm}^3$ . It is located at 30 cm from the last layer of the scatterer. The energetic resolution of the absorber is also modeled by a Gaussian distribution with a  $1-\sigma$  value of 13.7 keV at 1.275 MeV.

### 6.1.2 Simulated source

We simulated a monoenergetic  $\gamma$  source. The emitted photons have an energy of 1.275 MeV which is in the range of  $\gamma$ -rays encountered in hadrontherapy. This energy is specific to a  $^{22}\text{Na}$  emitter.

The source is a sphere of radius 0.5 cm, with the center located at  $(1, 1, 1)$  cm. It was placed at 11 cm from the imaging device. The simulated scene is shown in figure 6.2.

The number of detected photons must be large enough in order to carry out relevant studies on the reconstruction. We simulated a source that provided a large amount of  $\gamma$  particles. From  $561 \times 10^6$   $\gamma$  photons emitted isotropically by the source,  $10^6$  were triggered

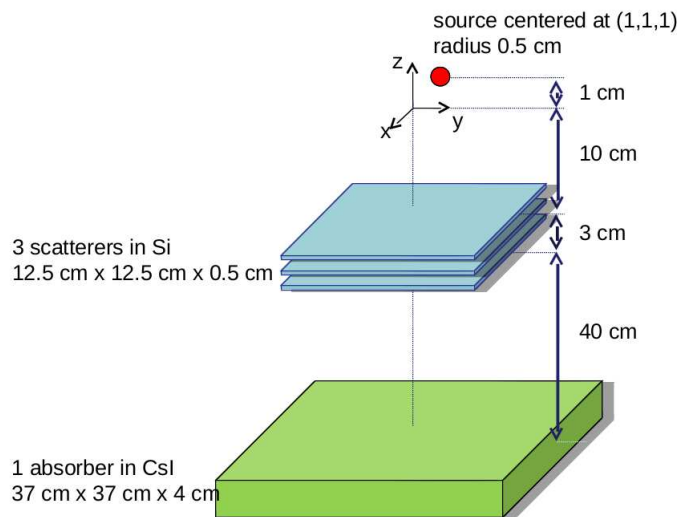


Figure 6.2: *Iterative reconstruction* - Scheme of the Compton camera and the simulated spherical source. The source is a sphere of radius 0.5 cm, located at (1, 1, 1) cm. The distance source-camera is of 11 cm.

by the Compton camera. The simulated data was then analyzed by the software *revan* providing the interaction sequence reconstruction for each photon.

We implemented a second analyzer module in order to select only the useful Compton events from the output data provided by *revan*. Useful events consist in photons that have been Compton scattered and that have interacted at least once in the scatterer, once in the absorber. They also need to verify the mathematical constraints on the Compton angle given by the equation (3.3) and the angular constraint  $\theta_g + \beta < \frac{\pi}{2}$ . The analysis step completed, the amount of useful particles that could be used reached  $328 \times 10^3$  events.

### 6.1.3 Influence of the number of bins

The application of equation (5.34) in the discrete domain required a prealable binning process. The events selected for the reconstruction are binned in a 4 dimensional array, similar to sinograms. One of the dimensions accounts for the three scatterers. The others account for the sampling of the angular parameters  $\theta_g$ ,  $\beta$ ,  $\delta$ . The reconstructed images are 3D volumes of  $12.5 \times 12.5 \times 12.5$  cm $^3$ , divided in  $65^3$  voxels. The aim of the current section is to investigate the quality of the reconstructed image with respect to the sampling rate of the different parameters. In a first test, we considered 5 bins for  $\theta_g$ , i.e. a sampling step of  $\frac{\pi}{10}$ , and 40 bins for  $\delta$ , i.e. a sampling step of  $\frac{\pi}{20}$ . The dependency on the sampling of  $\beta$  is illustrated in figure 6.3. From top to bottom, 5, 10 then 40 bins are generated. The quality of the images (slices through the origin of the spherical source) improves as the number of bins increases, although some aliasing due to insufficient zero-padding may be seen for the larger value.

In a second test, we considered 5 bins for  $\theta_g$ , and 20 bins for  $\beta$ , i.e. a sampling step

of  $\frac{1}{20}(\frac{\pi}{2} - \theta_g)$ . The number of bins of  $\beta$  is sufficient to obtain a well reconstructed image without the aliasing effect seen in the previous test. The dependency on the sampling of  $\delta$  is illustrated in figure 6.4. From top to bottom, 10, 20 then 40 bins are generated. The quality of the images also improves as the number of bins increases. A very fine sampling of  $\delta$  does not seem to introduce any kind of artefacts.

From the previous study, we chose to distribute the data over 5 bins for  $\theta_g \in [0, \frac{\pi}{2})$ , 20 bins for  $\beta \in [0, \frac{\pi}{2} - \theta_g)$  and 40 bins for  $\delta$  in  $(-\pi, \pi]$ . The outcome image is an average of 3 different reconstructed images (one per scatterer layer) and each layer provides an averaged reconstruction over the 5 values of  $\theta_g$ . Figure 6.5 shows the 3D reconstruction of the  $\gamma$  source. The 3D volume representing the source is obtained using isosurfaces with a threshold value empirically chosen (between 10% and 20% of the maximum value of the reconstructed image). The contours at the bottom of the volume correspond to the projection of the source along the  $z$  direction. Figure 6.6 (a) and 6.6 (b) show slices of the 3D reconstructed image at the altitude  $z = 1$  cm and at  $y = 1$  cm, respectively. Note that the analytical algorithm allows negative values in the reconstructed image and that the gray scale only gives relative information about the intensities of the voxels.

From the figure 6.6 (a), we can observe that the position of the source and its radius can be well identified in slices parallel to the detectors. Figure 6.6 (b) shows the poor quality of the reconstructed image in the orthogonal direction. The elongation of the source is a consequence of the finite size of the detectors as explained in the section 6.2. However, the direction orthogonal to the detectors is of less interest in hadrontherapy monitoring where the first requirement is to determine the beam range in the tissues.

## 6.2 Finite detector size consequences

In the mathematical development of the method, the planar detectors are considered as of infinite extent. For a realistic device, the finite sizes of the scatterers and of the absorber have specific repercussions on the reconstructed images.

### 6.2.1 Quality of the image as function of the angle $\theta_g$ for a small camera

For the considered prototype, the solid angle subtended by the absorber at a point from the scatterer is bounded from above: only projections corresponding to relatively small values of  $\theta_g$  are acquired. Theoretically, this restriction has no influence, since the image may be reconstructed as soon as a complete projection for one single value of  $\theta_g$  is available. Figures 6.7 and 6.8 show reconstructions of the source for the 5 values of  $\theta_g$ . For the last three bins, the number of acquired events is too small and the source is not visible on the reconstructed images. As already mentioned in section 5.4, an average image with an increased signal to noise ratio can be calculated from the reconstructions obtained for each value of  $\theta_g$ .

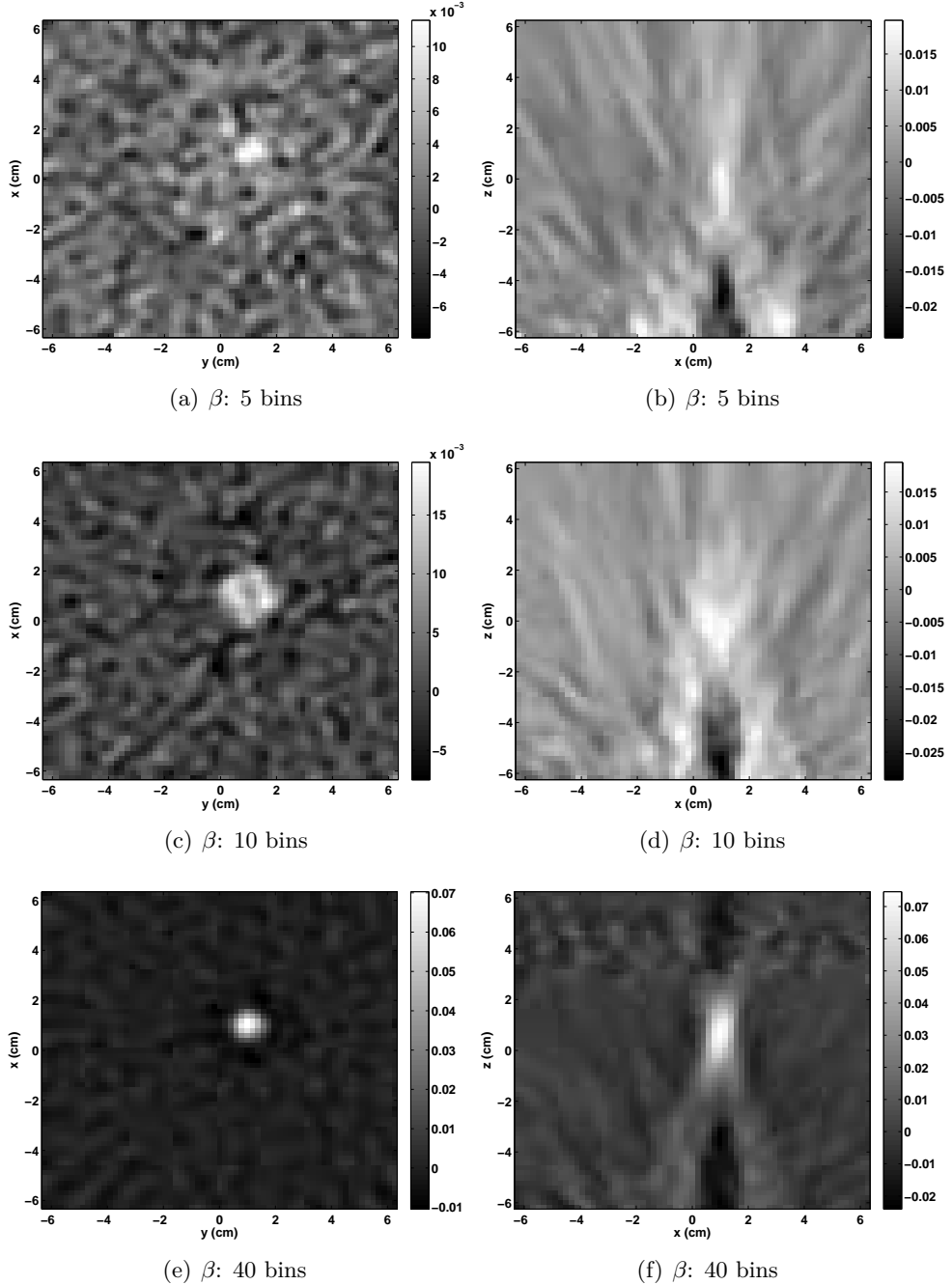


Figure 6.3: *Analytical reconstruction - Influence of the binning of the angular parameter  $\beta$ .* For all images, the values of  $\theta_g$  and  $\delta$  were distributed in 5 and 40 equal bins, respectively. Three values were considered for the binning with respect to  $\beta$ , corresponding to the three lines of the figure. The two columns show slices through the center of the spherical source: on the left, slices parallel to the detectors, at  $z = 1$  cm, on the right, slices orthogonal to the detectors, at  $y = 1$  cm were represented. The gray scale is in arbitrary units. Panels (a) and (c) show the effect of an undersampling. The source is not well identified, many line-shaped artefacts can be observed. Panels (e) and (f) show the effect of a fine sampling. In the slices parallel to the detectors, the source is well identified. In the slices orthogonal to the detectors, some artefacts appear on the top of the image, due to spatial domain aliasing. The quality of the images improves as the number of bins for  $\beta$  increases.

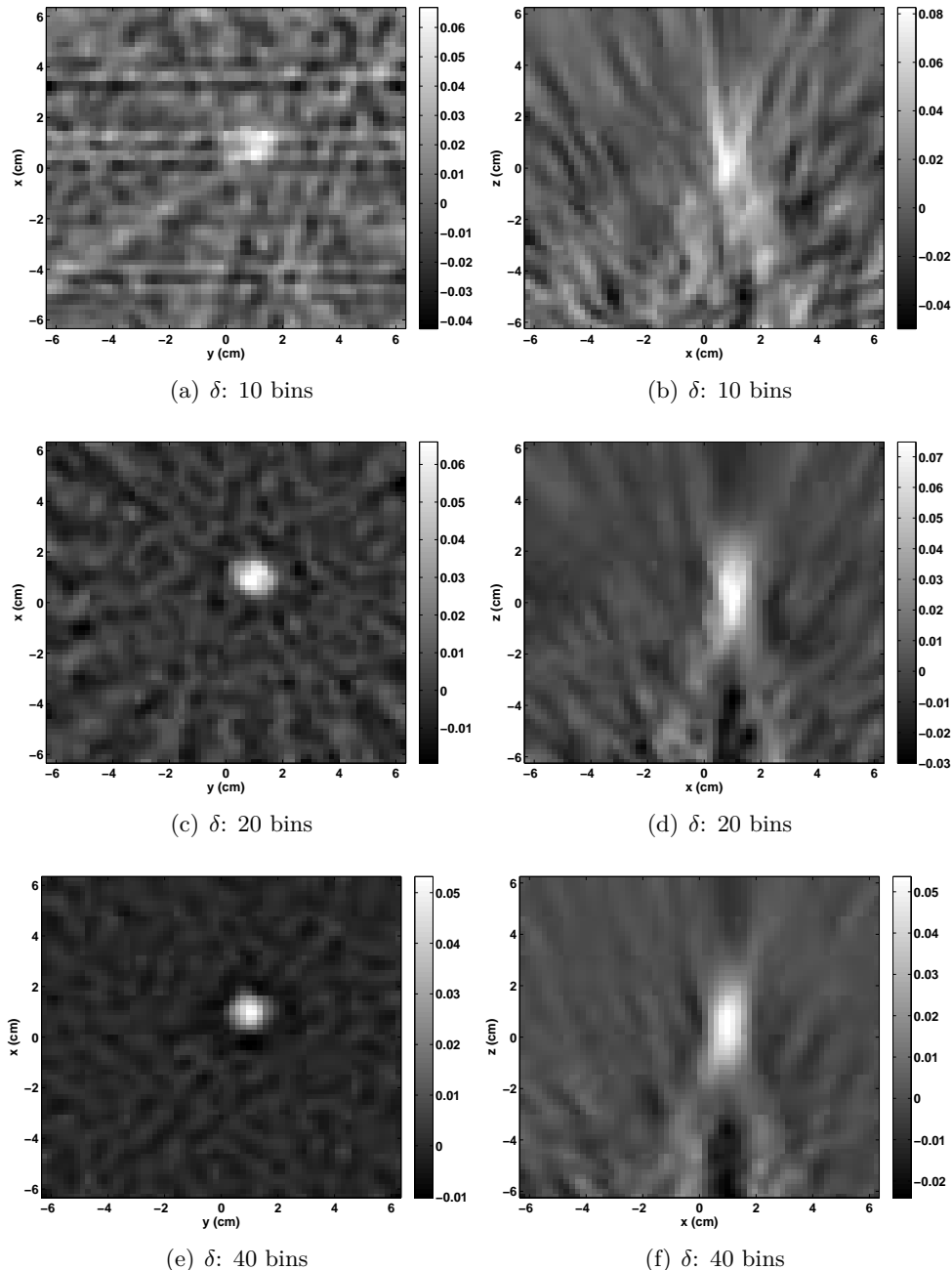


Figure 6.4: *Analytical reconstruction - Influence of the binning of the angular parameter  $\delta$ .* For all images, the values of  $\theta_g$  and  $\beta$  were distributed in 5 and 20 equal bins, respectively. Three values were considered for the binning with respect to  $\delta$ , corresponding to the three lines of the figure. The two columns show slices through the center of the spherical source: on the left, slices parallel to the detectors, at  $z = 1$  cm, on the right, slices orthogonal to the detectors, at  $y = 1$  cm were represented. The gray scale is in arbitrary units. Images (a) and (c) show the effect of an undersampling. The source can be identified but many line-shaped artefacts can be observed. The quality of the images improves as the number of bins for  $\delta$  increases.

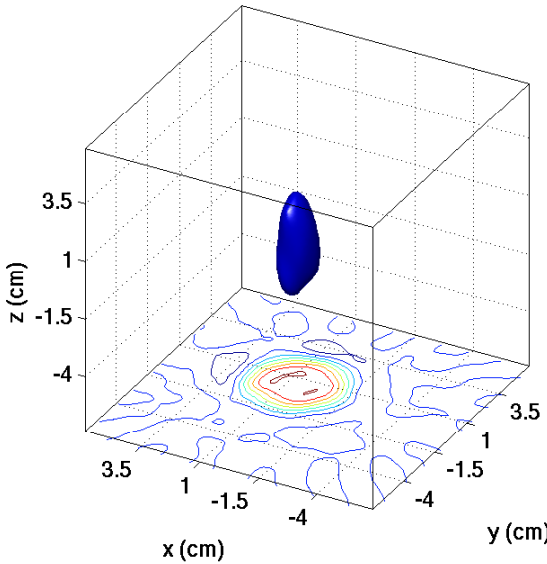


Figure 6.5: *Analytical reconstruction* - 3D reconstruction of the spherical source of photons from  $328 \times 10^3$  events. The number of bins is 5 for  $\theta_g$ , 20 for  $\beta$  and 40 for  $\delta$ . The contours correspond to the projection of the 3D image along the  $z$  direction.

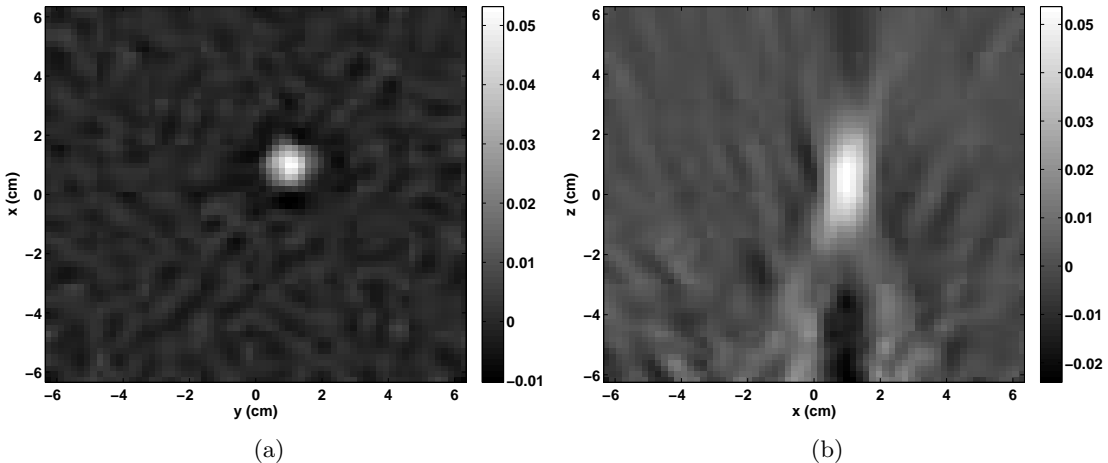


Figure 6.6: *Analytical reconstruction* - Images of the spherical source of photons reconstructed from  $328 \times 10^3$  events with 5 bins for  $\theta_g$ , 20 bins for  $\beta$  and 40 bins for  $\delta$ . (a) cut at  $z = 1$  cm, parallel to the detectors (b) cut at  $y = 1$  cm, parallel to the detectors. The gray scale is in arbitrary units.

### 6.2.2 Quality of the image as function of the angle $\beta$ for a small camera

Particularly striking is the influence of the small solid angle covered by the scatterer at a point of the source, meaning that the projections are truncated, especially for large values of  $\beta$ . Figure 6.9 illustrates this phenomenon when exact projections are calculated with the equation (5.3) for a finite size scatterer and an absorber of infinite length. In

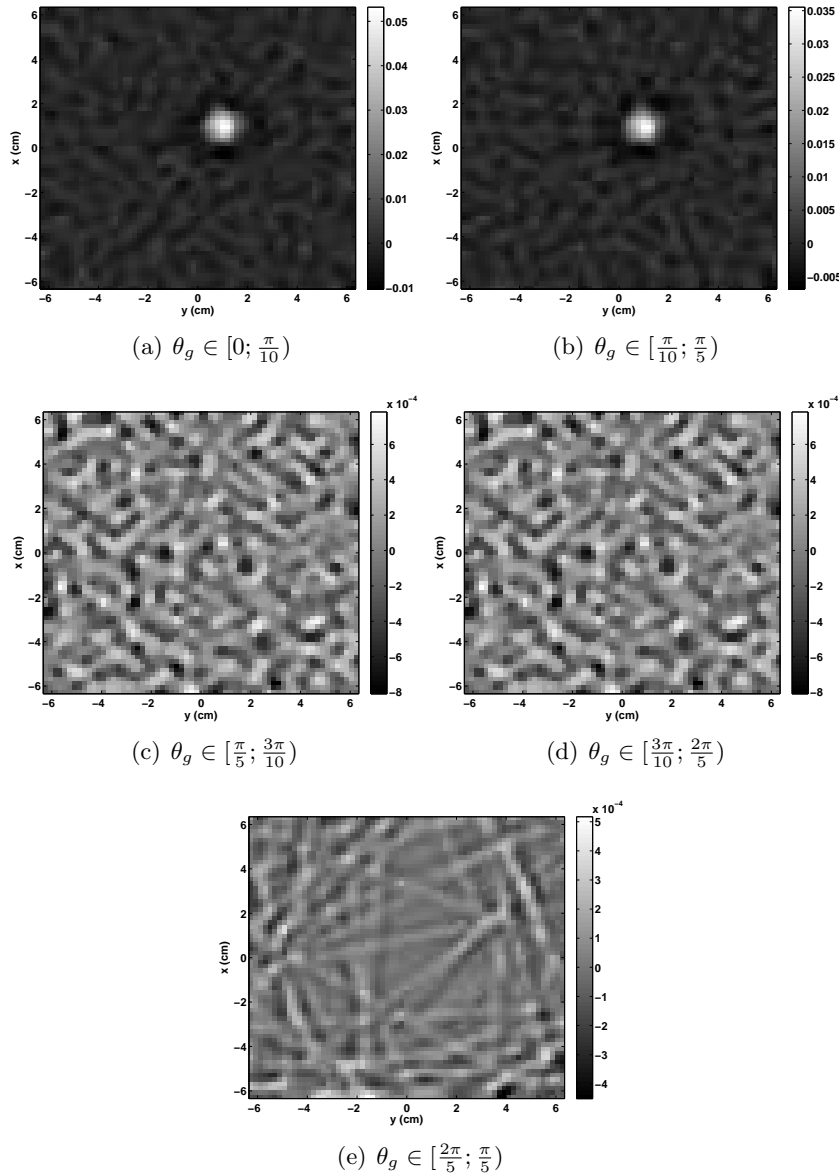


Figure 6.7: *Analytical reconstruction - Influence of the parameter  $\theta_g$ .* The images are slices parallel to the detectors, at  $z = 1$  cm and the values of  $\beta$  and  $\delta$  were distributed in 20 and 40 equal bins, respectively. The gray scale is in arbitrary units.

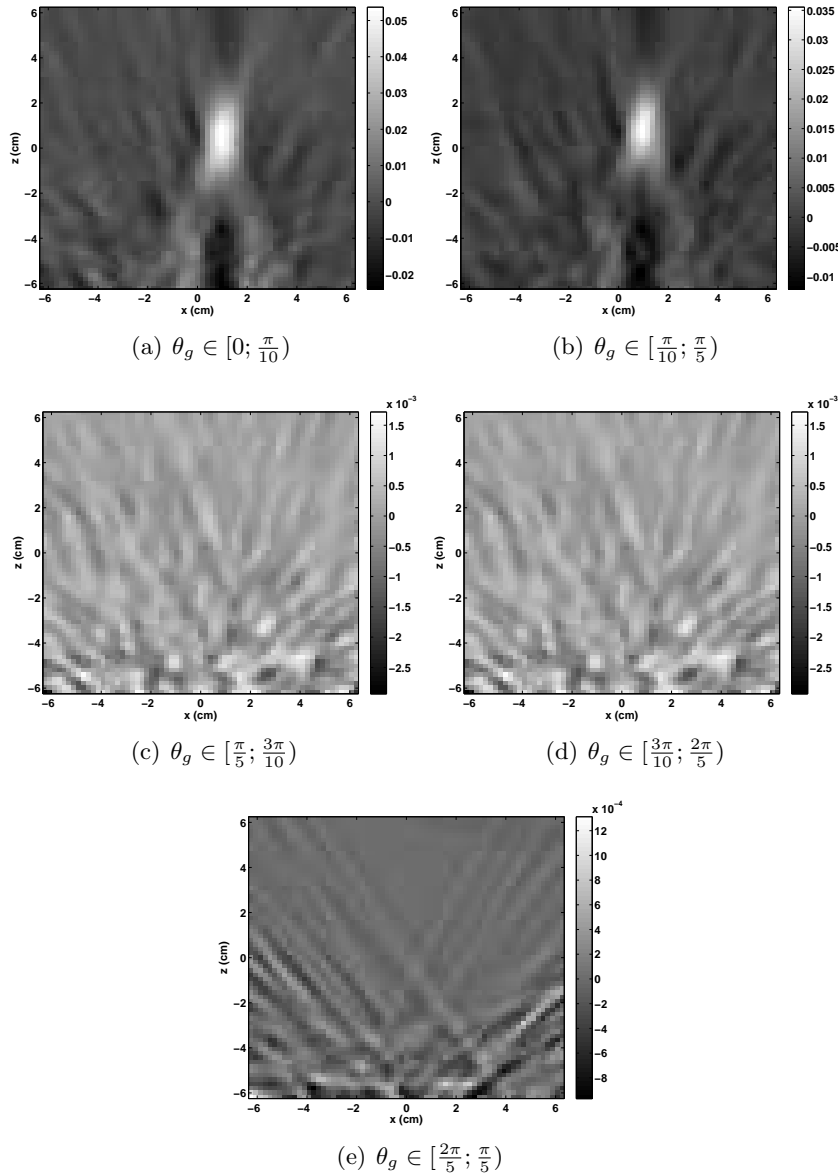


Figure 6.8: *Analytical reconstruction - Influence of the parameter  $\theta_g$ .* The images are slices orthogonal to the detectors, at  $y = 1$  cm and the values of  $\beta$  and  $\delta$  were distributed in 20 and 40 equal bins, respectively. The gray scale is in arbitrary units.

this example and only here, in order to illustrate the phenomenon, a spherical source of radius 1.5 pixels is used. Note the elongation of the reconstructed source when only 1/3 of projections ( $\beta \in [0, \frac{\pi}{6}]$ ) are measured.

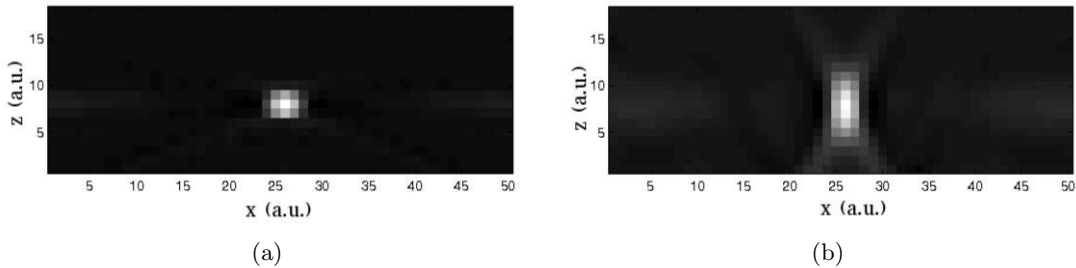


Figure 6.9: *Analytical reconstruction - Influence of the finite size of the detector on the reconstructed image. Units are arbitrary.* (a) The projections for all angles  $\beta$  are included. (b) Only projections for the 1/3 smallest values of  $\beta$  are used. The source is a sphere with a radius of 1.5 pixels.

The Compton camera presented in figure 6.1 is denoted from now on "small Compton camera". In a second experiment, we increased the size of the scatterers to  $25 \times 25 \times 0.5 \text{ cm}^3$ , twice the size of the previous scatterers in the direction parallel to the detector. This device, presented in figure 6.10, will be called the "large Compton camera".

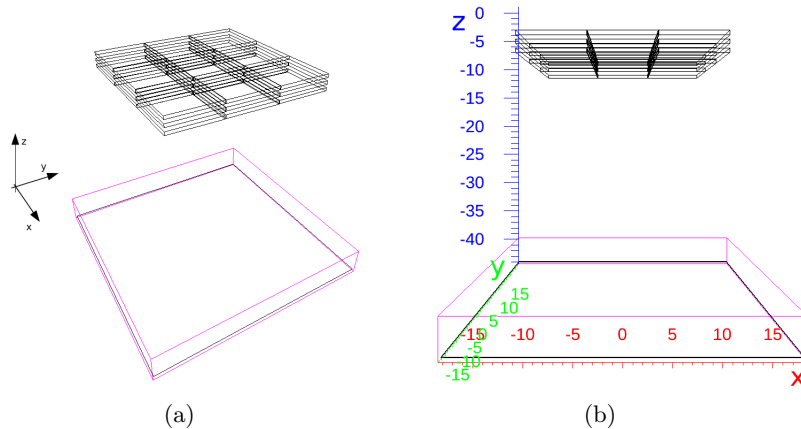


Figure 6.10: - Large simulated Compton camera composed of 3 scatterers of  $25 \times 25 \times 0.5 \text{ cm}^3$  in Silicon, and an absorber of  $37 \times 37 \times 4 \text{ cm}^3$  in Caesium Iodide crystals.

We used the same source pattern as described in 6.1.2, i.e. a monoenergetic  $\gamma$  source emitting photons of energy 1.275 MeV. We then performed a new acquisition using the large Compton camera device. The source emitted  $253 \times 10^6$  photons and  $10^6$  of them were triggered by the device. After analysis and treatment of the output data,  $250 \times 10^3$  events can be used in the reconstruction process.

Figure 6.11 show slices of the reconstructed image at  $z = 1 \text{ cm}$  and  $y = 1 \text{ cm}$ . The volume is composed of  $65 \times 65 \times 65$  voxels, the size of the voxel still is of 2 mm. We

chose 5 bins for  $\theta_g$ , 20 bins for  $\beta$  and 60 bins for  $\delta$ . We now compare the reconstructions with data obtained from the large and the small camera in the direction orthogonal to the detectors. From the comparison between figures 6.6 (b) and 6.11 (b), one may notice that the elongation is reduced when using wider scatterers.

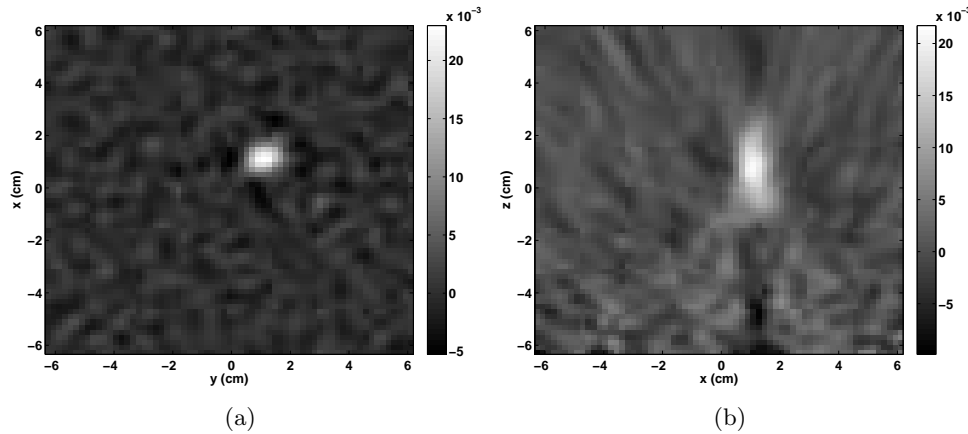


Figure 6.11: *Analytical reconstruction* - Images of the spherical source of photons reconstructed from  $250 \times 10^3$  events with 10 bins for  $\theta_g$ , 20 bins for  $\beta$  and 60 bins for  $\delta$ . The data is acquired with the large Compton camera. (a) cut at  $z = 1$  cm, parallel to the detectors (b) cut at  $y = 1$  cm, parallel to the detectors. The gray scale is in arbitrary units.

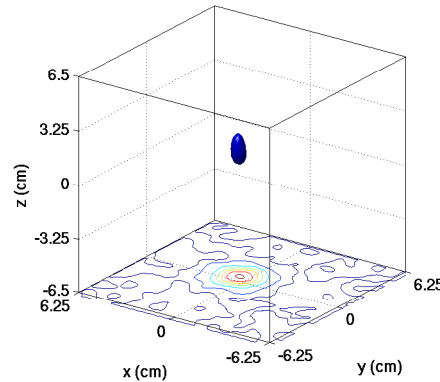


Figure 6.12: *Analytical reconstruction* - 3D reconstruction of the spherical source of photons from  $250 \times 10^3$  events. The number of bins is 5 for  $\theta_g$ , 20 for  $\beta$  and 40 for  $\delta$ . The data is acquired with the large Compton camera. The contours correspond to the projection of the 3D image along the  $z$  direction.

### 6.3 Conclusion

We have shown reconstructions of a  $^{22}\text{Na}$   $\gamma$  source using a Filtered BackProjection algorithm for Compton imaging. The finite extent of the detectors that limits the solid angle covered by the scatterer at a point of the source, leads to an elongation of the reconstructed source in the direction orthogonal to the detectors. We proposed to use a Compton camera with larger scatterers which has shown a reduction of the elongation.

Another issue that should be pointed out, is the complexity of the choice of an optimal binning of the angular parameters to avoid introducing artefacts. As for the spatial resolution, a too high number of bins leads to distribute too few events per voxels, consequently the reconstructed image will be degraded.

In the studies we carried out, the resolution was relatively fair with regards to the monitoring objective. But, we noticed that the method is very sensitive to the lack of events. A large amount of them have been used in the reconstructions performed in this section, i.e. enough events per bin were available. Since in hadrontherapy a relatively small number of photons are acquired, the binning process might lead to a too low amount of data per bin, and the reconstructed source will be blended in the noise. In this case, a decrease of the number of spatial bins can enable to recover the source, but the millimetric resolution required for hadrontherapy monitoring will not be achieved anymore. Thus, this reconstruction method will not give a real time millimetric resolution image but rather a reconstruction tool that is fast and adapted to situations where a large amount of data are available.

As already mentioned in section 4.1, another major limitation specific to any analytical methods is the difficulty to incorporate noise properties of the measured data in the reconstruction procedure. This is caused by the randomness in emission and detection processes. In the next chapter, we will see how the iterative methods enable to include these properties in the reconstruction process.

## IV Iterative methods

---



# Résumé en français (Abstract in French)

## LM-MLEM: nouvelle formulation mathématique pour l'estimation de la matrice système

### Modélisation

Le procédé itératif de reconstruction que nous utilisons est basé sur la maximisation de la fonction de vraisemblance par maximisation de l'espérance<sup>1</sup>. L'originalité de la méthode que nous proposons repose sur une nouvelle formulation pour l'estimation des éléments de la matrice système notée  $\mathbf{T}$ . Cette matrice est nécessaire au processus itératif. Elle modélise la géométrie de la caméra et les phénomènes qui se produisent durant l'acquisition.

D'abord, nous définissons le contexte mathématique de la reconstruction. Les données mesurées par la caméra sont enregistrées en mode liste (d'où le préfixe LM) et indexées par  $i = \overline{1, N_e}$  avec  $N_e$  le nombre d'événements enregistrés. Un événement  $e_i$  est décrit par les paramètres  $(V_{1,i}, E_{1,i}, V_{2,i}, E_{2,i})$ , où  $V_{1,i}$  et  $V_{2,i}$  sont respectivement la première et la deuxième position d'interaction avec la caméra et  $E_{1,i}$  l'énergie transférée à l'électron au cours de la première interaction et  $E_{2,i}$  l'énergie du photon diffusé. Pour alléger l'écriture, nous avons choisi d'abandonner l'indice  $i$  et nous écrivons les paramètres de l'événement  $e_i$  sous la forme  $(V_1, E_1, V_2, E_2)$ .

Nous considérons un volume voxelisé noté  $\mathcal{V}$ , qui sera l'image 3D à reconstruire. Les voxels sont indexés par  $j = \overline{1, N_v}$ , avec  $N_v$  le nombre de voxels de  $\mathcal{V}$ . Le volume est placé de sorte qu'il contienne la source de radiation.

Chaque voxel émet un nombre aléatoire de photons qui suit une loi de Poisson de paramètre  $\lambda_j$ . L'algorithme itératif LM-MLEM permet d'approcher  $\boldsymbol{\lambda}$  par une suite d'estimations  $\hat{\boldsymbol{\lambda}}^{(\ell)}$ , le paramètre  $\ell$  étant l'indice d'itération  $\ell = \overline{0, N_\ell}$  où  $N_\ell$  représente le nombre d'itérations accomplies. L'algorithme itératif LM-MLEM nous permet d'écrire:

$$\hat{\lambda}_j^{(\ell+1)} = \frac{\hat{\lambda}_j^{(\ell)}}{s_j} \sum_i \frac{t_{ij}}{\sum_k t_{ik} \hat{\lambda}_k^{(\ell)}},$$

---

<sup>1</sup>connu sous l'appellation MLEM Maximum Likelihood Expectation Maximization

---

le terme  $s_j$  correspondant à la probabilité pour un photon émis par le voxel  $v_j$  d'être détecté. On appelle aussi ce terme sensibilité. Pour nos travaux nous avons considéré que  $s_j = 1$  pour tous les voxels.

## Calcul des éléments de la matrice système

Un élément de la matrice  $\mathbf{T}$ , noté  $t_{ij}$ , représente la probabilité pour un photon émis par le voxel  $v_j$  d'être détecté en tant qu'événement  $e_i$ . Dans un premier temps, une étude sur le processus d'acquisition d'un photon  $\gamma$  par la caméra Compton, nous permet d'établir le modèle décrivant cette probabilité. Inspiré par [Wilderman *et al.* (1998)], nous proposons le modèle suivant:

$$t_{ij} = \int_{M \in v_j} K(\beta_M, E_0) \frac{|\cos(\theta_M)|}{\|\vec{V_1 M}\|_2^2} h(\beta_M | \beta, \sigma_\beta) dv$$

La probabilité  $t_{ij}$  est calculée en sommant sur tous les points  $M$  du voxel  $v_j$ , la fonction de densité de probabilité composée d'un noyau spatial  $h$  lié à l'événement, multipliée par la section efficace différentielle  $K(\beta_M, E_0)$ , pondérée par l'angle solide couvert par l'élément de diffuseur contenant le point  $V_1$  au point  $M$ . Ces facteurs sont tous propres à l'événement  $e_i$  considéré. La probabilité  $t_{ij}$  diminue avec l'augmentation de la distance angulaire  $\beta_M$  ainsi qu'avec la distance  $\|\vec{V_1 M}\|_2$  et  $\theta_M$  l'angle d'incidence du photon. Nous proposons deux noyaux spatiaux permettant la prise en compte ou non des incertitudes sur les énergies mesurées.

## Modèle qui néglige les incertitudes de mesure d'énergie

Dans une première approche, nous négligeons les incertitudes de mesures de l'énergie. Le noyau spatial est alors une distribution de Dirac qui correspond à la surface du cône Compton. Cette contrainte simplifie la dimension de l'intégrale à évaluer, passant de volumique à surfacique.

$$t_{ij} = \int_{M \in \mathcal{C}_i \cap v_j} K(\beta_M, E_0) \frac{|\cos(\theta_M)|}{\|\vec{V_1 M}\|_2^2} ds,$$

avec  $ds$  l'élément de surface. Une illustration du domaine d'intégration est donnée dans la figure 7.4.

Dans l'expression précédente, seuls les points  $M$  appartenant au cône Compton contribueront à la formule intégrale. Pour l'évaluation numérique d'un élément  $t_{ij}$ , on s'intéresse donc à la surface résultant de l'intersection entre le cône  $\mathcal{C}_i$  et le voxel  $v_j$ . L'idée est alors d'utiliser une discrétisation adéquate de l'intégrande. Pour cela, deux méthodes de discrétisation du cône sont proposées, illustrées figure 7.3. La première consiste à considérer le cône comme un empilement d'ellipses. La seconde, que nous avons choisie, consiste à discrétiser le cône par un ensemble de ses génératrices. Ce choix a été établi à la suite des travaux menés par [Kim *et al.* (2007)] qui tendent à montrer que les deux méthodes sont

---

identiques en terme de qualité de reconstruction, mais que la méthode des génératrices est plus rapide. Afin de sélectionner les génératrices du cône, nous proposons une méthode originale que nous détaillerons par la suite.

En supposant pour le moment que cette méthode est définie, et qu'un ensemble de génératrices est obtenu, intéressons nous à l'évaluation des éléments de la matrice système.

Pour effectuer le calcul numérique de l'expression précédente, nous procérons d'abord à un changement de repère. Le nouveau repère correspond à celui du cône noté  $\mathcal{R}_i(V_1x'y'z')$ , avec  $V_1$  l'origine et  $z'$  en alignement avec l'axe du cône (figure 7.5). En coordonnées sphériques, le cône  $\mathcal{C}_i$  est défini par le système d'équation:

$$\begin{cases} x' = \rho \sin(\beta) \cos(\varphi) \\ y' = \rho \sin(\beta) \sin(\varphi) & \rho \geq 0, \varphi \in [0, 2\pi], \\ z' = \rho \cos(\beta) \end{cases}$$

avec  $\rho = \|\overrightarrow{V_1M}\|_2$  et  $\varphi$  son angle azimut. Dans ce repère,  $M$  a pour coordonnées  $(x'_M, y'_M, z'_M)$ . Pour un angle  $\varphi$  donné, l'ensemble des points vérifiant le système d'équations précédent est une demi-droite d'origine  $V_1$ , donc une génératrice du cône. A présent, l'élément de surface  $ds$  peut être exprimé, en coordonnées sphériques:

$$ds = \rho \sin(\beta) d\rho d\varphi$$

En reportant dans l'expression intégrale, on a:

$$t_{ij} = K(\beta, E_0) \int_0^{2\pi} \int_0^\infty \frac{|\cos(\theta_M)|}{\rho^2} \sin(\beta) \chi_{v_j}(M) \rho d\rho d\varphi$$

avec  $\chi_{v_j}(M)$ , la fonction caractéristique indiquant l'appartenance de  $M$  au voxel  $v_j$ . On note  $\rho_1(\varphi)$  et  $\rho_2(\varphi)$  les limites inférieure et supérieure de  $\rho$  telles que  $M(\rho, \varphi)$  appartient au voxel  $v_j$ . Le terme  $\theta_M$  dépend de  $\varphi$  mais  $\rho$  n'en dépend pas, ainsi on peut écrire:

$$\begin{aligned} t_{ij} &= \sin(\beta) K(\beta, E_0) \int_0^{2\pi} |\cos(\theta_M)| \int_{\rho_1(\varphi)}^{\rho_2(\varphi)} \frac{1}{\rho} d\rho d\varphi \\ &= \sin(\beta) K(\beta, E_0) \int_0^{2\pi} |\cos(\theta_M)| \ln(\rho_2(\varphi)) - \ln(\rho_1(\varphi)) d\varphi \end{aligned}$$

Soit  $N_r^i$  le nombre de génératrices sélectionnées pour le cône associé à l'événement  $e_i$ . La  $k$ -ième génératrice intersecte la grille de voxels aux points  $M_{k,h}$ ,  $h = \overline{1, N_h^{i,k}}$  où  $N_h^{i,k} - 2$  est le nombre de fois que la  $k$ -ième génératrice du  $i$ -ème cône passe d'un voxel à l'autre. À chaque génératrice est associée une valeur de l'angle azimut  $\varphi = \varphi_k$ . Pour un angle  $\varphi_k$  donné,  $\theta_M$  est l'angle polaire de la génératrice considérée, dans le système de coordonnées  $Oxyz$ . On le notera dorénavant  $\theta_k$ . Pour effectuer le calcul numérique de l'intégrale, on choisit une méthode de quadrature pour l'intégration sur  $\varphi$  et on évalue

---

l'intégrande à chaque échantillon. Pour ce faire, nous choisissons la méthode des trapèzes pour un échantillonnage non uniforme. En notant  $\Delta\varphi_k = \varphi_{k+1} - \varphi_{k-1}$ , on obtient la formule d'évaluation des  $t_{ij}$  suivante:

$$\hat{t}_{ij} = \sin(\beta)K(\beta, E_0) \frac{1}{2} \sum_{k=1}^{N_r^i} \Delta\varphi_k |\cos(\theta_k)| \ln \left( 1 + \frac{\rho_2(\varphi_k) - \rho_1(\varphi_k)}{\rho_1(\varphi_k)} \right)$$

Notons que  $\rho_2(\varphi_k) - \rho_1(\varphi_k) \ll \rho_1(\varphi_k)$ . Nous pouvons alors utiliser un développement limité au premier ordre de la fonction logarithme. Après simplification des constantes multiplicatives, nous obtenons la formule suivante:

$$\hat{t}_{ij} = \sum_{k=1}^{N_r^i} (\varphi_{k+1} - \varphi_{k-1}) |\cos(\theta_k)| \frac{\rho_2(\varphi_k) - \rho_1(\varphi_k)}{\rho_1(\varphi_k)}$$

Pour réaliser le calcul de  $t_{ij}$ , nous calculons la longueur du segment représentant l'intersection entre la  $k$ -ième génératrice du cône et le voxel  $v_j$ , que nous multiplions par l'angle d'inclinaison de la génératrice et pondérons par la variation de l'angle azimut entre les génératrices précédente et suivante à celle considérée. Nous multiplions également par l'inverse de la distance entre le sommet du cône et le voxel. Enfin, nous sommes cette quantité sur l'ensemble des génératrices intersectant le voxel  $v_j$ . La longueur des segments de génératrices est calculée par un algorithme de lancer de rayon proposé dans [Zhao and Reader (2003)].

### Méthode de prise en compte des incertitudes sur les mesures d'énergie

Dans une seconde approche nous avons pris en compte les incertitudes sur les mesures d'énergie. Celles-ci sont inhérentes aux détecteurs, et dépendent de l'énergie initiale du photon. L'angle Compton étant directement calculé à partir de ces mesures, les erreurs de mesures se répercutent sur sa valeur. L'incertitude résultante sur la valeur de l'angle Compton nous amène à remplacer le cône Compton par un volume englobant. Nous modélisons alors ces incertitudes en choisissant pour noyau spatial une gaussienne tronquée, comme dans [Zoglauer (2005)]. Ainsi, l'intersection du cône épais avec le voxel  $v_j$  ne correspondra plus à une surface, mais à un volume, comme l'illustre la figure 7.6. Cette gaussienne aura pour moyenne  $\beta$ , calculé directement à partir des valeurs mesurées, et un écart-type  $\sigma_\beta$  donné par la formule suivante:

$$\sigma_\beta = \frac{m_e c^2}{\sin(\beta)} \sqrt{\left( \frac{1}{{E_2}^2} - \frac{1}{{E_0}^2} \right)^2 \sigma^2(E_2) + \frac{1}{{E_0}^4} \sigma^2(E_1)}$$

avec  $\sigma(E_1)$  et  $\sigma(E_2)$  représentant respectivement les résolutions énergétiques du diffuseur et de l'absorbeur. Nous supposons que la véritable valeur de l'angle Compton se trouve dans l'intervalle de valeurs donné par  $\beta \pm p\sigma_\beta$ ,  $p$  est un entier permettant de paramétriser la couverture des valeurs par la gaussienne notée  $g$ . Cette dernière est tronquée et, en dehors

de l'intervalle  $[\beta - p\sigma_\beta, \beta + p\sigma_\beta]$ , la gaussienne vaut 0. Ainsi le noyau spatial  $h(\beta_M | \beta, \sigma_\beta)$  s'écrit:

$$\begin{cases} g(\beta_M) &= \frac{1}{\sqrt{2\pi}\sigma_\beta} e^{-\frac{1}{2}\left(\frac{\beta_M-\beta}{\sigma_\beta}\right)^2} & \text{if } \beta_M \in [\beta - p\sigma_\beta, \beta + p\sigma_\beta] \\ g(\beta_M) &= 0 & \text{ailleurs} \end{cases}$$

En remplaçant le noyau par la gaussienne, on obtient la formule:

$$t_{ij} = \int_{M \in \mathcal{C}_i \cap v_j} K(\beta_M, E_0) \frac{|\cos(\theta_M)|}{\rho^2} g(\beta_M) dv$$

En exprimant  $dv$  en coordonnées sphériques, on a:

$$dv = \rho^2 \sin(\beta) d\rho d\varphi d\beta$$

La formule intégrale devient donc:

$$\begin{aligned} t_{ij} &= \int_{\beta-p\sigma_\beta}^{\beta+p\sigma_\beta} \int_0^{2\pi} \int_0^\infty K(\beta, E_0) |\cos(\theta_M)| \sin(\beta) \\ &\quad \times \frac{1}{\sqrt{2\pi}\sigma_\beta} e^{-\frac{1}{2}\left(\frac{\beta_M-\beta}{\sigma_\beta}\right)^2} \chi_{v_j}(M) d\rho d\varphi d\beta \end{aligned}$$

Pour réaliser le calcul des éléments  $t_{ij}$ , l'idée sera d'abord de discréteriser le cône épais en surfaces coniques puis d'effectuer la discréétisation des surfaces en génératrices. Pour une valeur donnée de  $\beta$  on obtient une surface de cône et pour une valeur donnée de  $\varphi$  on obtient une génératrice de cette surface. En notant  $\rho_1(\beta, \varphi)$  et  $\rho_2(\beta, \varphi)$  les limites inférieure et supérieure de  $\rho$  telles que  $M(\rho, \beta, \phi)$  appartienne à  $v_j$ , on a:

$$\begin{aligned} t_{ij} &= \int_{\beta-p\sigma_\beta}^{\beta+p\sigma_\beta} \int_0^{2\pi} K(\beta, E_0) |\cos(\theta_M)| \sin(\beta) \\ &\quad \times \frac{1}{\sqrt{2\pi}\sigma_\beta} e^{-\frac{1}{2}\left(\frac{\beta_M-\beta}{\sigma_\beta}\right)^2} \int_{\rho_1(\beta, \varphi)}^{\rho_2(\beta, \varphi)} d\rho d\varphi d\beta \\ &= \int_{\beta-p\sigma_\beta}^{\beta+p\sigma_\beta} \int_0^{2\pi} K(\beta, E_0) |\cos(\theta_M)| \sin(\beta) \\ &\quad \times \frac{1}{\sqrt{2\pi}\sigma_\beta} e^{-\frac{1}{2}\left(\frac{\beta_M-\beta}{\sigma_\beta}\right)^2} (\rho_2(\beta, \varphi) - \rho_1(\beta, \varphi)) d\varphi d\beta \end{aligned}$$

On discréteise donc l'intervalle  $[\beta - p\sigma_\beta, \beta + p\sigma_\beta]$  en  $2N_s + 1$  échantillons. La surface du  $i$ -ème cône est indexée par  $n = \overline{-N_s, N_s}$ . Le nombre de surfaces  $N_s$  doit être suffisamment grand pour obtenir un échantillonnage fin du cône épais. L'angle de demi-ouverture de la  $n - i$ ème surface de cône est donné par:

$$\beta_n = \beta + n \frac{p}{N_s} \sigma_\beta$$

---

Nous supposons maintenant que pour la  $n - i$ ème surface,  $N_r^{i,n}$  génératrices sont sélectionnées. L'angle azimut de la  $k - i$ ème génératrice de la  $n - i$ ème surface est noté  $\varphi_{n,k}$ . Cette génératrice intersecte la grille de voxels aux points  $M_{n,k,h}$ ,  $h = 1, N_h^{i,n,k}$  où  $N_h^{i,n,k} - 2$  est le nombre de fois que la  $k - i$ ème génératrice de la  $n - i$ ème surface du  $i - \text{ème}$  cône passe d'un voxel à l'autre. De même que pour la méthode précédente, nous choisissons la méthode des trapèzes pour l'évaluation des intégrales sur  $\beta$  et  $\varphi$ .

En exprimant  $\Delta\beta_n$  et  $\Delta\varphi_{n,k}$ , nous avons:

$$\Delta\beta_n = \beta_{n+1} - \beta_{n-1} = \frac{2p}{N_s}\sigma_\beta$$

$$\Delta\varphi_{n,k} = \varphi_{n,k+1} - \varphi_{n,k-1}$$

En reportant dans la formule intégrale et après simplification des constantes multiplicatives, nous obtenons finalement:

$$\begin{aligned} \hat{t}_{ij} &= \sum_{n=-N_s}^{N_s} K(\beta_n, E_0) \sin(\beta_n) e^{-\frac{1}{2} \left( \frac{pn}{N_s} \right)^2} \\ &\quad \sum_{k=1}^{N_r^{i,n}} (\varphi_{n,k+1} - \varphi_{n,k-1}) |\cos(\theta_{n,k})| (\rho_2(\beta_n, \varphi_{n,k}) - \rho_1(\beta_n, \varphi_{n,k})) \end{aligned}$$

Ainsi, pour le calcul des probabilités  $t_{ij}$  nous calculons la longueur de la génératrice traversant le voxel  $v_j$ , multipliée par l'angle d'inclinaison de la génératrice, pondérée par la variation de l'angle azimut entre les génératrices précédente et suivante à celle considérée. On somme pour chaque génératrice et on multiplie ensuite cette somme par la valeur de la gaussienne. Enfin nous sommes sur l'ensemble des surfaces de cône.

## Méthode simplifiée

Nous avons aussi testé une méthode de calcul numérique inspirée de [Zoglauer (2005)], plus simple que nos méthodes, appliquée à notre modèle d'estimation des éléments de la matrice système.

Dans les précédentes méthodes, les voxels qui n'étaient pas intersectés par le cône Compton n'étaient pas considérés, la probabilité  $t_{ij}$  associée étant implicitement égale à 0. Dans cette méthode, nous traitons l'intégralité des voxels en évaluant pour tous, la distance angulaire du centre du voxel au cône Compton. L'idée est de simplifier le calcul des éléments  $t_{ij}$  en se basant sur l'estimation de la formule intégrale en un point, le centre du voxel traité. Cette méthode a l'avantage d'être simple à implémenter et le nombre d'opérations pour calculer les éléments de la matrice est grandement réduit. On note  $\beta_{O_j}$  la distance angulaire du voxel  $v_j$  au cône (voir figure 7.7). Si et seulement si cette distance est plus petite qu'une valeur seuil,  $|\beta_{O_j} - \beta| < p\sigma_\beta$ , avec  $p$  un entier, on attribue à  $t_{ij}$  une valeur strictement positive. Cette valeur est donnée par le même noyau spatial que pour

---

la méthode précédente, i.e. une fonction gaussienne tronquée. On considère alors

$$\hat{t}_{ij} = \begin{cases} K(\beta, E_0) \frac{|\cos(\theta_{O_j})|}{\|\overrightarrow{V_1 O_j}\|_2^2} \frac{1}{\sqrt{2\pi}\sigma_\beta} e^{-\frac{1}{2}\left(\frac{\beta_{O_j}-\beta}{\sigma_\beta}\right)^2} & \text{si } |\beta_{O_j} - \beta| < p\sigma_\beta \\ 0 & \text{sinon} \end{cases}$$

Une seconde valeur "seuil" permet d'éviter le cas dégénéré où  $\sigma_\beta$  serait trop faible, entraînant la valeur  $t_{ij} = 0$  pour tout  $v_j$ . Cette valeur est établie suivant la condition homogène:

$$p\sigma_\beta \geq \frac{2d}{\|\overrightarrow{V_1 O_j}\|_2},$$

avec  $d$  la longueur d'un voxel. Ainsi, si nous avons  $p\sigma_\beta < \frac{2d}{\|\overrightarrow{V_1 O_j}\|_2}$ , nous posons  $p\sigma_\beta = \frac{2d}{\|\overrightarrow{V_1 O_j}\|_2}$  avant de calculer  $\hat{t}_{ij}$ .

## Méthode de sélection des génératrices du cône Compton

Comme mentionné précédemment, nous proposons une méthode de sélection des génératrices du cône Compton. L'originalité de cette sélection réside dans la non-uniformité de l'échantillonnage. La répartition des génératrices du cône est propre à l'événement traité et permet d'obtenir une estimation fine des  $t_{ij}$ .

Pour cela, nous définissons d'abord ce que nous appelons la surface guide. L'idée est d'établir une grille sur la face du volume  $\mathcal{V}$  (cubique) opposée au sommet du cône et de déterminer les points d'intersection entre ce dernier et la grille. Pour ce faire, intéressons nous à l'hyperpyramide définie par sa base  $ABCDEFGH$  et son sommet  $V_1$  comme le montre la figure 8.1. Chaque segment défini comme l'intersection d'une génératrice du cône avec le volume est inclus dans cette hyperpyramide. En projetant ensuite les sommets du cube sur la face opposée, nous obtenons la surface guide, la surface minimum formée par les points projetés qui couvre à la fois  $EFGH$  et  $A'B'C'D'$ . Sur la figure 8.2, cette surface est notée  $LFRD'$ .

On divise cette grille en pixels de taille au plus proche de celle des voxels du volume. Quand c'est nécessaire on suréchantillonne la grille. L'intersection du cône Compton avec la surface guide nous donne une conique. Les points d'intersection de la conique avec la grille de la surface guide, associés au sommet du cône, définiront les génératrices de ce dernier. Les régions grisées sur la figure présentent les parties de la grille où les points d'intersection trouvés ne correspondent pas à une génératrice intersectant le volume.

Pour déterminer les points d'intersection, nous nous sommes inspirés de [Wilderman *et al.* (1998)]. La méthode peut être décrite comme un suivi de conique. Supposant que la grille soit à une altitude  $z = z_g$ , l'équation de la conique définie comme l'intersection du cône et du plan  $z = z_g$  est :

$$[w_x(x - x_1) + w_y(y - y_1) + w_z(z_g - z_1)] = \cos(\beta) \sqrt{(x - x_1)^2 + (y - y_1)^2 + (z_g - z_1)^2}$$

---

avec  $(w_x, w_y, w_z)$  le vecteur unitaire de l'axe  $\overrightarrow{V_2V_1}$ , et  $(x_1, y_1, z_1)$  les coordonnées de  $V_1$ .

Pour effectuer la recherche des points d'intersection, l'idée est de trouver les points de coordonnées  $(x, y)$  qui vérifient l'équation précédente. Pour ce faire, on se place sur les lignes de la grille, on fixe alors une des coordonnées,  $x$  ou  $y$ . Dès lors, la résolution de l'équation précédente consiste à trouver les racines d'un polynôme d'ordre 2. Si des solutions réelles existent, une étape de validation est également nécessaire pour traiter les cas litigieux, par exemple éliminer les solutions en dehors de la surface.

Pour démarrer le suivi, on s'intéresse d'abord à la nature de l'inclusion de la conique dans la surface guide. En effet, elle peut ne pas intersecter la grille, l'intersecter partiellement ou être complètement incluse dans la surface. Pour différencier ces cas, nous procédons à une étape d'initialisation décrite par l'algorithme 1 qui consiste à rechercher des points d'intersections de la conique avec les bords de la surface guide. Si des solutions valides sont trouvées, on les enregistre et on lance l'algorithme de suivi de la conique. Si aucune solution n'est trouvée on se trouve dans le cas d'une conique interne ou externe à la grille. Nous déterminons alors les coordonnées du point  $\Omega$  d'intersection entre l'axe du cône et la surface guide. Par la suite, nous nous plaçons sur la ligne horizontale de la grille au dessus du point  $\Omega$  vis à vis de la coordonnée  $y$ , et nous recherchons des solutions à l'équation précédente. Si aucune solution n'est valide, alors, la conique est externe à la grille. Si on trouve des solutions valides alors elle est interne à la grille et on peut démarrer le suivi de cette dernière à partir d'une des deux solutions.

L'algorithme de suivi consiste à se placer au point déterminé précédemment, et à chercher sur les autres bords du pixel et sur le même bord au besoin, le prochain point d'intersection de la conique avec la grille. Le détail de cet algorithme peut être trouvé dans l'algorithme 2.

## Résultats

Nous avons utilisé les mêmes simulations que pour le chapitre analytique, à savoir : une source de photons d'énergie 1.275 MeV et les dispositifs "petite" et "grande" caméras Compton. Dans ces travaux, nous nous sommes focalisés sur l'utilisation d'un nombre relativement faible d'événements pour effectuer la reconstruction. Notons également que nous n'avons pas utilisé de critère d'arrêt pour stopper l'algorithme itératif. Cependant, le nombre d'itérations est suffisamment grand dans nos exemples pour que d'une itération à l'autre il n'y ait peu ou plus de changement dans les images reconstruites.

Nous reconstruisons un volume de  $10 \times 10 \times 10 \text{ cm}^3$  composé de  $100 \times 100 \times 100$  voxels. La valeur du paramètre  $p$  des distributions gaussiennes est fixé à 1. Nous appliquons un filtrage median aux images présentées pour les régulariser.

La figure 9.1 nous donne un aperçu de la nature de la reconstruction d'un seul événement avec les trois méthodes décrites précédemment.

Nous réalisons ensuite des reconstructions avec toutes les méthodes à partir de 5000 événements. Le nombre d'itérations est 20. Les résultats sont présentés dans les figures

---

9.2, 9.3, 9.4 pour les données obtenues à partir de la "petite caméra Compton" et figures 9.6, 9.7, 9.8 pour la "grande". Comme pour la méthode analytique, une élongation de la source sphérique peut être observée dans la direction orthogonale aux détecteurs. On peut observer notamment qu'avec la grande caméra, l'élongation et la quantité d'artefacts diminuent. L'erreur quadratique moyenne normalisée calculée à chaque itération pour l'ensemble des méthodes, tend à montrer que la méthode avec prise en compte des incertitudes donne des résultats similaires à ceux de la méthode simplifiée. Le reste de l'étude est réalisé avec la "grande" caméra. La figure 9.10 montre les reconstructions 3D obtenues pour chaque méthode en utilisant les isosurfaces de valeur seuil déterminée empiriquement (environ 85% de la valeur du maximum de l'image). Afin de confirmer ces résultats, nous reproduisons l'expérience avec 50 séries de 5000 événements. La figure 9.11 présente la dispersion de la mesure d'erreur pour la méthode simplifiée.

En hadronthérapie, l'énergie initiale des photons est inconnue. On l'estime comme la somme des énergies mises en jeu. Cependant, si le photon n'est pas complètement absorbé, cette estimation est imprécise et nous introduisons des erreurs dans la reconstruction. On peut observer cette influence dans les figures 9.12, 9.13, 9.14 présentant des reconstructions obtenues uniquement avec des photons totalement absorbés. Les courbes d'erreur sont présentées dans les figures 9.15, 9.16, 9.17. L'expérience montre que la possibilité de sélectionner les photons qui ont subi une absorption complète permet d'améliorer la qualité de l'image. Il existe des méthodes pour s'affranchir de ce problème comme dans [Xu and He (2007)].

Nous avons également réalisé la reconstruction d'une ligne avec le prototype de caméra présenté figure 9.18. Nous avons pu observer que les parties de la source non directement couvertes par les détecteurs sont moins bien reconstruites. Ici, le modèle que nous avons choisi pour l'estimation des éléments de la matrice système n'est peut être pas le plus adéquat. Nous avons donc réalisé une étude sur le modèle en s'affranchissant ou non de certains facteur comme la distance du point d'émission aux détecteurs, ou l'angle d'incidence du photon. La figure 9.26 présente les courbes d'erreur pour différents modèles. Elle montre que le modèle sans angle solide couvert par l'élément de diffuseur au point d'émission fournit des résultats relativement meilleurs, ce que l'on constate également sur les figures 9.24 et 9.25. L'étude sur le modèle d'estimation est à approfondir.



## Chapter 7

---

# LM-MLEM: Novel mathematical formulation for the estimation of the system matrix

---

We have developed reconstruction methods based on a List Mode Maximum Likelihood Expectation Maximization algorithm (MLEM) and using a novel mathematical formulation for the estimation of the system matrix. Let us first give some details on the LM-MLEM reconstruction.

An event, denoted  $e_i$ , is given by the measured parameters  $(V_{1,i}, E_{1,i}, V_{2,i}, E_{2,i})$ . They are recorded in list mode and indexed by  $i = \overline{1, N_e}$  with  $N_e$  being the number of recorded events. For writing convenience, from now on the index  $i$  will be omitted and the parameters of the event  $e_i$  will be simply denoted  $(V_1, E_1, V_2, E_2)$ .

We consider a voxelized volume  $\mathcal{V}$  which is to be the 3D image to reconstruct. The image space bins are the voxels which are indexed by  $j = \overline{1, N_v}$ , with  $N_v$  the number of voxels in  $\mathcal{V}$ . This volume contains the source of radiation we want to image. Each voxel emits a random number of photons that follows a Poisson law of parameter  $\lambda_j$ , denoted  $\mathcal{P}(\lambda_j)$ .

The LM-MLEM algorithm provides an estimation of  $\lambda_j$  at the end of an iterative process. At each iteration, the vector  $\boldsymbol{\lambda}$  is approximated by a vector  $\hat{\boldsymbol{\lambda}}^{(\ell)}$ . The parameter  $\ell$  is the index of the iteration. The total number of iterations completed is denoted  $N_\ell$ .

According to the equation (4.24) from section 4.2.1 we have:

$$\hat{\lambda}_j^{(\ell+1)} = \frac{\hat{\lambda}_j^{(\ell)}}{s_j} \sum_i \frac{t_{ij}}{\sum_k t_{ik} \hat{\lambda}_k^{(\ell)}}.$$

We recall that  $s_j$  is the probability for a photon emitted by the voxel  $v_j$  to be detected. This term is also called sensitivity. The coefficient  $t_{ij}$  is the probability for a photon emitted by the voxel  $v_j$  to be detected as event  $e_i$ . The initial guess  $\hat{\lambda}^{(0)}$  uses to be the backprojection of the acquired events.

We make the assumption that  $\forall j, s_j = 1$ . In [Wilderman *et al.* (1998)], it is argued that in the restrictive case of 2D imaging, considering the probabilities  $s_j$  to be constant have a little impact on the estimation of  $\boldsymbol{\lambda}$ . Indeed, in 2D the major effect of attenuations in the object is eliminated. Consequently, the variations in  $s_j$  will depend primarily on solid angle issues. Hence, for a small object at moderate distance from the detectors, the variation should be slow enough so that the degradation due to this assumption is fairly small. In our work, we consider 3D reconstruction. Hence, the assumption might lead to a more important degradation in the reconstructed image than in 2D. We will later study the role played by the solid angle on those degradations.

As for the probabilities  $t_{ij}$ , they are the elements of the system matrix denoted  $\mathbf{T}$ . In its more general form this matrix models the geometry of the device and all the phenomena taking place during the acquisition. In this work, it models the geometry of the camera. The computation of its elements is the main issue of this inverse problem. Several models have been investigated such as in [Wilderman *et al.* (1998), Xu and He (2007), Tornagé *et al.* (2009)].

## 7.1 Probabilistic model for the system matrix elements

The element  $t_{ij}$  is the probability of observing the event  $e_i$  when a photon is emitted by the voxel  $v_j$ . In order to express this probability, we focus on the probabilistic description of the acquisition process. For any detected photon, let us define the following random variables:

- $\mathcal{E}$ : the event measured by the detector (positions of interaction and energies)
- $\tilde{\mathcal{E}}$ : the real event (real positions of interaction and real energies)
- $\mathcal{M}$ : the point where the photon was emitted

Following [Wilderman *et al.* (1998)] we can write:

$$\begin{aligned}
 t_{ij} &= p(\mathcal{E} = e_i | v_j) \\
 &= \int_{\mathcal{V}} p(\mathcal{E} = e_i | \mathcal{M} = M) p(\mathcal{M} = M | M \in v_j) dv \\
 &= \int_{\mathcal{V}} p(\mathcal{E} = e_i | \mathcal{M} = M) p(M) \chi_{v_j}(M) dv
 \end{aligned} \tag{7.1}$$

where  $p(M)$  is the probability of emission at the point  $M$  and  $\chi_{v_j}(M)$  is the characteristic function that indicates membership of  $M$  to the voxel  $v_j$ . When all physical phenomena (such as Doppler broadening, noise in the detectors) and the resolution of the detector are taken into account, the probability  $p(\mathcal{E} = e_i | \mathcal{M} = M)$  may be expressed as the sum of probabilities on all the real events  $\tilde{e}_i$  that can lead to the measurement  $e_i$ ,

$$p(\mathcal{E} = e_i | \mathcal{M} = M) = \int p(\mathcal{E} = e_i | \tilde{\mathcal{E}} = \tilde{e}_i) p(\tilde{\mathcal{E}} = \tilde{e}_i | \mathcal{M} = M) d\tilde{e}_i, \tag{7.2}$$

where  $p(\mathcal{E} = e_i | \tilde{\mathcal{E}} = \tilde{e}_i)$  represents the probability to measure  $e_i$  given the real event  $\tilde{e}_i$ . A method to calculate  $p(\mathcal{E} = e_i | \tilde{\mathcal{E}} = \tilde{e}_i)$  is detailed in [Xu and He (2007)] where the authors assumed that the measurements of energies and positions follow Gaussian distributions. Next, the expression  $p(\tilde{\mathcal{E}} = \tilde{e}_i | \mathcal{M} = M)$  is the probability of occurrence of the real event  $\tilde{e}_i$  given the emission point  $M$ .

In the following, we neglect the uncertainties on the measured positions of interactions. The errors on the measured energies lead to uncertainties on the Compton angle  $\beta$ . Consequently, we assume that:

$$p(\mathcal{E} = e_i | \tilde{\mathcal{E}} = \tilde{e}_i) = p(\beta | \tilde{E}_1, \tilde{E}_2). \tag{7.3}$$

Two different expressions of this probability density function are further investigated.

- i) In the first one, we neglect uncertainties on  $\beta$  and we put:

$$p(\beta | \tilde{E}_1, \tilde{E}_2) = \delta(\beta - \tilde{\beta}), \tag{7.4}$$

where  $\delta$  is the Dirac function and  $\tilde{\beta}$  represent the real scattering angle.

- ii) In a second variant, we let the density function to account for energy measurement errors following a Gaussian distribution having as mean the real Compton angle  $\tilde{\beta}$ , and standard deviation  $\sigma_{\tilde{\beta}}$ , namely:

$$p(\beta | \tilde{E}_1, \tilde{E}_2) = \frac{1}{\sqrt{2\pi}\sigma_{\tilde{\beta}}} e^{-\frac{1}{2}\left(\frac{\beta-\tilde{\beta}}{\sigma_{\tilde{\beta}}}\right)^2} \tag{7.5}$$

In practice, the value of  $\sigma_{\tilde{\beta}}$  is estimated by an empirical standard deviation  $\sigma_{\beta}$  calculated from the measured energies  $E_1$  and  $E_2$  and the known energy uncertainties of the detectors

$\sigma(E_1)$  and  $\sigma(E_2)$ , as in [Zoglauer (2005)]:

$$\sigma_\beta = \frac{m_e c^2}{\sin(\beta)} \sqrt{\left( \frac{1}{{E_2}^2} - \frac{1}{{E_0}^2} \right) \sigma^2(E_2) + \frac{1}{{E_0}^4} \sigma^2(E_1)}. \quad (7.6)$$

Having in mind the expressions (7.5) and (7.6), we will write

$$p(\beta|\tilde{E}_1, \tilde{E}_2) = h(\tilde{\beta}|\beta, \sigma_\beta), \quad (7.7)$$

where  $h$  will represent a spatial kernel.

The probability  $p(\tilde{\mathcal{E}} = \tilde{e}_i | \mathcal{M} = M)$  is given by the product of the following probabilities [Wilderman *et al.* (1998), Zoglauer (2005)]:

- probability of emission of a  $\gamma$  ray at position  $M$
- Compton scattering probabilities
- Compton scattering process (including Doppler-broadening)
- absorption probabilities (in the different environments such as the object, air, of the scattered particle in the camera)
- absorption of the particle in the absorber

These probabilities describe the travel of the photon through the detection process illustrated in figure 7.1.

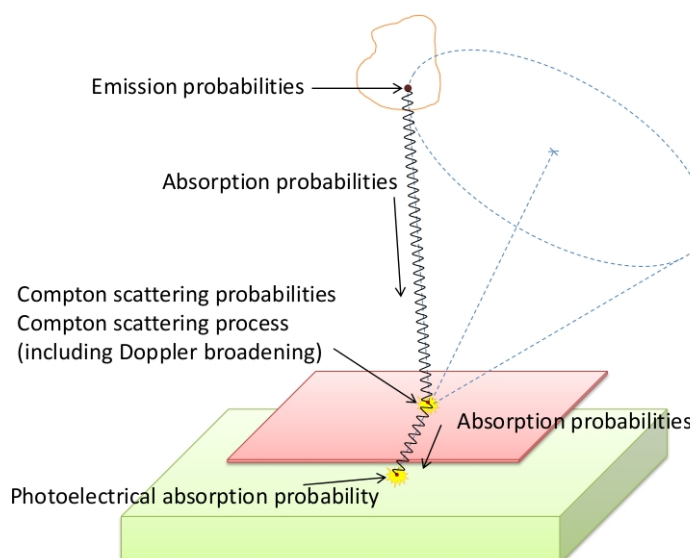


Figure 7.1: Illustration of the detection process of a photon by a Compton camera. This scheme presents the probabilities that are at stake during the travel of a  $\gamma$  particle.

The combination of these probabilities leads to the following model of  $p(\tilde{\mathcal{E}} = \tilde{e}_i | \mathcal{M} = M)$ , proposed in [Wilderman *et al.* (1998)]:

$$\begin{aligned} p(\tilde{\mathcal{E}} = \tilde{e}_i | \mathcal{M} = M) &= \frac{1}{8\pi^2} \frac{\mu_C}{\mu_{1,a}} K(\tilde{\beta}, E_0) (1 - e^{-\mu_C d_1}) e^{-\mu_{1,a} d_{12}} (1 - e^{-\mu_{2,a} d_2}) \\ &\times \frac{|\cos(\tilde{\theta}_g)| |\cos(\tilde{\theta}_m)|}{\|\tilde{V}_1 \tilde{V}_2\|_2^2 \|\tilde{V}_1 M\|_2^2} \delta \left( \arccos \left( \frac{\langle \tilde{V}_1 M, \tilde{V}_2 \tilde{V}_1 \rangle}{\|\tilde{V}_1 M\|_2 \|\tilde{V}_2 \tilde{V}_1\|_2} \right) - \tilde{\beta} \right) \end{aligned} \quad (7.8)$$

with  $\mu_C$ ,  $\mu_{1,a}$  and  $\mu_{2,a}$  the cross sections of Compton scattering, total absorption in the scatterer and total absorption in the absorber, respectively. The parameters  $d_1$ ,  $d_{12}$  and  $d_2$  represent the distances traveled by the initial photon until it is scattered in the scattering detector, by the scattered photon in the scattering detector and then in the absorber detector until the photon is absorbed respectively.  $\tilde{\theta}_M$  is the azimuth of the incident direction of the emitted  $\gamma$  photon and  $\tilde{\theta}_g$  the one of the scattered  $\gamma$  photon (see figure 7.2). Thus,  $\frac{\cos(\tilde{\theta}_M)}{\|M \tilde{V}_1\|_2^2}$  and  $\frac{\cos(\tilde{\theta}_g)}{\|\tilde{V}_1 \tilde{V}_2\|_2^2}$  are the solid angles subtended at the emitting point  $M$  by the element of scatterer containing  $\tilde{V}_1$  and subtended by the element of scatterer containing  $\tilde{V}_1$  at the element of absorber containing  $\tilde{V}_2$  respectively. The Dirac term conveys the fact that the emitting location  $M$  lies on the surface of the Compton cone defined by the event  $\tilde{e}_i$ .

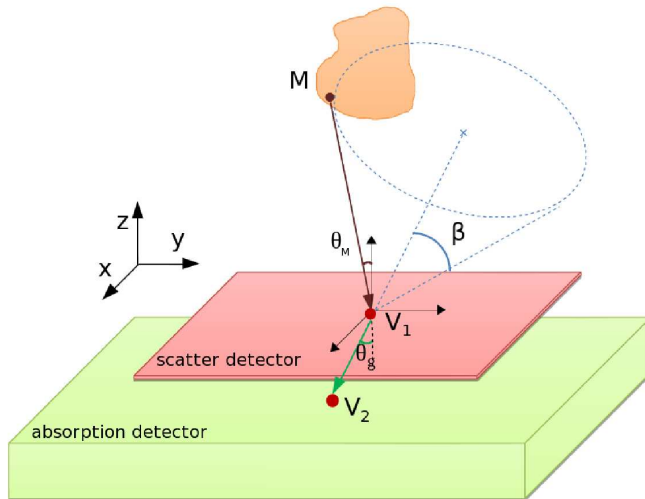


Figure 7.2: Scheme illustrating the parameters from the mathematical formulation of the probabilistic model.

Neglecting now the cross sections of Compton scattering and the undesired absorptions, the probability  $p(\tilde{\mathcal{E}} = \tilde{e}_i | \mathcal{M} = M)$  from (7.8) may be simplified to:

$$p(\tilde{\mathcal{E}} = \tilde{e}_i | \mathcal{M} = M) = K(\tilde{\beta}, E_0) \frac{|\cos(\tilde{\theta}_g)| |\cos(\tilde{\theta}_m)|}{\|\tilde{V}_1 \tilde{V}_2\|_2^2 \|\tilde{V}_1 M\|_2^2} \delta \left( \arccos \left( \frac{\langle \tilde{V}_1 M, \tilde{V}_2 \tilde{V}_1 \rangle}{\|\tilde{V}_1 M\|_2 \|\tilde{V}_2 \tilde{V}_1\|_2} \right) - \tilde{\beta} \right) \quad (7.9)$$

As already mentioned, we choose to neglect position measurement uncertainties, thus (7.9) becomes:

$$p(\tilde{\mathcal{E}} = \tilde{e}_i | \mathcal{M} = M) = K(\tilde{\beta}, E_0) \frac{|\cos(\theta_g)| |\cos(\theta_M)|}{\|\vec{V_1 V_2}\|_2^2 \|\vec{V_1 M}\|_2^2} \delta \left( \arccos \left( \frac{\langle \vec{V_1 M}, \vec{V_2 V_1} \rangle}{\|\vec{V_1 M}\|_2 \|\vec{V_2 V_1}\|_2} \right) - \tilde{\beta} \right) \quad (7.10)$$

We denote  $\beta_M = \arccos \left( \frac{\langle \vec{V_1 M}, \vec{V_2 V_1} \rangle}{\|\vec{V_1 M}\|_2 \|\vec{V_2 V_1}\|_2} \right)$ . Replacing (7.7) and (7.10) in (7.2), we obtain:

$$\begin{aligned} p(\mathcal{E} = e_i | \mathcal{M} = M) &= \int_0^\pi h(\tilde{\beta} | \beta, \sigma_\beta) K(\tilde{\beta}, E_0) \frac{|\cos(\theta_g)| |\cos(\theta_M)|}{\|\vec{V_1 V_2}\|_2^2 \|\vec{V_1 M}\|_2^2} \delta(\beta_M - \tilde{\beta}) d\tilde{\beta} \\ &= K(\beta_M, E_0) \frac{|\cos(\theta_g)| |\cos(\theta_M)|}{\|\vec{V_1 V_2}\|_2^2 \|\vec{V_1 M}\|_2^2} h(\beta_M | \beta, \sigma_\beta) \end{aligned} \quad (7.11)$$

We assume that all voxels have the same size and that they are small enough so that the probability of emission is uniform, i.e. we assume that  $p(M)$  is a constant inside a voxel. We can note that in LM-MLEM equation (4.24), the expressions  $t_{ij}$  and  $t_{ik}$  appear on the numerator and denominator respectively. The constants and the factors that do not depend on the voxels cancel. Then, replacing (7.11) in (7.1) we finally have:

$$\begin{aligned} t_{ij} &= \frac{|\cos(\theta_g)|}{\|\vec{V_1 V_2}\|_2^2} \int_{M \in \mathcal{V}} K(\beta_M, E_0) \frac{|\cos(\theta_M)|}{\|\vec{V_1 M}\|_2^2} h(\beta_M | \beta, \sigma_\beta) \chi_{v_j}(M) dv \\ &= \frac{|\cos(\theta_g)|}{\|\vec{V_1 V_2}\|_2^2} \int_{M \in v_j} K(\beta_M, E_0) \frac{|\cos(\theta_M)|}{\|\vec{V_1 M}\|_2^2} h(\beta_M | \beta, \sigma_\beta) dv \end{aligned} \quad (7.12)$$

As proportionality factors cancel in the iterative process equation (4.24), we consider the following simplified expression:

$$t_{ij} = \int_{M \in v_j} K(\beta_M, E_0) \frac{|\cos(\theta_M)|}{\|\vec{V_1 M}\|_2^2} h(\beta_M | \beta, \sigma_\beta) dv \quad (7.13)$$

Thus  $t_{ij}$ , which is proportional to the probability for a photon emitted by the voxel  $v_j$  to be detected as event  $e_i$  is calculated by summing on all the points  $M \in v_j$ , the probability density function composed of the spatial kernel  $h$  multiplied by the differential cross section  $K(\beta_M, E_0)$ , weightened by the solid angle subtended at the emitting point  $M$  by the element of scatterer that contains  $V_1$ . These factors are all event specific. The  $t_{ij}$  probability decreases as the angular distance  $\beta_M$ , the distance  $\|\vec{V_1 M}\|_2$  and the inclination angle  $\theta_M$  of the direction of the emitted photon increase.

We can note that for Xu and He in [Xu and He (2007)], the model is:

$$t_{ij} = \frac{1}{\sin(\beta)} e^{-\mu_{E_0} d_1} K(\beta, E_0) \frac{1}{(E_0 - E_1)^2} e^{-\mu_{E_0 - E_1} d} \frac{\sigma_p(E_2)}{\sqrt{2\pi(\sigma_{E_1}^2 + \sigma_{E_2}^2)}} e^{-\frac{1}{2} \frac{(E_0 - E_1 - E_2)^2}{\sigma_{E_1}^2 + \sigma_{E_2}^2}} \quad (7.14)$$

where  $e^{-\mu_E d_1}$  and  $e^{-\mu_E (E_0 - E_1)} d$  is the probability for the incident photon to reach the first interaction position and the second respectively, with  $d$  and  $d_1$  the distance traveled by the photon in the detectors until the first interaction and between the first and second interaction respectively, and  $\mu_E$  is the linear attenuation coefficient for  $\gamma$ -rays at energy  $E$ . The factor  $K(\beta, E_0) \frac{1}{(E_0 - E_1)^2}$  corresponds to the probability for the incident photon to deposit  $E_1$  in the scattering process and the factor  $\frac{\sigma_p(E_2)}{\sqrt{2\pi(\sigma_{E_1}^2 + \sigma_{E_2}^2)}} e^{-\frac{1}{2} \frac{(E_0 - E_1 - E_2)^2}{\sigma_{E_1}^2 + \sigma_{E_2}^2}}$  is the probability for the scattered photon to be photoelectrically absorbed. This model is quite different from our proposal. Indeed, the authors choose to neglect the distance between the source and the detectors, the incident angle of the photon, and the size of the voxel, leading to an expression of  $t_{ij}$  without a volume integral. They choose to keep the probabilities describing the acquisition process instead.

Another model can be found in [Tornga *et al.* (2009)]:

$$t_{ij} = K(\beta, E_0) \frac{(1 - e^{-\frac{t}{\lambda}})}{\|V_1 V_2\|_2^2 \cos(\theta_g)} \quad (7.15)$$

where  $\lambda$  is the interaction length that is material specific and  $t$  the thickness of the absorber that the scattered photon travels in the absorbing detector. We can note that here also the proposed model is quite different. The voxel as a volume is neglected. We can find instead partially the modelization of the absorption process.

Our model is also matter of discussion. We will provide in section 9.4, a study on the influence on the reconstructions of the distance  $\|V_2 V_1\|$  and of the incident angle  $\cos(\theta_g)$ , that are taken into account in our model.

## 7.2 Numerical evaluation of the system matrix

The evaluation of  $t_{ij}$  from the equation (7.13) is driven by the Compton cone, through the spatial kernel  $h$ . We considered 3 methods, which differ by the way the cone is represented by the discretization scheme and by the emphasis on the energy measurement uncertainties.

Then, as proposed in equations (7.40) and (7.5), two different spatial kernels are investigated. In the first approach, we neglect the energy measurement uncertainties. To describe this case, the spatial kernel is a Dirac distribution corresponding to the cone. This strong constrain simplifies the evaluation of the elements of the system matrix, but it moves aside from the ground truth. In the second approach, accounting for the energy measurement uncertainties enables to get closer to the ground truth, at the cost of a more complex discretization of the integrand. The spatial kernel is chosen as a truncated gaussian distribution in order to model the error on the Compton scattering angle. The gaussian distribution will be function of the angular distance of the emitting point to the Compton cone.

### 7.2.1 A model that neglects uncertainties on the energy measurements

In this section, we neglect the errors not only on positions but also on energy measurements. We consider that the events are obtained from a detector with ideal position and energy resolutions. The spatial kernel  $h$  from (7.13) represents the Dirac distribution corresponding to the cone surface. Equation (7.13) leads to:

$$\begin{aligned} t_{ij} &= \int_{M \in v_j} K(\beta_M, E_0) \frac{|\cos(\theta_M)|}{\|V_1 M\|_2^2} \delta(\beta_M - \beta) dv \\ &= K(\beta_M, E_0) \int_{M \in \mathcal{C}_i \cap v_j} \frac{|\cos(\theta_M)|}{\|V_1 M\|_2^2} ds, \end{aligned} \quad (7.16)$$

with  $ds$  the element of surface.

As mentioned previously, we first need to choose an appropriate sampling of the conical surface. There are two methods to do so, illustrated in figure 7.3: either we sample the Compton cone as a stack of ellipses or as a set of generatrices.

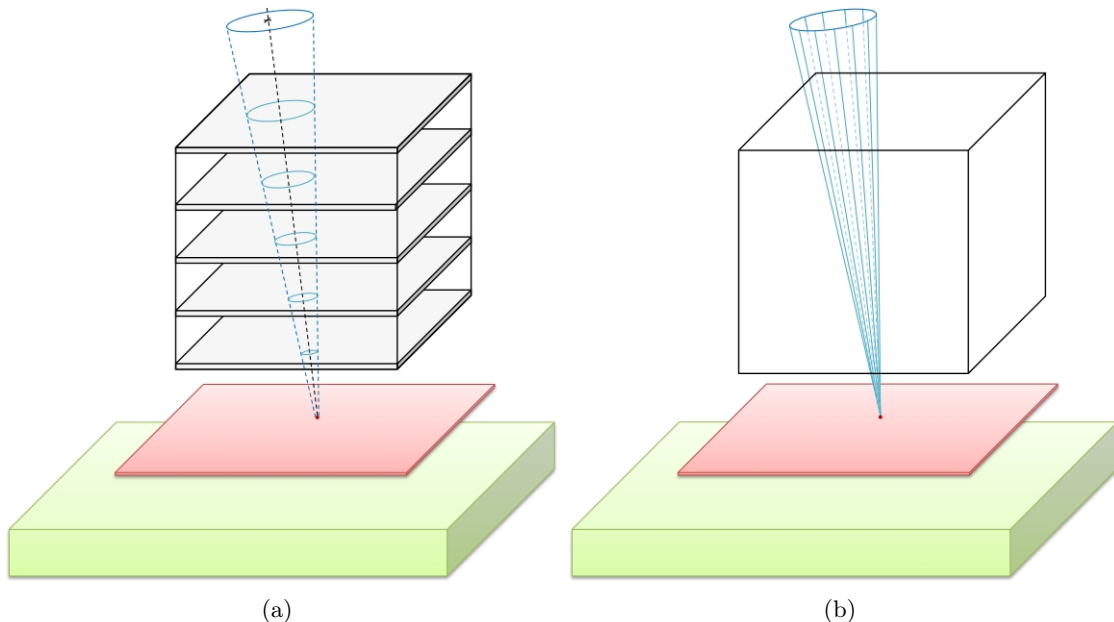


Figure 7.3: Illustration of two different methods to sample a conical surface: Panel (a) shows the Ellipse Stack Method where the conical surface is sampled as a stack of ellipses. Panel (b) shows the Ray Tracing Method where the conical surface is sampled as a set of generatrices.

In [Kim *et al.* (2007)], the authors concluded that both methods are similar in terms of reconstruction quality. However, the second one appears to be slightly faster in the computation of the system matrix and total number of iterations for convergence. For this reason, in the numerical evaluation of  $t_{ij}$  from equation (7.16), we have chosen to sample the surface of the cone  $\mathcal{C}_i$  by a set of generatrices, selected such that at least two of them pass through the voxel  $v_j$ . The surface of intersection between the cone and the voxel will

be given by the selected generatrices as shown in figure 7.4. One selection method that we

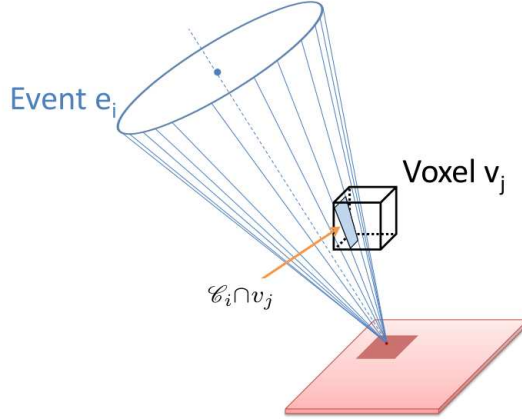


Figure 7.4: Illustration of the integration domain  $\mathcal{C}_i \cap v_j$  of the integral in equation (7.16). The cone is defined by its generatrices. The surface of intersection between the cone and the voxel is defined by the set of generatrices crossing  $v_j$ .

proposed in [Lojaccono *et al.* (2011)] will be described in section 8. For the time being, we suppose that such an algorithm is available and we focus on the derivation of a discrete formula for the equation (7.16).

First, we change the coordinate system to fit the one of the Compton cone. The new system will be denoted  $\mathcal{R}_i(V_1x'y'z')$ ,  $V_1$  being the origin of the frame and the axis  $z'$  is chosen in alignment with the cone axis (see figure 7.5). In local spherical coordinates, the cone  $\mathcal{C}_i$  is defined by the equation system:

$$\begin{cases} x' = \rho \sin(\beta) \cos(\varphi) \\ y' = \rho \sin(\beta) \sin(\varphi) \\ z' = \rho \cos(\beta) \end{cases} \quad \rho \geq 0, \quad \varphi \in [0, 2\pi), \quad (7.17)$$

with  $\varphi$  the azimuth angle and  $\rho = \|\overrightarrow{V_1M}\|_2$ . In this coordinate system, the coordinates of  $M$  are  $(x'_M, y'_M, z'_M)$ . Note that for some given value of  $\varphi$ , the set of points verifying (7.17) is a half line originated from  $V_1$ , thus a generatrix of the cone.

The expression of  $ds$  in spherical coordinates is:

$$ds = \rho \sin(\beta) d\rho d\varphi. \quad (7.18)$$

Replacing (7.18) in (7.16) gives:

$$t_{ij} = K(\beta_M, E_0) \int_0^{2\pi} \int_0^{\infty} \frac{|\cos(\theta_M)|}{\rho^2} \sin(\beta) \chi_{v_j}(M) \rho \, d\rho d\varphi. \quad (7.19)$$

Now let us denote by  $\rho_1(\varphi)$  and  $\rho_2(\varphi)$  the lower and upper values of  $\rho$  such that  $M(\rho, \varphi)$

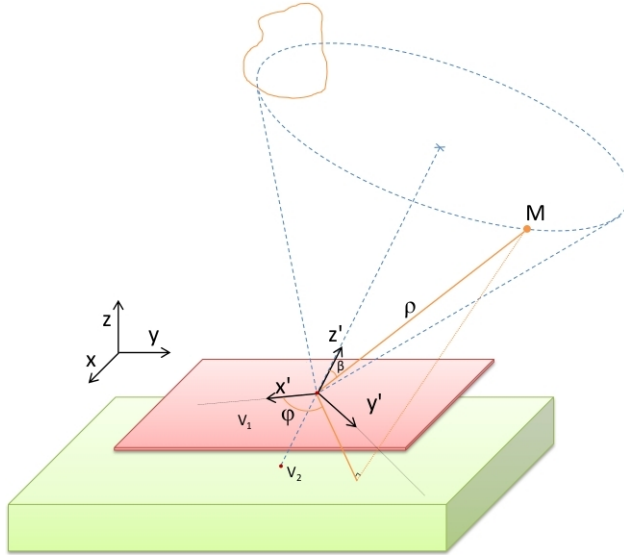


Figure 7.5: Illustration of the coordinate system  $\mathcal{R}_i(V_1x'y'z')$  that fits the one of the Compton cone. The origin of the frame is the apex of the cone  $V_1$  and the axis  $z'$  is chosen in alignment with the cone axis.

belongs to the voxel  $v_j$ . Then noting that  $\theta_M$  depends on  $\varphi$  only, not on  $\rho$ , we obtain:

$$\begin{aligned} t_{ij} &= \sin(\beta)K(\beta_M, E_0) \int_0^{2\pi} |\cos(\theta_M)| \int_{\rho_1(\varphi)}^{\rho_2(\varphi)} \frac{1}{\rho} d\rho d\varphi \\ &= \sin(\beta)K(\beta_M, E_0) \int_0^{2\pi} |\cos(\theta_M)| (\ln(\rho_2(\varphi)) - \ln(\rho_1(\varphi))) d\varphi. \end{aligned} \quad (7.20)$$

Let us suppose that for the event  $e_i$  and the associated cone,  $N_r^i$  generatrices were selected. The  $k^{\text{th}}$  generatrix intersects the grid of voxels at points  $M_{k,h}$ ,  $h = 1, N_h^{i,k}$ ,  $N_h^{i,k} - 2$  being the number of times the  $k^{\text{th}}$  generatrix of the  $i^{\text{th}}$  cone passes from one voxel to the other. Each generatrix corresponds to points whose coordinates verify the equation (7.17) for some given value  $\varphi = \varphi_k$ . For a given value of  $\varphi_k$ ,  $\theta_M$  is the polar angle of the considered generatrix in the coordinate system  $\mathcal{R}(V_1xyz)$ , thus it will be denoted  $\theta_k$ .

The second step in the numerical evaluation of (7.20) is to choose a quadrature rule for the integration on  $\varphi$  and to evaluate the integrand at each sampling point. We choose the trapezoidal rule for a non uniform grid. This rule states that for a function  $f$  we have:

$$\int_a^b f(x)dx \simeq \frac{1}{2} \sum_{k=1}^{N-1} (x_{k+1} - x_k)(f(x_{k+1}) + f(x_k)), \quad (7.21)$$

that can also be written as:

$$\int_a^b f(x)dx \simeq \frac{1}{2} \sum_{k=1}^{N-1} (x_{k+1} - x_k)f(x_{k+1}) + \frac{1}{2} \sum_{k=1}^{N-1} (x_{k+1} - x_k)f(x_k). \quad (7.22)$$

Changing the index of the first summation in equation (7.22) gives:

$$\begin{aligned}
 \int_a^b f(x)dx &\simeq \frac{1}{2} \sum_{k=2}^N (x_k - x_{k-1})f(x_k) + \frac{1}{2} \sum_{k=1}^{N-1} (x_{k+1} - x_k)f(x_k) \\
 &= \frac{(x_2 - x_1)}{2}f(x_1) + \frac{1}{2} \sum_{k=2}^{N-1} (x_k - x_{k-1})f(x_k) \\
 &\quad + \frac{1}{2} \sum_{k=2}^{N-1} (x_{k+1} - x_k)f(x_k) + \frac{(x_N - x_{N-1})}{2}f(x_N) \\
 &= \frac{(x_2 - x_1)}{2}f(x_1) + \frac{1}{2} \sum_{k=2}^{N-1} (x_{k+1} - x_{k-1})f(x_k) + \frac{(x_N - x_{N-1})}{2}f(x_N). \quad (7.23)
 \end{aligned}$$

Let us put  $x_0 = x_1$  and  $x_{N+1} = x_N$ . Then we finally write:

$$\int_a^b f(x)dx \simeq \frac{1}{2} \sum_{k=1}^N (x_{k+1} - x_{k-1})f(x_k). \quad (7.24)$$

Let us denote:

$$\Delta\varphi_k = \varphi_{k+1} - \varphi_{k-1}. \quad (7.25)$$

In the case of an equal distribution of the generatrices,  $\Delta\varphi$  would be a constant equal to  $\frac{2\pi}{N_r^i}$ . As already mentioned, we propose to distribute the rays irregularly with respect to  $\phi$ . The quadrature rule applied to (7.20), gives the following estimation of  $t_{ij}$ :

$$\hat{t}_{ij} = \sin(\beta)K(\beta, E_0) \frac{1}{2} \sum_{k=1}^{N_r^i} \Delta\varphi_k |\cos(\theta_k)| \ln \left( \frac{\rho_2(\varphi_k)}{\rho_1(\varphi_k)} \right). \quad (7.26)$$

In this expression, we can replace  $\rho_2(\varphi_k)$  by

$$\rho_2(\varphi_k) = \rho_1(\varphi_k) + \rho_2(\varphi_k) - \rho_1(\varphi_k). \quad (7.27)$$

Then the equation (7.26) becomes:

$$\hat{t}_{ij} = \sin(\beta)K(\beta, E_0) \frac{1}{2} \sum_{k=1}^{N_r^i} \Delta\varphi_k |\cos(\theta_k)| \ln \left( 1 + \frac{\rho_2(\varphi_k) - \rho_1(\varphi_k)}{\rho_1(\varphi_k)} \right) \quad (7.28)$$

One can note that  $\rho_2(\varphi_k) - \rho_1(\varphi_k) \ll \rho_1(\varphi_k)$ . So, we can use the Mercator series at the first order to simplify the natural logarithm term, leading to the following equation:

$$\hat{t}_{ij} = \sin(\beta)K(\beta, E_0) \frac{1}{2} \sum_{k=1}^{N_r^i} \Delta\varphi_k |\cos(\theta_k)| \frac{\rho_2(\varphi_k) - \rho_1(\varphi_k)}{\rho_1(\varphi_k)}. \quad (7.29)$$

As the variables  $t_{ij}$  and  $t_{ik}$  appear in the LM-MLEM equation (4.24) on the numerator and denominator respectively, the factor  $\frac{1}{2}\sin(\beta)$  can be simplified. By ignoring it, the

expression (7.29) finally becomes:

$$\hat{t}_{ij} = \sum_{k=1}^{N_r^i} (\varphi_{k+1} - \varphi_{k-1}) |\cos(\theta_k)| \frac{\rho_2(\varphi_k) - \rho_1(\varphi_k)}{\rho_1(\varphi_k)}. \quad (7.30)$$

The estimated probability for a photon emitted by the voxel  $v_j$  to be detected as event  $e_i$  is calculated by summing the length of the generatrices of the  $i^{\text{th}}$  cone crossing the considered voxel, multiplied by the inclination angle of the considered generatrix and weightened by the inverse of the distance from the apex to the voxel and the variation of the azimuthal angle between the previous and the following generatrices. The length of the generatrices are given by a ray-tracing algorithm [Siddon (1985), Zhao and Reader (2003)].

We also studied several variants of the model replacing the factor  $\frac{1}{\rho^2}$  by  $\frac{1}{\rho}$  and by 1. This leads to the following  $t_{ij}$  estimation formulas, respectively:

$$\hat{t}_{ij} = \sum_{k=1}^{N_r^i} (\varphi_{k+1} - \varphi_{k-1}) |\cos(\theta_k)| (\rho_2(\varphi_k) - \rho_1(\varphi_k)) \quad (7.31)$$

and

$$\hat{t}_{ij} = \sum_{k=1}^{N_r^i} (\varphi_{k+1} - \varphi_{k-1}) |\cos(\theta_k)| (\rho_2^2(\varphi_k) - \rho_1^2(\varphi_k)). \quad (7.32)$$

### 7.2.2 A model that accounts for uncertainties on the energy measurements

In the previous method, we considered that the detectors have ideal energetic resolutions. In practice, this is not the case, which leads to uncertainties on the energy measurements. These uncertainties depend on the inherent features of the scatterer and the absorber, but also on the energy of the incident photon. Since we calculate the scattering angle  $\beta$  directly from the measured energies with the equation (3.2), uncertainties on the energies lead to uncertainties on  $\beta$ . As a consequence, this limits the accuracy with which we can determine the position of emission of the  $\gamma$  particle. The real position of the photon origin is in a volume around the Compton cone of half opening angle  $\beta$ , i.e. inside a conical shell. Consequently, the intersection between a voxel and the thick cone will not be a surface anymore as in the previous method. It will be a volume as shown in figure 7.6.

In the method proposed in this section, the thick Compton cone will be first discretized into conical surfaces to recover the same pattern as in the previous section. Then, we will apply the decomposition of each conical surfaces into generatrices in order to evaluate the  $t_{ij}$  elements.

The elements of the system matrix are evaluated from (7.13) with the kernel  $h$  given by the equation (7.5). We calculate  $\beta$  with the Compton equation (3.2) as usually. Let

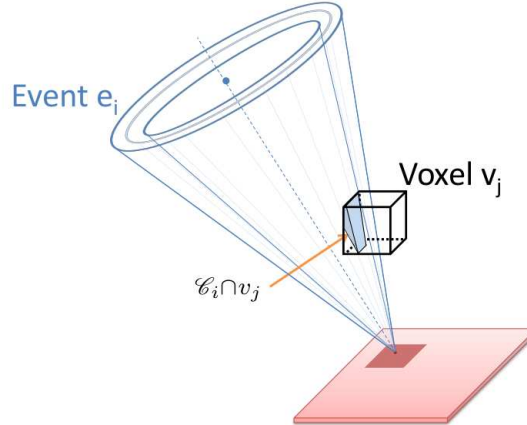


Figure 7.6: Illustration of the integration domain  $\mathcal{C}_i \cap v_j$  when accounting for the energy measurement uncertainties. The thickness of the cone leads to an intersection  $\mathcal{C}_i \cap v_j$  of volumic nature.

$\beta_M$  be the angular distance from some point  $M$  to the cone axis. A Gaussian distribution denoted  $g$  is taken as function of  $\beta_M$ . Then, the true scattering angle  $\beta_M$  will be bound to the interval  $\beta \pm p\sigma_\beta$ , with  $p$  some given integer. The spatial kernel  $h(\beta_M|\beta, \sigma_\beta)$  is replaced by:

$$\begin{cases} g(\beta_M) = \frac{1}{\sqrt{2\pi}\sigma_\beta} e^{-\frac{1}{2}\left(\frac{\beta_M-\beta}{\sigma_\beta}\right)^2} & \text{if } \beta_M \in [\beta - p\sigma_\beta, \beta + p\sigma_\beta] \\ g(\beta_M) = 0 & \text{otherwise} \end{cases} \quad (7.33)$$

The parameter  $p$  enables to choose the coverage of values of the gaussian distribution. For instance, with  $p = 1$ ,  $p = 2$  and  $p = 3$ , we cover 68.2%, 95.4% and 99.6% of values, respectively. This function conveys the idea that the greater the angular distance  $\beta_M$  is, the lower the probability that the photon came from  $M$ . However, only voxels intersected by the thick cone of equation

$$\begin{cases} x' = \rho \sin(\beta_M) \cos(\varphi) \\ y' = \rho \sin(\beta_M) \sin(\varphi) & \rho \geq 0, \quad \varphi \in [0, 2\pi), \quad |\beta_M - \beta| \leq p\sigma_\beta \\ z' = \rho \cos(\beta_M) \end{cases} \quad (7.34)$$

will be considered

Replacing (7.33) in the general model (7.13), we get:

$$t_{ij} = \int_{M \in \mathcal{C}_i \cap v_j} K(\beta_M, E_0) \frac{|\cos(\theta_M)|}{\rho^2} g(\beta_M) dv \quad (7.35)$$

We express now the element of volume  $dv$  from (7.34). In spherical coordinates we

have:

$$dv = \rho^2 \sin(\beta_M) d\rho d\varphi d\beta \quad (7.36)$$

Replacing (7.33) and (7.36) in (7.35), we get:

$$\begin{aligned} t_{ij} &= \int_{\beta-p\sigma_\beta}^{\beta+p\sigma_\beta} \int_0^{2\pi} \int_0^\infty K(\beta_M, E_0) |\cos(\theta_M)| \sin(\beta) \\ &\quad \times \frac{1}{\sqrt{2\pi}\sigma_\beta} e^{-\frac{1}{2}\left(\frac{\beta_M-\beta}{\sigma_\beta}\right)^2} \chi_{v_j}(M) d\rho d\varphi d\beta \end{aligned} \quad (7.37)$$

In this method, the thickness of the cone prevents from a direct use of the discretization in a set of generatrices. Hence, in order to recover the same pattern, we first discretize the volume with respect to the half-opening angle into conical surfaces. For some given values of  $\beta$  and  $\varphi$ , the set of points verifying the equation (7.34) is a half-line originated from  $V_1$ , thus is the generatrix of the conical surface of half-opening angle  $\beta$  and azimuthal angle  $\varphi$ . Denoting now  $\rho_1(\beta, \varphi)$  and  $\rho_2(\beta, \varphi)$  the lower and upper values of  $\rho$  such that  $M(\rho, \beta, \varphi)$  still belongs to the voxel  $v_j$ , we obtain:

$$\begin{aligned} t_{ij} &= \int_{\beta-p\sigma_\beta}^{\beta+p\sigma_\beta} \int_0^{2\pi} K(\beta_M, E_0) |\cos(\theta_M)| \sin(\beta_M) \\ &\quad \times \frac{1}{\sqrt{2\pi}\sigma_\beta} e^{-\frac{1}{2}\left(\frac{\beta_M-\beta}{\sigma_\beta}\right)^2} \int_{\rho_1(\beta_M, \varphi)}^{\rho_2(\beta_M, \varphi)} d\rho d\varphi d\beta \\ &= \int_{\beta-p\sigma_\beta}^{\beta+p\sigma_\beta} \int_0^{2\pi} K(\beta_M, E_0) |\cos(\theta_M)| \sin(\beta_M) \\ &\quad \times \frac{1}{\sqrt{2\pi}\sigma_\beta} e^{-\frac{1}{2}\left(\frac{\beta_M-\beta}{\sigma_\beta}\right)^2} (\rho_2(\beta_M, \varphi) - \rho_1(\beta_M, \varphi)) d\varphi d\beta \end{aligned} \quad (7.38)$$

In order to discretize the thick cone, the interval  $[\beta - p\sigma_\beta, \beta + p\sigma_\beta]$  is divided into  $2N_s + 1$  samples. The conical surfaces are indexed by  $n = \overline{-N_s, N_s}$ . The parameter  $N_s$  has to be sufficiently large to provide a fine coverage of the volume of the cone. For simplicity, we have chosen an equal sampling of the interval. Then, the half-opening angle of the  $n^{\text{th}}$  conical surface is given by:

$$\beta_n = \beta + n \frac{p}{N_s} \sigma_\beta \quad (7.39)$$

Let us suppose that for the event  $e_i$  and the associated thick cone, for the sampling of the  $n^{\text{th}}$  conical surface,  $N_r^{i,n}$  generatrices were selected. The azimuthal angle of the  $k^{\text{th}}$  generatrix of the  $n^{\text{th}}$  conical surface is denoted  $\varphi_{n,k}$ . This generatrix intersects the grid of voxels at points  $M_{n,k,h}$ ,  $h = \overline{1, N_h^{i,n,k}}$ ,  $N_h^{i,n,k} - 2$  being the number of times the  $k^{\text{th}}$  generatrix of the  $n^{\text{th}}$  conical surface of the  $i^{\text{th}}$  cone passes from one voxel to the other. For the numerical evaluation of the integral in (7.38), we use the trapezoidal rule for the

integration on  $\beta$  and  $\varphi$ . We denote now:

$$\Delta\beta_n = \beta_{n+1} - \beta_{n-1} = \frac{2p}{N_s}\sigma_\beta \quad (7.40)$$

and:

$$\Delta\varphi_{n,k} = \varphi_{n,k+1} - \varphi_{n,k-1} \quad (7.41)$$

Then, the equation (7.38) becomes:

$$\begin{aligned} \hat{t}_{ij} &= \frac{1}{\sqrt{2\pi}\sigma_\beta} \frac{\Delta\beta_n}{2} \sum_{n=-N_s}^{N_s} K(\beta_n, E_0) \sin(\beta_n) e^{-\frac{1}{2}(\frac{pn}{N_s})^2} \\ &\quad \int_0^{2\pi} |\cos(\theta_M)| (\rho_2(\beta_n, \varphi) - \rho_1(\beta_n, \varphi)) d\varphi \\ &= \frac{1}{\sqrt{2\pi}\sigma_\beta} \frac{\Delta\beta_n}{2} \sum_{n=-N_s}^{N_s} K(\beta_n, E_0) \sin(\beta_n) e^{-\frac{1}{2}(\frac{pn}{N_s})^2} \\ &\quad \sum_{k=1}^{N_r^{i,n}} \frac{\Delta\varphi_{n,k}}{2} |\cos(\theta_{n,k})| (\rho_2(\beta_n, \varphi_{n,k}) - \rho_1(\beta_n, \varphi_{n,k})) \end{aligned} \quad (7.42)$$

Replacing (7.40) and (7.41) in the expression (7.42) we obtain:

$$\begin{aligned} \hat{t}_{ij} &= \frac{p}{2\sqrt{2\pi}N_s} \sum_{n=-N_s}^{N_s} K(\beta_n, E_0) \sin(\beta_n) e^{-\frac{1}{2}(\frac{pn}{N_s})^2} \\ &\quad \sum_{k=1}^{N_r^{i,n}} (\varphi_{n,k+1} - \varphi_{n,k-1}) |\cos(\theta_{n,k})| (\rho_2(\beta_n, \varphi_{n,k}) - \rho_1(\beta_n, \varphi_{n,k})) \end{aligned} \quad (7.43)$$

We can once again simplify coefficients depending only on the event, since in the LM-MLEM equation (4.24) the expressions  $t_{ij}$  and  $t_{ik}$  appear on the numerator and denominator respectively. The expression (7.43) finally becomes:

$$\begin{aligned} \hat{t}_{ij} &= \sum_{n=-N_s}^{N_s} K(\beta_n, E_0) \sin(\beta_n) e^{-\frac{1}{2}(\frac{pn}{N_s})^2} \\ &\quad \sum_{k=1}^{N_r^{i,n}} (\varphi_{n,k+1} - \varphi_{n,k-1}) |\cos(\theta_{n,k})| (\rho_2(\beta_n, \varphi_{n,k}) - \rho_1(\beta_n, \varphi_{n,k})) \end{aligned} \quad (7.44)$$

When the energy measurement uncertainties are taken into account, the estimated probability  $\hat{t}_{ij}$  is calculated as follows. First, for each value of  $\beta_n$ , we sum up the lengths of the segments of the generatrices of the  $n^{\text{th}}$  conical surface of the  $i^{\text{th}}$  cone that are included in the voxel  $v_j$ , we multiply by the inclination angle of the considered generatrix and weighted by the variation of the azimuthal angle between the previous and the following generatrices. We then multiply the resulting value of the summation by an expression that represents the decrease of probability following the angular distance from the cone axis. We multiply by the Klein-Nishina coefficient, and by the value of the sinus of the

half-opening angle. We finally sum up over the conical surfaces to obtain  $\hat{t}_{ij}$ . As in the previous method, the length of the generatrices will be given by a ray-tracing algorithm.

### 7.3 Simplified method: $t_{ij}$ estimation using voxel centers

In the previously described methods, for some given event  $e_i$ , the voxels  $v_j$  intersected by some generatrices are identified as giving  $t_{ij} \neq 0$ . The other voxels are not considered by the method since implicitly the value of  $t_{ij}$  is equal to 0 for them. In this section, we present an algorithm where all the voxels of the volume are visited and their angular distance to the Compton cone is evaluated. If this distance is smaller than some threshold, a strictly positive value is given to  $t_{ij}$ . This algorithm inspired from [Zoglauer (2005)] has the advantage to be simple to implement and allows to calculate each value  $t_{ij}$  within a very small number of operations.

#### Method

The main idea is to simplify the computation of the integral in equation (7.13) by estimating it on the base of a single value. We calculate the integral by considering that the emitting point  $M$  is the center of the voxel. We denote by  $\beta_{O_j}$  the angular distance of the center  $O_j$  of the voxel  $v_j$  to the cone (see figure 7.7). We use the same model of

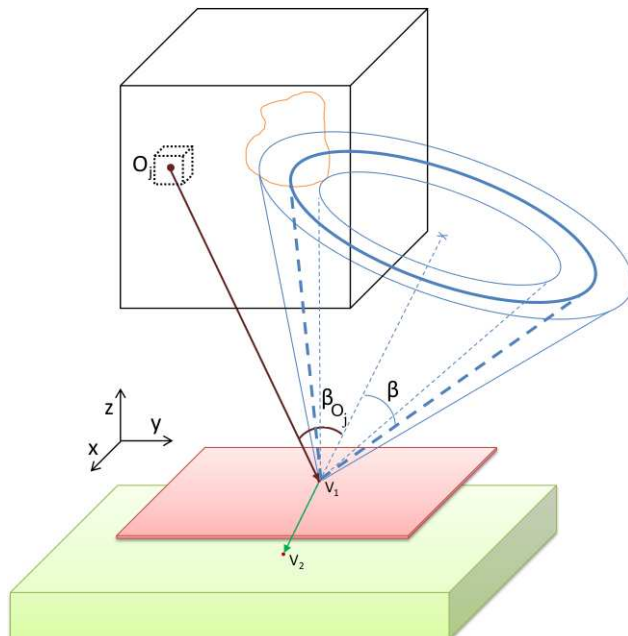


Figure 7.7: CV model

uncertainties as in the previous section. Hence, the spatial kernel  $h$  will be a truncated

Gaussian distribution of mean  $\beta$  and standard deviation  $\sigma_\beta$ . We consider then:

$$\int_{M \in v_j} K(\beta_M, E_0) \frac{|\cos(\theta_M)|}{\|\overrightarrow{V_1 M}\|_2^2} h(\beta_M | \beta, \sigma_\beta) dv \approx K(\beta_{O_j}, E_0) \frac{|\cos(\theta_{O_j})|}{\|\overrightarrow{V_1 O_j}\|_2^2} h(\beta_{O_j} | \beta, \sigma_\beta) vol(v_j), \quad (7.45)$$

where  $vol(v_j)$  represents the volume of the voxel  $v_j$ . Since the voxels have all the same volume, the term  $vol(v_j)$  is a constant coefficient that appears both on the numerator and denominator in the equation (4.24), and can be simplified.

We apply a threshold in order to avoid useless calculations. When the voxel is too far from the cone, i.e. when  $|\beta_{O_j} - \beta| > p\sigma_\beta$ , the value  $t_{ij}$  is forced to 0. In this threshold,  $p$  is an integer playing the same role as in the previous method. We can choose the coverage of the values of the gaussian distribution by choosing the value of this integer: with  $p = 1$ ,  $p = 2$  and  $p = 3$ , we cover 68.2%, 95.4% and 99.6% of values. When we have  $|\beta_{O_j} - \beta| < p\sigma_\beta$ , we are close to the Compton cone, and  $t_{ij} \neq 0$ .

After simplification of the factors depending only on the event, the estimation of the system matrix elements  $\hat{t}_{ij}$  is:

$$\hat{t}_{ij} = \begin{cases} K(\beta, E_0) \frac{|\cos(\theta_{O_j})|}{\|\overrightarrow{V_1 O_j}\|_2^2} \frac{1}{\sqrt{2\pi}\sigma_\beta} e^{-\frac{1}{2}\left(\frac{\beta_{O_j}-\beta}{\sigma_\beta}\right)^2} & \text{if } |\beta_{O_j} - \beta| < p\sigma_\beta \\ 0 & \text{otherwise} \end{cases} \quad (7.46)$$

However, we might have the case when  $\sigma_\beta$  is too low, which may lead to  $t_{ij} = 0$  for all  $v_j$ . In order to avoid this situation, we force a minimal value for  $\sigma_\beta$ . The condition  $|\beta_{O_j} - \beta| < p\sigma_\beta$  is satisfied when the solid angle subtended by the voxel  $v_j$  at the element of scatterer containing  $V_1$  is inferior to  $\sigma_\beta$ . In order to have a homogeneous condition, we choose a threshold that uses the side length of a voxel denoted  $d$ :

$$p\sigma_\beta \geqslant \frac{2d}{\|\overrightarrow{V_1 O_j}\|_2} \quad (7.47)$$

When  $p\sigma_\beta < \frac{2d}{\|\overrightarrow{V_1 O_j}\|_2}$ , we put  $p\sigma_\beta = \frac{2d}{\|\overrightarrow{V_1 O_j}\|_2}$ , and calculate  $\hat{t}_{ij}$  from equation (7.46).



# Chapter 8

---

## Selection of the generatrices

---

The originality of the methods we propose lies in the model but also in the selection of the generatrices. Indeed, we have chosen an event specific sampling of the cone with non-equispaced rays, in order to obtain a better evaluation of the elements of the system matrix. To understand the reason that had led us to this sampling, let us focus on a Compton cone with an important inclination angle. For instance, let us take the case where the angle of inclination of the axis  $\theta_g$  and the Compton angle  $\beta$  verify  $\theta_g + \beta > \frac{\pi}{2}$ . This situation might occur especially when absorber detectors surround the scatterer as in [Zoglauer (2005), Frandes *et al.* (2010)]. The intersection of the cone with a horizontal plane will be described by a hyperbola. With a regular sampling of the angular parameter of the cone, a very low number of generatrices will be intersecting the volume  $\mathcal{V}$ . It will lead to a poor estimation of the system matrix  $T$ . In cases less extreme, sometimes the regular sampling of the conical surface is also not adapted in order to sample the source.

### 8.1 The guiding surface

The algorithm proposed here enables to obtain a set of generatrices that naturally corresponds to the intersections of the rays with the volume. In order to both avoid searching for all the curves of intersection of the cone with the faces of the volume and manage the double intersections of the generatrices with the volume, we define a guiding surface. The idea is to take a mesh on the face of the volume opposed to the detectors, and to determine the intersection points of the cone with it. When we associate an intersection point with the apex, we construct a generatrix of the cone. Let us denote the volume  $\mathcal{V}$  as the parallelepiped  $ABCDEFGH$ . Actually, in most cases we used a cubic volume. Each

line segment defined as the intersection of a generatrix of the cone with the volume  $\mathcal{V}$  is included in the hyperpyramid defined by its base  $ABCDEFGH$  and the apex  $V_1$  (the cone apex) as shown in figure (8.1).

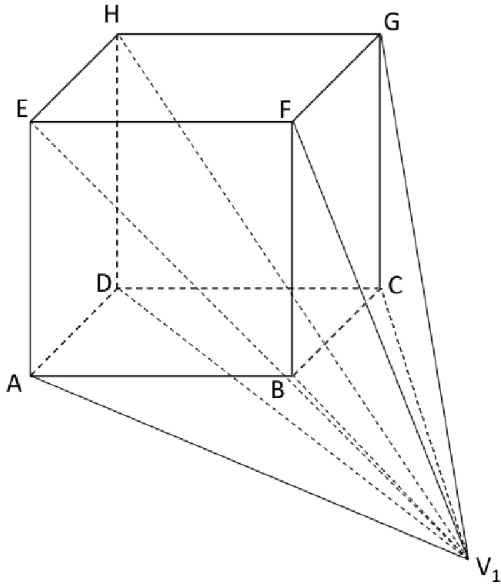


Figure 8.1: Illustration of the hyperpyramid defined by its base  $ABCDEFGH$  and the apex of the cone  $V_1$ . Each line segment defined as the intersection of a generatrix of the cone with the volume  $\mathcal{V}$  is included in this hyperpyramid.

The extensions of the edges  $[V_1A]$ ,  $[V_1B]$ ,  $[V_1C]$  and  $[V_1D]$  intersect the side  $EFGH$  at  $A'$ ,  $B'$ ,  $C'$  and  $D'$  respectively. We call guiding surface the minimum rectangular surface that covers both  $EFGH$  and  $A'B'C'D'$ . In figure (8.2), this surface is noted  $LFRD'$ .

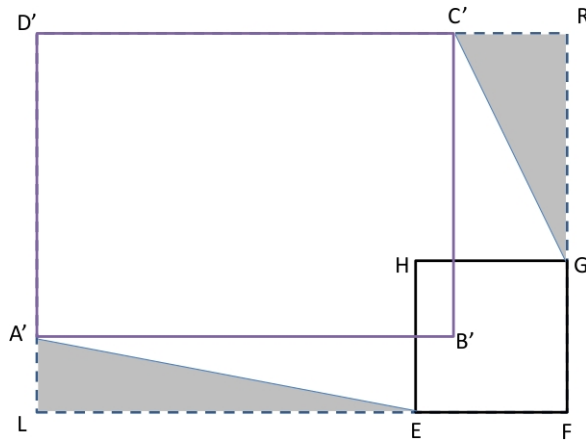


Figure 8.2: Illustration of the guiding surface defined by the minimum rectangular surface that covers both  $EFGH$  and  $A'B'C'D'$ .

A mesh that covers the guiding surface is defined, with the pixel side length approaching the one from the voxels of  $\mathcal{V}$ . A better sampling can be sometime necessary. It is possible to adjust the size of the pixel in order to obtain an oversampling of the conical surface.

Note that the dark regions in figure (8.2) represent part of the mesh where the intersection points that might be found will lead to the construction of generatrices that do not intersect the volume.

## 8.2 Conic section tracking: initialization

The next step consists in determining the intersection points of the Compton cone with the grid of the guiding surface. Our method is adapted from [Wilderman *et al.* (1998)] and can be described as a conic section tracking. Assuming the mesh is located at  $z = z_g$ , the conic section describing the intersection of the cone and the plane  $z = z_g$  is given by the equation:

$$[w_x(x - x_1) + w_y(y - y_1) + w_z(z_g - z_1)] = \cos(\beta) \sqrt{(x - x_1)^2 + (y - y_1)^2 + (z_g - z_1)^2} \quad (8.1)$$

where the  $(w_x, w_y, w_z)$  is a unit vector directing the axis  $\overrightarrow{V_2 V_1}$  of the cone and  $(x_1, y_1, z_1)$  are the coordinates of  $V_1$ .

Before starting to search for the intersection points, we must identify the nature of the intersection of the conic with the guiding surface. Three cases are possible as shown in figure 8.3: i) the conic section is completely inside the guiding surface, ii) the conic section is completely outside the guiding surface, iii) we are in the intermediate case where conic section arcs are inside the guiding surface. In order to identify the scenario, we first solve

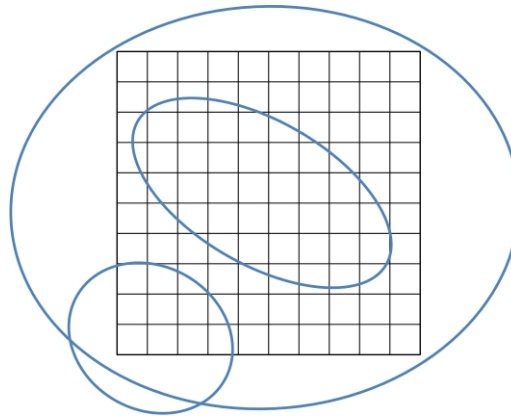


Figure 8.3: Illustration of the three possible scenarios of conic section intersecting the guiding surface. The conic section can either be inside the surface or partially included in the surface or outside of the surface.

the equation of the conic section (8.1). Let  $(x_{min}, y_{min}, z_g)$  and  $(x_{max}, y_{max}, z_g)$  be two opposite corners of the guiding surface. For instance, on figure 8.2 we have  $L(x_{min}, y_{min}, z_g)$  and  $R(x_{max}, y_{max}, z_g)$ . The edges of the mesh will be described by those coordinates. We search for a solution to the equation (8.1) giving the fact that we are located on an edge of the guiding surface. Consequently, we have to solve four different equations. For each of them, we have a given coordinate, the one that identifies the edge. For instance, if we are

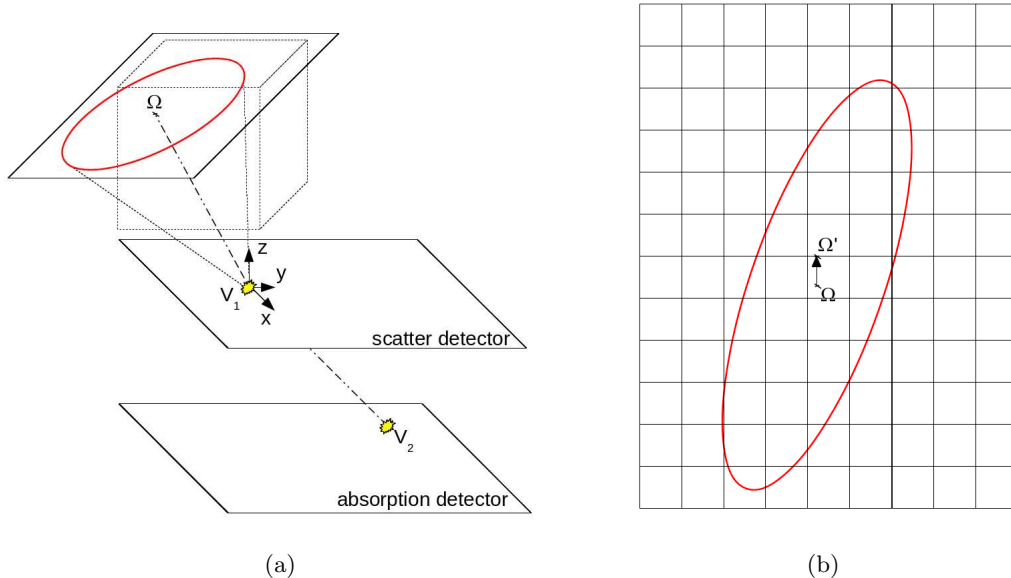


Figure 8.4: Illustration of the internal conic section case. (a)  $\Omega$  is the intersection point between the cone axis and the guiding surface. (b)  $\Omega'$  corresponds to the point  $\Omega$  constrained to be on a horizontal edge.

located on the edge  $D'L$  cf. figure 8.2, we have  $x = x_{min}$ . Replacing the known coordinate in the equation (8.1), we solve it simply as a second order equation. We then verify that the found solutions are on the side of the mesh.

After the four steps, if no intersection points is found, we are either in the internal conic section case, or in the external one. When the conic section is not inside the mesh, there are no generatrices that intersect the volume. If the conic section is inside, we need to determine a starting point for the tracking. Let  $\Omega$  be the intersection of the axis of the cone with the guiding surface. In most cases, this point won't be on an edge. Let  $\Omega'$  be the projection of  $\Omega$  on a horizontal edge bounding the pixel containing  $\Omega$  (see figure 8.4). We now can solve the equation (8.1) with as given coordinate  $y = y'_\Omega$ . If the solutions are not inside the guiding surface, we can conclude that the conic section is outside the mesh. Hence this event is not useful since the cone does not intersect the volume. Otherwise, out of the two found solutions, we choose arbitrarily one which will be the starting point of the tracking.

In the end of this initialization part, for the case of the internal conic section we obtain a single point being the starting location of our tracking algorithm. For the intermediate case where we need to track arcs of conic section, we obtain a set of points corresponding to the extremities of the arcs. These points are located on the edges of the guiding surface and they are ordered since we have to compute the variation of azimuth angle between the generatrices. Indeed, in order to avoid abnormal gaps, or undesired change in the direction of variation, we are being cautious that the arcs of the conic section are always traveled in the same direction. An algorithm in pseudo code selecting the right scenario and and

providing the points of the conic section, is presented in algorithm 1.

---

**Algorithm 1** conic section tracking algorithm in pseudo-code.

---

*Input:* Object-volume, Compton cone.

```
Define the mesh      % from the object-volume and the apex of the cone we define
                    % the hyperpyramid, then the mesh
Solve equation (8.1) with  $x = x_{min}$ , then with  $x = x_{max}$ 
Solve equation (8.1) with  $y = y_{min}$ , then with  $y = y_{max}$ 
if Solutions are in admissible range then
    Record solutions in Edge_points
end if
if Edge_points is empty then
    Find the intersection point  $\Omega(x_\Omega, y_\Omega, z_g)$  between the cone axis and the guiding
    surface.
    Solve equation (8.1) with  $x = x_\Omega$ 
    if Solutions are outside the range  $[y_{min}, y_{max}]$  then
        Compton cone considered as noise
    else
        Record solutions in Edge_points
    end if
end if

for each point in Edge_points do
    if !(point is already treated) then
        Launch Step-by-Step algorithm
    end if
end for
```

*Output:* Vector of points of the conic section  
% intersection points of the mesh and the Compton cone

---

### 8.3 Conic section tracking

In order to track the conic section, we now use a step-by-step algorithm that enables to follow the curve. From a selected starting location, that necessary is on an edge, we search for the next intersection of the conic section with the mesh. Focusing on the pixel containing our starting location and the arc of conic section, in order to find out which of the neighbouring edges is crossed by the conic section, we try to solve (8.1) given that one coordinate corresponds to the tested edge of the pixel. When solutions are found, a step of control is applied in order to get the correct solution. Since we solve a second order equation, three cases are possible: no solutions, then the conic section is not crossing the tested edge; a single solution, then the conic section crosses the edge once; two solutions, then the conic section is crossing the edge twice. In the last case, we have to select a solution out of two. To do so we used these criteria: the solution must be in the range of

the guiding surface, the solution must be on one edge of the considered pixel; the solution must be different from the starting location and be the closest intersecting point from the starting location. After verifying all this conditions, the validated solution is used to calculate the azimuth angle  $\varphi_k$  of the generatrix in the coordinate system of the cone, and the inclination angle  $\theta_k$  in the initial coordinate system  $Oxyz$ .

The intersection point is then recorded and will be used as the new starting location for finding the next intersection point. Step by step, we track the branch of conic section across the mesh and record all the intersection points as shown in figure 8.5. The ending criterion for this method depends on the conic section scenario we are dealing with. In the case of the internal conic section, the algorithm is repeating itself until it finds back the initial starting location determined during the initialization. In the scenario with arcs of conic section, the algorithm repeats its actions until it finds an extremity of an arc. Then, it starts again with a new arc of conic section until all extremities found in the initialization step are treated.

We can summarize the main actions of the algorithm in pseudo-code as presented in algorithm 2

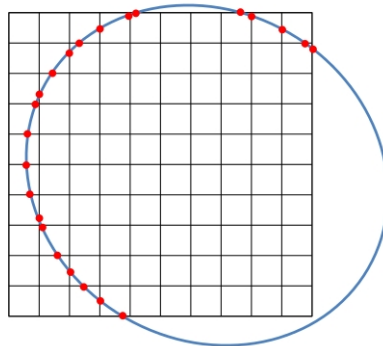


Figure 8.5: Illustration of a tracked conic section. The dots represent the intersection points between the mesh and the conic section.

## 8.4 Conic section tracking: discussion

The way the mesh and the intersection points are defined, lead us to the novel construction of generatrices sampling the Compton cone. This work is part of our contribution in the development of reconstruction methods for Compton imaging. However, as for the conic section tracking algorithm itself, it is quite standard. We implemented this method in order to carry on our work on the iterative reconstruction. Thus, the tracking can be improved in different ways.

We could improve the search for intersection points. We perform the tests on the neighbouring edges in an arbitrarily order. We could use the direction of the conic section

---

**Algorithm 2** Step-by-Step algorithm in pseudo-code.

---

*Input:* starting location point

```

if !(starting location point is already treated) then
    Compute_Record(starting location point)
    while (starting location point != point in Edge_points) do      % Edge_points contains starting/ending points
        Test for intersection point on the opposite edge of the considered pixel
        if !(Solutions is null) then
            Select_Verify(solutions)
            Compute_Record(selected_solution)
            continue
        else
            Test for intersection point on the upper adjacent edge of the considered pixel
            if !(Solutions is null) then
                Select_Verify(solutions)
                Compute_Record(selected_solution)
                continue
            else
                Test for intersection point on the bottom adjacent edge of the considered
                pixel
                if !(Solutions is null) then
                    Select_Verify(solutions)
                    Compute_Record(selected_solution)
                    continue
                else
                    Test for intersection point on the same edge of the considered pixel
                    if !(Solutions is null) then
                        Select_Verify(solutions)
                        Compute_Record(selected_solution)
                        continue
                    end if
                end if
            end if
        end if
        Update starting location point
    end while
end if
```

*Output:* intersection points (of a branch) of the conic section with the mesh

---

as a prior information in order to guide the tests. This would avoid a large quantity of operations, knowing that in the worst case we perform four tests by pixel. Hence it will enable to perform a quicker conic section tracking.

A second improvement may be achieved, especially in the case of the internal conic

section. When we solve the equation (8.1), most of the time we have two solutions. One solution corresponds to the point we are looking for, however, the second solution might be a valid intersection point of the conic section with the mesh. We have constrained the validation method in order to keep only the solution that fits the conditions "be in the treated pixel" and "be the closest solution to the starting location". For instance, let us consider that for a test performed in the pixel  $P_1$ , we find the solution  $S_1$  in  $P_1$  and the solution  $S_2$  in the pixel  $P_2$ . Consequently, even if the second solution  $S_2$  seems correct with regards to the conic section and the mesh, it is located in  $P_2$ , another pixel than  $P_1$ , thus the conditions are not met.  $S_2$  is not kept in favour of  $S_1$ . When the step-by-step method will treat  $P_2$ , it will find  $S_1$  and  $S_2$  again, but will keep  $S_2$  this time. The idea would be to introduce in the algorithm, a method that can manage the second solution in order to avoid a redundant operation. In the case of the internal conic section, the benefit would be important since half of the operations would be avoided.

# Chapter 9

---

## Results

---

The data used in this section are obtained by Monte Carlo simulations performed with MEGAlib. This suite of software was already presented in section 6.1.

One main limitation of the hadrontherapy application is the low number of prompt- $\gamma$  photons that can be acquired. Thus, in order to experience our iterative methods, we chose to restrict the number of events used to reconstruct the images. The number of iterations achieved by the LM-MLEM algorithm is arbitrarily defined by the user. No specific criterion has been implemented, consequently the choice in the number of iterations is not optimal. Nevertheless, we performed enough iterations so that the last state of the reconstructed image is almost identical to the previous one at the end of the iterative process.

### 9.1 Reconstruction of a spherical source

In order to keep a clear presentation of the results we call *Surface of Intersection* (SI), *Volume of Intersection* (VI) and *Center of Voxel* (CV), the three different methods presented in section 7.2.1, 7.2.2 and 7.3, respectively. We recall that the SI method does not take into account the uncertainties of energy measurements whereas the VI and CV methods do. We used the same simulated data in chapter 5 section 6.1.2. Let us recall that the source is a sphere of radius 0.5 cm, centered at (1, 1, 1) cm and emitting  $\gamma$  particles of 1.275 Mev. We first chose the acquisition achieved by the small Compton camera. The reconstructed volume is a cube of  $10 \times 10 \times 10$  cm<sup>3</sup> composed of  $100 \times 100 \times 100$  voxels. Then, the voxels are of 1 mm side length. The Gaussian distributions in the methods VI and CV cover 68.2% of values, i.e. we chose to use the value 1 for the parameter  $p$  from sections 7.2.2 and 7.3.

### 9.1.1 Single event back-projections

Figure 9.1 shows, for each method, the back-projection of a single event. We can note that the contours are roughly the same for all methods. Nevertheless, comparing the methods CV and VI, both accounting for the energy measurement uncertainties, we can observe that the conical-shaped volume is wider for CV. This is due to the threshold values used in the CV method.

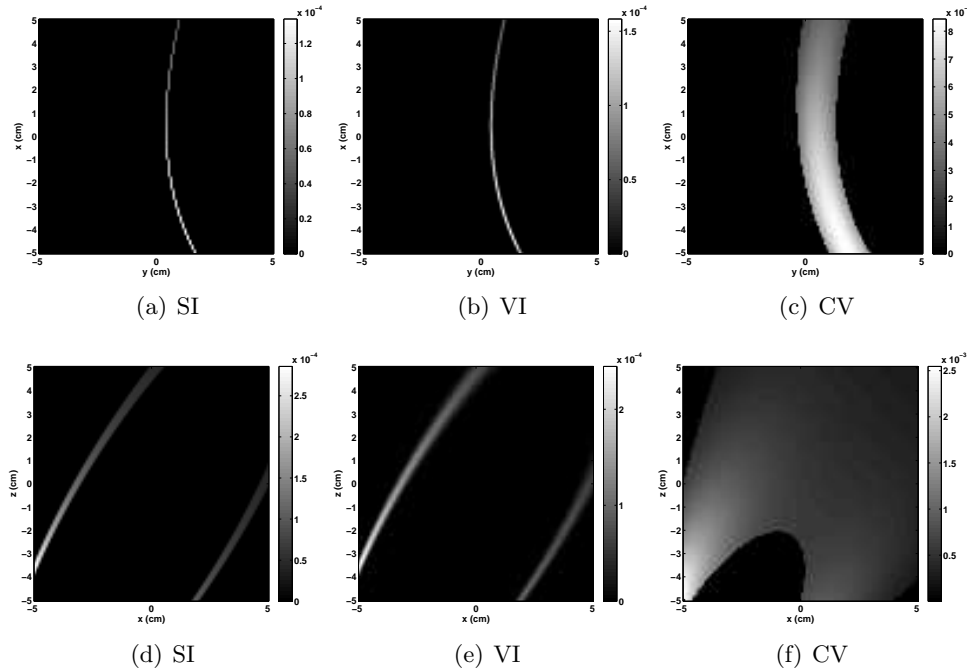


Figure 9.1: *Iterative reconstruction - Small Compton camera - Back-projection of a single event. Panels (a), (b) and (c) show slices at  $z = 1$  cm, parallel to the detectors. Panels (d), (e) and (f) show slices at  $y = 1$  cm, orthogonal to the detectors. The grey scale is in arbitrary units.*

### 9.1.2 Reconstructions with 5000 events

For each method, we reconstructed the images of the source using 5000 events. We performed 20 iterations and recorded at each iteration, the resulting reconstruction. In order to regularize the recorded images, we applied a median filter of size  $3 \times 3 \times 3$ . Figures 9.2, 9.3 and 9.4 show the slices at  $z = 1$  cm and  $y = 1$  cm of the reconstructed volume after 0, 5 and 10 iterations for the methods SI, VI and CV, respectively. The iteration 0 corresponds to the back-projected image before running the iterative algorithm.

The images presented in the second columns of figures 9.2, 9.3 and 9.4 show an elongation of the reconstructed source in the direction orthogonal to the detectors, elongation already noticed with the analytical method. Note also that in the direction parallel to the detectors, after a few iterations, i.e. 5 iterations, the image has already reached a stable state, the evolution from the 5<sup>th</sup> iteration to the 10<sup>th</sup> iteration is not significant.

In order to make a relevant comparison between the methods, we calculated the Normalized Mean Squared Error (NMSE) for each reconstructed images. To do so, we elaborated the expected image, a sphere of radius 0.5 cm located at (1, 1, 1) cm with an activity of 1. At each iteration, the reconstructed image has been normalized by dividing it by its maximum value. Then we calculated the NMSE, according to the formula:

$$NMSE = \frac{1}{N_v} \|\lambda - \hat{\lambda}\|^2 \quad (9.1)$$

with  $\lambda$  and  $\hat{\lambda}$  the normalized expected image and the normalized reconstructed one, respectively. Results are presented in figure 9.5.

We can first note that the results are coherent with the presented images. Before starting the iterative process, the methods VI and SI seems to perform slightly better reconstructions than with the method SI. From the first iteration, CV outperforms the two other methods with a drastic decrease of the NMSE due to superior regularisation for low uncertainties. Nevertheless, after a few iterations, the method VI catches up with the method CV. We note also that the SI method provides relatively similar images as the VI method, but with a less good NMSE. This is coherent with the fact that this method does not take into account the energy measurement uncertainties.

At the end of the iterative process, we observe that for the VI method the NMSE starts to increase. This is probably due to convergence issues. The iterative process does not always converge to a solution but may diverge after a few iterations. As a consequence, a too important number of iterations might lead to a reconstructed image of less good quality, thus to an increase of the NMSE.

We can notice also that even if we underlined the differences in the NSME for each method, after a few iterations, the gap between CV and VI is not really significant, in the order of  $10^{-4}$ .

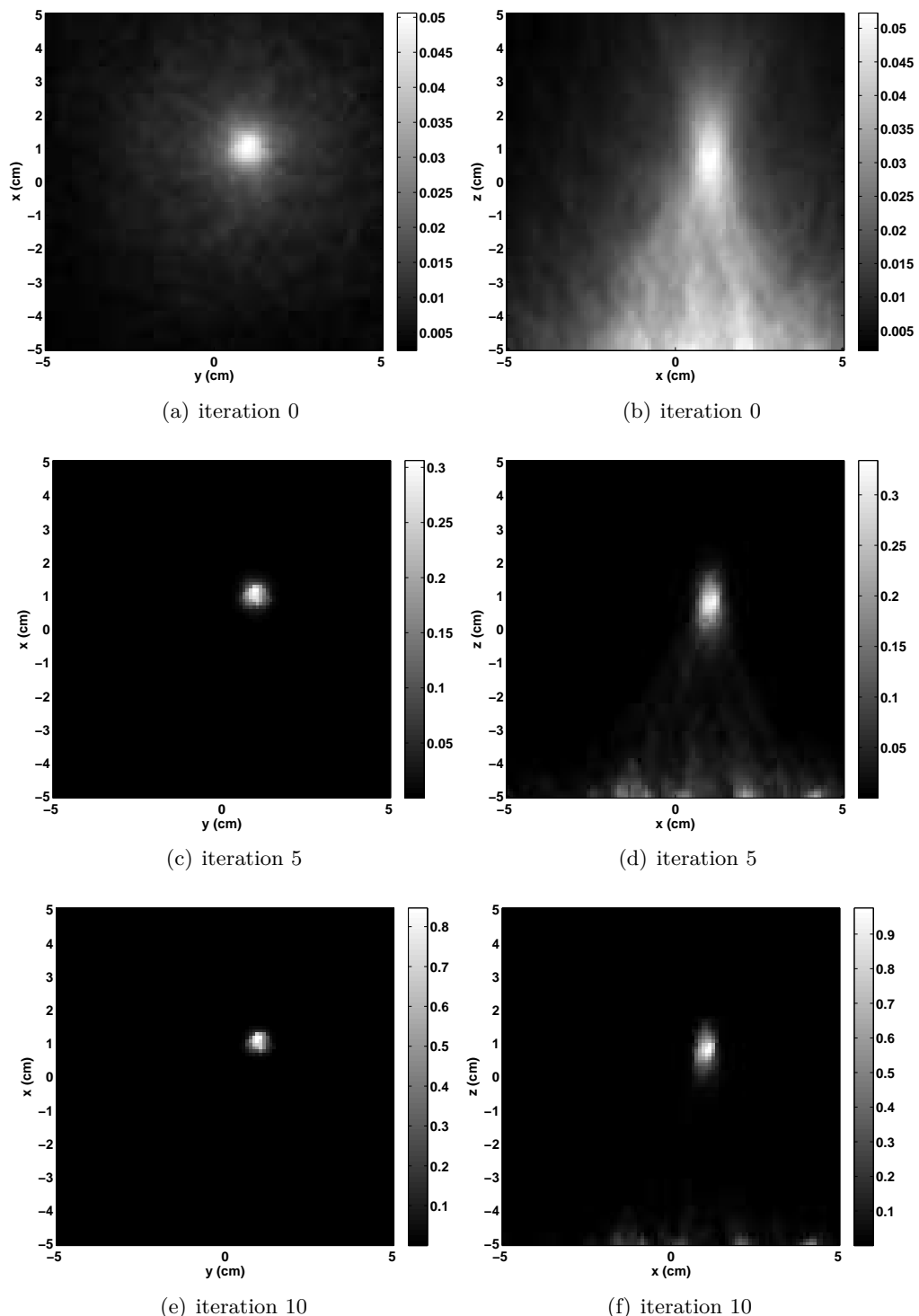


Figure 9.2: *Iterative reconstruction: Surface of Intersection - Small Compton camera - Reconstruction of a spherical source using 5000 events. Panels (a), (c) and (e) show slices at  $z = 1$  cm, parallel to the detectors. Panels (b), (d) and (f) show slices at  $y = 1$  cm, orthogonal to the detectors. The grey scale is in arbitrary units.*

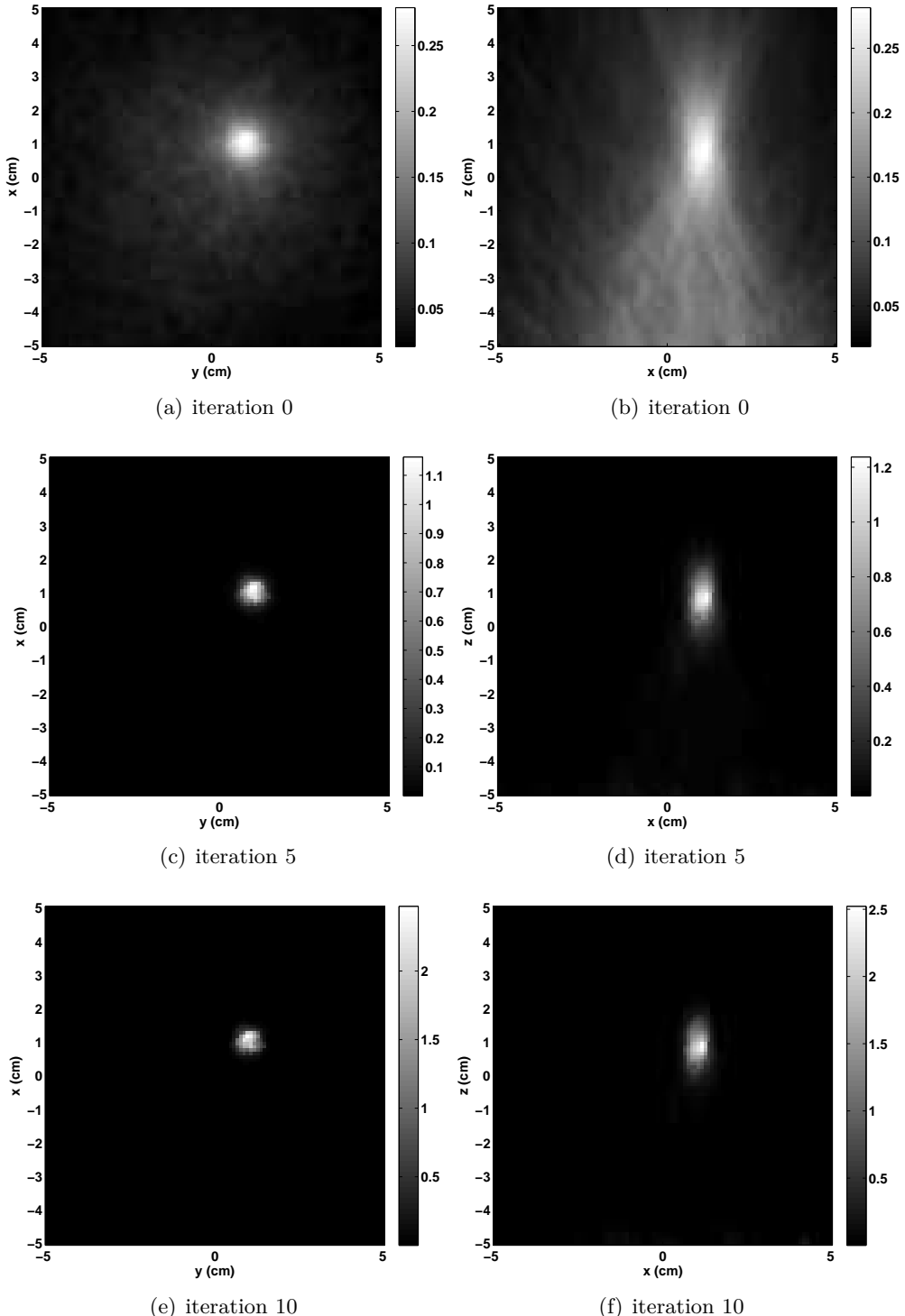


Figure 9.3: *Iterative reconstruction: Volume of Intersection - Small Compton camera - Reconstruction of a spherical source using 5000 events. Panels (a), (c) and (e) show slices at  $z = 1$  cm, parallel to the detectors. Panels (b), (d) and (f) show slices at  $y = 1$  cm, orthogonal to the detectors. The grey scale is in arbitrary units.*

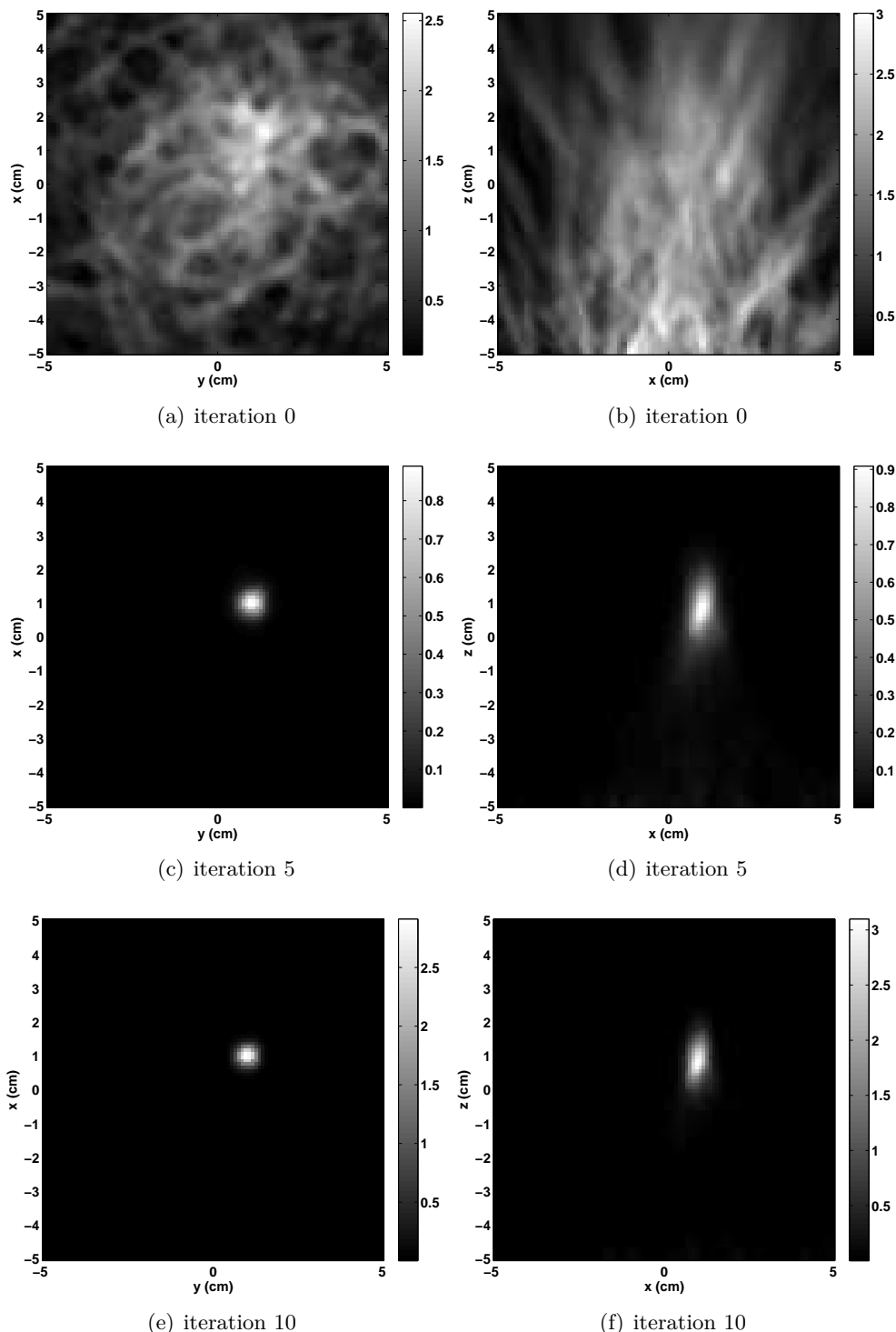


Figure 9.4: *Iterative reconstruction: Center of Voxel - Small Compton camera - Reconstruction of a spherical source using 5000 events.* Panels (a), (c) and (e) show slices at  $z = 1$  cm, parallel to the detectors. Panels (b), (d) and (f) show slices at  $y = 1$  cm, orthogonal to the detectors. The grey scale is in arbitrary units.

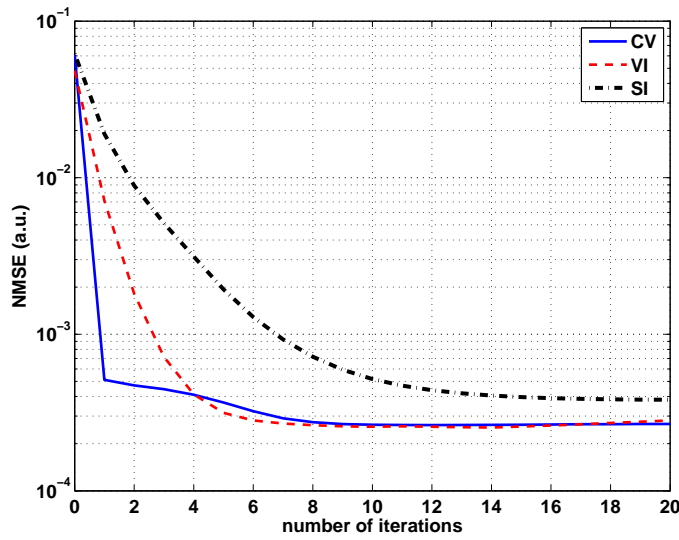


Figure 9.5: *Iterative reconstruction: Normalized Mean Squared Error - Small Compton camera - NMSE as function of the iterations calculated for the images reconstructed with the three methods. The solid line, dashed line, dash-dotted line correspond to the CV method, VI method, SI method, respectively.*

As already seen in section 6.2.2, enlarging the size of the scatterers reduces the effect of elongation. We then performed reconstruction with the larger Compton camera described in section 6.2.2. Figures 9.6, 9.7 and 9.8 show the reconstructions with the methods SI, VI and CV, respectively. We can note that the artefacts in the direction orthogonal to the detectors are drastically reduced in the case of the method SI.

The NMSE as function of the iteration number is presented in figure 9.9 for the three methods. We can observe that the curves follow the same trend as for the small Compton camera: the CV method outperforms the two others at the beginning of the iterative process and the VI method catches up with the CV method. A major evolution is the curve of the NMSE for the SI method which is closer to the ones of the other methods. This is related to the lower artefact level in the direction orthogonal to the detectors. Nevertheless, the difference between large and small Compton camera is in the order of  $10^{-4}$ .

Another main difference between the reconstructions using small and large Compton camera is the rapidity for reaching a stable state. It seems that with the large Compton device, the number of iterations required to obtain a stable image with the SI and VI methods, is reduced compared to when using the small Compton camera. Hence 12, 6 and 8 iterations are necessary for the SI, VI and CV methods, respectively, when using the small device. With the large one, 6, 4 and 8 iterations are required.

Figure 9.10 shows 3D reconstructed images. We have chosen the 10<sup>th</sup> iteration so that all algorithms have reached their minimum NMSE. The 3D volumes are represented using isosurfaces, the threshold value being chosen empirically according to the values of the voxels from the source (around 85% of the maximum value of the reconstructed image).

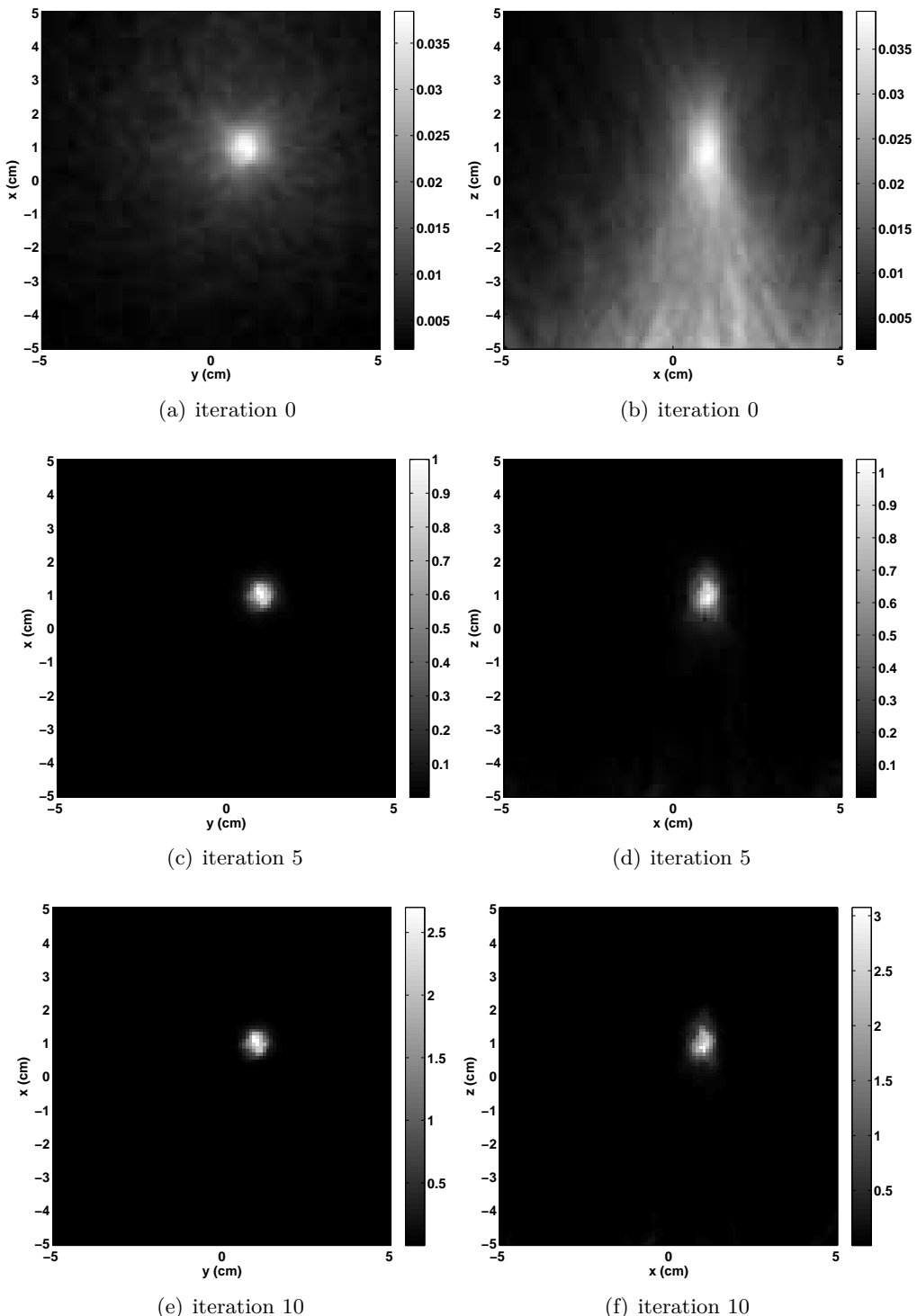


Figure 9.6: *Iterative reconstruction: Surface of Intersection - Large Compton camera - Reconstruction of a spherical source using 5000 events. Panels (a), (c) and (e) show slices at  $z = 1 \text{ cm}$ , parallel to the detectors. Panels (b), (d) and (f) show slices at  $y = 1 \text{ cm}$ , orthogonal to the detectors. The grey scale is in arbitrary units.*

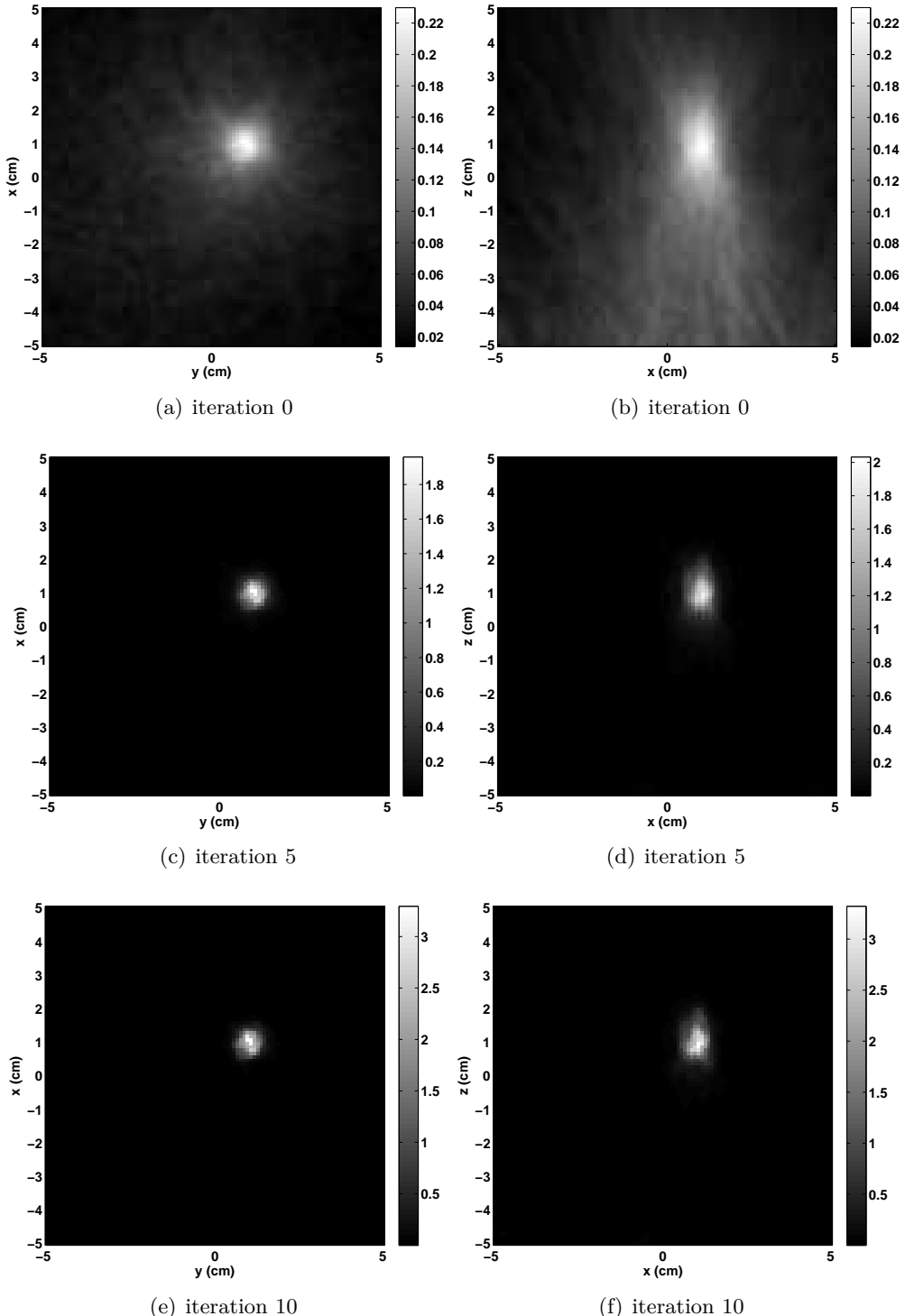


Figure 9.7: *Iterative reconstruction: Voxel of Intersection - Large Compton camera - Reconstruction of a spherical source using 5000 events.* Panels (a), (c) and (e) show slices at  $z = 1$  cm, parallel to the detectors. Panels (b), (d) and (f) show slices at  $y = 1$  cm, orthogonal to the detectors. The grey scale is in arbitrary units.

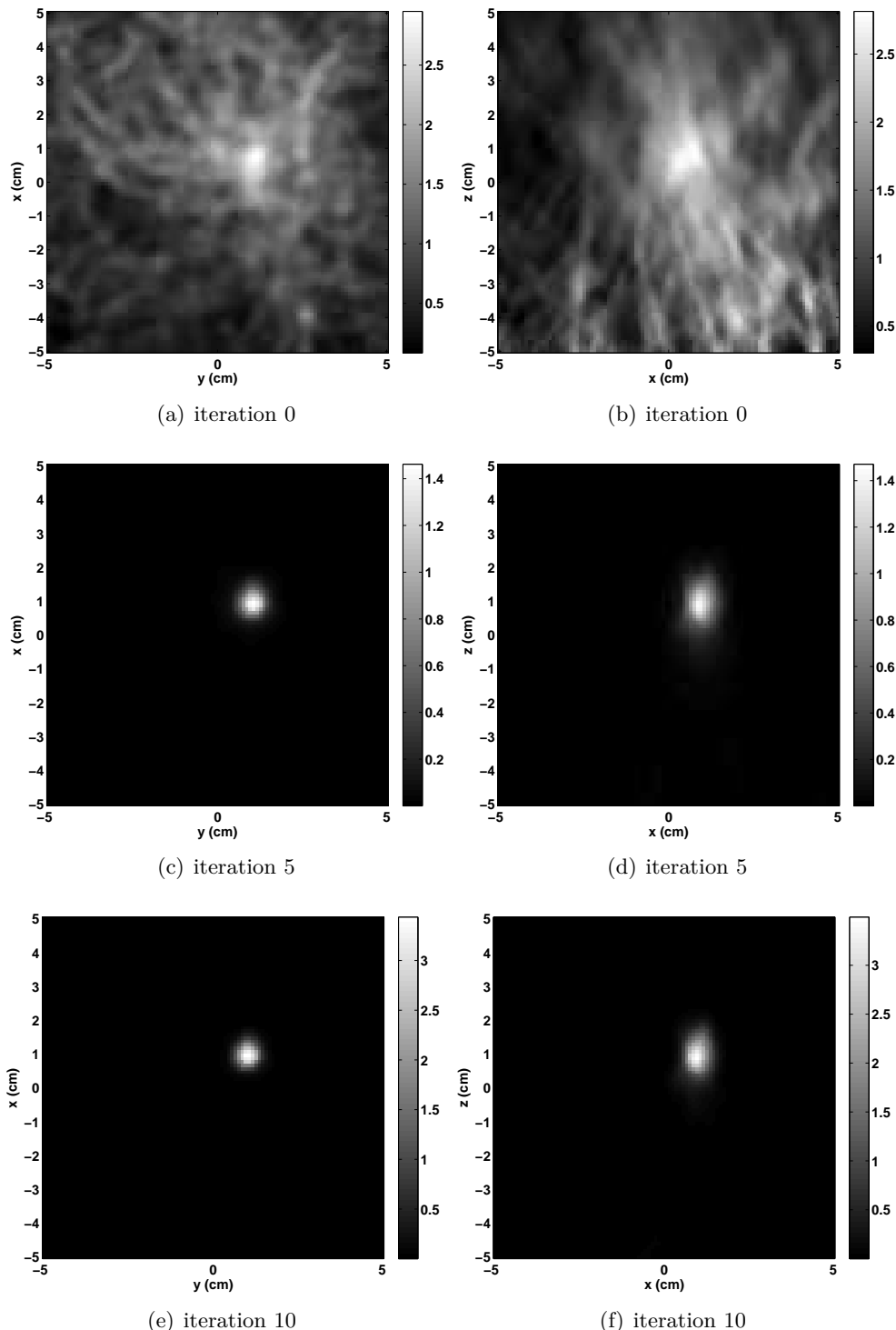


Figure 9.8: *Iterative reconstruction: Center of Voxels - Large Compton camera - Reconstruction of a spherical source using 5000 events.* Panels (a), (c) and (e) show slices at  $z = 1$  cm, parallel to the detectors. Panels (b), (d) and (f) show slices at  $y = 1$  cm, orthogonal to the detectors. The grey scale is in arbitrary units.

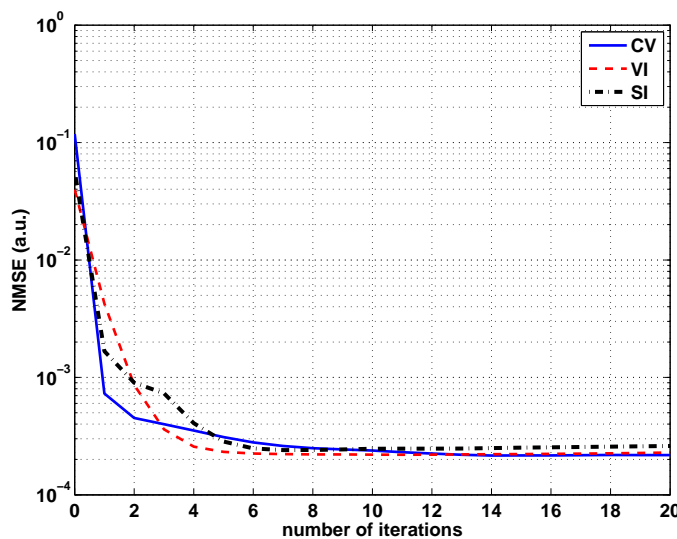


Figure 9.9: *Iterative reconstruction: Normalized Mean Squared Error - Large Compton camera - NMSE as function of the iterations calculated for the images reconstructed with the three methods. The solid line, dashed line, dash-dotted line correspond to the CV method, VI method, SI method, respectively.*

Since the large Compton camera provides better results and a reduced elongation of the source, we will pursue the study using this device.

The images we presented in this section are obtained for only one set of 5000 events. In order to evaluate the reproducibility of the results, we performed the reconstruction of 55 sets of 5000 events, using the CV method. We made 20 iterations for each set. We calculated the NMSE for each image at each iteration. The results are presented as box plots in figure 9.11. They represent the first and the third quartiles, as well as the median of the calculated NMSE. The end of the whiskers represent the lowest datum still within 1.5 Inter Quartile Range (IQR) of the lower quartile, and the highest datum still within 1.5 IQR of the upper quartile. First we can note that the reconstruction method is robust, with a low dispersion of the NMSE. The results are in the order of  $10^{-4}$  for all the series after a few iterations. We can note also that from the 8<sup>th</sup> iteration, the median value of the NMSE becomes stable at  $2.4 \times 10^{-4}$ . Another remark, the dispersion tends to increase in the end of the iterative process, due to convergence issues already discussed. The table 9.1 shows the standard measures, i.e. mean  $\mu$ , standard deviation  $\sigma$ , minimum and maximum values of the NMSE for the iterations 0, 10, and 20.

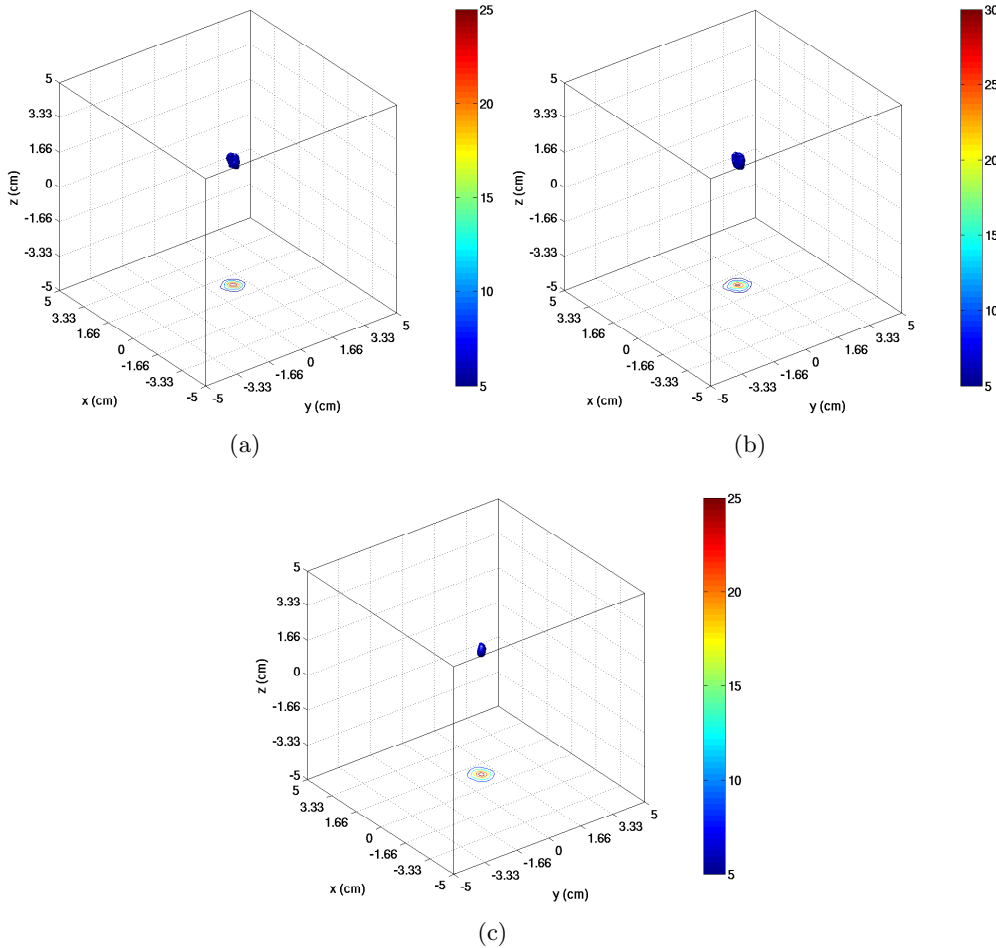


Figure 9.10: *Iterative reconstruction: - Large Compton camera - 3D Reconstructions of the spherical source using 5000 events, 10 iterations, with (a) the Surface of Intersection method, (b) the Volume of Intersection method and (c) the Center of Voxels method.*

iteration	0	5	10	15	20
$\mu$	0.097	$3.10 \times 10^{-4}$	$2.31 \times 10^{-4}$	$2.28 \times 10^{-4}$	$2.31 \times 10^{-4}$
$\sigma$	0.014	$3.02 \times 10^{-5}$	$2.26 \times 10^{-5}$	$2.22 \times 10^{-5}$	$2.37 \times 10^{-5}$
min	0.07	$2.42 \times 10^{-4}$	$2.00 \times 10^{-4}$	$1.92 \times 10^{-4}$	$1.93 \times 10^{-4}$
max	0.13	$3.87 \times 10^{-4}$	$3.30 \times 10^{-4}$	$3.23 \times 10^{-4}$	$3.26 \times 10^{-4}$

Table 9.1: *Iterative reconstruction: Large Compton camera - Center of Voxels* Standard measures: mean  $\mu$ , standard deviation  $\sigma$ , minimum and maximum values of the NMSE for the iterations 0, 10, and 20.

## 9.2 Influence of the incomplete absorptions

In hadrontherapy, the initial energy of the detected prompt- $\gamma$  particles is unknown. During the reconstruction process, we estimate it as the sum of the energies measured by the device. If the photon is not fully absorbed, this will lead to a wrong estimation of the initial energy and then to an error on the calculation of the half opening angle.

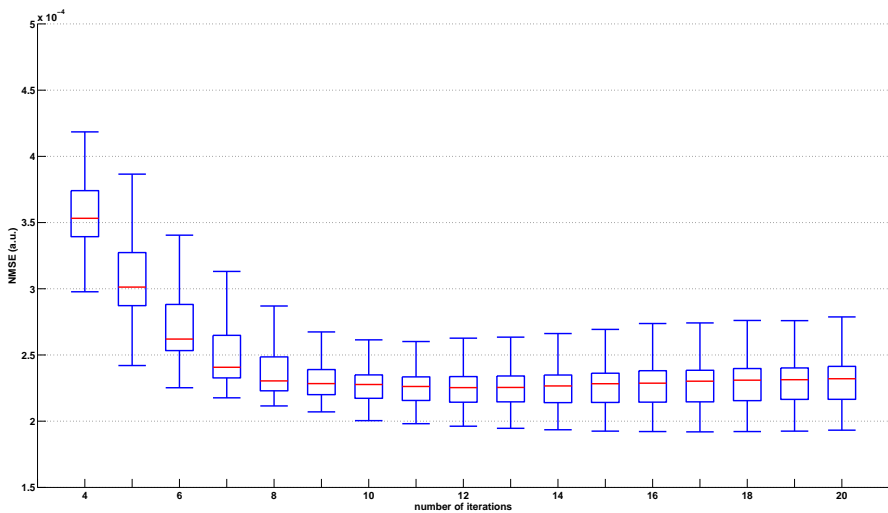


Figure 9.11: *Iterative reconstruction: Large Compton camera - Center of Voxels - Box plots representing the dispersion of the NMSE for the iterations 4 to 20.*

These wrong estimations will inevitably deteriorate the reconstructed images. Thus, it is possible to enhance the reconstruction by selecting only photons that have undergone a full absorption. Knowing a priori the initial energy enables to perform this selection. In this section, we compare reconstructions with and without applying a selection window on the estimated initial energy. We chose a window of  $\pm 10\%$  around 1.275 MeV, the energy of the source.

Figures 9.12, 9.13 and 9.14 show the reconstructed images for each method at the same iteration as before, i.e. 0, 5 and 10, respectively. From the images, we can observe that the spherical shape of the source seems to better reproduced. The artefacts towards the detector have been reduced and even faded away.

The figures 9.15, 9.16 and 9.17 show the calculated NMSE as function of the iterations for each method, compared to the NMSE calculated for the reconstructed images without the energy selection window. As expected, we can note that the minimum NMSE with each method is lower when a selection is made. However, the gap between the NMSE calculated with and without selection is not that significant in this study, since it was already quite low. The difference might be more important with a more complex source to reconstruct. Another observation must be underlined: the number of iterations to reach the minimum NMSE is lower with the event selection.

The known a priori initial energy of the photons is thus an important information in order to obtain better images. Nevertheless, we can note from this study that for a simple source, even without event selection on the base of full absorptions, our methods perform almost as well as with the event selection. In the next section, we will carry out reconstructions on a more complex source.

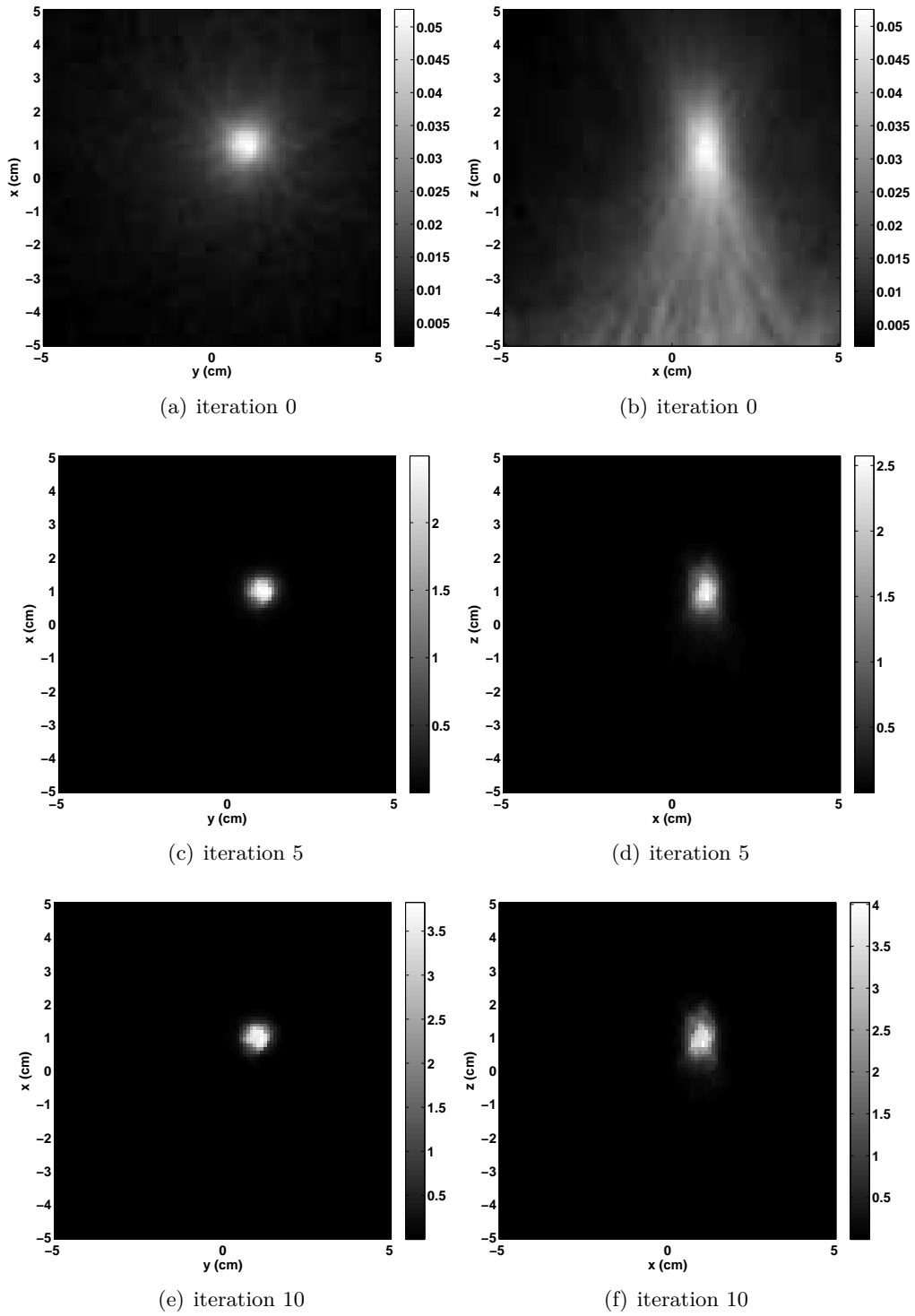


Figure 9.12: *Iterative reconstruction: Surface of Intersection - Large Compton camera*  
- Reconstruction of a spherical source using 5000 photons that have undergone a full absorption. The range of the energy selection window is given by  $1.275 \pm 10\%$  MeV. Panels (a), (c) and (e) show slices at  $z = 1$  cm, parallel to the detectors. Panels (b), (d) and (f) show slices at  $y = 1$  cm, orthogonal to the detectors.

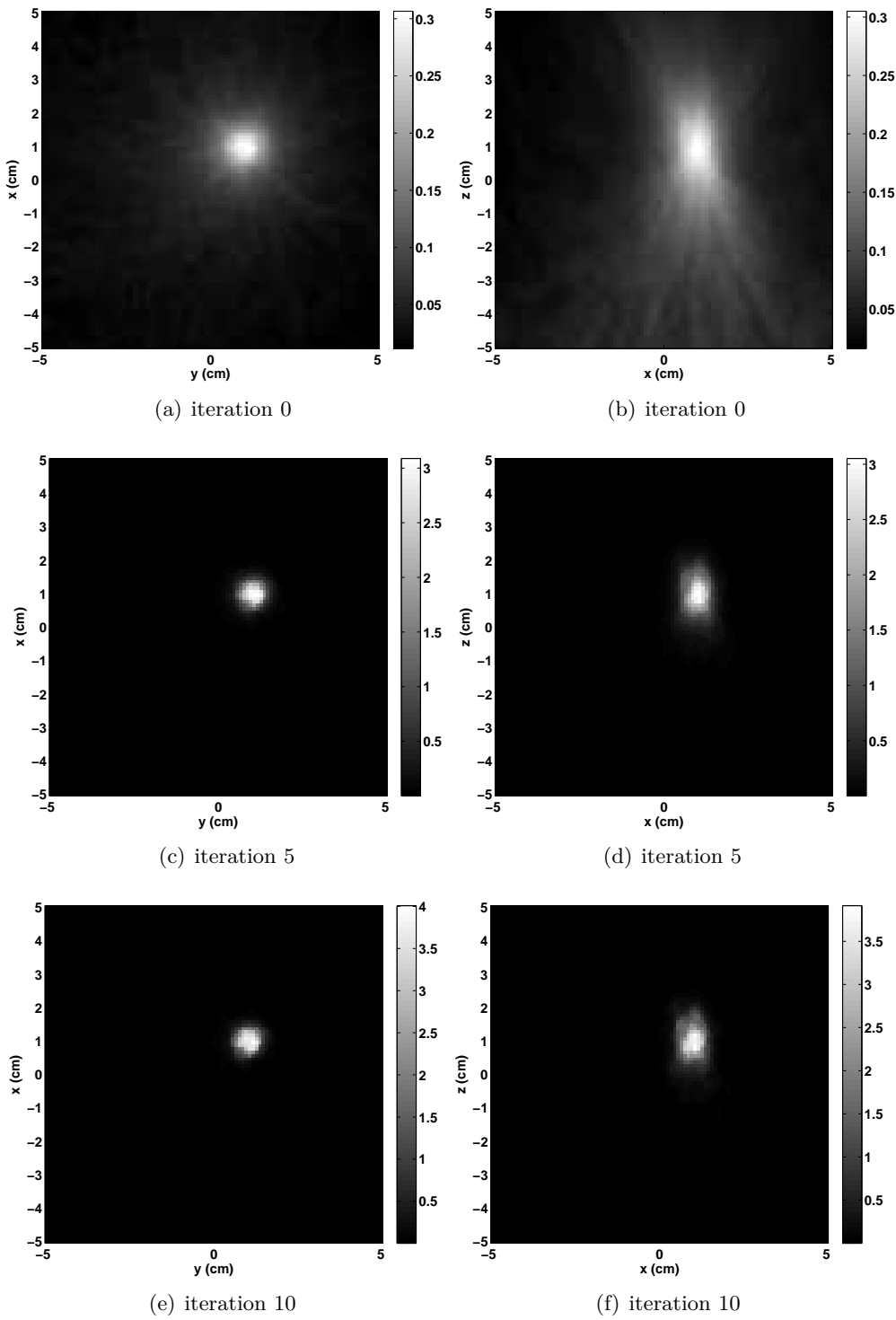


Figure 9.13: *Iterative reconstruction: Voxel of intersection - Large Compton camera - Reconstruction of a spherical source using 5000 photons that have undergone a full absorption. The range of the energy selection window is given by  $1.275 \pm 10\%$  MeV. Panels (a), (c) and (e) show slices at  $z = 1$  cm, parallel to the detectors. Panels (b), (d) and (f) show slices at  $y = 1$  cm, orthogonal to the detectors.*

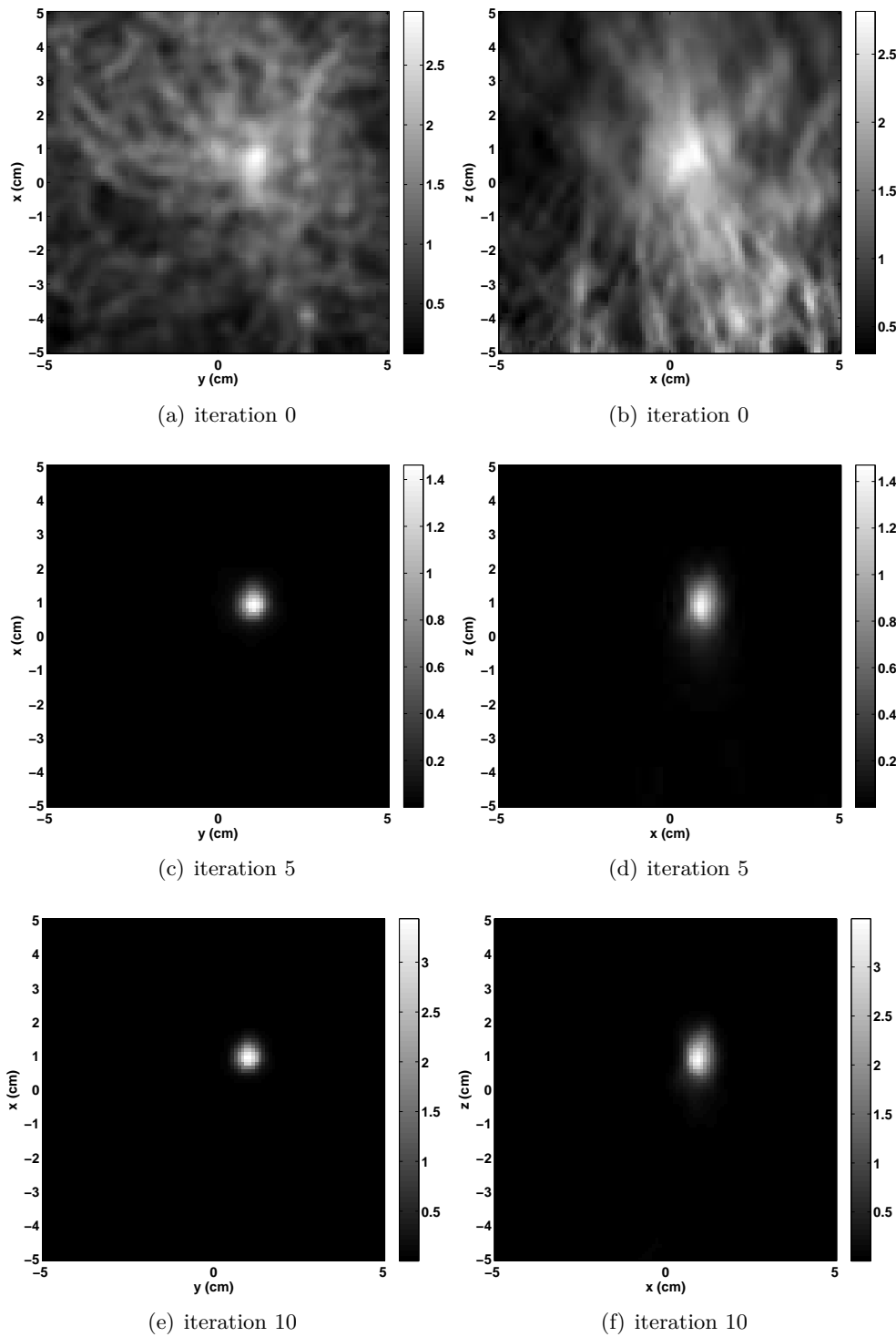


Figure 9.14: *Iterative reconstruction: Center of Voxels - Large Compton camera - Reconstruction of a spherical source using 5000 photons that have undergone a full absorption. The range of the energy selection window is given by  $1.275 \pm 10\%$  MeV. Panels (a), (c) and (e) show slices at  $z = 1$  cm, parallel to the detectors. Panels (b), (d) and (f) show slices at  $y = 1$  cm, orthogonal to the detectors.*

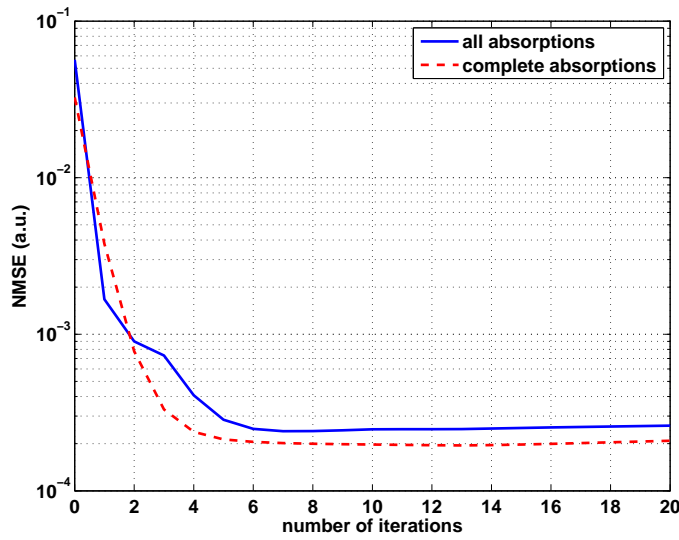


Figure 9.15: *Iterative reconstruction: Normalized Mean Squared Error - Large Compton camera - Surface of Intersection - NMSSE as function of the iterations calculated for the images reconstructed with the SI method. The dashed line and solid line correspond to the NMSE calculated for the reconstructed images with and without energy selection window, respectively.*

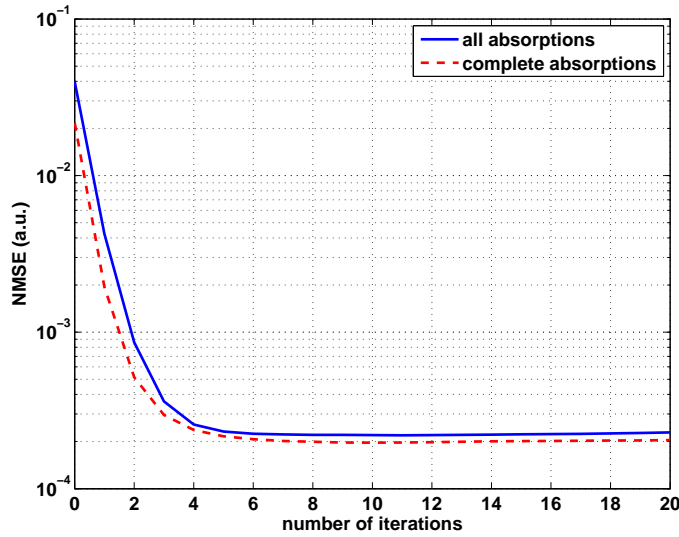


Figure 9.16: *Iterative reconstruction: Normalized Mean Squared Error - Large Compton camera - Volume of Intersection - NMSE as function of the iterations calculated for the images reconstructed with the VI method. The dashed line and solid line correspond to the NMSE calculated for the reconstructed images with and without energy selection window, respectively.*

### 9.3 Reconstruction of a line source

In this section, we now perform reconstructions of a monoenergetic line source. The purpose of this study is to experience the different reconstruction methods we proposed in

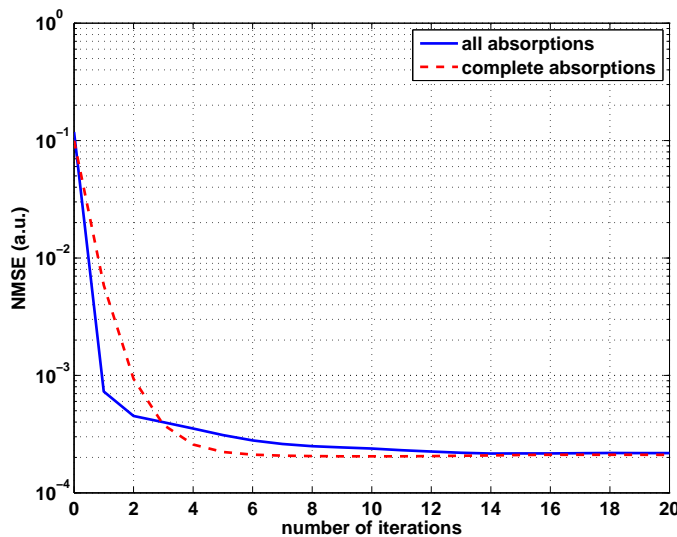


Figure 9.17: *Iterative reconstruction: Normalized Mean Squared Error - Large Compton camera - Center of Voxels - NMSE as function of the iterations calculated for the images reconstructed with the CV method. The dashed line and solid line correspond to the NMSE calculated for the reconstructed images with and without energy selection window, respectively.*

the case of a source with a shape a little bit more complex to reconstruct than the spherical source. It seems easy to reconstruct a line, however, the distributed nature of the source could be tricky. We chose an energy lower than in the previous study, at 364 keV. Note that this specific value of energy corresponds to the radioisotope iodine-131,  $^{131}I$ .

### 9.3.1 Context of the simulation

A scheme of the context of the simulation is shown figure 9.18. The Compton camera used for the simulation is composed of 3 scatterers in Si of  $18.4 \times 18.4 \times 0.5 \text{ cm}^3$  and an absorber in CsI of  $37 \times 37 \times 4 \text{ cm}^3$ . The line source starts at  $(-11, 0, 0)$  cm and ends at  $(0, 0, 0)$  cm. It has no width and no thickness. The imaging device is placed at 10 cm from the line source as shown in the sketch. The position of the camera with respect to the source is chosen to mimic a hadrontherapy monitoring, where the main purpose is to detect the position of the Bragg peak and subsequently the range of the beam in the tissue. The length of the source was chosen to exceed the surface of the scatterer. One of the purposes of the experiment was to investigate the influence of the spatially varying PSF on the reconstructed images.

### 9.3.2 Results

We reconstructed a cubic volume of  $14 \times 14 \times 14 \text{ cm}^3$ , composed of  $140 \times 140 \times 140$  voxels. A voxel is then of 1 mm side length. We only present the results for the slices parallel to the detector. We used 5000 events without energy selection. We performed 20

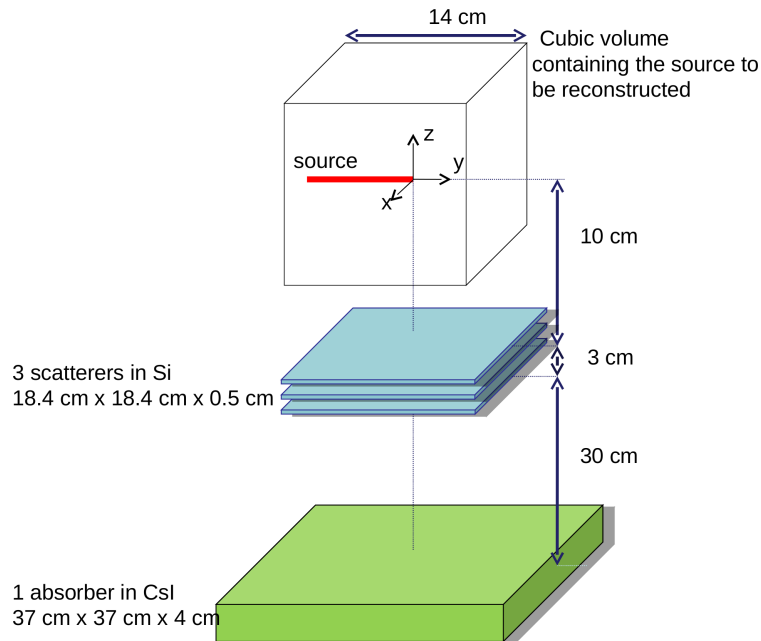


Figure 9.18: *Iterative reconstruction* - Scheme of the Compton camera and the simulated line source. The volume containing the source represents the image to be reconstructed.

iterations and applied a median filter of size  $3 \times 3$  to the output image. Figures 9.19, 9.20 and 9.21 show the reconstructed images with the SI method at the iteration 0, 2, 4 and 10 and the reconstructed images with the VI and CV methods at iteration 0, 5, 10 and 20, respectively.

We can note from these results that the method Surface of Intersection enables to reconstruct the source in the beginning of the iterative process. But the results deteriorate really fast during the iterations. We can see in figure 9.19 (a), the reconstructed line before the iterative process. The source is recognizable even if the result is blurred. Close to the center of the detector, the relative intensity is pretty high in comparison with the relative intensity when moving away from the center. The iterative algorithm tends to increase this discrepancy leading to the concentration of the data in a spot. Figures 9.19 (b), (c) and (d) illustrate this phenomenon. The other methods, i.e. Voxel of Intersection and Center of Voxel, performed better reconstructions even if this phenomenon still is visible. We will come back with some hints to explain this issue in the next section.

In order to analyze the reconstructed line, we calculated the Full Width at Half Mean. The nature of this measurement is presented in figure 9.22. We first took the profile of the reconstructed line source. In this case, the extremities of the source are known, we selected the central 80% range of the source, i.e. we selected the values in the interval  $[-9.9, -1.1]$ , and calculated the mean of relative intensity. We then calculated the Full Width at Half Mean. The closer it gets to the length of the line, the better the reconstruction is.

In order to make a relevant measure, we chose the iteration 5 for all methods, the resulting images after more iterations being too close to a shape of a spot. The figure

9.23 presents the reconstructed profiles along the direction  $y = 0$ . As expected for the SI method in figure 9.23 (a), the profile is not really convincing. In figures 9.23 (b) and (c), the profiles are fairly better. Indeed, the value of the profile is close to 0 except in the range of the expected line source. Then, the Full Width at Half Mean are 8.6 cm for the SI method and 9.2 cm for the two others. It confirms that the CV method and VI method provide quite similar results and also outperform the SI method.

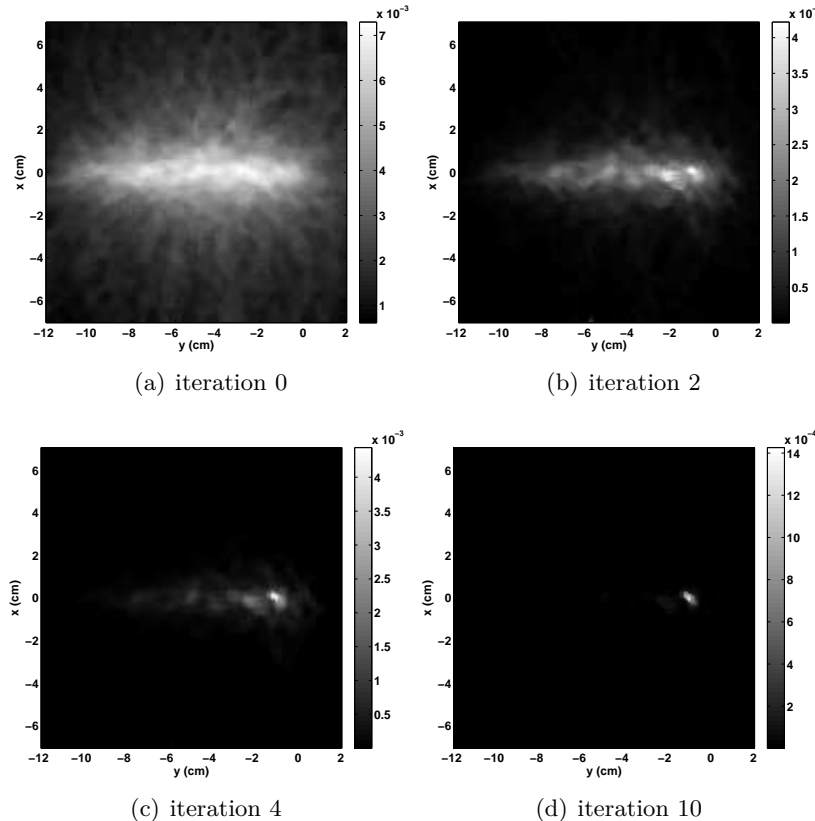


Figure 9.19: *Iterative reconstruction: Surface of Intersection* - Reconstruction of a line source using 5000 events. Panels (a), (b) and (c) show slices at  $z = 0$  cm, parallel to the detectors. The grey scale is in arbitrary units.

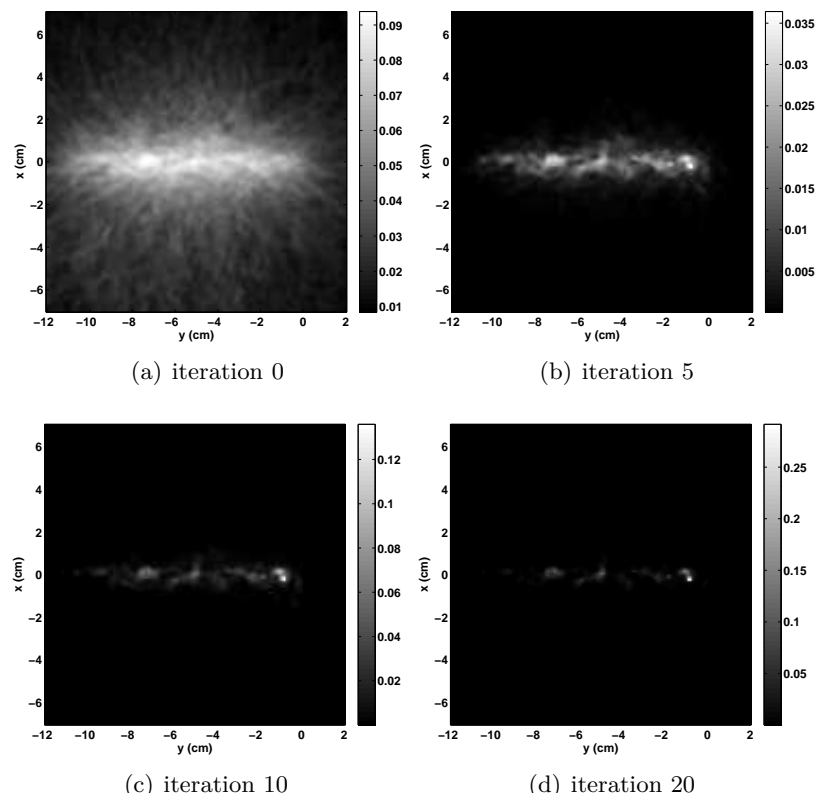


Figure 9.20: *Iterative reconstruction: Voxel of Intersection* - Reconstruction of a line source using 5000 events. Panels (a), (b) and (c) show slices at  $z = 0$  cm, parallel to the detectors. The grey scale is in arbitrary units.

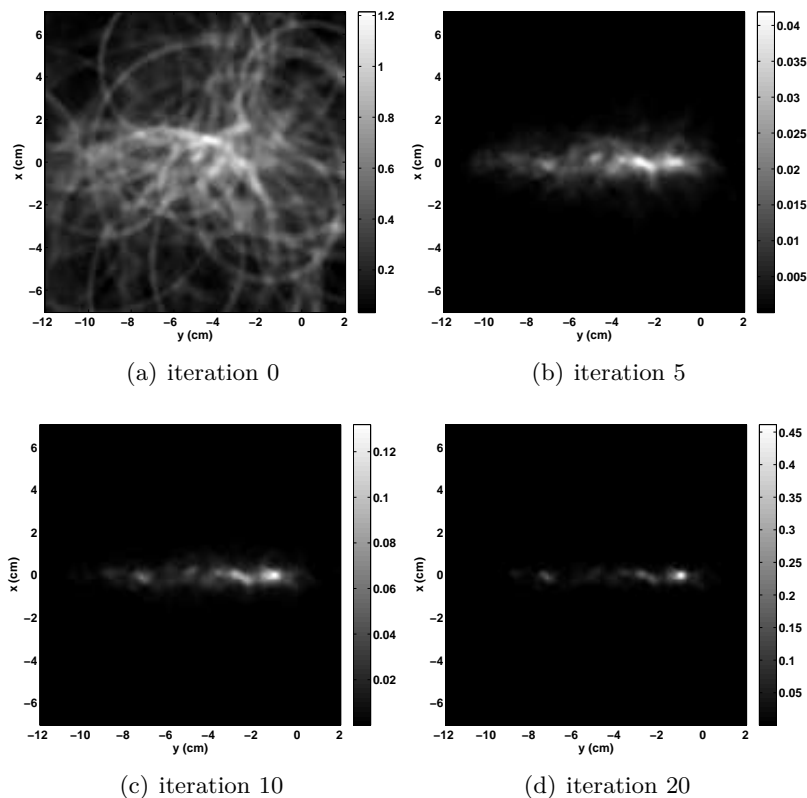


Figure 9.21: *Iterative reconstruction: Center of Voxels* - Reconstruction of a line source using 5000 events. Panels (a), (b) and (c) show slices at  $z = 0$  cm, parallel to the detectors. The grey scale is in arbitrary units.

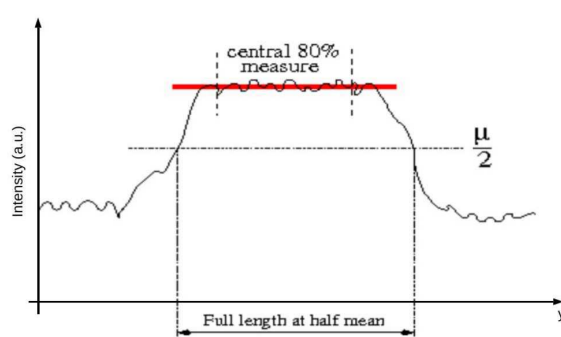


Figure 9.22: Sketch for the calculation of the Full Width at Half Mean.  $\mu$  represents the mean of the values of the central 80% measure.

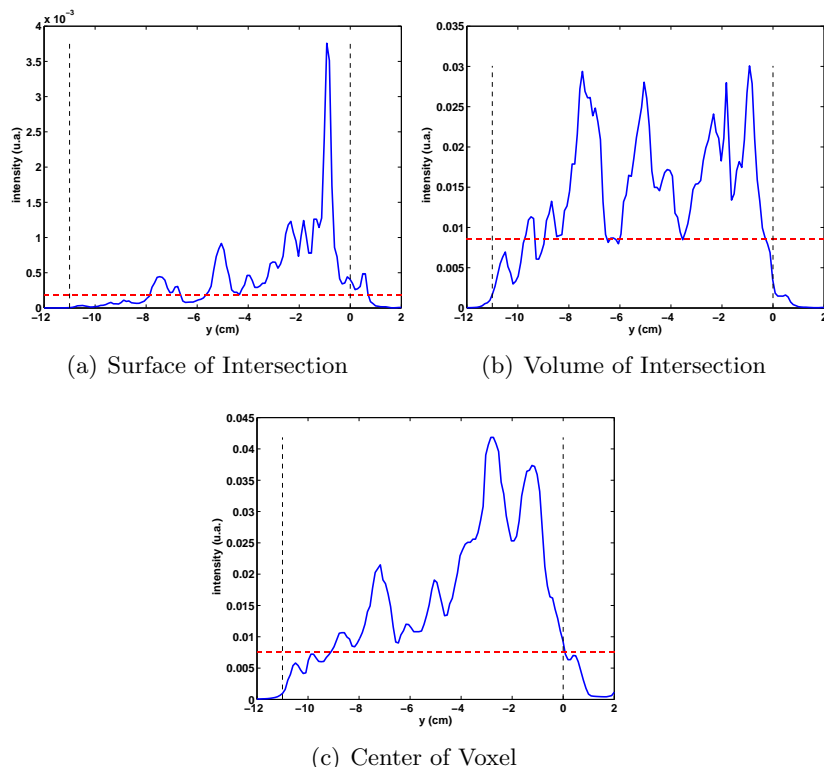


Figure 9.23: *Iterative reconstruction:* - Profiles of the line source in the direction  $x = 0$ . The horizontal dashed line represents the half mean. The vertical dashed lines represent the range of the expected reconstructed line. The Full Width at Half Mean is 8.6 cm for the SI method and 9.2 cm for the VI and CV methods. The iterative process was stopped after 5 iterations.

## 9.4 Influence of the probabilistic model

As mentioned in section 7.1, there are several models for the estimation of the elements of the system matrix. In the analytical reconstruction, as in PET imaging modalities, the factor  $\rho$  is neglected. In this section, we carried out a study of the influence of the factor  $\frac{\cos(\theta_M)}{\rho^2}$  on the reconstruction of the line source. We recall that  $\rho$  is the distance from the source to the first interaction point, namely  $V_1 M$ . We performed reconstructions with the CV method using the following models:

1. accounting for  $\theta_M$  and  $\rho^2$
2. accounting for  $\theta_M$  and  $\rho$
3. accounting only for  $\theta_M$
4. accounting only for  $\rho^2$
5. accounting only for  $\rho$
6. not accounting for  $\theta_M$  and  $\rho^2$  either

We made the same reconstructions as before, using 5000 events, and performing 20 iterations. The figures 9.24 and 9.25 show the images of the line source obtained at the iteration 10 and 20 for each model. We can note from these images that when removing the factor  $\cos(\theta_M)$  and even more when removing  $\rho^2$ , the attenuation noticed in the previous section, i.e. in figures 9.24 (a) and 9.24 (b), is reduced. One explanation would be that a photon is coming from the area not directly covered by the camera, it collides with the scatterer with an important incident angle  $\theta_M$ . As a consequence  $\cos(\theta_M)$  is low, which weakens the weight of the estimated  $t_{ij}$ . At the same time, far away from the camera,  $\rho^2$  is important which also decreases the weight of the element of the system matrix. The iterative process then increases the resulting discrepancy between the events coming from the area far from the detectors and the area directly covered by the device. Then, by not accounting for the solid angle, we reduce the discrepancy and we should have a better Full Width at Half Mean, the length of the line being better complied. Figures 9.24 (f) and 9.25 (f) compared to 9.24 (a) and 9.25 (a) give some insight of this enhancement.

We then performed the calculation of the NMSE as function of the iteration for each model. The results are presented in figure 9.26. Figure 9.26 (b) presents a zoom on iterations from 4 to 20. From these results we confirmed that the model from which the solid angle was withdrawn, seems to provide better reconstructions. Nevertheless, we made the assumption  $\forall j, s_j = 1$ . The sensitivity values should have varied instead with the position of the voxels with respect to the camera. This may also have an impact on the reconstruction and on the model that should be selected.

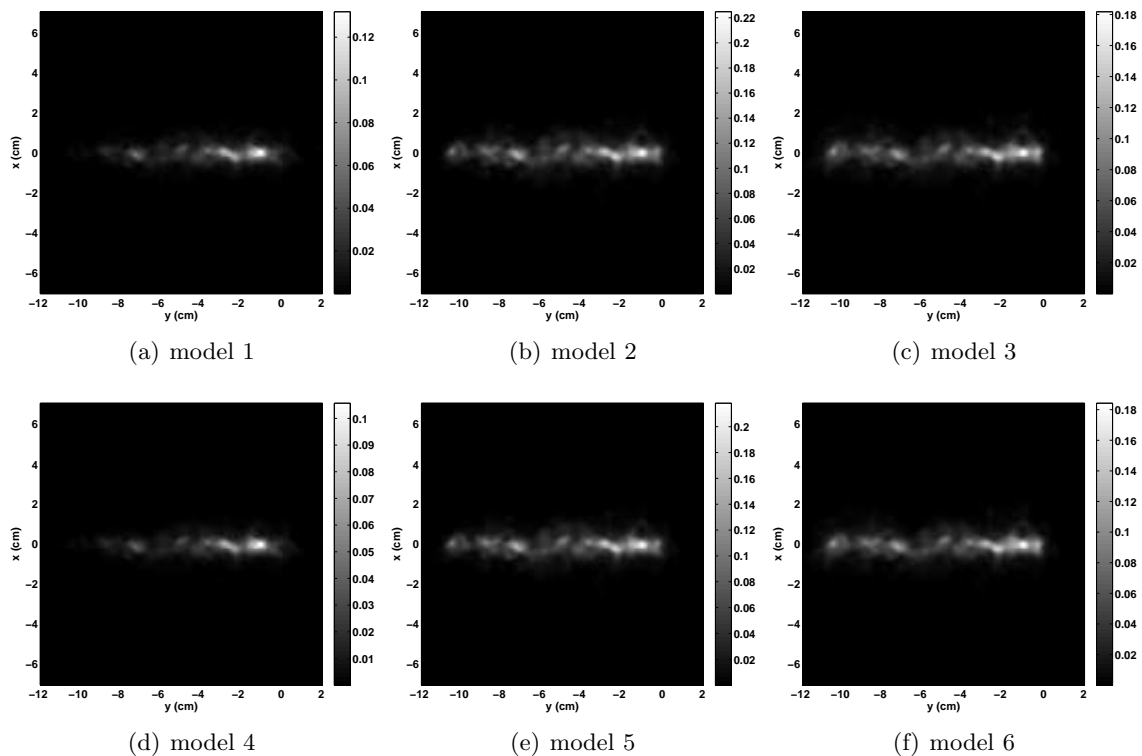


Figure 9.24: *Iterative reconstruction: Center of Voxel* - Reconstruction of a line source performed with 5000 events at iteration 10, for several models accounting or not for the solid angle subtended by the element of scatterer at the emitting point. The images are slices at  $z = 0$  cm, parallel to the detectors.

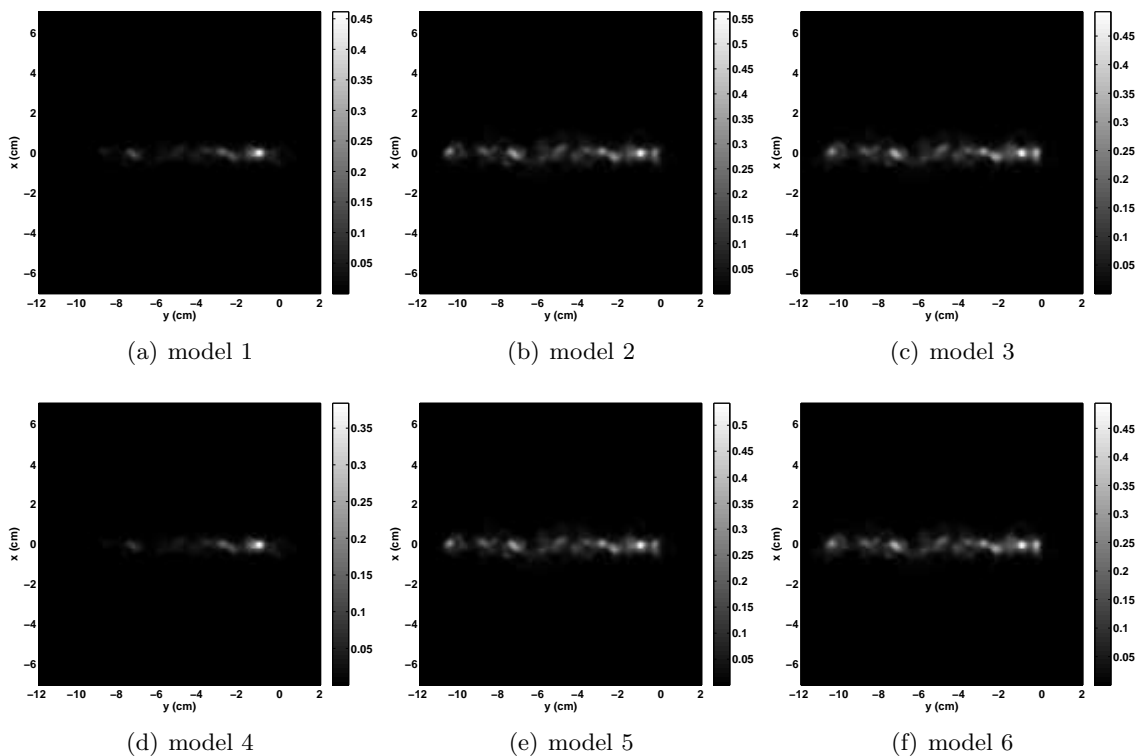
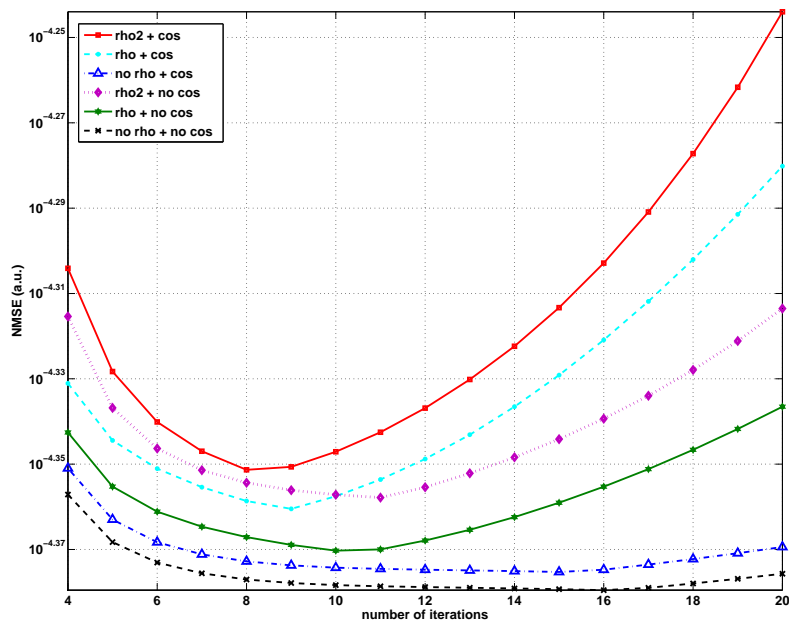
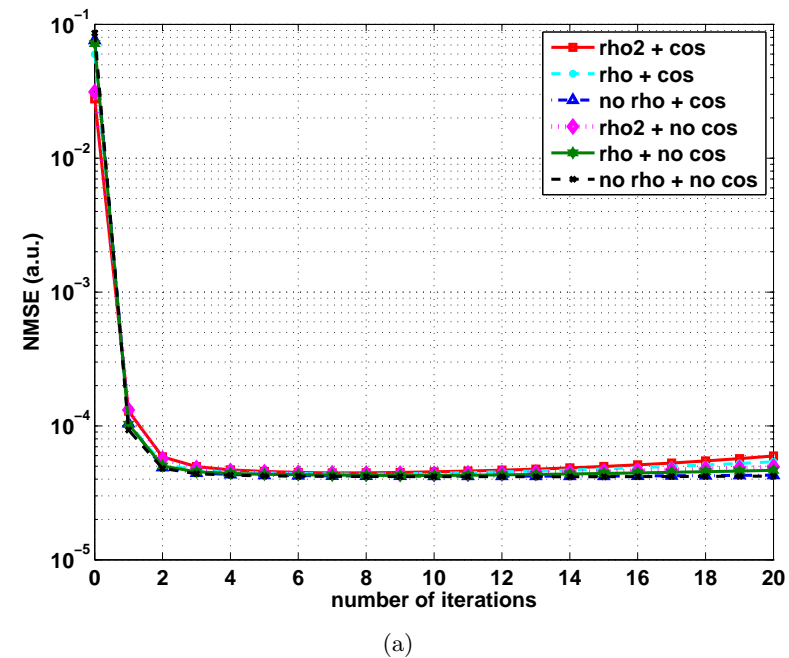


Figure 9.25: *Iterative reconstruction: Center of Voxel* - Reconstruction of a line source performed with 5000 events at iteration 20, for several models accounting or not for the solid angle subtended by the element of scatterer at the emitting point. The images are slices at  $z = 0$  cm, parallel to the detectors.



(b) iterations from 4 to 20

Figure 9.26: *Iterative reconstruction: Normalized Mean Squared Error - Large Compton camera - Center of Voxel - NMSE as function of the iterations calculated for the images reconstructed for several models accounting or not for the solid angle subtended by the element of scatterer at the emitting point.*

## 9.5 Conclusion

In this chapter, we presented iterative reconstructions of two different kinds of  $\gamma$  sources, the first spherical with the specific energy 1.275 MeV corresponding to the  $^{22}\text{Na}$  isotope, the second, a line source with the specific energy 364 keV corresponding to the  $^{131}\text{I}$  isotope. We performed reconstructions using three methods that we called, Surface of Intersection, Volume of Intersection, Center of Voxels. The VI and CV methods account for the energy measurement uncertainties.

We can note from this study that the VI and CV methods outperform the SI method, and provide relatively similar reconstructions. For simple source reconstruction as conducted in our work, a way to choose between the Center of Voxel method or Volume of Intersection would be to study the reconstruction speed. The current implementation of the algorithms favors the CV method which is faster and easy to implement whereas the VI method is more time consuming. Nevertheless, at the moment, the comparison cannot be relevant since the implementations are not optimal for both. A more suitable implementation might reduce the gap in time consumption. Moreover, for more complex sources, closer to a hadrontherapy treatment, the differences between the two methods might be more significant, and then should lead to an optimal selection of the reconstruction algorithm.

The spatial variability of the source has an impact on the quality of reconstruction. This is particularly the case when the source is out of the range of the detectors. A careful positioning of the Compton camera before the acquisition is thus required. In case of a wide source, the idea of using large scatterers is also relevant, since it increases the range covered by the camera and at the same time reduces the elongation in the direction orthogonal to the detectors. However, large scatterers also mean an increase of the bulk of the camera.

The probabilistic model is still a topic of discussion, especially whether the model should account or not for the solid angle subtended by the element of scatterer at the emitting point. Our study tends to show that we should not account it for at least when the  $s_j$  values are uniformly set to 1. Further investigations with more realistic conditions should be performed in order to confirm it.

In the next part, we applied our methods to data provided by different teams in charge of the development of a Compton camera for hadrontherapy monitoring. The specificity of this application enables to experience the methods on data a step closer to realistic simulations.

## V Application: reconstructions from data simulated within the framework of the ENVISION project

---



# Chapter 10

---

## Application to data from the Institut de Physique Nucléaire de Lyon, France

---

Within the framework of the european project ENVISION, the objective of the Workpackage 3 we belong to, is to investigate different feasible concepts for in-beam single particle tomography at therapeutic proton and ion beams. Several prompt  $\gamma$ -rays detectors are currently in investigation, such as passive collimation slit cameras, and also electronic collimation Compton cameras. The study of the Compton detectors concerns with its design, material composition and image reconstruction algorithms.

In this chapter we conducted a study on the Point Spread Function (PSF) of the simulated prototype currently under development at the Institut de Physique Nucléaire de Lyon (IPNL). A point source having a broad energy spectrum compatible with hadron-therapy has been simulated and we experienced the Filtered BackProjection method and the Surface of Intersection method in condition of low statistics reconstruction. We then compared the reconstructed image of the source with a line-cone approach.

### 10.1 Compton camera design

The Compton camera prototype is composed of a stack of Silicon scatterers and scintillator absorber. Figure 10.1 shows the geometry of a Compton camera prototype, submitted to preliminary tests before being built [[Roellinghoff \*et al.\* \(2011\)](#)].

The scatterer is composed of 10 layers of silicon strip detectors of  $8\text{ cm} \times 8\text{ cm} \times 0.2\text{ cm}$ , with a 1 cm gap between two consecutive layers. When a  $\gamma$  particle collides with one of the strip detectors, the position and the energy delivered to an electron during the

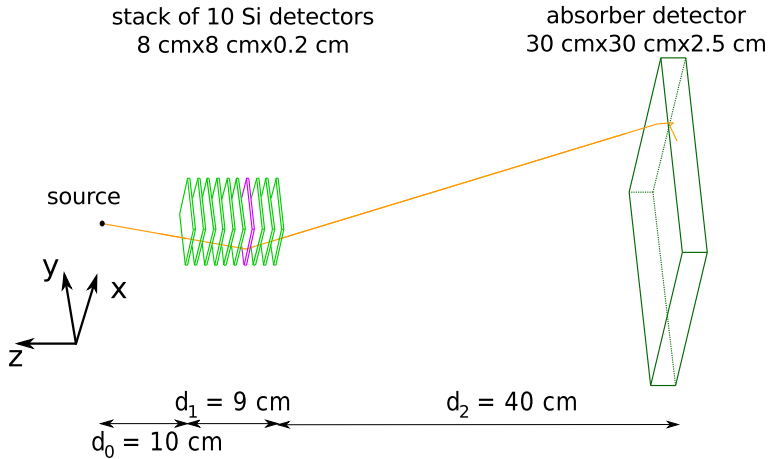


Figure 10.1: The simulated Compton camera with the scatterer composed of a stack of 10 layers of Si strip detectors, and the absorber composed of a LYSO scintillator [Roellinghoff *et al.* (2011), Richard *et al.* (2012)].

scattering process are recorded.

The absorber is a scintillator of  $30 \text{ cm} \times 30 \text{ cm} \times 2.5 \text{ cm}$  made of LYSO crystals and is 40 cm away from the last layer of the scatterer.

Simulations were performed according to realistic detectors and their specific resolutions. Both positions and energies present uncertainties. Each silicon strip detector has a lateral resolution of 1 mm, and there is no depth information. The expected Equivalent Noise Charge (*i.e.* the root mean square fluctuation of the readout noise, expressed in number of electrons) is 600. The energy resolution of the silicon detectors is modeled by a gaussian distribution with Full Width at Half Maximum (FWHM) calculated with the Fano formula:

$$E_{FWHM} = 2.355w\sqrt{ENC^2 + \frac{FE_1}{w}}, \quad (10.1)$$

where  $w = 3.65 \times 10^{-4} \text{ MeV}$  is the pair creation energy in a Si semiconductor,  $ENC$  is the Equivalent Noise Charge,  $F = 0.115$  the Fano factor, and  $E_1$  the deposited energy in the Si strip detector in MeV. In the absorber, the lateral resolution is 5 mm and no depth information is available. The energy resolution for 1 MeV deposited is expected to be as good as 8.3 %. With this prototype, it is possible to reach a detection efficiency of  $2.5 \times 10^{-4}$ .

For more details on the camera design, we refer the interested reader to [Roellinghoff *et al.* (2011), Richard *et al.* (2012)].

## 10.2 Simulations

The simulations are performed with Geant4 version 9.4 [Agostinelli *et al.* (2003), Allison *et al.* (2006)]. Compton scattering is modeled using the G4LivermorePolarized-ComptonModel process which takes Doppler broadening and polarization into account. The standard physics lists of Geant4 were used for other interaction models, as detailed in Table 10.2.

Process	protons	ions	neutrons
Electromagnetic	standard option3		
Inelastic	G4BinaryCascade	G4QMDReaction (G4IonsShenCrossSection)	G4BinaryCascade G4NeutronHPInelastic (<19MeV)
Elastic	G4LElastic + G4NeutronHPElastic (<19 MeV - for neutrons only) or G4HadronElastic		
Fission	/	/	G4LFission + G4NeutronHPFission(<19MeV)
Capture	/	/	G4LCapture + G4NeutronHPCapture(<19MeV)
Radioactivedecay	/	G4Radioactivedecay	/

Figure 10.2: Models used for the simulations performed with Geant4 version 9.4

## 10.3 Low statistics reconstruction of the Compton camera Point Spread Function in 3D prompt- $\gamma$ imaging of ion beam therapy

The aim of this experiment is to estimate the Point Spread Function (PSF) for both iterative and analytical methods using this specific device. The measured data is obtained by simulating the detection of a polyenergetic source. The PSF is compared to the one of the line cone approach [Roellinghoff *et al.* (2011)]. Although the data were simulated with measurement uncertainties, the reconstruction methods we implemented for this work do not model them. We used the Surface of Intersection method. Reconstructed images and statistical evaluation on repeated simulations are presented.

### 10.3.1 Source

A simulated polyenergetic photon point source emits  $\gamma$  particles according to the emission spectrum plotted in Figure 10.3. The source is located at  $(0, 0, 0)$  and  $7 \times 10^7$  photons are emitted isotropically. This statistics corresponds roughly to the amount of particles emitted by the distal slice when using about  $7 \times 10^8$   $^{12}\text{C}$  ions for irradiating a tumor of  $120 \text{ cm}^3$  within 39 energy slices and approximately  $10^4$  raster positions [Krämer *et al.* (2000)]. In this statistics, we have considered that the carbon ions are equally distributed over the energy slices to obtain a mean amount of detected photons. In fact, the number of incident ions in the proximal and distal energy slices (the shallowest and deepest energy layer respectively) are very different, the proximal one counting one tenth of the total of  $^{12}\text{C}$  [Park (2009)].

With the efficiency of the prototype,  $3.5 \times 10^5$  prompt- $\gamma$  photons are detected out of the  $7 \times 10^7$  particles emitted.

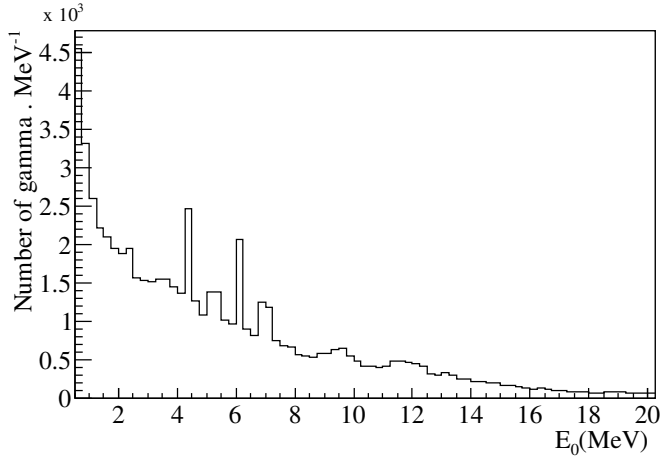


Figure 10.3: Emission spectrum of prompt- $\gamma$  particles between 0.5 and 20 MeV obtained with a carbon ion beam at 350 MeV/u irradiating a water phantom with  $10^5$  ions. Studies by Polf et al. [Polf et al. (2009)] showed that the prompt- $\gamma$  spectrum distribution measured during a proton irradiation is similar.

### 10.3.2 Data

In our data, a photon that scatters, delivering energy in only one layer of the stack, and interacts with the LYSO scintillator is defined as an event. We do not perform any energy selection thus the interaction in the scintillator might be an incomplete absorption of the particle. Random coincidences, as well as interactions made by other particles than photons that would hit the detector in a real hadrontherapy monitoring setup, were not simulated.

### 10.3.3 Results

#### Analytical reconstruction

Using the analytical approach, photons must meet the constraints imposed by the reconstruction method as mentioned in sections 3.1.2 and 5.4, which explains a difference between the number of detected photons and the number of valid ones. Figure 10.5 show images of the source described in section 10.3.1, reconstructed from  $3.2 \times 10^5$  selected photons out of  $3.5 \times 10^5$  detected. All images in figures are averages of 10 different reconstructed images (one per scatterer layer) and each layer provides an averaged reconstruction over 10 values of  $\theta_g \in [0, \frac{\pi}{4}]$ . With this prototype, for greater values of  $\theta_g$ , too few data items are acquired to generate images. We considered 40 bins for  $\beta \in [0, \frac{\pi}{2} - \theta_g]$  and 40 bins for  $\delta$  in  $(-\pi, \pi]$ . The reconstructed volume is composed of  $46^3$  cubic voxels of 1.7 mm size. During backprojection, we applied the Hanning filter  $h(\rho) = \frac{1}{2}(1 + \cos(2\pi \frac{\rho}{N}))$ , where  $N$  is the number of samples and  $r$  the coordinate in the frequency domain.

As expected from the previous studies in chapter 5, the position of the source is well identified in slices parallel to the detectors (see Figure 10.5 (a)) but is poorly reconstructed in the direction orthogonal to the detectors (Figure 10.5 (b)). The gray scale only gives relative information about the intensities of the voxels.

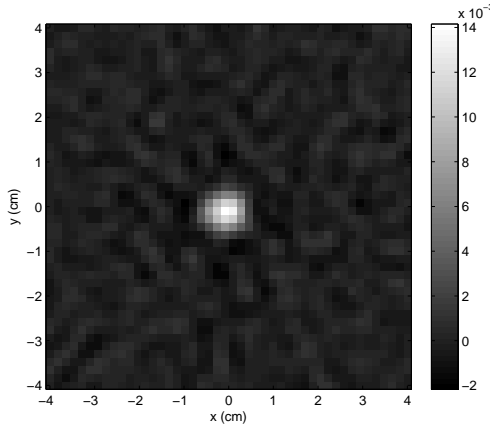


Figure 10.4: *Analytical reconstruction: cut at  $z = 0$  cm, parallel to the detectors* - Image of a point source reconstructed from simulated data acquired with a Compton camera having resolutions as indicated in section 10.1. The gray scale is in arbitrary units.

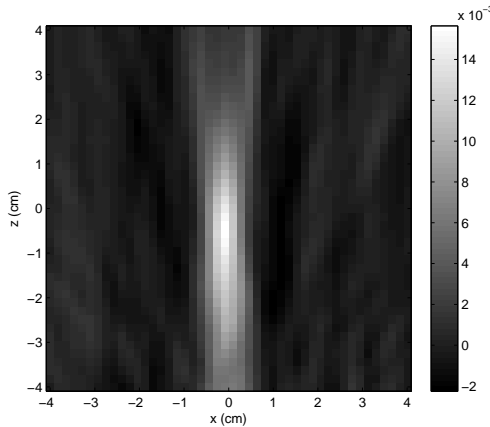


Figure 10.5: *Analytical reconstruction: cut at  $y = 0$  cm, orthogonal to the detectors* - Image of a point source reconstructed from simulated data acquired with a Compton camera having resolutions as indicated in section 10.1. The gray scale is in arbitrary units.

The reconstruction is performed with a relatively large amount of events. In order to reconstruct the source with a low amount of data as required for hadrontherapy monitoring, we need to decrease the number of spatial bin. But the resolution also undergoes an important decrease. As a consequence, the current version of our Filtered BackProjection method cannot provide a relevant tool for online monitoring of ion beam therapy.

## Iterative reconstruction

During a treatment, the yields of photons with energies above 1 MeV, as given by FLUKA, are 0.44 and 0.049 prompt- $\gamma$  per carbon ion and proton respectively [Robert *et al.* (2013)]. With the considered prototype, these rates lead to 100 and 1200 prompt- $\gamma$  detected per pencil beam respectively. Less sensitive to the lack of data thanks to the iterations and the probability model, this method may reconstruct images with a lower amount of events than required by analytical methods. Figure 10.6 shows reconstructed images with 3000 and 500 events. The algorithm was stopped after 15 iterations (no specific criterion was used). We applied then a median filter of size 3x3x3 to the reconstructed images. The volume surrounding the source is composed of  $81^3$  cubic voxels of 0.9 mm size. In slices parallel to the detectors, the source can be identified even with as few as 500 events. We note that the solid angle issue producing an elongation of the source in the direction orthogonal to the detectors is once again visible on the reconstructed images. In some of them, artifacts can be observed towards the detectors. One example is illustrated in Figure 10.7.

### 10.3.4 Point Spread Function

Images reconstructed are a realization of the three dimensional Point Spread Function (PSF) of the detector. By projecting the 3D image on some virtual beam trajectory, a 1D PSF may be obtained on a post-reconstruction image based profile. We compare it to a 1D PSF calculated on a pre-reconstruction, per-cone based profile. For each event, the associated cone intersects the beam trajectory supposed to be known, in at most two points. One of them is (close to) the emission point. The distribution of the points obtained by intersecting all the cones with the beam gives a 1D profile where the main peak corresponds to the source. This fast and easy to implement method was applied to PSF reconstruction in [Roellinghoff *et al.* (2011)]. Hereafter, we will call it the line-cone reconstruction method.

We fitted the sum of two gaussian distributions, one corresponding to the source, the other corresponding to the background, to each profile. The FWHM were then calculated from the fits.

## Analytical reconstruction method

Figure 10.8 shows the PSF calculated from the analytical reconstruction method and the line-cone reconstruction method, both reconstructed from  $3.2 \times 10^5$  photons. The solid line corresponds to the one generated with our reconstruction method and the dashed line corresponds to the line-cone intersection result. The two profiles are in good agreement, the analytical method improving slightly the resolution in directions parallel to the detectors. In this example, we obtained a FWHM of 7 mm for the 1D PSF (line-cone 10 mm). For the analytical method, the oscillations corresponds to the Gibbs phenomenon.

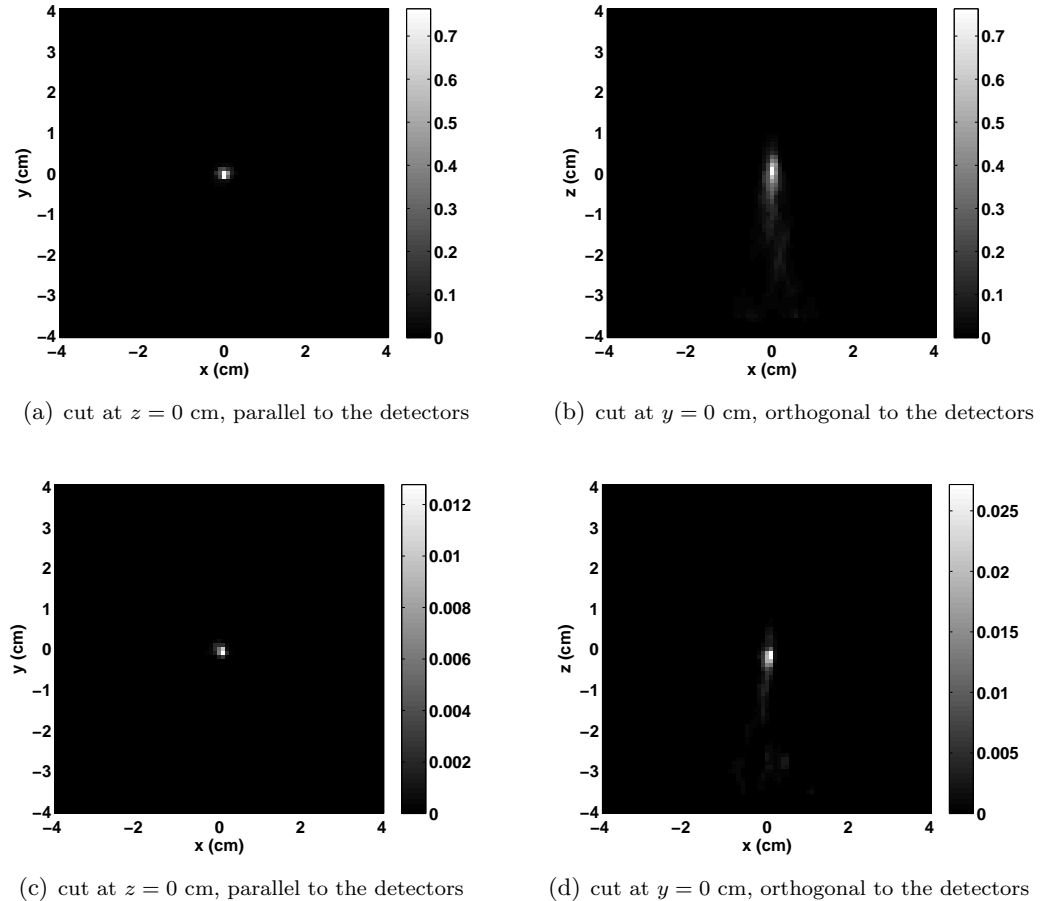


Figure 10.6: *Iterative reconstruction* - Image of a point source reconstructed from simulated data acquired with a Compton camera having resolutions as indicated in section 10.1 with the iterative method. The number of events is limited to 3000 (a) and (b), 500 (c) and (d).

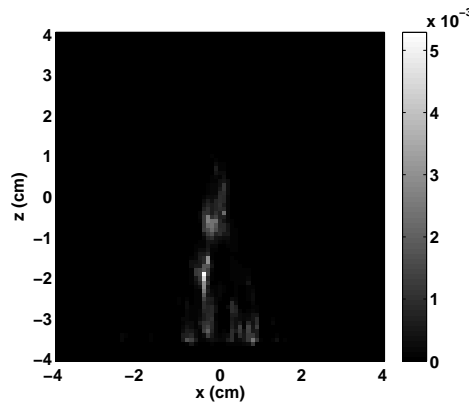


Figure 10.7: *Iterative reconstruction* - Example of poor reconstruction in the orthogonal direction on the detectors. Reconstruction with 500 events, 15 iterations. Cut at  $y = 0$  cm.

### Iterative reconstruction method

The 1D profile of the reconstruction with 500 events (Figure 10.6) is shown in Figure 10.9. The value of the FWHM for the 1D PSF is 4 mm for this example (line-cone

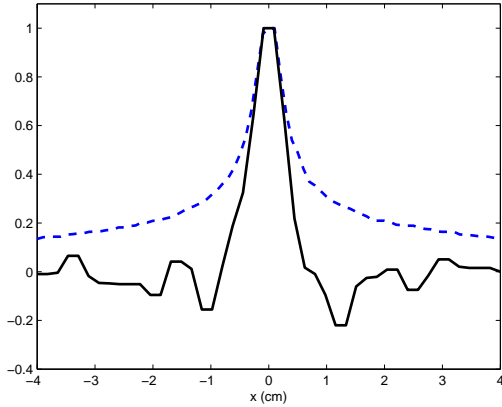


Figure 10.8: *Analytical reconstruction* - 1D Point Spread Functions of a point source. The solid line corresponds to the profile of the reconstructed source with the analytical method, FWHM = 7 mm. The dashed line corresponds to the line-cone reconstructed profile, FWHM = 10 mm. For both cases,  $3.2 \times 10^5$  photons were used.

6.5 mm).

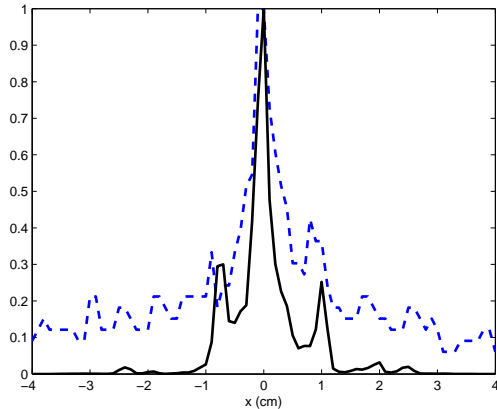


Figure 10.9: *Iterative reconstruction* - 1D profiles along the  $x$  direction of a point source. 500 events are used for the reconstruction. The solid line corresponds to the profile of the reconstructed source with the iterative method. FWHM = 4 mm. The dashed line corresponds to the line-cone reconstructed profile, FWHM = 6.5 mm.

In order to evaluate the reproducibility of the results, we reconstructed a large number of images for data samples composed of (a) 500, (b) 1000 and (c) 3000 events, respectively. We computed the 1D profiles along the  $x$  direction, and we calculated the FWHM and the error in the position of the reconstructed source with regards to the expected position. The data file was the same for all the cases (a), (b) and (c). The number of reconstructed images was 488 for (a) and 88 for (b) and (c). Box plots calculated for the 3 setups represent the first and the third quartiles, as well as the median of the data. The end of the whiskers represent the lowest datum still within 1.5 Inter Quartile Range (IQR)

of the lower quartile, and the highest datum still within 1.5 IQR of the upper quartile. Figure 10.10 (a) shows results obtained for the FWHM along the  $x$  direction. Results in the  $y$  direction and in the  $x$  direction are similar and only the last ones are reported here. For these directions, we can achieve with high probability a FWHM of less than 10 mm even with only 500 events, the median value being around 5 mm. This value depends on the good detection of particles which, in turn, is dependent on the total absorption and measurement uncertainties. The dispersion of the values decreases when the size of the data set increases, but medians remains roughly the same.

In Figure 10.10 (a), box plots in dashed line represent the dispersion of the FWHM values obtained with line-cone reconstructed profiles. We note that the median values are higher, around 9 mm.

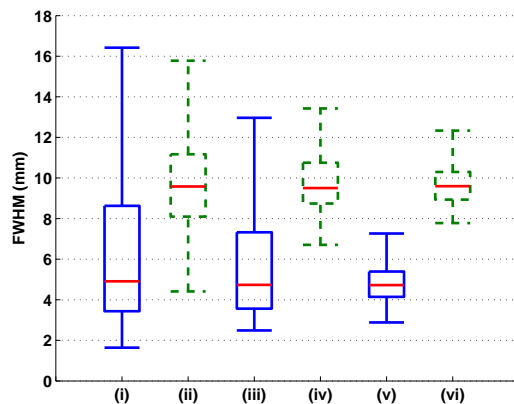


Figure 10.10: *Iterative reconstruction* - Box plots representing the dispersion of the FWHM values of 1D PSF along the  $x$  direction when (i), (ii) 500 events, (iii), (iv) 1000 events and (v), (vi) 3000 events are selected for each reconstruction. Box plots in solid line represent the dispersion of the values obtained using the iterative reconstruction method. Dashed box plots represent the dispersion of the values obtained using the line-cone reconstruction method.

In Figure 10.11 we show the bias of the estimated position of the maximum intensity of the 1D fitted PSF. The bias rapidly decreases when the number of events increases.

### 10.3.5 Influence of the position of the source

In order to study the spatial dependency of the 3D PSF, we compared the image of a centered point source to images of point sources shifted with respect to the center of the detector, in the  $y$  direction. Two shifts, the first one of 2 cm (still on the top of the detector) and 5 cm (out of the surface of the scatter detector) were considered. For each shift, 3000 acquired events were simulated and the images were reconstructed with the iterative LM-MLEM method. Although the number of events was hold the same, the reduction of the solid angle covered by the camera at the source position is expected to worsen the results. The reconstructed images were scaled to have the same maximum value

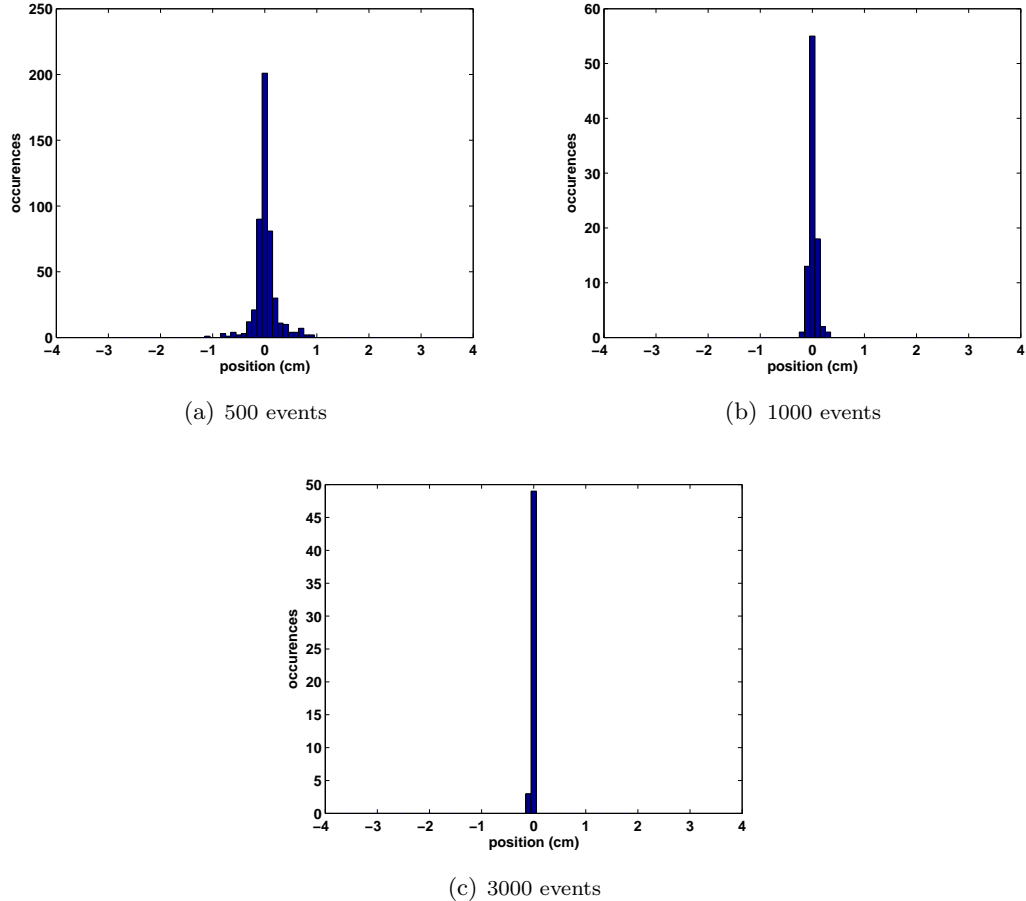


Figure 10.11: *Iterative reconstruction* - Histograms of the estimated position of the maximum intensity of the 1D fitted PSF.

then superimposed in Figure 10.12 (a) where the slice at  $z = 0$  cm is shown. As the shift gets larger, a lower spatial resolution, as well as a loss of the symmetry may be observed. A visual inspection of the 1D PSF functions, plotted in Figure 10.12 (b), followed by the calculation of the Modulation Transfer Functions (MTF) plotted in Figure 10.12 (c) confirm that the spatial resolution degrades with the shift. It is likely that accounting for the variations of the sensitivity  $s_j$  would lead to some improvement of the results.

### 10.3.6 Discussion

The 1D PSF gives a first insight into the achievable resolution of the detection system. As the prompt- $\gamma$  photons are emitted roughly along the incident ion trajectory, the 1D PSF may be obtained by projecting the 3D image onto this direction. However, determining the position of the distal dose fall-off (i.e. the position of the Bragg peak) is an edge-finding problem. Nevertheless, the uncertainty on the fall-off localization should be smaller than the FWHM of the PSF. The achievable precision is conditioned by the properties of the detectors but also by the  $\gamma$  and background statistics. Note that millimeter accuracy was

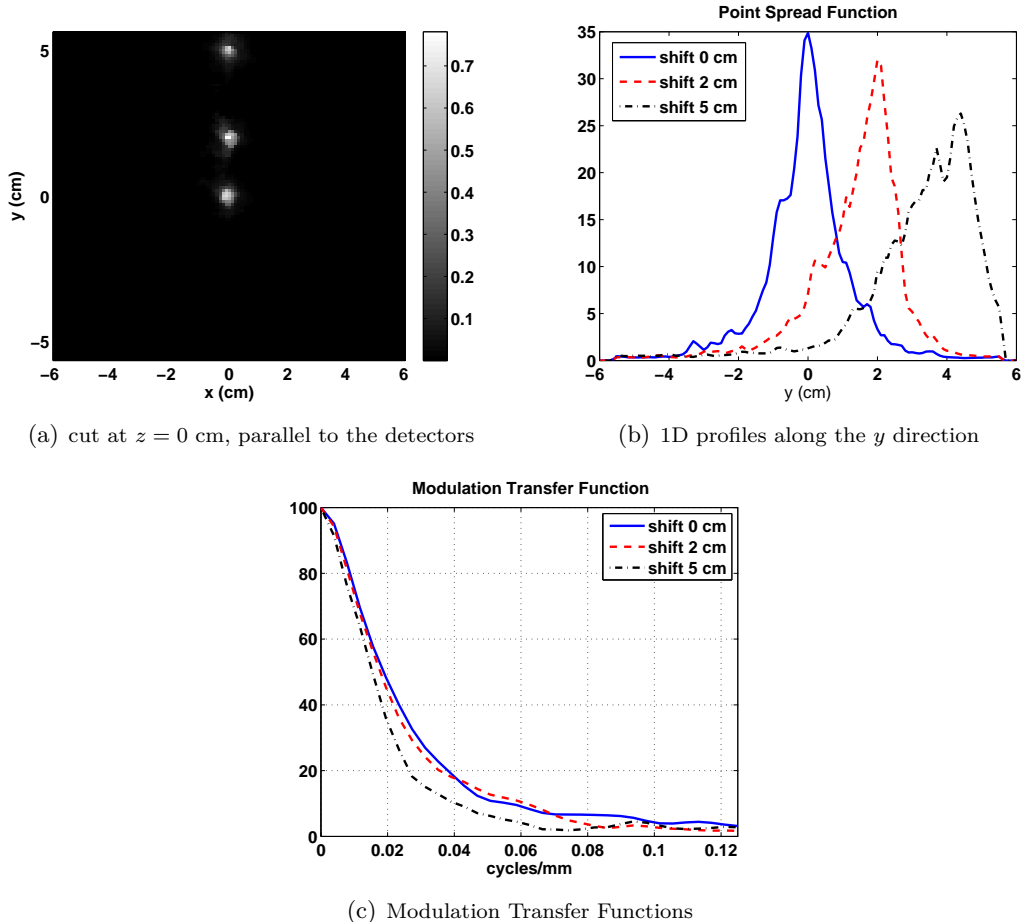


Figure 10.12: *Iterative reconstruction - Influence of the shift of the source on the reconstruction.* (a) Reconstructed sources, cut at  $z = 0$  cm. (b) Profile along the  $y$  direction for each reconstructed image. The solid line, the dashed line and the dash-point line represent the source centered, shifted of 2 cm and 5 cm respectively. (c) Modulation Transfer Functions of each profile. The continuous line, the dashed line and the dash-point line represent the source centered, shifted of 2 cm and 5 cm respectively.

reported in [Mackin *et al.* (2012)], on the basis of data simulated from an ideal detector and with  $10^6$  acquired events Hadrontherapy monitoring by means of nuclear imaging currently aims at controlling ion ranges. Both analytical and iterative methods we investigated may achieve a few millimeter resolution compatible with requirements of the hadrontherapy monitoring in directions parallel to the detectors. The use of a second orthogonal camera would allow the recovery of the resolution of the image in the direction orthogonal to the detectors. The analytical method is faster than the iterative one, but is more sensitive to the lack of data, a main issue in this medical application. On the contrary, the iterative method allows a very fine resolution in the directions parallel to the detectors and high quality of reconstructed images even with a low event statistics, but the computation time and the memory capacity needed may be limiting factors. GPU implementation, or ordered-subsets approaches may overcome these limitations.



# Chapter 11

---

## Application to data from the Research Center of Dresden-Rossendorf, Germany

---

This study is part of a collaborative work between the different teams in charge of developing reconstruction algorithms within the Workpackage 3 of ENVISION. The objective is to compare all proposed methods by performing 2D reconstructions and by analyzing the performances for each method. Although our methods enable to reconstruct 3D images, we only focus on the 2D slices where the sources are located. We only present here the results obtained for the CV method.

### 11.1 Simulation context

At the Research Center of Dresden-Rossendorf, Department of Radiation Physics, another Compton camera prototype is developed. The device is composed of a scatterer in Cadmium Zinc Telluride (CZT) of size  $2 \times 2 \times 0.5$  cm $^3$ . The absorber is composed of a scintillator in Cerium-doped Lutetium Oxyorthosilicate (LSO) of size  $5.4 \times 5.4 \times 1$  cm $^3$ . We can note that in comparison with all the previous simulated devices, this Compton camera is pretty small. Figure 11.1 shows a sketch of the Compton camera prototype and the image to be reconstructed. The scatterer has a lateral spatial resolution of 1 mm. Its energy resolution  $\delta E_{sct}$  is modeled by a Gaussian distribution with FWHM calculated with the following formula:

$$E_{FWHM} = 6 + 0.45 \times \sqrt{E_1} \quad (11.1)$$

The absorber has a lateral spatial resolution of 2 mm. The energy resolution  $\delta E_{abs}$  is also modeled by a Gaussian distribution with FWHM calculated with the following formula:

$$E_{FWHM} = 4.12 \times \sqrt{E_2} \quad (11.2)$$

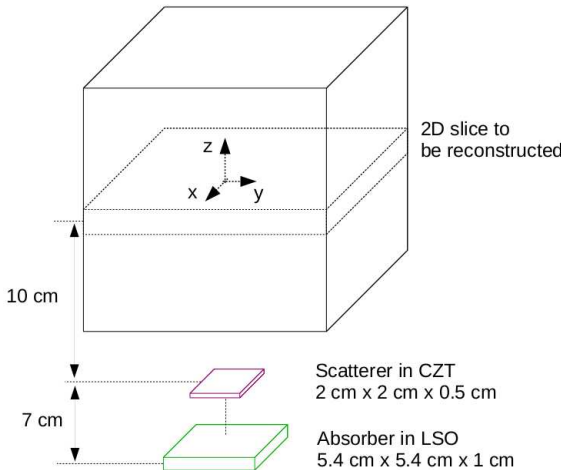


Figure 11.1: Sketch of the simulated Compton camera with the scatterer composed of a layer in CZT and the absorber composed of a LSO scintillator.

Different monoenergetic  $\gamma$  sources emitting photons of energy 1.275 MeV that are detected by the simulated device, have been simulated. Simulations used GEANT4 version 9.3 with the physicslist QGSP\_BIC together with the LivermorePolarizedModel in order to model the Compton scattering as exactly as possible. By using the LivermorePolarizedModel, the Doppler-broadening is also included. Only the coincident interactions in the detector layers are measured. Each photon is simulated individually.

Three scenarii have been simulated: (i) 3 point sources ; (ii) a line source ; (iii) a hot-cold phantom. We reconstructed images of  $20\text{ cm} \times 20\text{ cm}$  divided in  $200 \times 200$  pixels. Thus, the pixels are of 1 mm side length. We do not perform the selection of the detected particle on the base of a full absorption. We apply a median filter of size  $3 \times 3$ . For the system matrix calculation, we used the model that does not account for the solid angle subtended by the element of scatterer at the emitting point since it provided better results in our study from section 9.4.

## 11.2 Three Point Sources

In this section, we reconstructed three point sources located at  $(0, 0, 0)$  cm,  $(2, 2, 0)$  cm and  $(5, 5, 0)$  cm, respectively. Figure 11.2 shows reconstructions performed with 7500 events, at the iteration 0, 5, 10 and 20 respectively. We can observe that 2 out of the 3 point sources are well reconstructed. The last one, located at  $(5, 5, 0)$  cm is barely identifiable. This is due to the localization of the source with respect to the detectors.

We already noticed this phenomenon in chapter 9 section 9.3.2. The source is visible but seems to be too far from the scatterer even using the model without accounting for the solid angle. The difficulty in reconstructing this point certainly comes from the low proportion of events coming from the farthest source in the data.

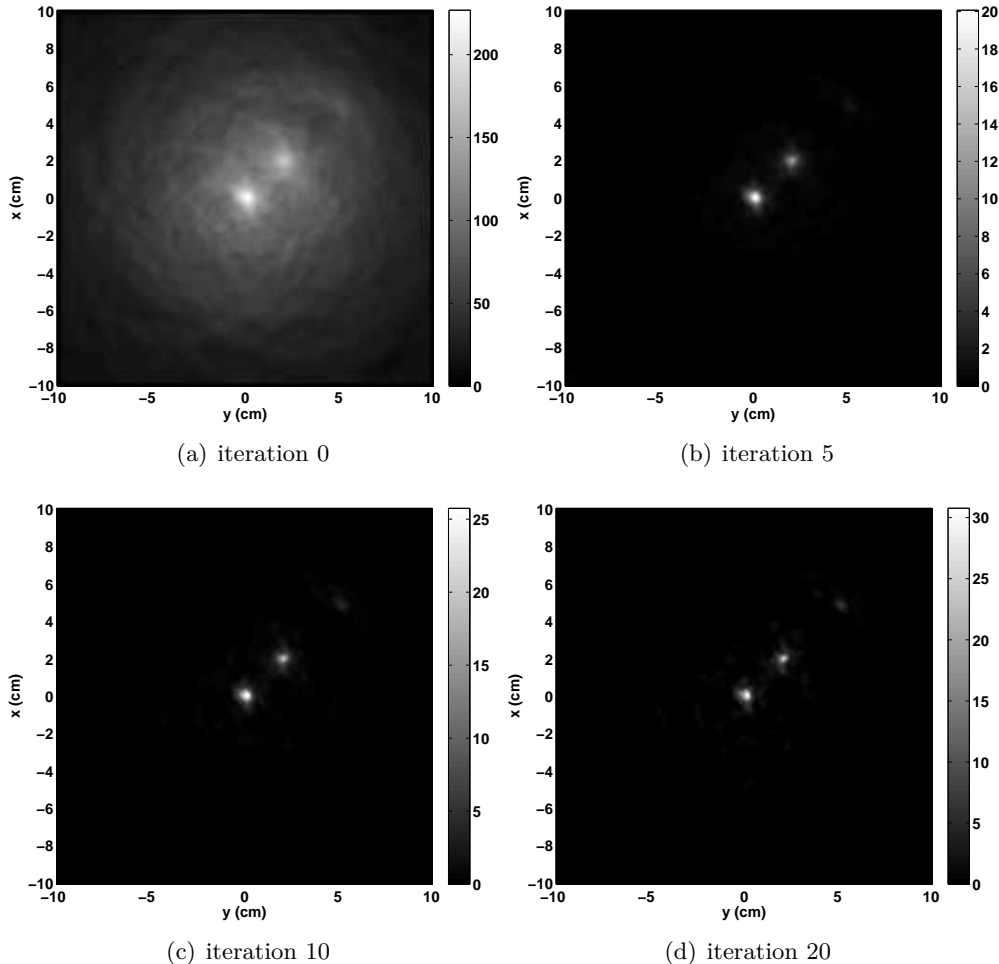


Figure 11.2: *Iterative reconstruction:* - Reconstruction of 3 point sources with the method CV, using 7500 events. 2D slice at  $z = 0$  cm.

### 11.3 Line source

In this section, we reconstructed a line source of 5 cm length starting from  $(-2, 0, 0)$  cm and ending at  $(3, 0, 0)$  cm. Figure 11.3 shows reconstructions performed with  $10^4$  events, at the iteration 0, 5, 10, and 20 respectively. From the reconstructed images, we can note that the method seems to provide relatively good results. In order to confirm this trend and since the source is a line, we calculated the Full Width at Half Mean. The reconstructed profile is shown figure 11.4, the dashed line representing the calculated half mean. The Full Width at Half Mean is 5.01 cm, close to the length of the simulated line,

which confirms that the source is relatively well reconstructed.

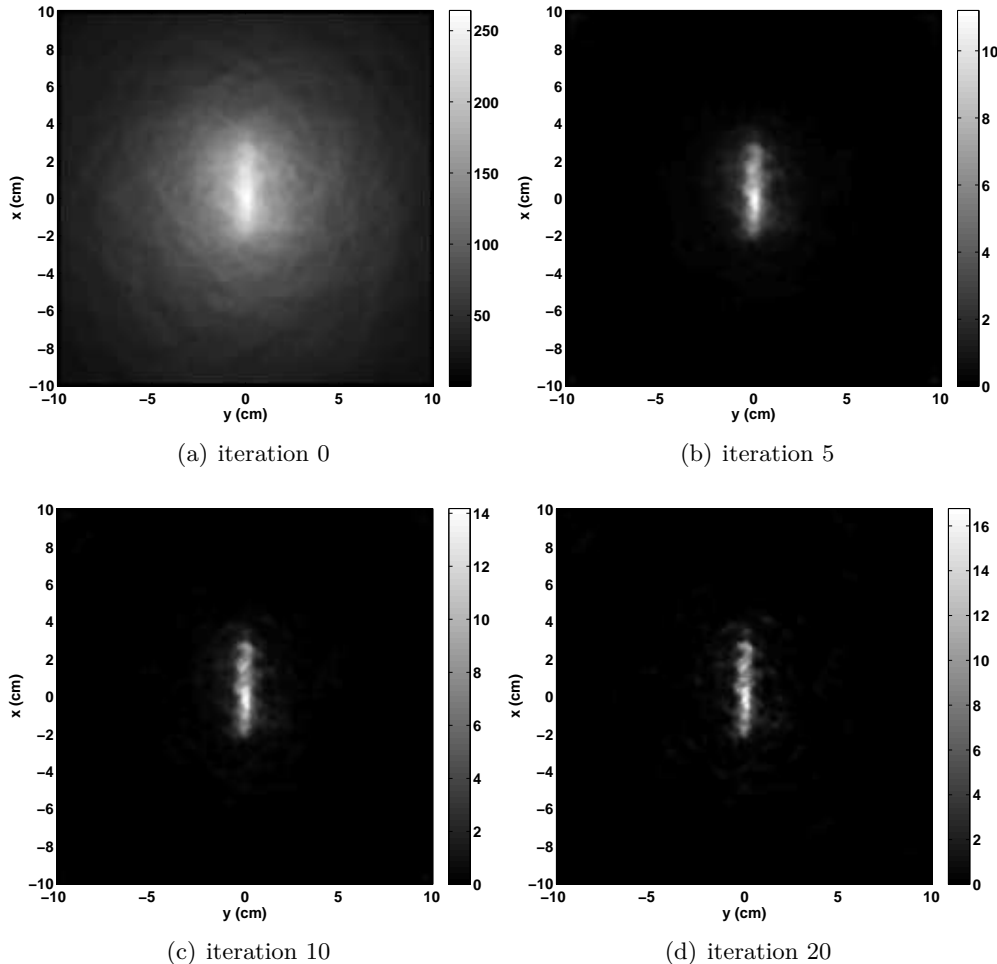


Figure 11.3: *Iterative reconstruction:* - Reconstruction of a line source with the method CV, using  $10^4$  events.

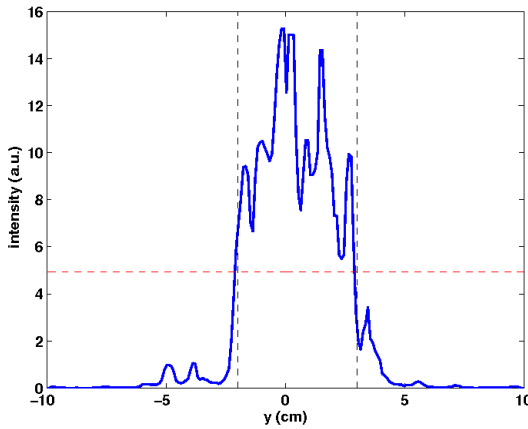


Figure 11.4: Reconstructed profile of the line source in the direction  $y = 0$  cm. The horizontal dashed line represents the half mean. The vertical dashed lines represent the range of the expected reconstructed line. The mean and standard deviation of the central 80% measurement are 9.9 and 2.9 in arbitrary units, respectively. The Full Width at Half Mean for this reconstruction is 5.01 cm, close to the length of the source which is of 5 cm.

## 11.4 Hot-Cold phantom

In this section, a 2D hot-cold  $\gamma$  source phantom has been reconstructed. The idea is that depending on the area, the activity of the source will change leading to hot and cold regions. The figure 11.5, the phantom is composed of a disk of 5 cm of radius, centered at  $(1, 1, 0)$  cm with an activity of  $A = 1$ . The hot disk has an activity of  $A = 2$  and is centered at  $(-1, 0, 0)$  cm. The hot disk is of 2 cm radius. The cold disk is also of 2 cm radius. Its activity is of  $A = 0$  and is centered at  $(3, 2, 0)$  cm.

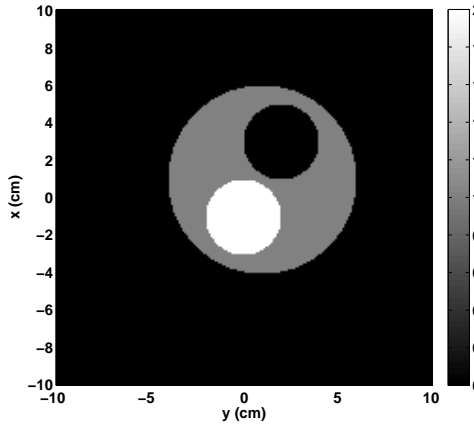


Figure 11.5: Sketch of the 2D hot and cold phantom. The disks B, H, C correspond to the background, hot and cold zones respectively, with an activity of  $A = 1$ ,  $A = 2$  and  $A = 0$ , respectively.

Giving the nature of the source to reconstruct, a large number of events is necessary. We performed a reconstruction using  $35 \times 10^3$  events and made 20 iterations. Figure 11.6 show the reconstructed source at iteration 0, 5, 10 and 20. From the resulting images, we

can identify the hot and cold ROIs, the source is relatively well reconstructed. However, the cold part is not exactly in the shape of a disk. Increasing the number of iterations increases the granular aspect of the reconstructed image. The distributed nature of the source makes it difficult to reconstruct as precisely as with the previous sources. This is clearly visible on the calculated NMSE presented in figure 11.7 where the value after 20 iterations is in the order of  $10^{-2}$ .

We also reconstructed the source using only photons that have undergone a full absorption and calculated also the NMSE from the equation (9.1). Results are presented in figures 11.8 for the 2D slices and 11.7 for the NMSE. As expected the NMSE is better when applying a energy window selection. But we also can note from the images that the shape of the cold disk and the background disk are better complied.

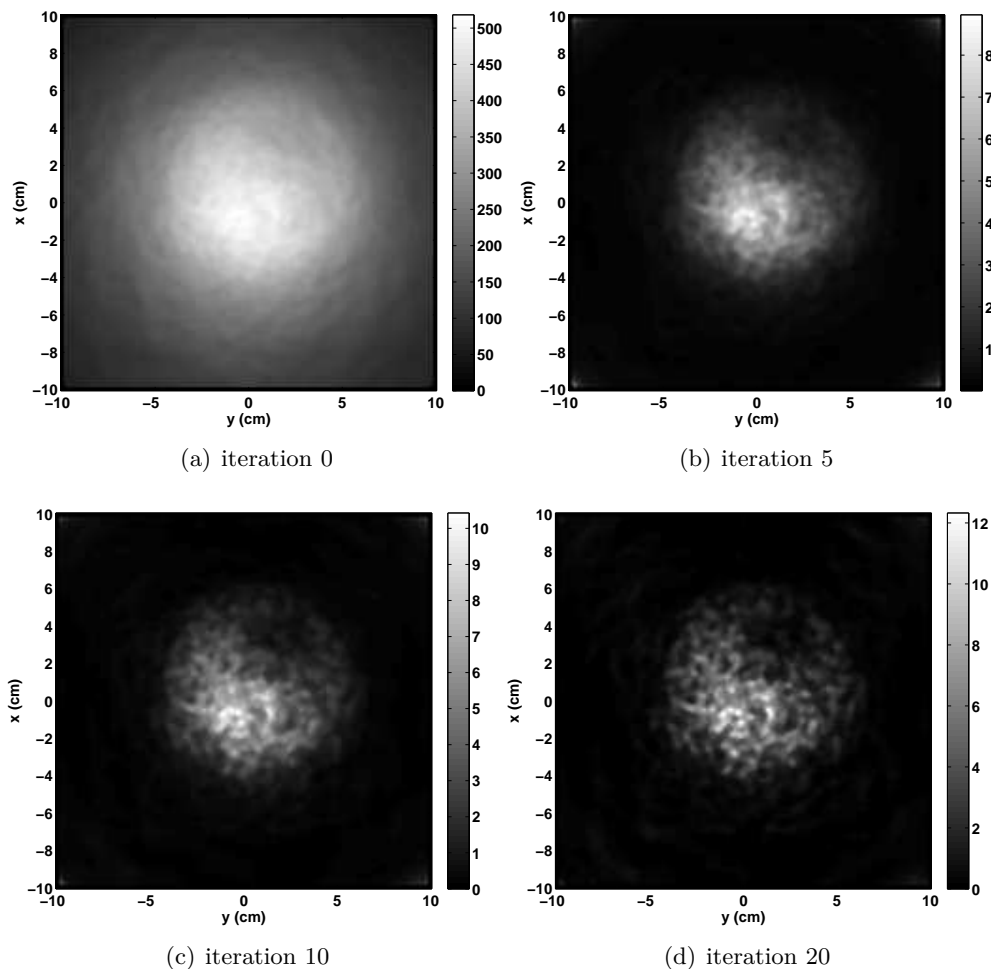


Figure 11.6: *Iterative reconstruction: Center of Voxel* - Reconstruction of a hot-cold phantom source with the method CV, using  $35 \times 10^3$  events, without energy selection.

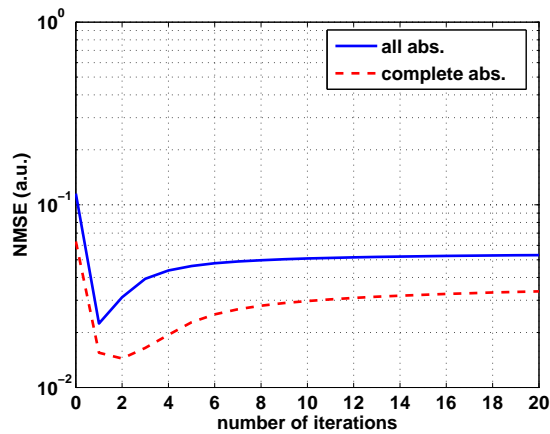


Figure 11.7: *Iterative reconstruction: Normalized Mean Squared Error - NMSE as function of the iteration calculated from the reconstructed 2D hot-cold phantom. The dashed line and the solid line respresent the NMSE calculated from the reconstructed image with and without absorption selection, respectively.*

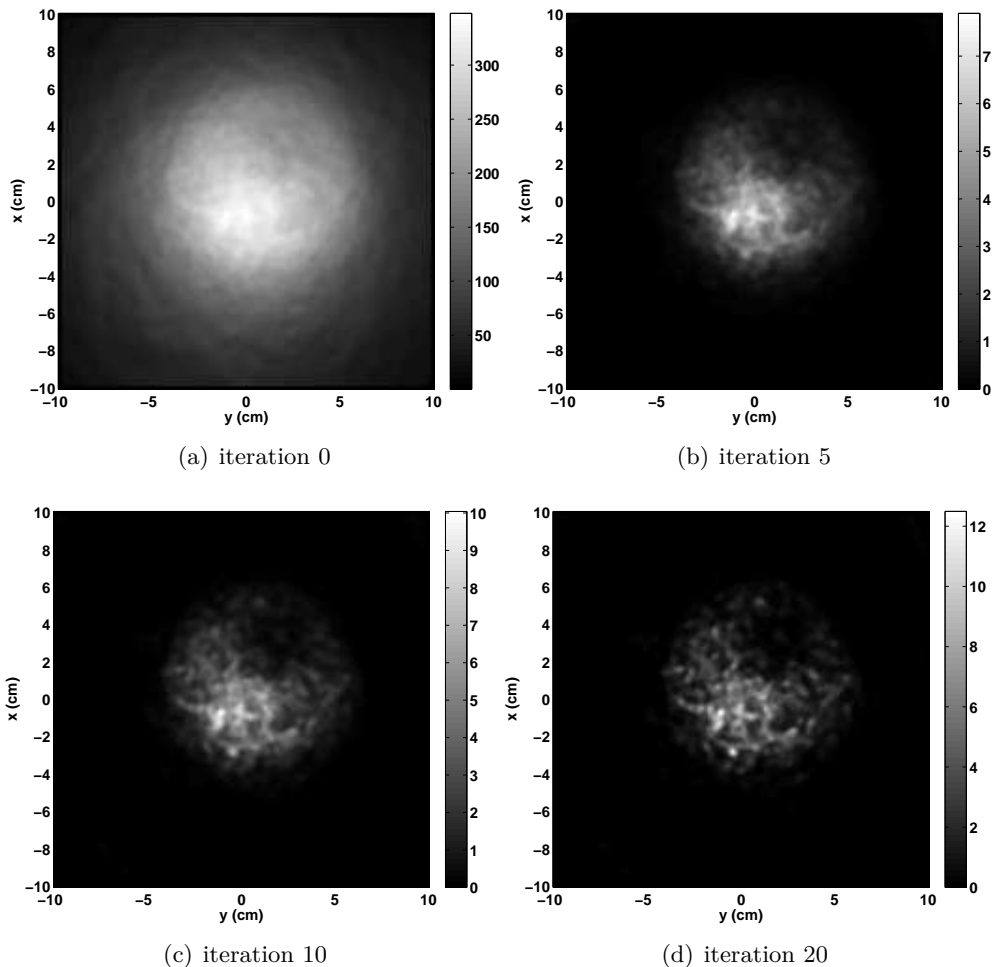


Figure 11.8: *Iterative reconstruction: Center of Voxel - Reconstruction of a hot-cold phantom source with the method CV, using  $19 \times 10^3$  events, with energy selection.*

## 11.5 Conclusion

This study is at its preliminary state. We note that the proposed CV method perform quite good reconstructions and the next step will be to compare the performances with the other methods developed by the different teams of the WP3.

For the moment, this study has enabled to show the importance of a right coverage of the source by the device, as seen in the case of the 3 points source. The results are also in good agreement with the required precision in hadrontherapy monitoring, since we can perform reconstructions with a few millimeter resolution for a line source.

The reconstruction of the 2D phantom provides promising results. Nevertheless it has shown that it needs further investigation to obtain reconstructed image closer to the one expected especially in the case of wide and distributed sources. The median filter that is applied to the resulting image attenuates the granular aspect. We only apply it after the iterative process. It may be interesting trying to apply this filter at each iteration.

## VI Conclusion

---



# Conclusions and perspectives (in French)

L'objectif de ces travaux de thèse était de développer des méthodes de reconstruction d'image 3D pour la caméra Compton. Ces méthodes devaient être développées dans l'optique d'une utilisation en contrôle de traitement par hadronthérapie. Par conséquent, une des exigences principales était la qualité des résultats dans un contexte de reconstruction avec peu de données.

Nous avons proposé une méthode analytique et deux méthodes itératives pour l'imagerie Compton. Dans ce chapitre, nous résumons dans un premier temps nos contributions, puis nous proposons quelques perspectives.

## Contributions

Nous avons d'abord mis au point une méthode analytique de rétroprojection filtrée. Nous avons vu que cette méthode est trop sensible à l'absence de données afin de se conformer aux exigences du contrôle en ligne en hadronthérapie (faibles nombre de données, la résolution millimétrique). Néanmoins, elle permet une reconstruction satisfaisante lorsqu'une grande quantité d'événements est acquise.

Dans le cadre des méthodes itératives, une première contribution est l'étude du modèle probabiliste pour l'estimation des éléments de la matrice système. Nous avons ensuite mis en place un algorithme de maximisation de la fonction de vraisemblance et nous avons proposé deux approches numériques pour le calcul de la matrice système, basées sur une discréétisation originale du cône Compton. Une première version de cette méthode, la méthode Surface of Intersection, ne tient pas compte des incertitudes de mesure d'énergie. La deuxième version, la méthode Volume of Intersection, prend en compte ces incertitudes. Nous avons remarqué que l'algorithme proposé permet d'effectuer des reconstructions efficaces avec un faible nombre d'événements, comme l'exige le contrôle en hadronthérapie, la méthode VI étant plus performante en termes de qualité de reconstruction que la méthode SI. Néanmoins, les méthodes en sont à leur première étape de développement, par conséquent, les reconstructions sont réalisées pour des sources de rayonnement relativement simples. Les résultats prometteurs doivent être confirmés par des simulations plus réalistes, et par la suite avec des données réelles.

---

Une troisième méthode, Center of Voxel, a été également implémentée. Cette méthode est un algorithme basé sur le même modèle probabiliste que nous avons proposé mais avec une approche numérique simplifiée. Le calcul est inspiré de la méthode décrite dans [Zoglauer (2005)] utilisée à l'origine pour des applications en astronomie. Nous avons remarqué alors que cet algorithme donnait des résultats relativement similaires à ceux de la méthode VI, mais semble être plus rapide et plus facile à implémenter.

Dans le cadre du projet ENVISION, nous avons également mis à l'essai nos méthodes en utilisant des données obtenues à partir de simulations de prototypes de caméra Compton développées par des équipes du Groupe de Travail 3 auquel nous appartenons. Au travers des études réalisées, nous avons pu constater que nos algorithmes de reconstruction présentaient certaines limites. Certaines caractéristiques du système d'imagerie tels que la taille des détecteurs impliquent des effets indésirables sur les images reconstruites. Dans le cas d'un dispositif seul et immobile, la résolution dans la direction orthogonale par rapport aux détecteurs est peu satisfaisante, lorsque ces derniers ne sont pas assez larges. En outre, nous avons pu constater que les points de la source n'étant pas directement couverts par le dispositif peuvent ne pas être reconstruits de manière précise. Ces questions nécessitent davantage d'études, mais l'utilisation d'un second dispositif de caméra Compton, ou acquérir plus de photons, pourraient diminuer les effets indésirables. Ces travaux mettent en évidence le lien étroit entre le processus d'acquisition avec un dispositif particulier et une reconstruction de qualité. Une contrainte de l'application de l'imagerie en hadronthérapie est le contrôle en temps réel. A leur stade de développement, nos méthodes ne fonctionnent pas en temps réel. Le calcul de la matrice système requiert d'importantes ressources temporelles et de mémoire. Ces deux facteurs dépendent intrinsèquement du nombre d'événements utilisés lors de la reconstitution et du nombre de voxels dans l'image 3D à reconstruire.

## Perspectives

Notre travail sur les méthodes de reconstruction en imagerie Compton avec application en hadronthérapie ouvre plusieurs perspectives.

Actuellement, la méthode de RétroProjection Filtrée n'est pas adaptée pour effectuer des reconstructions avec un faible nombre de données. Néanmoins, surmonter cette limitation serait très intéressant car les méthodes analytiques sont rapides et évitent les problèmes de convergence, l'utilisation de ressources de mémoire est beaucoup plus faible que dans le cas des méthodes itératives, au moins pour les applications en médecine nucléaire.

Des études plus poussées sur les performances des méthodes de reconstruction itérative doivent être effectuées. Le modèle théorique que nous proposons dans ce manuscrit, pour l'estimation des éléments de la matrice système, ne semblent pas être optimal, du moins, lorsque la sensibilité du détecteur est considérée comme uniforme en chacun des points de l'image. Des tests supplémentaires seront nécessaires afin de choisir le modèle qui sera le plus adéquat pour la reconstruction à effectuer.

---

Une comparaison avec les méthodes développées dans le cadre du projet ENVISION est un objectif à court terme. Les études menées sur le développement du dispositif de caméra Compton fourniront des contraintes opérationnelles plus précises qui donneront un contexte impartial afin de comparer et de conclure sur la méthode qui doit prévaloir.

En termes de développement, les méthodes proposées peuvent être grandement améliorées. L'utilisation de la variante OSEM à la place de l'algorithme LM-MLEM, ainsi que la mise en place d'une implémentation GPU permettra une réduction importante du temps de nécessaire à la reconstruction qui est actuellement un obstacle majeur à l'application de nos méthodes.

En outre, les études seront à mener sur des sources plus complexe, en terme de forme ou de contexte. Des travaux à partir d'un traitement en hadronthérapie simulé, puis sur des données réelles font en effet parti d'un objectif majeur.



# Chapter 12

---

## Conclusions and perspectives

---

The aim of this thesis work was to develop 3D image reconstruction methods for Compton cameras. The associated operational constraint was the application of these methods to hadrontherapy monitoring. Hence, one main requirement is the quality of the results in condition of low number of acquired data.

We proposed an analytical method and two iterative ones, to perform Compton imaging. In this chapter, we first summarize our contributions, and then propose some perspectives.

### 12.1 Main contributions

We first developed an analytical method in the form of a Filtered BackProjection algorithm. We have seen that this method is too sensitive to the lack of data in order to comply with the hadrontherapy requirements, i.e. low statistics data, millimetric resolution. Nevertheless it yields a satisfactory reconstruction when a large amount of events is acquired.

In the scope of iterative methods, a contribution is the study of the probabilistic model for the estimation of the elements of the system matrix. We then implemented a List-Mode Maximum Likelihood Expectation Maximization algorithm and we derived two numerical methods to calculate the system matrix based on a novel discretization of the Compton cone. A first version of this method, the Surface of Intersection method, does not account for the energy measurement uncertainties. The second version, the Volume of Intersection method, accounts for these uncertainties. We noticed that the proposed algorithms enable to perform effective reconstructions with a low number of events, as required for the

hadrontherapy monitoring application, the VI method being more performant in terms of quality of reconstruction than the SI method. Nevertheless, this study we carried out is at its early stages of development, hence, the reconstructions are made for relatively simple sources. The promising results must be confirmed with more realistic simulations, and even real data.

A third method, Center of Voxel method, has been implemented. It consists in a simplified algorithm that is based on the same probabilistic model and on lower level quadrature formula. The calculation is inspired from the method described in [Zoglauer (2005)] originally used for astronomy applications. We noticed then that this algorithm provided relatively similar results as with the VI method, and also appears to be faster and easier to implement.

Within the framework of the ENVISION project, we also experienced our method using simulated data obtained from simulated Compton camera prototypes of the WorkPackage 3 we belong to. With the studies carried out, we could notice several limitations of our proposed methods. Some features of the device such as the size of the detectors implies undesirable effects on the reconstructed images. In the case of a single stationnary device, the resolution in the direction orthogonal to the detector is unsatisfactory when the size of the scatterers are not large enough. In addition, we could note that the points from the source not being directly covered by the device might not be well reconstructed. These issues requires more investigations, but the use of a second Compton camera device, or acquiring more photons might reduce the limitation. This work highlights the close link between the acquisition process with a specific device and performing a good reconstruction. One operationnal constraint of hadrontherapy monitoring is real time control. At their state of development, our methods do not work on real time. The calculation of the system matrix is really time consuming and requires important memory resources. The time consumption and memory required depends on the number of events used during the reconstruction and the number of voxels of the volume to reconstruct.

## 12.2 Perspectives

Our work with the reconstruction methods for Compton imaging for hadrontherapy application open several perspectives.

The FBP method in its current state of development is not well suited for reconstruction with low statistics data. Nevertheless, overcoming this limitation would be of great benefit since FBP methods are fast and avoid convergence issues, use much lower memory resources than iterative methods, at least for nuclear medical applications.

Further investigation on the performances of the iterative reconstruction methods should be performed. The theoretical model we proposed in this manuscript, for the estimation of the elements of the system matrix does not seem to be optimal at least when the sensitivity of the detector is considered uniform at each points from the image. Further studies will enable to decide which model fits the best the reconstruction to perform.

Comparison with the methods developed within the framework of the ENVISION project is a short-term objective. The studies carried out on the development of the Compton camera device will provide more precise operational constraints that will give a impartial context in order to compare and conclude on which method should prevail.

In terms of development, the proposed methods can be greatly enhanced. The use of the Order Subset method instead of the LM-MLEM, and a GPU implementation will provide an important reduction of the consumption time that is currently a major limitation in the application of our methods.

Since this work is at its early stages, studies conducted on more compex source, on simulated treatment and then on real data is indeed a next objective.

# Publications

## INTERNATIONAL PEER-REVIEWED JOURNAL

**X. Lojacono**, M.-H. Richard, J.-L. Ley, E. Testa, C. Ray, N. Freud, J.-M. Létang, D. Dauvergne, V. Maxim, R. Prost, “Low statistics reconstruction of the Compton camera Point Spread Function in 3D prompt- $\gamma$  imaging of ion beam therapy”, in press, IEEE – Transaction on Nuclear Science

M.-H. Richard, M. Dahoumane, D. Dauvergne, M. De Rydt, G. Dedes, N. Freud, J. Krimmer, J.-M. Letang, **X. Lojacono**, V. Maxim, G. Montarou, C. Ray, F. Roellinghoff, E. Testa, A.-H. Walenta, “*Design Study of the Absorber Detector of a Compton Camera for On-Line Control in Ion Beam Therapy*”, *IEEE Transactions on Nuclear Science* 59-5 (1850-1855), 2012

## INTERNATIONAL PEER-REVIEWED CONFERENCE PROCEEDINGS

**X. Lojacono**, V. Maxim, A. Zoglauer, F. Peyrin, R. Prost, “*A filtered backprojection reconstruction algorithm for Compton camera*”, Fully 3D, Potsdam – Germany, 2011, Conference proceedings (96:99) <http://www.fully3d.org/2011/Fully3D2011Proceedings.pdf>

**X. Lojacono**, M.-H. Richard, C. Ray, D. Dauvergne, E. Testa, N. Freud, J.-M. Létang, V. Maxim, R. Prost, “*Image reconstruction for Compton camera applied to 3D prompt gamma imaging during ion beam therapy*”, NSS-MIC, Valencia – Spain, 2011

M.-H. Richard, M. Dahoumane, D. Dauvergne, G. Dedes, M. De Rydt, N. Freud, J.-M. Letang, **X. Lojacono**, J. Krimmer, V. Maxim, G. Montarou, C. Ray, F. Roellinghoff, E. Testa, A.-H. Walenta, “*Design Study of the Absorber Detector of a Compton Camera for On-line Control in Ion Beam Therapy*”, NSS-MIC, Valencia – Spain, 2011

## NATIONAL PEER-REVIEWED CONFERENCE PROCEEDINGS

**X. Lojacono**, V. Maxim, A. Zoglauer, F. Peyrin, R. Prost, “*A filtered backprojection reconstruction algorithm for Compton camera*”, RITS, Rennes - France, 2011

**X. Lojacono**, V. Maxim, R. Prost, “*Calcul de la matrice de probabilités de transfert en imagerie Compton 3D*”, GRETSI, Bordeaux – France, 2011

**X. Lojacono**, E. Hilaire, V. Maxim, R. Prost, “*3D LM-MLEM image reconstruction algorithms for Compton camera*”, Imagerie du Vivant, Lyon – France, 2012

J. Krimmer, L. Balleyguier, J. Baudot, S. Brons, L. Caponetto, M. Chabot, X. Chen, M. Dahoumane, D. Dauvergne, M. De Rydt, G. Dedes, R. Della Negra, S. M. Deng, C. Finck, N. Freud, J. Héroult, C. La Tessa, J.M. Létang, J.-L. Ley, **X. Lojacono**, H. Mathez, V. Maxim, G. Montarou, K. Parodi, M. Pinto, R. Pleskac D. Prieels, R. Prost, C. Ray, R. Rescigno, M.H. Richard, V. Reithinger, I. Rinaldi, F. Roellinghoff, M. Rousseau, J. Smeets, E. Testa, M. Vanstalle, M. Winter and Y. Zoccarato, “*Real-Time Online Monitoring of the Ion Range by Means of Prompt Secondary Radiations*”, ANIMMA Conference Record (Advancements in Nuclear Instrumentation Measurement Methods and their Applications), Marseille – France, 2013

E. Hilaire, C. Robert, **X. Lojacono**, C. Lartizien, I. Buvat, V. Maxim, “*Imagerie Compton en protonthérapie : de la simulation Gate à la reconstruction d’images*”, GRETSI, Brest – France, 2013

## NATIONAL PEER-REVIEWED CONFERENCE

**X. Lojacono**, M.-H. Richard, C. Ray, D. Dauvergne, E. Testa, N. Freud, J.-M. Létang, V. Maxim, R. Prost, “*Image reconstruction for Compton camera applied to 3D prompt gamma imaging during ion beam therapy*”, FranceHadron, Lyon – France, 2011

**X. Lojacono**, E. Hilaire, V. Maxim, R. Prost, “*Image reconstruction for the Compton camera: calculation of the system matrix*”, ISSSMA - Medical Imaging, Paris – France, 2013

E. Hilaire, C. Robert, **X. Lojacono**, C. Lartizien, I. Buvat, V. Maxim, “Compton imaging in proton beam therapy : from GATE simulations to image reconstruction”, ISSSMA – Medical Imaging, Paris – France, 2013



# Bibliography

- [Agostinelli *et al.* (2003)] Agostinelli, S., Allison, J., Amako, K., Apostolakis, J., Araujo, H., Arce, P., *et al.* (2003). Geant4—a simulation toolkit. *Nucl. Instrum. Methods*, 506(3):250–303.
- [Allison *et al.* (2006)] Allison, J., Amako, K., Apostolakis, J., Araujo, H., Dubois, P. A., Asai, M., *et al.* (2006). Geant4 developments and applications. *IEEE Transactions on Nuclear Science*, 53(1):270–278.
- [Ando and Kase (2009)] Ando, K. and Kase, Y. (2009). Biological characteristics of carbon-ion therapy. *International journal of radiation biology*, 85(9):715–728.
- [Andreyev *et al.* (2011)] Andreyev, A., Sitek, A., and Celler, A. (2011). Fast image reconstruction for Compton camera using stochastic origin ensemble approach. *Medical physics*, 38:429.
- [Anger (1958)] Anger, H. O. (1958). Scintillation camera. *Review of scientific instruments*, 29(1):27–33.
- [Bandstra *et al.* (2011)] Bandstra, M. S., Bellm, E. C., Boggs, S. E., Perez-Becker, D., Zoglauer, A., Chang, H.-K., Chiu, J.-L., Liang, J.-S., Chang, Y.-H., Liu, Z.-K., and Others (2011). Detection and Imaging of the Crab Nebula with the Nuclear Compton Telescope. *The Astrophysical Journal*, 738(1):8.
- [Basko *et al.* (1997)] Basko, R., Zeng, G. L., and Gullberg, G. T. (1997). Analytical reconstruction formula for one-dimensional Compton camera. *IEEE Transactions on Nuclear Science*, 44(3):1342–1346.
- [Basko *et al.* (1998)] Basko, R., Zeng, G. L., and Gullberg, G. T. (1998). Application of spherical harmonics to image reconstruction for the Compton camera. *PhysMedBiol*, 43(4):887–894.
- [Bushberg and Boone (2011)] Bushberg, J. T. and Boone, J. M. (2011). *The essential physics of medical imaging*. Lippincott Williams & Wilkins.
- [Cree and Bones (1994)] Cree, M. J. and Bones, P. J. (1994). Towards direct reconstruction from a gamma camera based on compton scattering. *IEEE Transactions on Medical Imaging*, 13(2):398–407.
- [España *et al.* (2010)] España, S., Zhu, X., Daartz, J., Liebsch, N., El Fakhri, G., Bortfeld, T., and Paganetti, H. (2010). Feasibility of In-Room PET Imaging for in Vivo Proton Beam Range Verification. *Medical Physics*, 37:3180.

- [Everett *et al.* (1977)] Everett, D. B., Fleming, J. S., Todd, R. W., and Nightingale, J. M. (1977). Gamma-radiation imaging system based on the Compton effect. *Proceedings of the Institution of Electrical Engineers*, 124(11):995.
- [Fokas *et al.* (2009)] Fokas, E., Kraft, G., An, H., and R., E.-C. (2009). Ion beam radiotherapy and cancer: Time to update ourselves. *Biochimica et Biophysica Acta (BBA) - Reviews on Cancer*, 1796(2):216 – 229.
- [Frandes *et al.* (2010)] Frandes, M., Zoglauer, A., Maxim, V., and Prost, R. (2010). A tracking compton-scattering imaging system for hadron therapy monitoring. *IEEE Transactions on Nuclear Science*, 57(1):144–150.
- [Gordon *et al.* (1970)] Gordon, R., Bender, R., and Herman, G. T. (1970). Algebraic Reconstruction Techniques (ART) for three-dimensional electron microscopy and X-ray photography. *Journal of Theoretical Biology*, 29(3):471–481.
- [Gormley *et al.* (1996)] Gormley, J. E., Clinthorne, N., Knoll, G. F., LeBlanc, J. W., Rogers, W. L., Wehe, D. K., and Wilderman, S. J. (1996). Effects of shared charge collection on Compton camera performance using pixellated Ge arrays. In *Journal of Nuclear Medicine*, volume 37, page 745. Soc Nuclear Medicine Inc 1850 Samuel Morse Dr, Reston, VA 22090-5316.
- [Gormley *et al.* (1997)] Gormley, J. E., Rogers, W. L., Clinthorne, N. H., Wehe, D. K., and Knoll, G. F. (1997). Experimental comparison of mechanical and electronic gamma-ray collimation. *Nuclear Instruments and Methods in Physics Research Section A: Accelerators, Spectrometers, Detectors and Associated Equipment*, 397(2):440–447.
- [Gunter (2006)] Gunter, D. L. (2006). Filtered backprojection algorithms for compton cameras in nuclear medicine. US Patent 7,015,477.
- [Han *et al.* (2008)] Han, L., Rogers, W. L., Huh, S. S., and Clinthorne, N. (2008). Statistical performance evaluation and comparison of a Compton medical imaging system and a collimated Anger camera for higher energy photon imaging. *Physics in Medicine and Biology*, 53(24):7029.
- [Hebert *et al.* (1990)] Hebert, T., Leahy, R., and Singh, M. (1990). Three-dimensional maximum-likelihood reconstruction for an electronically collimated single-photon-emission imaging system. *JOSA A*, 7(7):1305–1313.
- [Henriet *et al.* (2012)] Henriet, P., Testa, E., Chevallier, M., Dauvergne, D., Dedes, G., Freud, N., Krimmer, J., Létang, J. M., Ray, C., Richard, M. H., and Others (2012). Interaction vertex imaging (IVI) for carbon ion therapy monitoring: a feasibility study. *Physics in medicine and biology*, 57(14):4655.
- [Herbach *et al.* (2009)] Herbach, C.-M., Gueorguiev, A., Kong, Y., Lentering, R., Pausch, G., Plettner, C., and Stein, J. (2009). Concept study of a two-plane Compton camera designed for location and nuclide identification of remote radiation sources. In *Nuclear Science Symposium Conference Record (NSS/MIC), 2009 IEEE*, pages 909–911. IEEE.
- [Herman and Lent (1976)] Herman, G. T. and Lent, A. (1976). Iterative reconstruction algorithms. *Computers in Biology and Medicine*, 6(4):273–294.

- [Hirasawa and Tomitani (2003)] Hirasawa, M. and Tomitani, T. (2003). An analytical image reconstruction algorithm to compensate for scattering angle broadening in Compton cameras. *Physics in medicine and biology*, 48(8):1009–26.
- [Hudson and Larkin (1994)] Hudson, H. M. and Larkin, R. S. (1994). Accelerated image reconstruction using ordered subsets of projection data. *IEEE Transactions on Medical Imaging*, 13(4):601–609.
- [Huesman *et al.* (2000)] Huesman, R. H., Klein, G. J., Moses, W. W., Qi, J., Reutter, B. W., and Virador, P. R. G. (2000). List-mode maximum-likelihood reconstruction applied to positron emission mammography (PEM) with irregular sampling. *IEEE Transactions on Medical Imaging*, 19(5):532–537.
- [Ishikawa *et al.* (2001)] Ishikawa, M., Kobayashi, T., Sakurai, Y., and Kanda, K. (2001). Optimization technique for a Prompt Gamma-ray SPECT collimator system. *Journal of radiation research*, 42(4):387–400.
- [Kang and Kim (2009)] Kang, B.-H. and Kim, J.-W. (2009). Monte Carlo design study of a gamma detector system to locate distal dose falloff in proton therapy. *IEEE Transactions on Nuclear Science*, 56(1):46–50.
- [Kim *et al.* (2007)] Kim, S. M., Lee, J. S., Lee, M. N., Lee, J. H., Lee, C. S., Kim, C.-H., Lee, D. S., and Lee, S.-J. (2007). Two approaches to implementing projector-backprojector pairs for 3D reconstruction from Compton scattered data. *Nuclear Instruments and Methods in Physics Research Section A Accelerators Spectrometers Detectors and Associated Equipment*, 571(1-2):255 –258.
- [Kim *et al.* (2010)] Kim, S. M., Lee, J. S., Lee, C. S., Kim, C. H., Lee, M. C., Lee, D. S., and Lee, S.-J. (2010). Fully three-dimensional OSEM-based image reconstruction for Compton imaging using optimized ordering schemes. *Physics in medicine and biology*, 55(17):5007–27.
- [Kim *et al.* (2012)] Kim, C. H., Park, J. H., Seo, H., and Lee, H. R. (2012). Gamma electron vertex imaging and application to beam range verification in proton therapy. *Medical physics*, 39:1001.
- [Kippen (2004)] Kippen, R. M. (2004). The GEANT low energy Compton scattering (GLECS) package for use in simulating advanced Compton telescopes. *New Astronomy Reviews*, 48(1):221–225.
- [Klein and Nishina (1929)] Klein, O. and Nishina, T. (1929). Über die Streuung von Strahlung durch freie Elektronen nach der neuen relativistischen Quantendynamik von Dirac. *Zeitschrift für Physik*, 52(11-12):853–868.
- [Kormoll *et al.* (2011)] Kormoll, T., Fiedler, F., Schöne, S., Wüstemann, J., Zuber, K., and Enghardt, W. (2011). A Compton imager for in-vivo dosimetry of proton beams–A design study. *Nuclear Instruments and Methods in Physics Research Section A: Accelerators, Spectrometers, Detectors and Associated Equipment*, 626:114–119.
- [Krämer *et al.* (2000)] Krämer, M., Jäkel, O., Haberer, T., Kraft, G., Schardt, D., and Weber, U. (2000). Treatment planning for heavy-ion radiotherapy: physical beam model and dose optimization. *Physics in medicine and biology*, 45(11):3299–317.

- [Kuykens and Audet (1988)] Kuykens, H. J. P. and Audet, S. A. (1988). A 3\(\times\)3 silicon drift chamber array for application in an electronic collimator. *Nuclear Instruments and Methods in Physics Research Section A: Accelerators, Spectrometers, Detectors and Associated Equipment*, 273(2):570–574.
- [Lange *et al.* (1987)] Lange, K., Bahn, M., and Little, R. (1987). A theoretical study of some maximum likelihood algorithms for emission and transmission tomography. *IEEE Transactions on Medical Imaging*, 6(2):106–114.
- [Lange and Carson (1984)] Lange, K. and Carson, R. (1984). EM reconstruction algorithms for emission and transmission tomography. *J Comput Assist Tomogr*, 8(2):306–316.
- [LeBlanc *et al.* (1999)] LeBlanc, J. W., Clinthorne, N. H., Hua, C., Rogers, W. L., Wehe, D. K., and Wilderman, S. J. (1999). A Compton camera for nuclear medicine applications using  $^{113m}\text{In}^1$ . *Nuclear Instruments and Methods in Physics Research Section A: Accelerators, Spectrometers, Detectors and Associated Equipment*, 422(1):735–739.
- [Lee *et al.* (2008)] Lee, S.-J., Lee, M. N., Nguyen, V.-G., Kim, S. M., and Lee, J. S. (2008). Three-dimensional edge-preserving regularization for Compton camera reconstruction. In *Nuclear Science Symposium Conference Record, 2008. NSS'08. IEEE*, pages 4223–4228. IEEE.
- [Liang *et al.* (1989)] Liang, Z., Jaszcak, R., and Greer, K. (1989). On Bayesian image reconstruction from projections: uniform and nonuniform a priori source information. *IEEE Transactions on Medical Imaging*, 8(3):227–235.
- [Llosá *et al.* (2011)] Llosá, G., Barrio, J., Lacasta, C., Callier, S., Raux, L., and de La Taille, C. (2011). First tests in the application of silicon photomultiplier arrays to dose monitoring in hadron therapy. *Nuclear Instruments and Methods in Physics Research Section A: Accelerators, Spectrometers, Detectors and Associated Equipment*, 648:S96–S99.
- [Lojacono *et al.* (2011)] Lojacono, X., Maxim, V., and Prost, R. (2011). Calcul de la matrice des probabilités de transfert en imagerie compton 3d. In *XXIIIe Colloque GRETSI - Traitement du Signal et des Images (GRETSI'11)*, page ID432, Bordeaux, France.
- [Mackin *et al.* (2012)] Mackin, D., Peterson, S., Beddar, S., and Polf, J. (2012). Evaluation of a stochastic reconstruction algorithm for use in Compton camera imaging and beam range verification from secondary gamma emission during proton therapy. *Physics in medicine and biology*, 57(11):3537.
- [Maxim *et al.* (2009)] Maxim, V., Frandès, M., and Prost, R. (2009). Analytical inversion of the Compton transform using the full set of available projections. *Inverse Problems*, 25(9):95001.
- [Min *et al.* (2006)] Min, C.-H., Kim, C. H., Youn, M.-Y., and Kim, J.-W. (2006). Prompt gamma measurements for locating the dose falloff region in the proton therapy. *Applied physics letters*, 89(18):183517.
- [Moteabbed *et al.* (2011)] Moteabbed, M., Espana, S., and Paganetti, H. (2011). Monte Carlo patient study on the comparison of prompt gamma and PET imaging for range verification in proton therapy. *Physics in medicine and biology*, 56(4):1063.

- [Park (2009)] Park, I. (2009). A new approach to produce spread-out Bragg peak using the MINUIT fit. *Current Applied Physics*, 9(4):852–855.
- [Parodi *et al.* (2007)] Parodi, K., Paganetti, H., Cascio, E., Flanz, J. B., Bonab, A. A., Alpert, N. M., Lohmann, K., and Bortfeld, T. (2007). PET/CT imaging for treatment verification after proton therapy: a study with plastic phantoms and metallic implants. *Medical physics*, 34:419.
- [Parodi *et al.* (2008)] Parodi, K., Bortfeld, T., and Haberer, T. (2008). Comparison between in-beam and offline positron emission tomography imaging of proton and carbon ion therapeutic irradiation at synchrotron-and cyclotron-based facilities. *International Journal of Radiation Oncology Biology Physics*, 71(3):945–956.
- [Parra (2000)] Parra, L. C. (2000). Reconstruction of cone-beam projections from compton scattered data. *IEEE Transactions on Nuclear Science*, 47(4):1543–1550.
- [Peloso *et al.* (2011)] Peloso, R., Fiorini, C., Basilavecchia, M., Frizzi, T., Smeets, J., Roellinghoff, F., Prieels, D., Stichelbaut, F., Benilov, A., and Others (2011). Application of the HICAM camera for imaging of prompt gamma rays in measurements of proton beam range. In *Nuclear Science Symposium and Medical Imaging Conference (NSS/MIC), 2011 IEEE*, pages 2285–2289. IEEE.
- [Peterson *et al.* (2010)] Peterson, S. W., Robertson, D., and Polf, J. (2010). Optimizing a three-stage Compton camera for measuring prompt gamma rays emitted during proton radiotherapy. *Physics in medicine and biology*, 55(22):6841.
- [Polf *et al.* (2009)] Polf, J. C., Peterson, S., Ciangaru, G., Gillin, M., and Beddar, S. (2009). Prompt gamma-ray emission from biological tissues during proton irradiation: a preliminary study. *Physics in medicine and biology*, 54(3):731.
- [Qi and Leahy (2006)] Qi, J. and Leahy, R. M. (2006). Iterative reconstruction techniques in emission computed tomography. *Physics in Medicine and Biology*, 51(15):R541.
- [Richard *et al.* (2011)] Richard, M.-H., Chevallier, M., Dauvergne, D., Freud, N., Henriquet, P., Le Foulher, F., Letang, J. M., Montarou, G., Ray, C., Roellinghoff, F., and Others (2011). Design Guidelines for a Double Scattering Compton Camera for Prompt- $\gamma$ . *IEEE Transactions on Nuclear Science*, 58(1):87–94.
- [Richard *et al.* (2012)] Richard, M. H., Dahoumane, M., Dauvergne, D., De Rydt, M., Dedes, G., Freud, N., Krimmer, J., Letang, J.-M., Lojacono, X., Maxim, V., Montarou, G., Ray, C., Roellinghoff, F., Testa, E., and Walenta, A. H. (2012). Design Study of the Absorber Detector of a Compton Camera for On-Line Control in Ion Beam Therapy. *IEEE Transactions on Nuclear Science*, 59(5):1850–1855.
- [Robert *et al.* (2013)] Robert, C., Dedes, G., Battistoni, G., Böhnen, T. T., Buvat, I., Cerutti, F., Chin, M. P. W., Ferrari, A., Gueth, P., Kurz, C., and Others (2013). Distributions of secondary particles in proton and carbon-ion therapy: a comparison between GATE/Geant4 and FLUKA Monte Carlo codes. *Physics in medicine and biology*, 58(9):2879.
- [Robertson *et al.* (2011)] Robertson, D., Polf, J. C., Peterson, S. W., Gillin, M. T., and Beddar, S. (2011). Material efficiency studies for a Compton camera designed to measure characteristic prompt gamma rays emitted during proton beam radiotherapy. *Physics in medicine and biology*, 56(10):3047.

- [Roellinghoff *et al.* (2011)] Roellinghoff, F., Richard, M.-H., Chevallier, M., Constanzo, J., Dauvergne, D., Freud, N., Henriet, P., Le Foulher, F., Létang, J. M., Montarou, G., and Others (2011). Design of a Compton camera for 3D prompt- $\gamma$  imaging during ion beam therapy. *Nuclear Instruments and Methods in Physics Research Section A: Accelerators, Spectrometers, Detectors and Associated Equipment*, 648:S20—S23.
- [Sauve *et al.* (1999)] Sauve, A. C., Hero III, A. O., Rogers, W. L., Wilderman, S. J., and Clinthorne, N. H. (1999). 3D image reconstruction for a Compton SPECT camera model. *IEEE Transactions on Nuclear Science*, 46(6):2075–2084.
- [Schönfelder *et al.* (1973)] Schönfelder, V., Hirner, A., and Schneider, K. (1973). A telescope for soft gamma ray astronomy. *Nuclear Instruments and Methods*, 107(2):385–394.
- [Siddon (1985)] Siddon, R. L. (1985). Fast calculation of the exact radiological path for a three-dimensional ct array. *Medical Physics*, 12(2):252–255.
- [Singh and Brechner (1990)] Singh, M. and Brechner, R. R. (1990). Experimental test-object study of electronically collimated SPECT. *J. Nucl. Med*, 31(2):178–186.
- [Singh and Doria (1983)] Singh, M. and Doria, D. (1983). An electronically collimated gamma camera for single photon emission computed tomography. Part II: Image reconstruction and preliminary experimental measurements. *Medical Physics*, 10:428.
- [Singh and Doria (1985)] Singh, M. and Doria, D. (1985). Single photon imaging with electronic collimation. *IEEE Transactions on Nuclear Science*, 32(1):843–847.
- [Smith (2005)] Smith, B. (2005). Reconstruction methods and completeness conditions for two compton data models. *JOSA A*, 22(3):445–459.
- [Solomon and Ott (1988)] Solomon, C. J. and Ott, R. J. (1988). Gamma ray imaging with silicon detectors - a Compton camera for radionuclide imaging in medicine. *Nuclear Instruments and Methods in Physics Research Section A: Accelerators, Spectrometers, Detectors and Associated Equipment*, 273(2):787–792.
- [Strong (2003)] Strong, A. W. (2003). Maximum Entropy imaging with INTEGRAL/SPI data. *Astronomy and astrophysics - Berlin*, 411(1):L127–L130.
- [Strong *et al.* (1990)] Strong, W. A., Bennett, K., Cabeza-Orcel, P., Deerenberg, A., Diehl, R., den Herder, W. J., Hermsen, W., Lichti, G., Lockwood, J., McConnell, M., and Others (1990). Maximum Entropy Imaging with COMPTEL data. In *International Cosmic Ray Conference*, volume 4, page 154.
- [Testa *et al.* (2009)] Testa, E., Bajard, M., Chevallier, M., Dauvergne, D., Le Foulher, F., Freud, N., Létang, J. M., Poizat, J.-C., Ray, C., and Testa, M. (2009). Dose profile monitoring with carbon ions by means of prompt-gamma measurements. *Nuclear Instruments and Methods in Physics Research Section B: Beam Interactions with Materials and Atoms*, 267(6):993–996.
- [Todd *et al.* (1974)] Todd, R. W., Nightingale, J. M., and Everett, D. B. (1974). A proposed gamma camera. *Nature*, 251:132–134.
- [Tomitani and Hirasawa (2002)] Tomitani, T. and Hirasawa, M. (2002). Image reconstruction from limited angle Compton camera data. *Physics in Medicine and Biology*, 47(12):2129–2145.

- [Tornga *et al.* (2009)] Tornga, S. R., Sullivan, M. R., and Sullivan, J. P. (2009). Three-dimensional compton imaging using list-mode maximum likelihood expectation maximization. *IEEE Transactions on Nuclear Science*, 56(3):1372–1376.
- [Truong *et al.* (2007)] Truong, T. T., Nguyen, M. K., and Zaidi, H. (2007). The Mathematical Foundations of 3D Compton Scatter Emission Imaging. *International Journal of Biomedical Imaging*, 2007:92780.
- [Wilderman *et al.* (1998)] Wilderman, S. J., Clinthorne, N. H., Fessler, J. A., and Rogers, W. L. (1998). List-mode maximum likelihood reconstruction of compton scatter camera images in nuclear medicine. In *Nuclear Science Symposium, 1998. Conference Record. 1998 IEEE*, volume 3, pages 1716–1720. IEEE.
- [Xu and He (2007)] Xu, D. and He, Z. (2007). Gamma-ray energy-imaging integrated spectral deconvolution. *Nuclear Instruments and Methods in Physics Research Section A: Accelerators, Spectrometers, Detectors and Associated Equipment*, 574(1):98–109.
- [Zhao and Reader (2003)] Zhao, H. and Reader, A. J. (2003). Fast ray-tracing technique to calculate line integral paths in voxel arrays. In *Nuclear Science Symposium Conference Record, 2003 IEEE*, volume 4, pages 2808–2812. IEEE.
- [Zoglauer (2005)] Zoglauer, A. (2005). *First Light for the next Generation of Compton and Pair telescopes*. PhD thesis.
- [Zoglauer *et al.* (2007)] Zoglauer, A., Andritschke, R., Kanbach, G., and Boggs, S. E. (2007). A Bayesian-based Method for Particle Track Identification in Low-energy Pair-creation Telescopes. In *AIP Conference Proceedings*, volume 921, page 584.
- [Zoglauer *et al.* (2008)] Zoglauer, A., Andritschke, R., Boggs, S. E., Schopper, F., Weidenpointner, G., and Wunderer, C. B. (2008). MEGAlib: simulation and data analysis for low-to-medium-energy gamma-ray telescopes. In *Society of Photo-Optical Instrumentation Engineers (SPIE) Conference Series*, volume 7011 of *Society of Photo-Optical Instrumentation Engineers (SPIE) Conference Series*.
- [Zoglauer and Boggs (2007)] Zoglauer, A. and Boggs, S. E. (2007). Application of neural networks to the identification of the compton interaction sequence in compton imagers. In *Nuclear Science Symposium Conference Record, 2007. NSS'07. IEEE*, volume 6, pages 4436–4441. IEEE.



---

**TITRE EN FRANCAIS**

Reconstruction d'images pour la caméra Compton avec application en hadronthérapie

---

**RESUME EN FRANCAIS**

La caméra Compton est un dispositif permettant d'imager les sources de rayonnement gamma. Ses avantages sont sa sensibilité (absence de collimateur mécanique) et la possibilité de reconstruire des images 3D avec un dispositif immobile. Elle également adaptée pour des sources à large spectre énergétique. Ce dispositif est un candidat prometteur en médecine nucléaire et en hadronthérapie. Ces travaux, financés par le projet européen ENVISION (European NoVel Imaging Systems for ION therapy) Coopération-FP7, portent sur le développement de méthodes de reconstruction d'images pour la caméra Compton pour la surveillance de la thérapie par ions. Celle-ci nécessite idéalement une reconstruction temps réel avec une précision millimétrique, même si le nombre de données acquises est relativement faible. Nous avons développé des méthodes analytiques et itératives. Leurs performances sont analysées dans le contexte d'acquisitions réalistes (géométrie de la caméra, nombre d'événements). Nous avons développé une méthode analytique de rétroprojection filtrée. Cette méthode est rapide mais nécessite beaucoup de données. Nous avons également développé des méthodes itératives utilisant un algorithme de maximisation de la fonction de vraisemblance. Nous avons proposé un modèle probabiliste pour l'estimation des éléments de la matrice système nécessaire à la reconstruction et nous avons développé différentes approches pour le calcul de ses éléments : l'une néglige les incertitudes de mesure sur l'énergie, l'autre les prend en compte en utilisant une distribution gaussienne. Nous avons étudié une méthode simplifiée utilisant notre modèle probabiliste. Plusieurs reconstructions sont menées à partir de données simulées, obtenues avec Geant4, mais provenant aussi de plusieurs prototypes simulés de caméra Compton proposés par l'Institut de Physique Nucléaire de Lyon (IPNL) et par le Centre de recherche de Dresden-Rossendorf en Allemagne. Les résultats sont prometteurs et des études plus poussées, à partir de données encore plus réalistes, viseront à les confirmer.

---

**TITRE EN ANGLAIS**

Image reconstructions for Compton camera with application in hadrontherapy

---

**RESUME EN ANGLAIS**

The Compton camera is a device for imaging gamma radiation sources. The advantages of the system lie in its sensitivity, due to the absence of mechanical collimator, and the possibility of imaging wide energy spectrum sources. These advantages make it a promising candidate for application in hadrontherapy. Funded by the european project ENVISION, FP7-Cooperation Work Program, this work deals with the development of image reconstruction methods for the Compton camera. We developed both analytical and iterative methods in order to reconstruct the source from cone-surface projections. Their performances are analyzed with regards to the context (geometry of the camera, number of events). We developed an analytical method using a Filtered BackProjection (FBP) formulation. This method is fast but really sensitive to the noise. We have also developed iterative methods using a List Mode-Maximum Likelihood Expectation Maximization (LM-MLEM) algorithm. We proposed a new probabilistic model for the computation of the elements of the system matrix and different approaches for the calculation of these elements neglecting or not the measurement uncertainties. We also implemented a simplified method using the probabilistic model we proposed. The novelty of the method also lies on the specific discretization of the cone-surface projections. Several studies are carried out upon the reconstructions of simulated data worked out with Geant4, but also simulated data obtained from several prototypes of Compton cameras under study at the Institut de Physique Nucléaire de Lyon (IPNL) and at the Research Center of Dresden-Rossendorf. Results are promising, and further investigations on more realistic data are to be done.

---

**MOTS-CLES**

Compton imaging, Single Photon Emission Computed tomography, gamma-ray detectors, hadrontherapy, image reconstruction, prompt-gamma ray, reconstruction algorithms

---

**INTITULE ET ADRESSE DE L'U.F.R. OU DU LABORATOIRE**

Université de Lyon, CREATIS ; CNRS UMR5220 ; Inserm U1044 ; INSA-Lyon ; Université Lyon 1, 7 Av. Jean Capelle, 69621 VILLEURBANNE, France.